UNIVERSITY OF CAPE TOWN
IYUNIVESITHI YASEKAPA • UNIVERSITEIT VAN KAAPSTAD

# Kinematic State Estimation using Multiple DGPS/MEMS-IMU Sensors

**Do Yeou Ku**

Prepared for: Dr. A. Patel

University of Cape Town
Department of Electrical and Electronics Engineering

Submitted in partial fulfilment of the requirements for the degree of
Master's in Electrical Engineering of the University of Cape Town

25 February 2020

# Declaration

I, Do Yeou Ku, hereby declare that:

1. neither the substance nor any part of the above thesis has been submitted in the past, or is being, or is to be submitted for a degree at this University or at any other university.
2. I know that plagiarism is wrong. Plagiarism is to use another's work and pretend that it is one's own.
3. I have used the IEEE convention for citation and referencing. Each contribution to, and quotation in, this report from the work(s) of other people has been attributed, and has been cited and referenced.
4. I have not allowed, and will not allow, anyone to copy my work with the intention of passing it off as their own work or part thereof.
5. I know the meaning of plagiarism and declare that all the work in the document, save for that which is properly acknowledged, is my own. This thesis/dissertation has been submitted to the Turnitin module (or equivalent similarity and originality checking software) and I confirm that my supervisor has seen my report and any concerns revealed by such have been resolved with my supervisor.

Do Yeou Ku

25 February 2020

# Acknowledgement

I have been encouraged and motivated by many people past two years to complete this study and a page is not nearly enough to list every person. Therefore, I am using this page to highlight a number of people who have shown me continuous support.

Dr. Amir Patel, my supervisor. Amir, your continuous interest and investment in this project have inspired me to complete this project. We both know that I would have given up a long time ago without your care and understanding.

My family. I am aware that it is unlikely that you would read this but I want to let everyone know how amazing you are. I want to apologize for my lack of presence to pursue my career in engineering and I am very grateful for your understanding and unconditional love.

Mr. Justin Pead, my best friend and partner. We both know that you were my favourite rubber duck throughout the debugging process. I cannot thank you enough for listening to all my grunts whenever I got lost in the black hole of research and I thank you for reminding me of the values in life other than my career.

Mr. Callen Fisher (soon Dr. Callen Fisher), my friend and best colleague. You have assisted me throughout this project. You were always willing to give a hand and never rejected my request for help.

My fellow Mechatronics lab colleagues. One person in particular that I would like to thank is Mr Josh van Zyl. Without his ability to build a testing rig, my results would have been meaningless.

Lastly, I would like to thank the Research Contracts and Innovation (RCI) department of University of Cape Town. You have financially assisted this project and without your investment, this project could have not come this far.

# Abstract

Animals have evolved over billions of years and understanding these complex and intertwined systems have potential to advance the technology in the field of sports science, robotics and more. As such, a gait analysis using Motion Capture (MOCAP) technology is the subject of a number of research and development projects aimed at obtaining quantitative measurements. Existing MOCAP technology has limited the majority of studies to the analysis of the steady-state locomotion in a controlled (indoor) laboratory environment.

MOCAP systems such as the optical, non-optical acoustic and non-optical magnetic MOCAP systems require predefined capture volume and controlled environmental conditions whilst the non-optical mechanical MOCAP system impedes the motion of the subject. Although the non-optical inertial MOCAP system allows MOCAP in an outdoor environment, it suffers from measurement noise and drift and lacks global trajectory information. The accuracy of these MOCAP systems are known to decrease during the tracking of the transient locomotion.

Quantifying the manoeuvrability of animals in their natural habitat to answer the question ***"Why are animals so manoeuvrable?"*** remains a challenge. This research aims to develop an outdoor MOCAP system that will allow tracking of the steady-state as well as the transient locomotion of an animal in its natural habitat outside a controlled laboratory condition.

A number of researchers have developed novel MOCAP systems with the same aim of creating an outdoor MOCAP system that is aimed at tracking the motion outside a controlled laboratory (indoor) environment with unlimited capture volume. These novel MOCAP systems are either not validated against the commercial MOCAP systems or do not have comparable sub-millimetre accuracy as the commercial MOCAP systems.

The developed *DGPS/MEMS-IMU multi-receiver* fusion MOCAP system was assessed to have global trajectory accuracy of $\pm 0.0394m$, relative limb position accuracy of $\pm 0.006497m$. To conclude the research, several recommendations are made to improve the developed MOCAP system and to prepare for a field-testing with a wild animal from a family of a terrestrial *megafauna*.

**Keywords:** *MOCAP, MEMS-IMU, Kalman, single-differenced, double-differenced, DGPS, LAMBDA*.

# Contents

# List of Figures

# List of Tables

# Acronyms

| | |
|---|---|
| **2D** | Two Dimension(al) |
| **3D** | Three Dimension(al) |
| **ADC** | Analogue to Digital Converter |
| **BIOS** | Basic Input/Output System |
| **BPB** | Basic Parameter Block |
| **CCD** | Custom Clearance Declaration |
| **CDMA** | Code Division Multiple Access |
| **CIR** | Cascading Integer Resolution |
| **CPU** | Central Processing Unit |
| **DD** | Double Difference(d) |
| **DGNSS** | Differential Global Navigation Satellite Systems |
| **DGPS** | Differential Global Positioning Systems |
| **DMA** | Direct Memory Access |
| **DOP** | Dilution of Precision |
| **ECEF** | Earth-Centered Earth-Fixed |
| **ECI** | Earth-Centered Inertial |
| **EEPROM** | Electrically Erasable Programmable Read-Only Memory |
| **EKF** | Extended Kalman filter |
| **EMI** | Electromagnetic Interference |
| **ENU** | East-North-Up |
| **ESD** | Electrostatic Discharge |

| | |
|---|---|
| **FATFS** | FAT/exFAT File System |
| **FDMA** | Frequency Division Multiple Access |
| **GNSS** | Global Navigation Satellite Systems |
| **GPS** | Global Positioning Systems |
| **HSE** | High Speed External |
| **HSI** | High Speed Internal |
| **I$^2$C** | Inter Integrated Circuit |
| **IA** | Integer Aperture |
| **ICA** | Ionosphere Correction Algorithm |
| **IMU** | Inertial Measurement Units |
| **INS** | Inertial Navigation System |
| **ISR** | Interrupt Service Routine |
| **LAMBDA** | Least Squares Ambiguity Decorrelation Adjustment |
| **LNA** | Low-Noise Amplifier |
| **LOS** | Line-of-Sight |
| **LQG** | Linear Quadratic Gaussian |
| **LS** | Least Squares |
| **MCO** | Micro-controller Clock Output |
| **MEMS** | Micro Electro Mechanical Systems |
| **MMC** | Multi Media Card |
| **MOCAP** | Motion Capture |
| **MOS** | Metal Oxide Semiconductor |
| **NLOS** | Non-Line-of-Sight |
| **OCXO** | Oven Controlled Crystal Oscillator |
| **ODR** | Output Data Rate |
| **PCB** | Printed Circuit Board |
| **PCO** | Phase Center Offset |
| **PDOP** | Positional Dilution of Precision |

| | |
|---|---|
| **PLL** | Phase Locked Loop |
| **PPS** | Pulse per Second |
| **PRN** | Pseudo Random Noise |
| **RAM** | Read Access Memory |
| **RF** | Radio Frequency |
| **RINEX** | Receiver Independent Exchange Format |
| **RMS** | Root Mean Square |
| **RTK** | Real Time Kinematic |
| **RTOS** | Real-Time Operating System |
| **SAW** | Surface Acoustic Wave |
| **SBAS** | Satellite-Based Augmentation Systems |
| **SD** | Single Difference(d) |
| **SDHC** | SD High Capacity |
| **SDIO** | Secure Digital Input Output |
| **SDSC** | SD Small Capacity |
| **SMD** | Surface Mount Device |
| **SNR** | Signal-to-Noise Ratio |
| **SoC** | State-of-Charge |
| **SoC** | System-on-Chip |
| **SPI** | Serial Peripheral Interface |
| **TCAR** | Three Carrier Ambiguity Resolution |
| **TCXO** | Temperature Compensated Crystal Oscillator |
| **UART** | Universal Asynchronous Receiver Transmitter |
| **UERE** | User Equivalent Range Error |
| **USB** | Universal Serial Bus |
| **WPAN** | Wireless Personal Area Network |
| **ZHD** | Zenith Hydro-static Delay |
| **ZTD** | Zenith Total Delay |
| **ZWD** | Zenith Wet Delay |

# List of Symbols

| | |
|---|---|
| $\alpha$ | Angular acceleration |
| $\omega$ | Angular rate |
| $\Phi$ | Carrier-phase measurement |
| $P$ | Code measurement |
| $\sigma^2$ | Covariance |
| $\nabla\Delta\Phi$ | DD carrier-phase measurement |
| $\nabla\Delta P$ | DD code measurement |
| $I$ | Identity matrix |
| $\theta$ | Pitch angle |
| $\phi$ | Roll angle |
| $\Delta t$ | Sample interval |
| $\Delta\Phi$ | SD carrier-phase measurement |
| $\Delta P$ | SD code measurement |
| $f$ | Specific force |
| $\psi$ | Yaw angle |

# Chapter 1

# Introduction

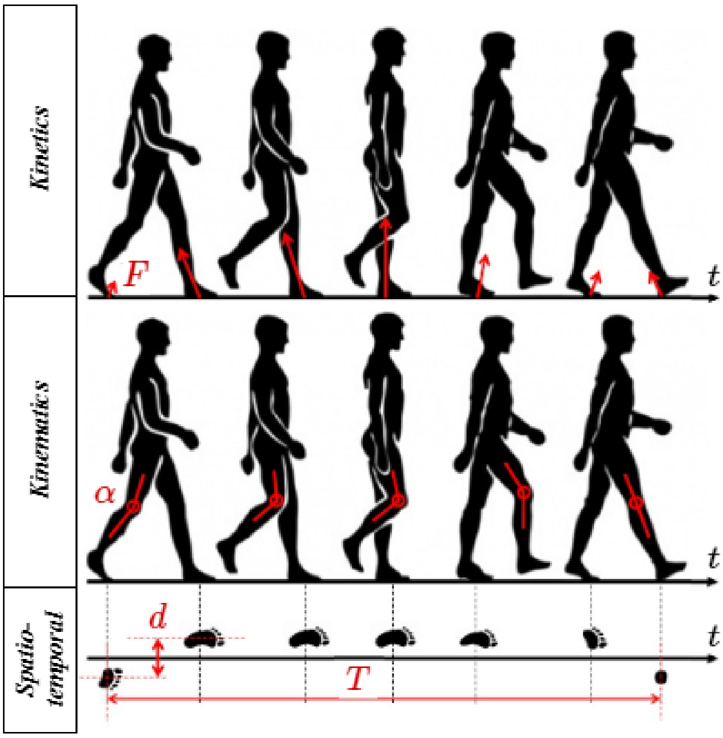

**Figure 1.1:** The different domains in gait analysis: kinetics, kinematics and spatio-temporal domains. Image from [1].

Nature is a complex, intertwined and optimised system that evolved over billions of years. Therefore, inspiration from nature has potential to advance research, especially in the field of sport science and robotics. Researchers, therefore, constantly seek methods to understand the kinematics and kinetics of animals as shown in Figure 1.1. Accordingly, advancement in technologies such as Motion Capture (MOCAP) systems that allow quantitative analysis of different animal gaits are of great importance.

## 1.1 Background and Motivation to the Study

With the advancement in technology, the times of subjective gait analysis based on observations are over and researchers seek to obtain quantitative measurements of the different kinematic and kinetic quantities associated with different gaits [23]. Such systematic study of animal locomotion is known as the gait analysis.

Gait analysis dates back to the nineteenth century and it is currently the subject of numerous research and development projects as the knowledge gained from such research advances a variety of fields such as sports science and robotics. Therefore, there is an increasing need for MOCAP systems that allows one to answer the question: ***"Why are animals so manoeuvrable?"*** quantitatively.

In the field of medicine, MOCAP systems allow clinicians to monitor and evaluate their patients' gait quantitatively over time, facilitating early diagnosis of chronic musculo-skeletal injuries, neurological diseases and disorders [23]. Not only that, clinicians are given the capability to assign treatment procedures that are tailored for the patients' unique needs and can estimate the clinical treatment outcome [24].

Savic et al. [25] utilised the *OptiTrack* MOCAP system with a neural network classification algorithm to discern clinically healthy knee joints from knee joints with ligament deficiency or degenerative disease. They recognised and emphasised the necessity of portable and accessible equipment to monitor and quantify everyday physical activities to evaluate the quality of life of patients and to treat them with the appropriate therapy.

In sports science, athletes, trainers and scientists utilise MOCAP systems to analyse a particular motion and identify errors and improvements in the execution of the technique [26] [27] [28]. Furthermore, MOCAP systems are utilised to pre-determine and prevent risks and possible injuries due to incorrect execution of the technique [28].

Recently, kinematic and kinetic analysis of Olympic Alpine ski racers using MOCAP system revealed information directly related to the safety of the athletes during competitions [29]. This in turn raised the desire for individualised training and skiing equipment amongst the athletes and led to the promulgation of new regulations by the International Ski Federation (FIS), demonstrating the benefit of the use of MOCAP technology in the field of sport science [29].

In the field of bio-mimicry, researchers and engineers seek solutions to complex problems by studying animals found in nature [30] [31]. MOCAP technology is used by Gong et al. [32] to discover the necessity of waist flexibility in maintaining balance and transferring the zero moment point promptly during transient motion. Such discovery has found to have the potential to improve the resemblance of the human gait in anthropomorphic robots whose goals are to interact and coexist with humans without becoming an object of aversion.

In [33] and [34], Yunardi et al. extensively demonstrated the use of MOCAP technology in the field of robotics. Yunardi et al. employed the trajectory plan obtained from MOCAP data of a human to simulate a leg swing manoeuvre of Homo sapiens on a robotic leg platform [33]. The performance of the leg swing robot was then validated using MOCAP technology [34].

The accuracy of the motion recognition technology is crucial in the applications and innovations that are expected to function promptly in response to the motion of a human such as a service robot with a goal to improve the quality of living [35] and it is continuously improved by adding the MOCAP data [36] [37] [38] [35].

The MOCAP technology is integrated into the content creation process by the video game production and film industry to create naturally animated character and add special effects. Accurate MOCAP data of an actor is re-targeted onto a new character, resulting in an animated subject with the same motion and facial expression but with new appearances [39].

Apart from medical science, sports science, robotics, automation and animation, MOCAP technology is also used in the field of oceanography and fisheries science [40]; work-space determination for virtual reality [41] and production quality control [42]. However, majority gait analysis studies are heavily influenced by a number of constraints posed by a type of MOCAP system used.

A commercial optical MOCAP system from *Charn-wood Dynamics Ltd.*, *OptiTrack*, *PhaseSpace Inc.*, *Qualisys AB* or *Vicon Motion Systems Ltd.* is commonly used by researchers for their sub-centimetre accuracy [43]. However, an optical MOCAP system restricts the capture volume and is often limited to a controlled indoor environment [27]. Therefore, an optical MOCAP system is not feasible for tracking a terrestrial *megafauna* in its natural habitat because it is incomprehensible and cannot respond to requests or orders unless it is trained by humans.

An inertial MOCAP system is another type of MOCAP systems that is favoured by many researchers as it allows gait analysis of a subject outside of a controlled laboratory environment [23] [28]. However, it is known that an inertial MOCAP system suffers from inherent sensor errors and is, therefore, less accurate than an optical MOCAP system [43]. Besides, an inertial MOCAP system lacks global positional information and is not feasible for estimation of kinetic quantities.

Most importantly, the complexity and difficulty in the implementation of a MOCAP system increases with an increase in dynamics of locomotion. Consequently, in comparison to steady-state locomotion, transient locomotion such as rapid acceleration and deceleration as well as near-instantaneous stops and turns that are fundamental to animal survival in nature are not well understood by researchers [43]. As a result, technologies such as prostheses and nature-inspired robots cannot achieve the level of manoeuvrability of their counterparts found in nature.

With great difficulty in quantifying the manoeuvrability of the animals in their natural habitat, Wilson et al. [44] and [45] remain to be the only researchers who have utilised a strapped-down MOCAP system on the fastest terrestrial *megafauna*, a cheetah (an *acinonyx jubatus*), in its natural habitat. Nath et al. [2] recently utilised a *DeepLabCut*-based optical MOCAP system to track an *acinonyx jubatus* in its natural habitat.

Meanwhile, Brodie et al. [46], Supej [47] and Gilgien et al. [48] are the only researchers who managed to track the motion and the global trajectory of an athlete (a ski racer) outside a controlled (indoor) laboratory environment over a 300 m track [46]. Unfortunately, their system is not validated quantitatively as no commercial MOCAP system was available as a comparison.

Henceforth, this report investigates the development of an outdoor MOCAP system which delivers high positional accuracy during the tracking of the steady-state and transient locomotion.

## 1.2 Aim of the Study

This research was aimed at developing a MOCAP system that was capable of tracking the steady-state locomotion as well as the transient locomotion of an animal outside a controlled laboratory environment (indoor), that is an outdoor environment that is less restrictive than the controlled laboratory condition. To achieve this aim, a number of objectives needed to be satisfied.

### 1.2.1 Objectives of the Study

The objectives of the research were to develop a novel MOCAP system and evaluate its capability in tracking the steady-state and transient locomotion, outside a laboratory environment. Consequently, the objectives required to achieve this goal are as follows:

1. Literature review on the existing MOCAP systems and their advantages and disadvantages;
2. Definition of a novel MOCAP system that is feasible to meet the aim of the study;
3. Development of the hardware and firmware integrated sensors;
4. Modelling and characterisation of the sensor measurement errors;
5. Development of the state estimation algorithm to reconstruct the observed motion;
6. Evaluation of the developed novel MOCAP system on a mechanical rig of known motion.

### 1.2.2 Research Questions

The following research questions were asked and answered throughout the study:

1. Which type of MOCAP system allows accurate positional tracking of the steady-state and transient locomotion of an animal in a less-restrictive outdoor environment?
2. Does integration of Global Positioning Systems (GPS) or Differential Global Positioning Systems (DGPS) improve the applicability and/or performance of the traditional Micro Electro Mechanical Systems (MEMS)-Inertial Measurement Units (IMU) MOCAP system?
3. Is it possible to achieve the positional accuracy of the existing commercial MOCAP systems using a DGPS/MEMS-IMU integrated fusion MOCAP system?
4. Is integration of DGPS on each limb segment beneficial compared to the Micro Electro Mechanical Systems (MEMS)-Inertial Measurement Units (IMU) MOCAP system with a single DGPS?

## 1.3 Scope, Limitations and Constraints

The following factors placed limits and constraints to the project and influenced the decision making process.

- Project budget;
- Pre-determined project time of 24 months;
- Pre-determined electronics component distributors;
- Pre-determined Printed Circuit Board (PCB) manufacturer and assembly vendor;
- Unavailability of a commercial outdoor MOCAP system for validation;
- following assumptions that were given:
    - The users of the system are students, researchers and engineers who study gait analysis;
    - The users are familiar with STM32 series micro-controllers;
    - The users are only to use the novel MOCAP system to observe the motion of a family of a terrestrial *megafauna* (that is a terrestrial animal with minimum weight threshold of 40 kg);
    - The users only intend to capture the motion of a terrestrial *megafauna* for the maximum duration of 6 hours.

This report only details the process involved in the development of a proposed fusion MOCAP system which only includes hardware, firmware and state estimation algorithms. Therefore, the sensor strapped-down system was outside the scope of this research.

In addition, the developed MOCAP system was only validated on a mechanical rig for several reasons. Firstly, a commercial outdoor MOCAP system was not available to assess the developed system quantitatively and compare its performance to that of a commercial outdoor MOCAP system. Secondly, ethics clearance for trials on animals was not obtained.

Due to the limited project budget and time, the sensor-network was only developed to operate in dry-condition (not water-proof) and the state estimation algorithm was limited to post-processing (not real-time application). Furthermore, the research was limited to the estimation of kinematic quantities as the estimation of kinetic quantities was outside the scope of this project.

## 1.4 Plan of Development

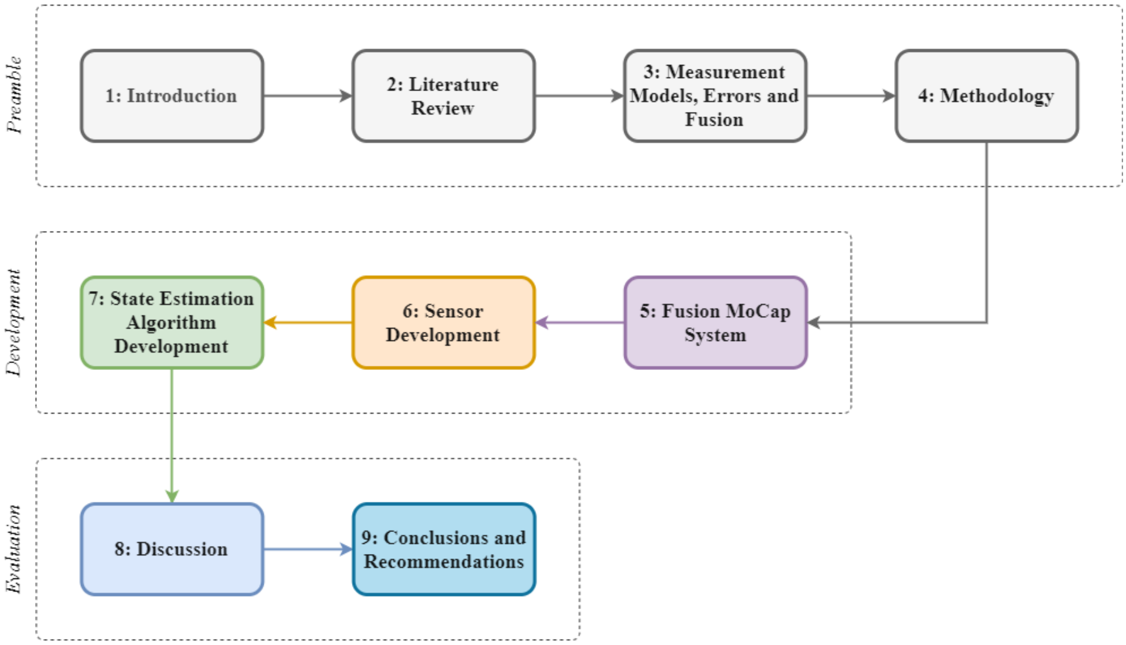

**Figure 1.2:** The layout of the dissertation.

The dissertation begins by providing the reader with a background to the research and the aim of the study in Chapter 1. In Chapter 2, different types of traditional MOCAP systems are explained with reference to relevant literature then a brief idea on the novel MOCAP system is developed. Relevant measurement models and errors are described along with the required filtering and state estimation algorithms in Chapter 3. To complete the preamble, the methodology in Chapter 4 discusses how the novel MOCAP system was developed and evaluated.

Detailed system overview of the novel MOCAP system is established in Chapter 5. In Chapter 6, detailed hardware and firmware technical specifications are developed. Continuing in Chapter 6, the design of the device for the novel MOCAP system is described and then the acceptance testing procedure and results are provided. The state estimation algorithm is developed in Chapter 7 along with the results of its performance.

The discussion section follows in Chapter 8. Finally, the dissertation culminates with the conclusions and recommendations section in Chapter 9. The full layout of the dissertation is shown in Figure 1.2.

# Chapter 2

# Literature Review

MOCAP technology provides researchers and engineers in various fields with a method to capture and analyse dynamic motion from a variety of perspectives [34]. The kinematic data obtained from these systems includes position, velocity and acceleration. Using this kinematic data along with the information on the external forces the kinetic information which explains the causes of the motion such as the applied force and inertia, can be estimated [49] [50] [51].

Despite the abundant need and use of MOCAP technology, existing literature states that there is no MOCAP system that can be used for all applications. This is because MOCAP systems have their own unique advantages, disadvantages and constraints [52]. Currently, there are two classes of MOCAP systems, optical and non-optical.

Optical MOCAP systems are further classified into marker-based and marker-less MOCAP systems. Non-optical MOCAP systems are typically further classified into acoustic, magnetic, mechanical and inertial MOCAP systems. These types of MOCAP systems are shown in Figure 2.1 detailed below:

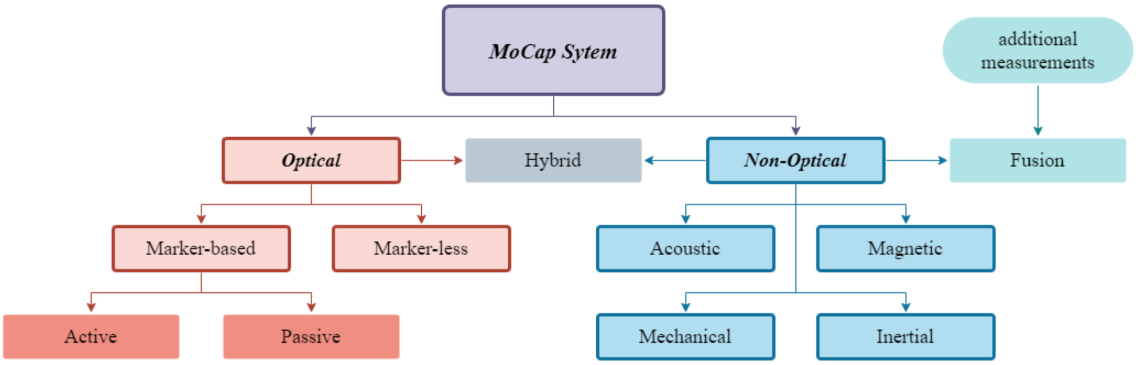

**Figure 2.1:** Different types of traditional MOCAP systems.

## 2.1 Optical MOCAP Systems

In the literature, optical MOCAP systems are considered to be a gold-standard because they are exceptionally accurate with sub-centimetre accuracy [43]. For this reason, optical MOCAP systems are often used as a reference to validate the performance and reliability of new MOCAP systems [28] and favoured over other existing MOCAP systems especially in the animation and film industry [52] [53].

Optical MOCAP systems use cameras to conduct 3D full-body motion reconstruction. It is then further classified according to the use of markers (marker-based or markerless) and the number of views (monocular or multi-view) [28] [54].

Monocular systems use images acquired by a single camera and suffer from inherent kinematic singularities and reflective ambiguity. Therefore, multi-view systems, which use images acquired simultaneously and synchronously by two or more cameras, are preferred by researchers[1] [55]. A marker-based system determines the trajectories of the markers on the body, whilst markerless system computes kinematic parameters from extracted body edges or silhouettes [55].

According to [56], the major key players in the commercial optical MOCAP system market are *Charnwood Dynamics Ltd.*, *OptiTrack*, *PhaseSpace Inc.*, *Qualisys AB* and *Vicon Motion Systems Ltd.* 2.1. They are all capable of providing indoor real-time 3D motion reconstruction with gold-standard accuracy with some capable of outdoor motion reconstruction. Brief descriptions of their systems are given in Table 2.1.

**Table 2.1:** Summary on the specifications of the existing commercial optical MOCAP systems

| Company | Type | Outdoor | System Mobility | Marker weight | Camera |
|---|---|---|---|---|---|
| *Charnwood Dynamics* | active | Y | N | $< 10g$ | N/A |
| *OptiTrack* | passive | N | N | $< 10g$ | 180 FPS @ 4.1 MP<br>360 FPS @ 1.7 MP |
| *PhaseSpace* | active | N | N | suit | 960 FPS @ 130 MP |
| *Qualisys AB* | active & passive | Y | N | $< 10g$ | 180 FPS @ 4 MP<br>1750 FPS @ 0.3 MP |
| *Vicon* | passive | Y | N | $< 10g$ | 120 FPS @ 16 MP<br>420 FPS @ 5 MP |

---

[1] From this point forward, optical MOCAP refers to multi-view system.

### 2.1.1 Marker-based Optical MOCAP Systems

A marker-based optical MOCAP system is further classified according to the type of markers used, namely: active or passive. This type of system requires markers or a tailored suit with markers attached and a capturing area, a strategically arranged static array of synchronised cameras and an acquisition system [28] [54].

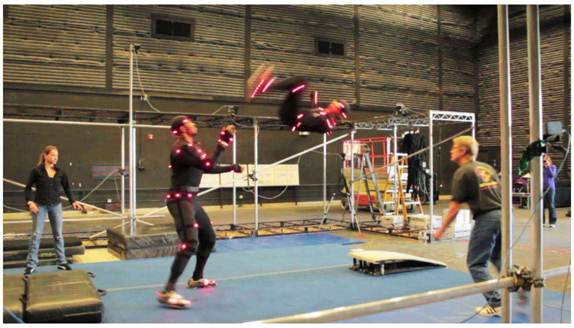

**(a)** *PhaseSpace* active marker-based MOCAP system. Image from [57].

**(b)** *Vicon* passive marker-based MOCAP system. Image from [58].

**Figure 2.2:** Two commercial optical marker-based MOCAP systems.

An active marker-based system uses light emitting markers as shown in the Figure 2.2a which requires additional electronics and power. This adds the risk of having to re-position the markers due to the mass and lifetime limitations [52]. Passive marker-based system as shown in Figure 2.2b uses retro-reflective markers alleviating the fore-mentioned limitations of active marker-based system but it is less robust due to marker swapping and false reflections [43].

The markers must be attached strategically because only large motions similar to flexion and extension have acceptable error limits for skin-based marker systems [59]. According to Cappozzo et al. [60], skin-based markers located on the area near the joints such as great trochanter and lateral epicondyle of the femur undergo displacements relative to the underlying bone in the range of 10 to 30 mm during walking.

The volume of the capturing area must be sufficiently large to host recording by a number of cameras at a distance. Background subtraction can be improved by achieving a uniform background using opaque curtains and maintaining uniform lighting to avoid sharp shadows or highlights in the images as shown in Figure 2.2b [55].

The cameras are strategically arranged so that at least two cameras record the markers at a time. This confines the assessment to a controlled laboratory environment with limited and immobile capture volume to accommodate the use of a static array of cameras [28] [54].

To achieve its gold-standard accuracy, the system requires a sufficient number of cameras which increase in number with an increase in capture volume. Aurand et al. [61] conducted an assessment where the accuracy as a function of location within the capture volume of two optical MOCAP systems, one with 21 and the other 42 cameras, was compared. The accuracy was found to decrease non-linearly approaching the edges of the capture volume and a higher mean error was observed for the system with fewer cameras [61].

The cameras must deliver high frame rates at a suitable resolution to maintain its gold-standard accuracy. As such, a higher frame rate is desired when tracking complex and highly dynamic tasks. However a higher frame rate decreases the resolution as can be observed in Table 2.1 [27]. The lenses must be selected with consideration of image distortion and field of view [55].

Typically, a marker-based optical MOCAP system consists of the following sequential challenges for implementation: initialisation, marker detection, spatial correspondence, temporal correspondence and post-processing [55]. Techniques such as a volumetric reconstruction, inverse kinematics and inverse dynamics are selectively used to improve coherency in the motion data [55].

Initialisation involves camera intrinsic (camera properties) and extrinsic (camera position and orientation) calibration, metric (world coordinate) calibration, background calibration and skeleton calibration. There currently exists two common intrinsic and extrinsic algorithms: Tsai [62] [63] and Svoboda [64] which uses a checker-board pattern and light points respectively. For metric calibration, objects with known physical dimensions and global positions must be captured in the images.

Marker detection involves identification of 2D pixel coordinates of markers in the images. This is done by means of threshold-based intensity segmentation or curvature segmentation to output a binary image where the markers are represented negatively from others. Spacial correspondence involves pairing of detected markers in images captured at the same time by different cameras to evaluate 3D global coordinates of markers by means of stereo triangulation on rays [55].

Temporal correspondence involves stitching of 3D points from spacial correspondence to reconstruct the motion. However, the trajectories are not complete for all markers in practice due to asynchronisation, marker occlusions and missing information. Therefore, post-processing is required to align and label each track and correct the marker occlusions [28] [55].

Researchers constantly seek to improve the performance of a marker-based optical MOCAP system. In [65], Dorfmüller-Ulhaas integrated an Extended Kalman filter (EKF) into the temporal correspondence to enhance a reliability of the marker-based optical MOCAP system. Wu et al. [66] and Aristidou et al. [67] mitigated the missing marker problem whilst Lugŕis et al. [68] mitigated the marker occlusion problem in a marker-based optical MOCAP system by integrating a Kalman filter into the temporal correspondence stage.

Despite a number of researchers' input over the decades to improve the performance of a marker-based optical MOCAP system, the literature suggests that they are inappropriate for accurate tracking of both the steady-state and the transient locomotion of an animal outside a controlled indoor environment for a number of reasons.

The accuracy of the system is determined by many factors: experimental set-up; arrangement of markers; quality of cameras and accuracy of the initialisation [43]. Moreover, its accuracy decreases with the shift in camera positions; the changes in background and ambient light conditions and displacement of markers. These factors inhibit motion tracking in an outdoor environment with undefined capture volume [43].

Decrease in accuracy due to changes in experimental set-up and condition can be overcome with an increase in resources such as markers, cameras, additional sensors, chroma key composition and more. However, this results in drastic increase in the cost of the system. For instance, *PhaseSpace* 12-camera indoor system costs USD 29,000.00 whilst 64-camera system costs USD 133,000.00.[2] Being a costly and a time-consuming system [27] with lack of portability [53], a commercial marker-based optical MOCAP system is inaccessible especially to individuals and small organisations.

### 2.1.2 Markerless Optical MOCAP Systems

A markerless optical MOCAP system reconstructs 3D full-body motion based on the image data without preparation of the subject and marker [69]. This eliminates participant preparation and reduces system calibration time in comparison to the marker-based system [43] [70] [54]. However, a markerless optical MOCAP system is not as accurate as a marker-based optical system [52] [70] [71].

---

[2] See Appendix G for pricing.

A markerless optical MOCAP system is typically classified as an active or passive system. An active system uses laser light, light patterns or pulses and requires a static array of laser scanners. It can provide very accurate 3D co-ordinates but it is limited to static locomotion. Therefore, the development of a markerless optical MOCAP system is limited to a passive system which relies purely on the captured images [59].[3]

Similar to the marker-based system, a markerless optical MOCAP system requires a capturing area, a strategically arranged static array of synchronised cameras and an acquisition system. The Use of a static array of cameras requires camera intrinsic, extrinsic and metric calibrations and confines the system to a controlled laboratory environment (with a limited and immobile capture volume) [27]. Moreover, the absence of the markers introduces line-of-sight problems although it facilitates motion reconstruction of multiple subjects and alleviates unknown experimental artefacts such as a skin movement artefact [59].

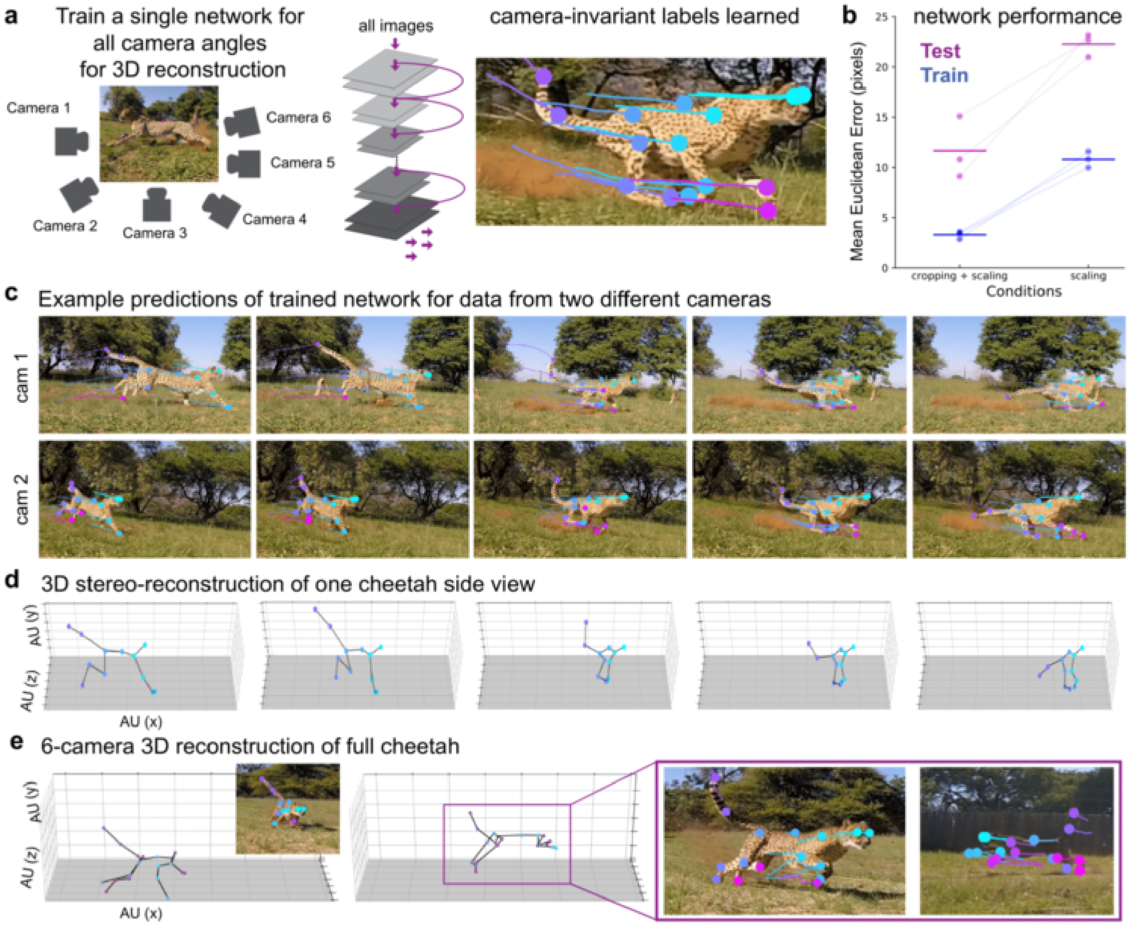

**Figure 2.3:** A 3D pose classification and stitching trained on data from a static array of cameras in conjunction with the standard triangulation methods. Image from [2].

---

[3] From this point forward, a markerless optical MOCAP system refers to a passive markerless system.

Reconstruction algorithms for a markerless optical MOCAP system can be classified into discriminative and generative approaches [54]. The discriminative approach relies on data driven machine learning algorithms and converts the nature of the MOCAP problem (tracking) into a pose classification problem where the subject's pose is identified frame by frame, by fitting the skeletal model of the subject as shown in Figure 2.3. As such, the discriminative approach is better suited for interactive applications [54].

The generative approach is preferred for applications that ask for accuracy and is further classified into model-based and feature-based tracking algorithm [43]. The model-based tracking algorithm requires a model of the tracked object to fit the model frame-by-frame whereas the feature-based tracking algorithm tracks points of interest defined by their shape and texture, raising the risk of occlusion [43].

As with the marker-based optical MOCAP system, the limits of the experimental set-up and influence of the changes in the experimental condition on the accuracy on the markerless optical MOCAP system cannot be neglected [71]. Furthermore, a commercial markerless optical MOCAP system is also inaccessible to some due to their high cost. A complete 8-camera markerless optical MOCAP system package with a capture volume of $36m^2$ from *Organic Motion* costs USD $80,000.00$ [72]. Therefore, it is not suitable for the tracking of an animal in its natural habitat.

## 2.2 Non-Optical MOCAP Systems

An acoustic MOCAP system uses sound emitting markers and receptors located within the capture volume [53]. Each marker, distinguished by their unique emitting frequencies, sequentially emits a signal that is received by the receptors. The position of the markers are computed using time-of-flight information by means of triangulation [73].

As a consequence of using an acoustic medium, the emitters and receptors are susceptible to ambient noise and must be sequentially activated to avoid signal occlusion [53]. Therefore, acoustic MOCAP is not appropriate for the MOCAP in an uncontrolled outdoor environment with unpredictable ambient noise.

A magnetic MOCAP system consists of an artificial magnetic source which generates a low-frequency magnetic field and the sensors that can measure this low-frequency magnetic field [74]. The orientation and position are calculated by computing the change in the magnetic field [74].

Despite offering an accuracy close to a gold-standard optical MOCAP system with no line-of-sight requirement, a magnetic MOCAP system is challenging to implement. This is because the system is sensitive to any metallic and magnetic objects in the environment, demanding a controlled and shielded indoor environment [53]. Therefore, a magnetic MOCAP system is too not appropriate for use in an outdoor environment.

**(a)** *Gypsy* mechanical MOCAP system. Image from [75]

**(b)** *Xsens* inertial MOCAP system. Image from [76]

**Figure 2.4:** Two commercial non-optical MOCAP systems. Above is the exo-skeletal suit of the *Gypsy* mechanical MOCAP system and below is the wireless inertial MOCAP system of the *Xsens Technologies*.

A mechanical MOCAP system typically involves an exo-skeletal suit with sensors such as potentiometers and sliders that are attached on the subject's articulations of interest as shown in Figure 2.4a [74]. It is free from a polynomial interpolation error, a calibration process, a controlled environment and a complex estimation and reconstruction process as the users have direct access to the inverse kinematic measurements [53].

Despite the advantages of a mechanical MOCAP system, it cannot deliver tracking of the steady state and transient locomotion of a family of a terrestrial *megafauna*. An exo-skeletal suit forbids generalisation of a subject, requiring customisation and most importantly, the rigid suit impedes the motion [53].

An inertial MOCAP system is the second most popular in the 3D MOCAP system market with key players such as *Notch Interfaces* and *Xsens Technologies* (shown in Figure 2.4b) [56]. It is based on the inertial sensors such as accelerometers, gyroscopes and magnetometers. The local orientation and kinematic quantities of the relevant limb segments are estimated by feeding the sensor measurements into a complex algorithm such as the Kalman filter [23] [46].

An inertial MOCAP system is often implemented real-time. For real-time operation, measurements from a set of non-invasive and light-weight inertial sensors communicate with and are synchronised to a main-processor wirelessly, typically on Wireless Personal Area Network (WPAN) [50] [27]. WPAN is an inexpensive, power-efficient and small network that is used to transfer information over short distances ($< 10m$) among a private group of devices [15]. *Bluetooth*, described in Table 2.2, is a widely used WPAN technology (*IEEE 802.15.1*) and is implemented by both *Notch Interfaces* and *Xsens Technologies* [76] [77].

**Table 2.2:** Summary of WPAN Bluetooth characteristics [15]

| **Parameters** | **Descriptions** |
|---|---|
| Topology | Unlimited paired devices<br>Typically up to 7 connected devices<br>Practically up to 4 connected devices<br>One actively communicating device |
| Data rate | 1 Mbps (v1.2)<br>2 Mbps (v2.1 + EDR)<br>24 Mbps (v3.0 + HS)<br>0.27 Mbps (v4.0 + BLE) |
| Range | $<$ 1 m (Class 3 transmitting at 1 mW)<br>$<$ 10 m (Class 2 transmitting at 2.5 mW)<br>$<$ 100 m (Class 1 transmitting at 100 mW) |
| RF bandwidth | 220 kHz, 1 MHz |
| RF band | 2.4 GHz ISM frequency band |

As can be deduced from Table 2.2, the wireless method requires sophisticated network topology with multiple piconet masters to track more than seven limb segments and has potential risks such as data corruption and signal loss. Therefore, the applications that do not require real-time processing or systems with a vast quantity of data, record measurements on external memory devices for post-processing [28].

The sampling frequency of the system must be selected based on the assessed motion and according to the Nyquist-Shannon theorem [28]. This theorem states that the sampling frequency must be at least twice the highest frequency component in the sampled signal. Thus, incorrect choice of sampling frequency may lead to loss of motion information. For instance, Lapinski et al. chose two sampling frequencies, 100 Hz and 1000 Hz, to capture slow and fast motion whilst maintaining memory and computational efficiency [78].

A fundamental problem in an inertial MOCAP system is the inherently noisy sensor measurements that are prone to drift. This compounds over time, requiring frequent sensor re-calibration [79]. An inertial MOCAP system cannot provide global trajectory information of each limb segment [79]. Researchers, therefore, make use of additional sensors such as GNSS to correct the measurement drifts and to obtain global trajectory information [23] [49].

In addition, sensors' local co-ordinate axes do not align with any physiologically meaningful axes, leading to an assumption that the sensors are mounted precisely in a predetermined orientation. To minimise the error due to imprecise mounting, manual measurements of the sensors' position on limb segments and reference posture calibration must be conducted to find the relationship between the sensors' local co-ordinate axes and the limb segments' axes [49].

Although a commercial inertial MOCAP system is cheaper than a commercial optical MOCAP systems, it is also inaccessible to individuals and small organisations due to its high cost [28]. For instance, a full *Xsens Technologies* inertial MOCAP kit costs EUR $52,140.00$.

Nevertheless, the use of an inertial MOCAP system is increasing as it allows gait analysis of activities in an outdoor environment [23] [28]. Therefore, it is desirable to study inertial MOCAP system further for the development of an outdoor MOCAP system to track steady state and transient locomotion of an animal outdoors.

## 2.3 Novel MOCAP Systems

To overcome the shortcomings of the traditional MOCAP systems, researchers and engineers have been developing novel MOCAP systems which are classified into a hybrid and fusion MOCAP system. A hybrid system integrates two or more traditional MOCAP systems whereas a fusion system fuses one or more data streams into a traditional MOCAP system. Typically, these systems are aimed to improve the performance and portability of the aforementioned traditional MOCAP systems but often lead to an increase in cost [53].

Lin, et al. [80] presented a hybrid MOCAP system that was an integration of a passive marker-based optical MOCAP system and an inertial MOCAP system. It was aimed at improving the accuracy of the reconstruction of the transient motion with high acceleration and deceleration that is often observed in volleyball players [80].

The proposed system by Lin, et al. inherited the requirements of a marker-based optical MOCAP system such as fixed capture volume; confinement to a controlled laboratory environment with constant background and lighting; time-consuming calibration processes and a line-of-sight problem [80]. Consequently, the motion of volleyball players during their encounter with a ball and the other players on a court could not be reconstructed.

Jung, et al. [81] presented a hybrid MOCAP system which integrates an active marker-based optical MOCAP system and an inertial MOCAP system. This integration was aimed to eliminate the marker occlusion problem during MOCAP of multiple subjects. Although they demonstrated the reconstruction of two subjects' interactive motion, the system was only validated qualitatively. Similarly to the hybrid system of Lin, et al., their hybrid system also inherited the requirements of a marker-based optical system.

Xu, et al. [54] employed unmanned aerial vehicles (UAVs) mounted with a RGBD video camera instead of a static array of cameras to implement a markerless optical MOCAP system, *FlyCap* [54]. Such employment was aimed at improving the portability of the traditional markerless optical MOCAP system and adding the mobility to the capture volume [54].

*FlyCap* was able to take the gold-standard optical MOCAP outside a controlled laboratory environment. However, *FlyCap* is regrettably limited to capturing steady-state and slow transient locomotion in a legally approved fly-zone to guarantee the safety of the participants from UAVs [54].

Brodie et al. [46] developed a fusion MOCAP system by integrating pressure insoles and a GPS to an inertial MOCAP system by means of a Kalman filter to track the motion as well as the global trajectory of a New Zealand Alpine Ski racer. Their development enabled motion tracking over a 300 m track on a mountain but its accuracy is not validated quantitatively due to unavailability of a gold-standard method [46].

Improved upon [46], Supej [47] and Gilgien et al. [48] fused a Real Time Kinematic (RTK) and a Differential Global Navigation Satellite Systems (DGNSS) to an inertial MOCAP system respectively. In [47], global trajectories computed by RTK are evaluated to have a horizontal accuracy of $10 \pm 0.5mm$ and vertical accuracy of $20 \pm 0.5mm$ during dynamic tests.

## 2.4 Summary

A literature review on traditional types of MOCAP systems and current applications of MOCAP technology was conducted with a goal to understand their capabilities and limitations. Novel MOCAP systems were then reviewed to understand how other researchers mitigate the limitations of traditional MOCAP systems.

The literature suggests that a optical MOCAP system, non-optical acoustic and a non-optical magnetic MOCAP system are not feasible for applications with undefined capture volume and environmental conditions. A non-optical mechanical MOCAP system was also deemed to be infeasible as the system impedes the motion of the subject, violating the aim of the study. In contrast, a non-optical inertial MOCAP system is considered to be feasible in the tracking of the steady-state and transient locomotion in an outdoor environment.

Having said that, an inertial MOCAP system suffers from measurement noise and drift and it cannot provide global trajectory information. Consequently, an inertial MOCAP system alone cannot be used to answer the question: ***"Why are animals so manoeuvrable?"***.

Brodie et al. [46], Supej [47] and Gilgien et al. [48] demonstrated the benefit of feeding navigational information to an inertial MOCAP system to track the subject's motion and global trajectory in an outdoor environment with undefined capture volume and environmental conditions. **However, they only integrated navigational information from a single point on a body.**

Consequently, based on the literature review, this research will pursue the development of a fusion outdoor MOCAP system that involves integration of a traditional inertial MOCAP system fused with the navigational information *from each limb segment*. This development is aimed at inheriting the advantages of the inertial MOCAP system while obtaining accurate global trajectory information of each limb segment.

# Chapter 3

# Theory Development: Measurement Models, Errors and Sensor Fusion

In Chapter 2, it was decided to develop a fusion MOCAP system by fusing navigational information from each limb segment to a traditional inertial MOCAP system. Such development was aimed at allowing the tracking of steady-state and transient locomotion of an animal in an outdoor environment that is less restrictive than the indoor laboratory environment.

However, the inherent benefits of a traditional inertial MOCAP system may be compromised during the development process if carried out without an in-depth understanding of Micro Electro Mechanical Systems (MEMS)-Inertial Measurement Units (IMU), Global Navigation Satellite Systems (GNSS), Differential Global Navigation Satellite Systems (DGNSS), Global Positioning Systems (GPS) and Differential Global Positioning Systems (DGPS). Therefore, this chapter provides the relevant theory needed to fully understand these systems.

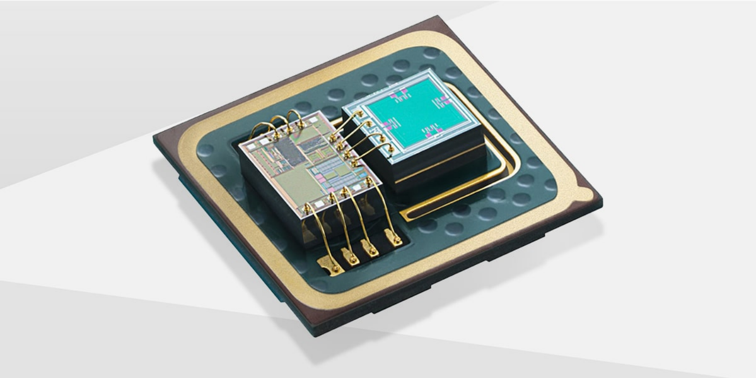

**Figure 3.1:** Bosch MEMS sensor module with MEMS sensor element packed in a semiconductor housing. Image from [3].

## 3.1 Inertial Measurement Units (IMU)

In recent years, MEMS-based IMUs contributed to development of a cost-effective, lightweight, non-invasive, portable and accurate inertial motion capture systems [82]. MEMS technology implements a System-on-Chip (SoC) as shown in Figure 3.1 by adapting the micro-fabrication technology to combine electronic and mechanical elements, sensors and actuators [83].

An IMU commonly refers to a combination of a 3-axis accelerometer and 3-axis gyroscope [84]. However, with the development of an attitude determination technique using a 3-axis magnetometer and an IMU, 9-axis IMUs are developed containing a 3-axis accelerometer, a 3-axis gyroscope and a 3-axis magnetometer[1] [85].

### 3.1.1 Accelerometer Measurement Model

An accelerometer measures the specific force (measured in $m/s^2$ ) acting on the sensor relative to the inertial frame resolved along the sensor's sensitive axis [85]. The specific force is not a force but a type of acceleration which includes both the sensor's linear acceleration and gravitational acceleration as expressed in (3.1):

$$\boldsymbol{f}^b = \boldsymbol{R}_n^b(\boldsymbol{a}_{ii}^n - \boldsymbol{g}^n), \tag{3.1}$$

where $\boldsymbol{g}$ is the gravitational acceleration vector; $\boldsymbol{R}_n^b$ is the orthonormal rotation matrix from the navigation frame to body frame and $\boldsymbol{a}_{ii}^n$ is the sensor's linear acceleration vector with respect to the inertial frame expressed in the navigation frame. Attitude representation using an orthonormal rotation matrix, and coordinate system and transformation are explained in Appendix A and Appendix B.

For tracking purposes, the sensor's linear acceleration with respect to the navigation frame expressed in the navigation frame ($\boldsymbol{a}_{nn}^n$) is of interest. The relationship between $\boldsymbol{a}_{ii}^n$ and $\boldsymbol{a}_{nn}^n$ is found in [84] as:

$$\boldsymbol{a}_{ii}^n = \boldsymbol{a}_{nn}^n + \boldsymbol{\omega}_{ie}^n \times \boldsymbol{\omega}_{ie}^n \times \boldsymbol{p}^n + 2\boldsymbol{\omega}_{ie}^n \times \boldsymbol{v}_n^n, \tag{3.2}$$

where $\boldsymbol{\omega}_{ie}^n \times \boldsymbol{\omega}_{ie}^n \times \boldsymbol{p}^n$ is the centrifugal acceleration vector and $2\boldsymbol{\omega}_{ie}^n \times \boldsymbol{v}_n^n$ is the Coriolis acceleration vector.

---

[1] From this point forward, an IMU refers to a 9-axis IMU.

Given that the Earth rate ($\boldsymbol{\omega}_{ie}$) is approximately $7.29 \times 10^{-5} rad/s$, the centrifugal acceleration and Coriolis acceleration can be assumed to be negligible in comparison to the magnitude of the $\boldsymbol{a}_{nn}^{n}$ [84]. Further considering the sensor errors, the governing equation for an accelerometer measurement model is as follows:

$$\boldsymbol{f}_t^b = \boldsymbol{R}_{n,t}^b(\boldsymbol{a}_{nn,t}^n - \boldsymbol{g}^n) + \boldsymbol{\delta}_{a,t}^b + \boldsymbol{\varepsilon}_{a,t}^b, \tag{3.3}$$

where $\boldsymbol{\delta}_{a,t}^b$ is the accelerometer bias error vector and $\boldsymbol{\varepsilon}_{a,t}^b$ is the error vector due to noise and accelerometer model uncertainty at time $t$.

### 3.1.2 Gyroscope Measurement Model

A gyroscope measures the angular velocity of the body frame with respect to the inertial frame resolved along the sensor's sensitive axis expressed in the sensor's body frame ($\boldsymbol{\omega}_{ib}^b$). This angular velocity is given in (3.4):

$$\boldsymbol{\omega}_{ib}^b = \boldsymbol{R}_n^b(\boldsymbol{\omega}_{ie}^n + \boldsymbol{\omega}_{en}^n) + \boldsymbol{\omega}_{nb}^b, \tag{3.4}$$

where $\boldsymbol{\omega}_{nb}^b$ is the angular velocity vector of the sensor's body frame with respect to the navigation frame expressed in the body frame and $\boldsymbol{R}_n^b(\boldsymbol{\omega}_{ie}^n + \boldsymbol{\omega}_{en}^n)$ is the angular velocity vector of the navigation frame with respect to inertial frame expressed in the navigation frame.

The Earth rate ($\boldsymbol{\omega}_{ie}^n$) is approximately $7.29 \times 10^{-5} rad/s$ and the navigation frame can be assumed to be stationary with respect to the inertial frame if the sensor does not travel over significant distances in comparison to the size of the Earth [84]. Therefore, (3.4) can be simplified to (3.5):

$$\boldsymbol{\omega}_{ib}^b = \boldsymbol{\omega}_{nb}^b. \tag{3.5}$$

Taking into account the sensor errors, the governing equation for a gyroscope measurement model is:

$$\boldsymbol{\omega}_{ib,t}^b = \boldsymbol{\omega}_{nb,t}^b + \boldsymbol{\delta}_{\omega,t}^b + \boldsymbol{\varepsilon}_{\omega,t}^b, \tag{3.6}$$

where $\boldsymbol{\delta}_{\omega,t}^b$ is the gyroscope bias error vector and $\boldsymbol{\varepsilon}_{\omega,t}^b$ is the error vector due to noise and gyroscope model uncertainty at time $t$.

### 3.1.3 Magnetometer Measurement Model

A magnetometer measures the local magnetic field, consisting of both the Earth magnetic field and the magnetic field induced by near-by magnetic materials [85]. The local Earth magnetic field ($\boldsymbol{m}^n$) can be assumed to be constant if the sensor does not travel over significant distances in comparison to the size of the Earth [84]. Given the Earth magnetic field:

$$\boldsymbol{m}^n \quad = \quad B\big(cos\delta \quad 0 \quad sin\delta\big)^T, \tag{3.7}$$

where $B$ is the local Earth magnetic field strength and $\delta$ is the inclination.

Under the assumption that there is no magnetic material present in the vicinity of the magnetometer, the magnetometer measurement can be modelled as in (3.8):

$$\boldsymbol{m}_t^b \quad = \quad \boldsymbol{R}_{n,t}^b \boldsymbol{m}^n + \boldsymbol{\varepsilon}_{m,t}^b, \tag{3.8}$$

where $\boldsymbol{\varepsilon}_{m,t}^b$ is the error vector due to noise and magnetometer model uncertainty at time $t$.

In practice, the above assumption is not true and the magnetometer measurement differs from the Earth magnetic field. This is due to the hard and soft iron interference caused by a permanently magnetised object and induced external magnetic field respectively [84]. Hard iron interference adds an offset to known Earth magnetic field plot whilst soft iron interference causes a distortion [82].

### 3.1.4 IMU Errors

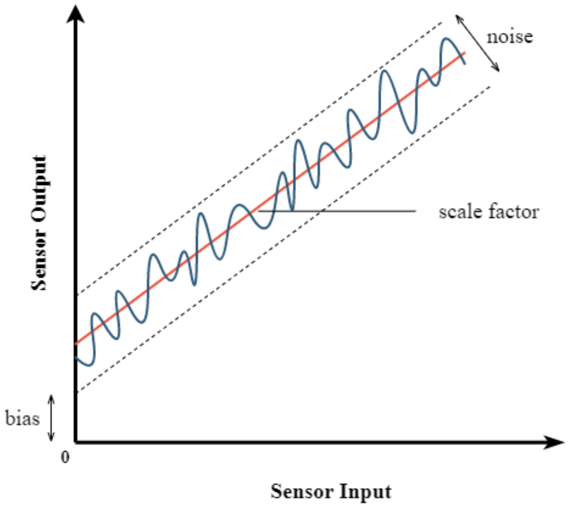

**Figure 3.2:** A simple diagram showing three types of common errors inherent to MEMS-IMU [4].

IMU measurements are influenced by several sources of errors: bias, scale factor and sensor noise (random walk), depicted in Figure 3.2, as well as sensor non-orthogonality [86]. These errors cannot be disregarded and must be corrected by means of temperature-based calibration, external restriction calibration and additional measurements as they reduce the accuracy of the MOCAP system significantly.

An accelerometer provides information with regard to the derivatives of position and orientation. Therefore, a bias $\Delta$ in the accelerometer measurement leads to a positional error of $\Delta(t-t_0)^2$ [85]. For the same reason, a bias $\Delta$ in the gyroscope measurement can result in erroneous computation of position. As an illustration, a component of the gravitational acceleration with magnitude $0.0086m/s^2$ will be projected onto the horizontal axes due to a tilt error of $0.05^\circ$. This in turn will cause a drift in the horizontal position by $7.7m$ after 30 seconds into computation [85].

Bias error refers to an offset present on the IMU measurement output for a given physical input as shown in Figure 3.2. For each power-up and while IMU is powered on, the initial bias error may be different and change over time respectively [86]. Therefore, the repeatability and stability of the bias error of an IMU is critical. Bias error can be removed by means of external restriction calibration where the sensor is brought to a well-known position and orientation and bias is computed on initial power-up and periodically [85].

Scale factor error refers to a relationship, that is typically linear, between a physical input and sensor measurement output as shown in Figure 3.2. There exists common algorithms to compute the scale factor, namely: six-parameter and twelve-parameter calibration algorithms [4]. The six-parameter calibration algorithm assumes linear relationship and zero cross-correlation between axes whilst the twelve-parameter calibration algorithm assumes a linear relationship only.

Sensor noise refers to a random noise in the measurement given a constant signal and must be minimised using statistical techniques [85]. Sensor non-orthogonality refers to a misalignment of the sensor axes and leads to a cross-correlation between sensor sets and between sensor sets and the enclosure [85]. Continuous estimation and a bore-sight alignment can remove the effect of sensor non-orthogonality [4].

### 3.1.5 Data Fusion

The IMU does not provide direct measurements of motion but it provides an indirect measurement such as the specific force, angular velocity and local magnetic field. Therefore, using a well-defined statistical technique, an algorithm which optimally estimates the position by combining predictions based on the understanding of the body parts modelled in kinematic chains and measurements from sensors, is necessary.

Kalman filters are one of the common prediction and estimation algorithms used in the implementation of the inertial MOCAP systems by researchers [68] [23] [46] [47] [48]. It is a recursive algorithm based on the statistical characterisation of an estimator problem. In contrast to Least Squares (LS) algorithms whose estimation is solely based on the current measurement, the Kalman filter propagates the probability distribution of the variables throughout its estimation [87].

In essence, the Kalman filter is regarded as the optimal estimator for the Linear Quadratic Gaussian (LQG) problem [88]. LQG problems refer to the estimation of the instantaneous state of a linear dynamic system perturbed by Gaussian white noise by using measurements with inherent Gaussian white noise that are linearly related to the state.

### Discrete Kalman Filter Derivation [5] [89]

Derivation of the Kalman filter must be appreciated as it provides an understanding of the constraints inherent to the algorithm. Only the discrete Kalman filter derivation is described below as the continuous Kalman filter will not be employed in this research.

A discrete LQG problem considers a discrete-time controlled process governed by a linear stochastic difference equation:

$$\boldsymbol{x}_t = \boldsymbol{A}\boldsymbol{x}_{t-1} + \boldsymbol{B}\boldsymbol{u}_t + \boldsymbol{w}_{t-1}, \tag{3.9}$$

where $\boldsymbol{x}_t$ and $\boldsymbol{x}_{t-1}$ are the state vector of the process at time $t$ and $t-1$ respectively based on $\boldsymbol{x}_{t-1}$; $\boldsymbol{A}$ is the state transition matrix of the process; $\boldsymbol{B}$ relates the *optimal* control input $\boldsymbol{u} \in \Re$ to the state $\boldsymbol{x}_t$ and $\boldsymbol{w}_{t-1}$ is the noise of the process.

The sampled measurement is expressed as:

$$\boldsymbol{z}_t = \boldsymbol{H}\boldsymbol{x}_t + \boldsymbol{v}_t, \tag{3.10}$$

where $\boldsymbol{z}_t$ is the actual measurement vector at time $t$; $\boldsymbol{H}$ is the noiseless connection between the state vector and the measurement vector that is assumed stationary over time and $\boldsymbol{v}_t$ is the noise of the measurement.

The random variables $\boldsymbol{w}_t$ and $\boldsymbol{v}_t$ are assumed to have zero cross-correlation with each other and white with Gaussian probability distributions. As such:

$$p(\boldsymbol{w}_t) \sim N(\mathbf{0}, \boldsymbol{Q}_t) \tag{3.11}$$

$$p(\boldsymbol{v}_t) \sim N(\mathbf{0}, \boldsymbol{R}_t), \tag{3.12}$$

where $\boldsymbol{Q}_t = E[\boldsymbol{w}_t\boldsymbol{w}_t^T]$ and $\boldsymbol{R}_t = E[\boldsymbol{v}_t\boldsymbol{v}_t^T]$ are process noise covariance and measurement noise covariance matrices respectively that are not necessarily constant throughout the process.

If $\boldsymbol{x}_t^- \in \Re^n$ is defined as a *priori* state estimate at $t$ based on the process at $t-1$, and $\boldsymbol{x}_t^+ \in \Re^n$ is defined as a *posteriori* state estimate at $t$ based on the measurement $\boldsymbol{z}_t$, a *priori* error ($\boldsymbol{e}_t^-$) and *posteriori* estimate error ($\boldsymbol{e}_t^+$) are:

$$\begin{aligned} \boldsymbol{e}_t^- &= \boldsymbol{x}_t - \boldsymbol{x}_t^- && (3.13) \\ \boldsymbol{e}_t^+ &= \boldsymbol{x}_t - \boldsymbol{x}_t^+, && (3.14) \end{aligned}$$

with a *priori* estimate error covariance ($\boldsymbol{P}_t^-$) and *posteriori* estimate error covariance ($\boldsymbol{P}_t^+$) defined as follow:

$$\begin{aligned} \boldsymbol{P}_t^- &= E[\boldsymbol{e}_t^- \boldsymbol{e}_t^{-T}] && (3.15) \\ \boldsymbol{P}_t^+ &= E[\boldsymbol{e}_t^+ \boldsymbol{e}_t^{+T}]. && (3.16) \end{aligned}$$

A *posteriori* state estimate ($\boldsymbol{x}_t^+$) can be represented as a linear combination of a *priori* estimate ($\boldsymbol{x}_t^-$) and a measurement residual ($z_k - \boldsymbol{H}\boldsymbol{x}_t^-$) as expressed in (3.17):

$$\boldsymbol{x}_t^+ = \boldsymbol{x}_t^- + \boldsymbol{K}_t(z_k - \boldsymbol{H}\boldsymbol{x}_t^-). \quad (3.17)$$

The aim of the Kalman filter is to find the optical gain ($\boldsymbol{K}$) that achieves complete agreement between $\boldsymbol{x}_t^+$ and $z_k - \boldsymbol{H}\boldsymbol{x}_t^-$. Substitution of (3.17) into (3.16) gives:

$$\begin{aligned} \boldsymbol{P}_t^+ &= E[(\boldsymbol{x}_t - \boldsymbol{x}_t^+)(\boldsymbol{x}_t - \boldsymbol{x}_t^+)^T] \\ &= E[[(\boldsymbol{I} - \boldsymbol{K}_t\boldsymbol{H})(\boldsymbol{x}_t - \boldsymbol{x}_t^-) - \boldsymbol{K}_t\boldsymbol{v}_t][(\boldsymbol{I} - \boldsymbol{K}_t\boldsymbol{H})(\boldsymbol{x}_t - \boldsymbol{x}_t^-) - \boldsymbol{K}_t\boldsymbol{v}_t]^T] \\ &= (\boldsymbol{I} - \boldsymbol{K}_t\boldsymbol{H})E[(\boldsymbol{x}_t - \boldsymbol{x}_t^-)(\boldsymbol{x}_t - \boldsymbol{x}_t^-)^T](\boldsymbol{I} - \boldsymbol{K}_t\boldsymbol{H}) + \boldsymbol{K}_t E[\boldsymbol{v}_t\boldsymbol{v}_t^T]\boldsymbol{K}_t^T \\ &= (\boldsymbol{I} - \boldsymbol{K}_t\boldsymbol{H})\boldsymbol{P}_t^-(\boldsymbol{I} - \boldsymbol{K}_t\boldsymbol{H})^T + \boldsymbol{K}_t\boldsymbol{R}_t\boldsymbol{K}_t^T. && (3.18) \end{aligned}$$

Then equating the differentiation of the trace of (3.18) with respect to $\boldsymbol{K}_t$ to zero, gives the optimal gain ($\boldsymbol{K}_t$):

$$\boldsymbol{K}_t = \boldsymbol{P}_t^- \boldsymbol{H}^T(\boldsymbol{H}\boldsymbol{P}_t^-\boldsymbol{H}^T + \boldsymbol{R}_t)^{-1}. \quad (3.19)$$

Substitution of (3.19) into (3.18) gives:

$$\boldsymbol{P}_t^+ = (\boldsymbol{I} - \boldsymbol{K}_t\boldsymbol{H})\boldsymbol{P}_t^-, \quad (3.20)$$

which is the update equation for the error covariance matrix with optimal gain.

By substituting (3.9) into (3.15) to find $\boldsymbol{P}_{t+1}^-$ gives the expression to propagate the error covariance matrix into the next time interval, $t+1$:

$$\begin{aligned} \boldsymbol{P}_{t+1}^- &= \boldsymbol{A}\boldsymbol{P}_t^+\boldsymbol{A}^T + \boldsymbol{Q}_t \\ \rightarrow \boldsymbol{P}_t^- &= \boldsymbol{A}\boldsymbol{P}_{t-1}^+\boldsymbol{A}^T + \boldsymbol{Q}_{t-1}. && (3.21) \end{aligned}$$

Figure 3.3 depicts the complete process of the discrete Kalman filter.

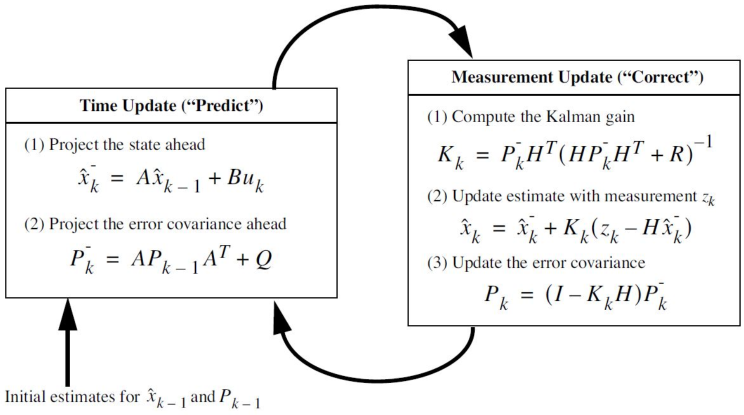

**Figure 3.3:** The operation of the Kalman filter. Image from [5].

### Discrete Extended Kalman Filter Derivation [5] [89]

As described in Section 3.1.5, the discrete Kalman filter estimates the state of a discrete-time controlled process governed by a linear stochastic difference equation. However, it is often the case that the process to be estimated is non-linear and/or the measurement is non-linearly related to the process as described in (3.22) and (3.23):

$$\boldsymbol{x}_t = f(\boldsymbol{x}_{t-1}, \boldsymbol{u}_t, \boldsymbol{w}_{t-1}), \tag{3.22}$$

$$\boldsymbol{z}_t = h(\boldsymbol{x}_t, \boldsymbol{v}_t). \tag{3.23}$$

The non-linear version of the Kalman filter is known as an Extended Kalman filter (EKF). The EKF is based on the concept that the linearised dynamics can approximately represent the true non-linear dynamics in the local region of the operation as in (3.24) and (3.25):

$$\boldsymbol{x}_t \approx \tilde{\boldsymbol{x}}_t + \boldsymbol{A}(\boldsymbol{x}_{t-1} - \boldsymbol{x}^+_{t-1}) + \boldsymbol{W}\boldsymbol{w}_{t-1} \tag{3.24}$$

$$\boldsymbol{z}_t \approx \tilde{\boldsymbol{z}}_t + \boldsymbol{H}(\boldsymbol{x}_t - \boldsymbol{x}^-_t) + \boldsymbol{V}\boldsymbol{v}_t, \tag{3.25}$$

where $\boldsymbol{x}$ and $\boldsymbol{z}$ are the actual state and measurement vectors; $\tilde{\boldsymbol{x}}$ and $\tilde{\boldsymbol{z}}$ are the approximate state and measurement vectors; $\boldsymbol{w}$ and $\boldsymbol{v}$ represent process and measurement noise with zero cross-correlation with each other and white with Gaussian probability distribution; $\boldsymbol{A}$ and $\boldsymbol{W}$ are the Jacobian matrix of partial derivatives of $f$ with respect to $\boldsymbol{x}$ and $\boldsymbol{w}$ respectively; and $\boldsymbol{H}$ and $\boldsymbol{V}$ are the Jacobian matrix of partial derivatives of $h$ with respect to $\boldsymbol{x}$ and $\boldsymbol{v}$ respectively.

The derivation of discrete EKF follows the mathematical process of the discrete Kalman filter. Figure 3.4 depicts the complete process of the discrete EKF filter.

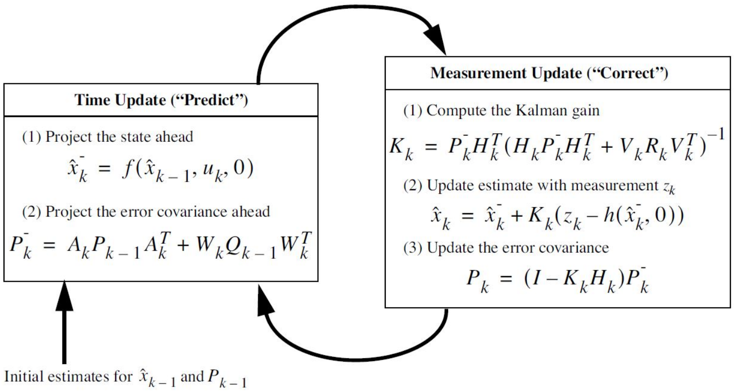

**Figure 3.4:** The operation of the Extended Kalman filter. Image from [5].

## 3.2 Global Navigation Satellite Systems (GNSS)

The purpose of the GNSS is to provide technical compatibility and inter-operability between various satellite navigation systems such as GPS (United States), GLONASS (Russia), Galileo (European Union) and Beidou (China), to be used by civilians. GNSS architecture comprises of three segments, namely: space, control and user segments [6].

The space segment consists of a constellation of satellites intended to orbit so that at least four satellites are available at all times across the globe. The control segment consists of control centres that control satellites' position, attitude and orbit; monitor broadcasting signals and correct clock alignment and navigation message. The user segment consists of GNSS receivers to compute the signals received from the satellites and estimate their position and time on the globe.

### 3.2.1 GNSS Signals

The overview of GNSS signals are given in Table 3.1. Global Positioning Systems (GPS), GLONASS since 2011, Galileo and Beidou signals employ the Code Division Multiple Access (CDMA) structure while the legacy GLONASS signals remain to employ Frequency Division Multiple Access (FDMA) structure [6].

**Table 3.1:** GNSS signals [16] [17]

| Constellation | Carrier frequency | Frequency (MHz) | Multiple access |
|---|---|---|---|
| GPS | L1 C/A | 1575.42 | CDMA |
| | L2 C | 1227.6 | |
| | L2 P | 1227.6 | |
| | L5 | 1176.45 | |
| GLONASS | L1 C/A | 1598.0625-1609.3125 | FDMA/CDMA |
| | L2 C | 1242.9375-1251.6875 | |
| | L2 P | 1242.9375-1251.6875 | |
| | L3 OC | 1202.025 | |
| Galileo | E1 C/A | 1575.42 | CDMA |
| | E5a C | 1176.45 | |
| | E5b P | 1207.14 | |
| | E5 AltBOC | 1191.795 | |
| | E6 | 1278.75 | |
| Beidou | B1 C/A | 1575.42 | CDMA |
| | B1 I C/A | 1575.42 | |
| | B2 C | 1176.45 | |
| | B2 C | 1176.45 | |
| | B3 P | 1207.14 | |
| | E5 AltBOC | 1191.795 | |
| | E6 | 1278.75 | |

FDMA structure divides the entire band of frequencies into multiple non-overlapping Radio Frequency (RF) channels and each channel is allocated to a specific satellite whereas CDMA provides an entire bandwidth to different satellites and differentiates them by assigning unique codes to each satellite known as Pseudo Random Noise (PRN) code. Whilst FDMA ensures signal separation, it adds complexity to the antenna and receiver design process as well as computation of GLONASS signals [90].

### 3.2.2 GNSS Error Sources

GNSS errors originate from three segments of GNSS architecture involved in the evaluation of position and time of a GNSS receiver [6]. These GNSS errors, which originate from the segments of GNSS architecture, are classified into constellation satellite error, signal propagation error and signal reception error [91]. Techniques to resolve these errors can be outlined as follows [6]:

- Averaging of multiple observations at the same position;
- Modelling the error source and estimating the correction values; and
- Differential GNSS (most efficient method).

GNSS constellation satellite error includes orbital position error of a satellite and satellite clock error [91]. The former is caused by orbital perturbation; inaccuracy in the operation of control segments and latency of ephemeris information. The latter is caused by the satellite frequency offset, clock drift and deviation from GNSS standard time.

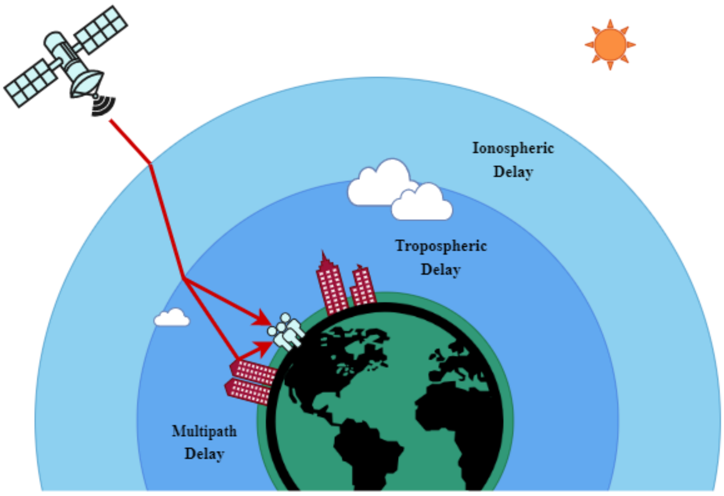

**Figure 3.5:** A diagram depicting the sources of GNSS signal propagation error.

GNSS signal propagation error includes ionospheric refraction, tropospheric refraction and multipath error as depicted in Figure 3.5. Ionospheric refraction adds the group time delay to a signal travelling through the ionosphere. The group time delay is proportional to atmospheric electron density and inversely proportional to the square of electromagnetic wave frequency as given in (3.26) [18]:

$$\Delta t = \frac{1.34 \times 10^{-3} TEC}{f^2}, \tag{3.26}$$

where $\Delta t$ is the group delay time in second; $TEC$ is the total electron content along the signal trajectory and $f$ is the frequency of a signal.

There exists no precise model of ionospheric refraction as it is influenced by the randomness of solar activity, but an Ionosphere Correction Algorithm (ICA) exists for stand-alone single-frequency GNSS receivers. ICA is expected to reduce RMS ionospheric range error by 50% worldwide. The ICA employed by different satellite navigation system is shown in Table 3.2.

**Table 3.2:** ICA employed by different satellite navigation systems [18]

| Constellation | ICA |
|---|---|
| Global Positioning Systems (GPS) | Klobuchar |
| Galileo | NeQuick |
| GLONASS | DNE |
| Beidou | BDGIM |

Tropospheric refraction adds Zenith Total Delay (ZTD), which is also known as atmospheric delay, to a signal travelling through the troposphere. ZTD is composed of the Zenith Hydro-static Delay (ZHD) and Zenith Wet Delay (ZWD) [92]. There are three widely use ZTD model, namely: Saastamoinen, Hopfield and GPT2w models [93].

Multipath error is caused by the superimposition of GNSS constellation satellite signals that reach the receiver from two or more paths, one directly from the satellite and the others reflected from nearby obstacles such as buildings and trees [91]. The uncertainty of the reflection makes the modelling of the multipath error complex and difficult.

A regional Satellite-Based Augmentation Systems (SBAS) can provide wide-area correction information on GNSS constellation satellite error and GNSS signal propagation error (excluding multipath error) to improve the GNSS accuracy and reliability [6]. Currently, SBAS is available in USA (WAAS), Japan (MSAS), India (GAGAN), China (SNAS), South Korea (WADGPAS) and Russia (SDCM) [94].

GNSS signal reception error includes receiver measurement error, clock error, antenna Phase Center Offset (PCO) as well as inappropriate choice and installation of GNSS receiver antenna [91]. GNSS User Equivalent Range Error (UERE) provide a summary of the error budget that influences the accuracy of position acquired from GNSS and is given in the Table 3.3.

**Table 3.3:** GNSS UERE [6]

| Error source | Error range | Error source | Error range |
|---|---|---|---|
| Satellite clock error | ±2 m | Multipath | ±1 m |
| Satellite orbit error | ±2.5 m | Receiver error | ±0.3 m |
| Ionospheric delays | ±5 m | $3\sigma_R$ C/A | ±6.7 m |
| Tropospheric delays | ±0.5 m | $3\sigma_R$ P(Y) | ±6.0 m |

The geometric arrangement of satellites seen by the receiver also influences the accuracy of calculated position and time. Dilution of Precision (DOP) is the metric used to represent the effect of satellite geometry on a receiver position error numerically [6]. DOP is explained in Appendix C with more details.

### 3.2.3 GPS Observation Model

A differential GNSS (DGNSS), the most efficient technique to improve the GNSS performance, is based on the understanding of the GNSS measurement model. DGNSS can be implemented geometry-free or geometry-based. Geometry-free model refers to the computation of position using a combination of measurements from different frequency bands whilst the geometry-based model uses the geometry between multiple receivers.

Due to the limitations and constraints of the project, the implementation of multi-band differential GNSS using multi-constellations was out of the scope of this project. Therefore, the DGNSS technique is limited to single-frequency geometry-based and only Global Positioning Systems (GPS) (L1) measurement model is given in Section 3.2.3. Notations used for single and differential observation models are taken from [7]).

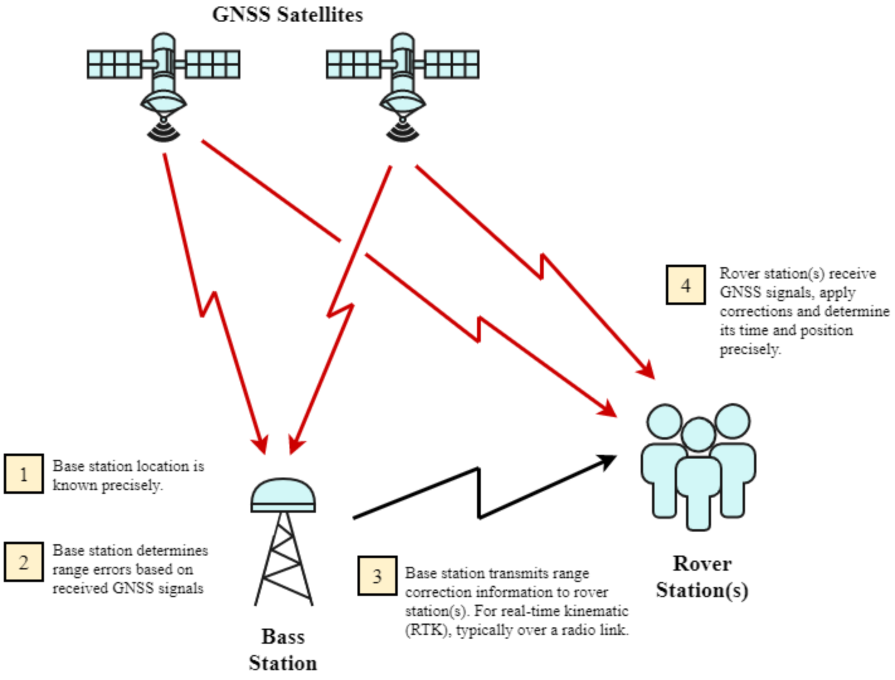

**Figure 3.6:** A diagram of typical differential GNSS system. Image from [6].

Geometry-based DGNSS technique involves a base station and one or more rover station(s) as shown in Figure 3.6 [6]. A base station refers to a GNSS receiver which acts as a stationary reference point with a known position. A rover station refers to a GNSS receiver with unknown position and requires correction information from a base station to evaluate its precise position.

Receiver Independent Exchange Format (RINEX) (a geodetic data interchange format for raw satellite navigation system data) observation and navigation files are assembled from raw GNSS measurements. Observables include time and PRNs per epoch and, depending on the receiver, observables include all or some of the following information for each PRN of corresponding epoch: code ($P$), carrier-phase ($\Phi$), Doppler ($D$) and signal strength ($SNR$) [95].

For a particular epoch, GPS time is the receiver time of the received signals and it is identical for code, carrier-phase, Doppler and signal strength measurements. GPS code measurement is mathematically modelled as follows [96]:

$$P_u^i = \rho_u^i + c(dt_u - dT^i) + b_u - B^i + I_u^i + T_u^i + m_u^i + \varepsilon_u^i, \tag{3.27}$$

where $P_u^i$ is the code measurement of receiver $u$ in meters on frequency $i$ signal; $\rho_u^i$ is the true geometric range between satellite on frequency $i$ and antenna of receiver $u$ (see Figure 3.7) in meters; $c$ is the speed of light; $dt_u$ and $dT^i$ are the clock errors of the receiver $u$ and satellite on frequency $i$ respectively with reference to the GPS standard time; $b_u$ and $B^i$ are hardware delays of the receiver $u$ and satellite on frequency $i$ respectively in meters; $I_u^i$ is the ionospheric delay in meters; $T_u^i$ is the tropospheric delay in meters; $m_u^i$ is the multipath error in meters and $\varepsilon_u^i$ is the unmodelled error in meters.

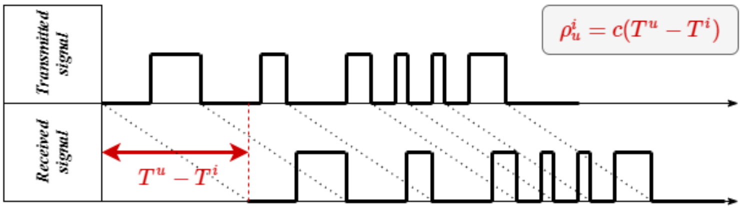

**Figure 3.7:** A diagram depicting how the true geometric range between a satellite and a receiver is related to the satellite and receiver clocks.

Carrier-phase measurement is a reading of a carrier beat signal ($B(t)$) where GPS carrier signal ($G(t)$) from the satellite is multiplied with the receiver's own replica carrier signal ($R(t)$). This in turn is equal to the difference in phase between the replica signal and the GPS signal as expressed by (3.28), providing a direct measurement on the duration it took for a signal to travel from a satellite to a receiver [7]:

$$\Phi_B(t) = \Phi_R(t) - \Phi_G(t). \tag{3.28}$$

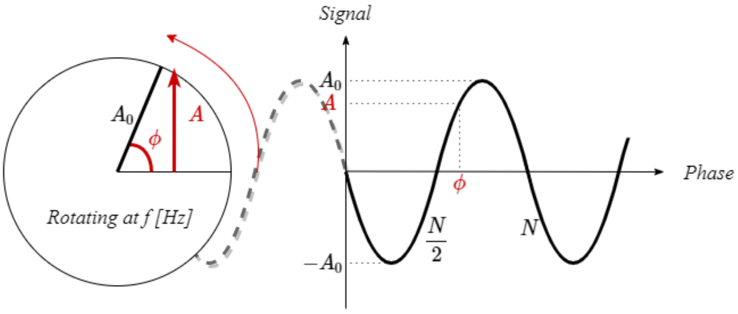

**Figure 3.8:** A diagram explaining the concept of phase where the shadowed dotted signal depicts the ambiguity in the phase of the signal. Image from [7].

The underlying challenge in the processing of a carrier-phase observable lies in the concept of phase. Based on a close analogy to the clock, phase is an angle of rotation in units of cycles and it can be defined as the angle through which a needle has rotated around the center of the circle at any given time $t$ as shown in Figure 3.8 [7]. As such the phase is intimately connected with the concept of clock time. The utility of the clock time depends on the constancy of the frequency in units of cycles per second. Therefore, by the definition clock time is defined as:

$$T(t) \quad = \quad \frac{\Phi(t) - \Phi_0}{f_0}. \tag{3.29}$$

Following above definition of phase and clock time, exactly the same carrier-phase observable will be measured with an arbitrary integer number of cycles added to the phase of a carrier beat signal as expressed by (3.30). Consequently, this arbitrary integer number of cycles known as a phase ambiguity ($N$) must be estimated as well.

$$\begin{aligned} \Phi_B(t) + N \quad &= \quad \Phi_B(t) \\ &= \quad \Phi_R(t) - \Phi_G(t). \end{aligned} \tag{3.30}$$

GPS carrier-phase measurement is mathematically modelled as follows [96]:

$$\Phi_u^i \quad = \quad \rho_u^i + c(dt_u - dT^i) + b_u - B^i - I_u^i + T_u^i + m_u^i + \varepsilon_u^i - \lambda N_u^i, \tag{3.31}$$

where $\Phi_u^i$ is the carrier-phase measurement of receiver $u$ in meters on frequency $i$ signal; $\lambda$ is the wavelength of a frequency $i$ signal and $N_u^i$ is the phase ambiguity which is the integer number ($N \in \mathbb{Z}$) representing the carrier-phase cycle between satellite on frequency $i$ and receiver $u$ at the start of tracking.

GPS Doppler measurement infers information about the change in frequency of the signal wave due to the movement of its source, the satellite, relative to the receiver and it is mathematically modelled as follows [96]:

$$D_u^i \quad = \quad \dot{\rho}_u^i + c(\dot{d}t_u - \dot{dT}^i) - \dot{I}_u^i + \dot{T}_u^i + m_u^i + \varepsilon_u^i, \tag{3.32}$$

where $D_u^i$ is the Doppler measurement of receiver $u$ in meters/second on frequency $i$ signal; $\dot{\rho}_u^i$ is the true geometric range rate between satellite on frequency $i$ and antenna of receiver $u$ in meters/second; $\dot{d}t_u$ and $\dot{dT}^i$ are the clock error rate of the receiver $u$ and satellite on frequency $i$ respectively with reference to GPS standard time; $\dot{I}_u^i$ is the ionospheric delay rate in meters/second; $\dot{T}_u^i$ is the tropospheric delay rate in meters/second.

### 3.2.4 GPS Single Differenced (SD) Observation Model

Signal propagation error is a spatially and temporally correlated error. Therefore, it is valid to assume that time-synchronised observables from a base receiver and rover receiver(s) are exposed to identical signal propagation error [96]. The SD observation model for GPS code and carrier-phase are:

$$\begin{aligned}\Delta P^i_{u,r} &= P^i_u - P^i_r \\ &= \Delta\rho^i_{u,r} + c\Delta dt_{u,r} + \Delta b_{u,r} + \Delta m^i_{u,r} + \Delta\varepsilon^i_{u,r} \qquad (3.33)\\ \Delta\Phi^i_{u,r} &= \Phi^i_u - \Phi^i_r \\ &= \Delta\rho^i_{u,r} + c\Delta dt_{u,r} + \Delta b_{u,r} + \Delta m^i_{u,r} + \Delta\varepsilon^i_{u,r} - \lambda\Delta N^i_{u,r}. \qquad (3.34)\end{aligned}$$

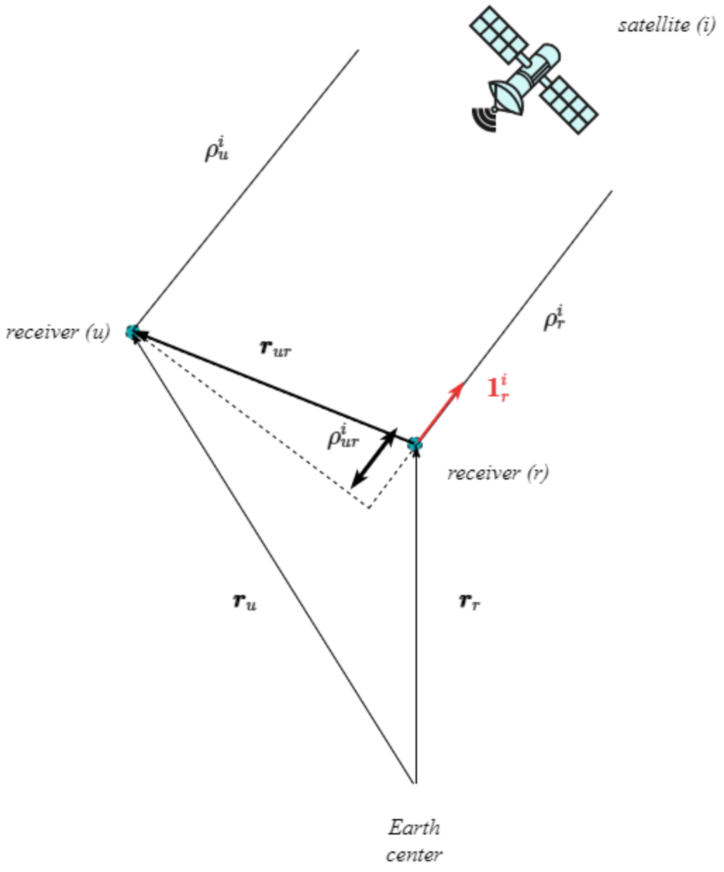

**Figure 3.9:** The geometry of the GPS SD observable [8].

The relative position vector is found from the geometry of the SD measurement shown in Figure 3.9. Using the relative position vector ($\boldsymbol{r}_{u,r}$) and the unit vector in the direction of the satellite on frequency $i$ ($\mathbf{1}^i_r$), the difference in the distances from the receiver $u$ and receiver $r$ to the satellite on frequency $i$ ($\Delta\rho^i_{u,r}$) can be expressed as:

$$\Delta\rho^i_{u,r} = -\mathbf{1}^i_r \cdot \boldsymbol{r}_{u,r} \qquad (3.35)$$

Therefore, the error-less relationship between the navigational position and GPS SD observation model for code and carrier-phase can be expressed by (3.36) and (3.37) respectively [8]:

$$\begin{bmatrix}\Delta P_u^1\\ \Delta P_u^2\\ \vdots\\ \Delta P_u^i\end{bmatrix} = \begin{bmatrix}-\mathbf{1}_r^1\\ -\mathbf{1}_r^2\\ \vdots\\ -\mathbf{1}_r^i\end{bmatrix}\cdot \boldsymbol{r}_{u,r} \tag{3.36}$$

$$\begin{bmatrix}\Delta \Phi_u^1\\ \Delta \Phi_u^2\\ \vdots\\ \Delta \Phi_u^i\end{bmatrix} = \begin{bmatrix}-\mathbf{1}_r^1\\ -\mathbf{1}_r^2\\ \vdots\\ -\mathbf{1}_r^i\end{bmatrix}\cdot \boldsymbol{r}_{u,r} - \lambda \begin{bmatrix}\Delta N_{u,r}^1\\ \Delta N_{u,r}^2\\ \vdots\\ \Delta N_{u,r}^i\end{bmatrix}. \tag{3.37}$$

The SD observation model can be used for precise positioning where $\Delta\rho_{u,r}^i$, $\Delta\varepsilon_{u,r}^i$ and $\Delta N_{u,r}^i$ for both code and carrier-phase of frequency $i$ signal are estimated using statistical techniques such as the Kalman filter (see Section 3.1.5). However, due to the estimation of a number of differential errors such as $\Delta dt_{u,r}$, $\Delta b_{u,r}$ and $\Delta m_{u,r}^i$, the estimated SD carrier-phase ambiguity is likely to be a float value instead of an integer value [97].

### 3.2.5 GPS Double Differenced (DD) Observation Model

Under the condition that both base and rover receivers are from the same manufacturer, their receiver clock error and hardware delay can be assumed to be approximately the same [96]. The DD observation model for GPS code and carrier-phase are:

$$\begin{aligned}\nabla\Delta P_{u,r}^{i,k} &= \Delta P_{u,r}^i - \Delta P_{u,r}^k\\ &= \nabla\Delta\rho_{u,r}^{i,k} + \nabla\Delta m_{u,r}^{i,k} + \nabla\Delta\varepsilon_{u,r}^{i,k} \qquad (3.38)\\ \nabla\Delta\Phi_{u,r}^{i,k} &= \Delta\Phi_{u,r}^i - \Delta\Phi_{u,r}^k\\ &= \nabla\Delta\rho_{u,r}^{i,k} + \nabla\Delta m_{u,r}^{i,k} + \nabla\Delta\varepsilon_{u,r}^{i,k} - \lambda\nabla\Delta N_{u,r}^{i,k}. \qquad (3.39)\end{aligned}$$

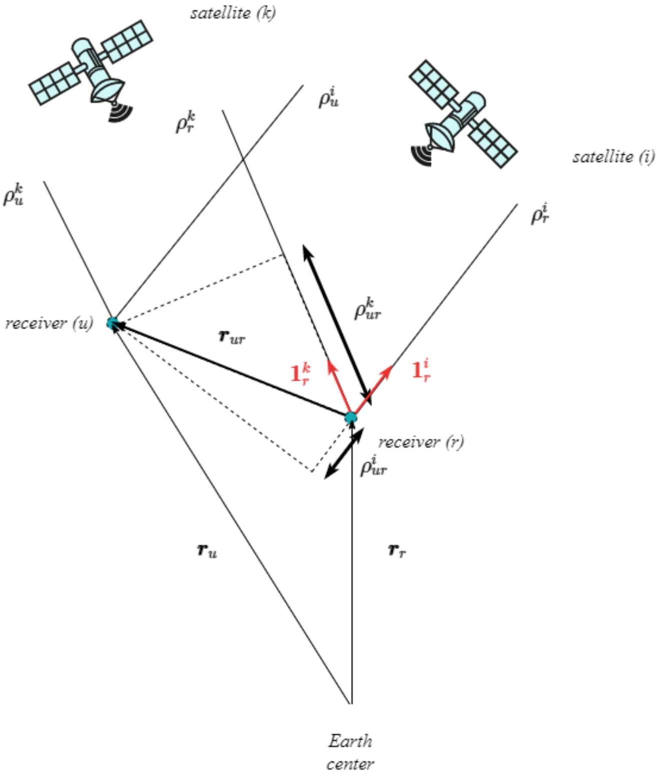

**Figure 3.10:** The geometry of the GPS DD observable [8].

Similar to the GPS SD observation model, the error-less relationship between the navigational position and GPS DD observation model for code and carrier-phase is found based on the geometry shown in Figure 3.10. The relationship for code and carrier-phase is expressed by (3.40) and (3.41) respectively [8]:

$$\begin{bmatrix} \nabla\Delta P_{u,r}^{1,k} \\ \nabla\Delta P_{u,r}^{2,k} \\ \vdots \\ \nabla\Delta P_{u,r}^{i,k} \end{bmatrix} = \begin{bmatrix} -(\mathbf{1}_r^1 - \mathbf{1}_r^k) \\ -(\mathbf{1}_r^2 - \mathbf{1}_r^k) \\ \vdots \\ -(\mathbf{1}_r^i - \mathbf{1}_r^k) \end{bmatrix} \cdot \boldsymbol{r}_{u,r} \tag{3.40}$$

$$\begin{bmatrix} \nabla\Delta \Phi_{u,r}^{1,k} \\ \nabla\Delta \Phi_{u,r}^{2,k} \\ \vdots \\ \nabla\Delta \Phi_{u,r}^{i,k} \end{bmatrix} = \begin{bmatrix} -(\mathbf{1}_r^1 - \mathbf{1}_r^k) \\ -(\mathbf{1}_r^2 - \mathbf{1}_r^k) \\ \vdots \\ -(\mathbf{1}_r^i - \mathbf{1}_r^k) \end{bmatrix} \cdot \boldsymbol{r}_{u,r} - \lambda \begin{bmatrix} \nabla\Delta N_{u,r}^{1,k} \\ \nabla\Delta N_{u,r}^{2,k} \\ \vdots \\ \nabla\Delta N_{u,r}^{i,k} \end{bmatrix}. \tag{3.41}$$

### 3.2.6 Least Squares Ambiguity Decorrelation Adjustment (LAMBDA) Method

Correct estimation of the Double Differenced (DD) carrier-phase ambiguities ($N$) is vital for a precise GNSS navigation. This is because an incorrect estimation of $N$ by 1 can result in a $19.05cm$ positional error. Consequently, researchers have robust methods to determine the number of integers, namely: Cascading Integer Resolution (CIR), Three Carrier Ambiguity Resolution (TCAR) and Least Squares Ambiguity Decorrelation Adjustment (LAMBDA) [98].

CIR and TCAR methods are distinct from the LAMBDA method because they are based on a geometry-free model requiring three-bands whilst LAMBDA supports both geometry-free and geometry-based models [19]. Conceptual comparison between the three methods is given in Table 3.4. Due to the use of single-frequency geometry-based DGNSS technique, only the LAMBDA method will be discussed.

**Table 3.4:** Summary of the comparison of the CIR, TCAR and LAMBDA conducted by Teunissen et al. [19]

| Method | Model | Ambiguity transformation | Estimator algorithm |
|---|---|---|---|
| CIR | Geometry-free<br>modernised GPS<br>(L1, L2 and L5) | pre-defined<br>based on frequencies | Pair-wise<br>Bootstrapping |
| TCAR | Geometry-free<br>Galileo<br>(E1, E5a, E5b) | pre-defined<br>based on frequencies | Pair-wise<br>Bootstrapping |
| LAMBDA | Geometry-free or<br>geometry-based<br>GNSS model | determined based on<br>observation scenario<br>based on entire model | Integer LS |

The LAMBDA method is aimed at finding an optimal integer to meet the following condition [99]:

$$\check{a} = min_{z \in \mathbb{Z}} (\hat{a} - z)^T Q_{\hat{a}\hat{a}}^{-1} (\hat{a} - z), \tag{3.42}$$

where $\hat{a}$ is the estimated ambiguity float solution, $Q_{\hat{a}\hat{a}}$ is the noise covariance of $\hat{a}$ with zero cross-correlation and $\check{a}$ is the corresponding LAMBDA solution.

Re-paramaetrisation of the ambiguities by means of the Z-transformation is necessary to reduce the search time as well as the high correlation between the ambiguity vector elements and poor precision of these elements [100]. Thus, (3.42) becomes:

$$F(z) \quad = \quad (\hat{z}-z)^T Q_{\hat{z}\hat{z}}^{-1}(\hat{z}-z) < \chi, \text{ with } z \in \mathbb{Z}, \tag{3.43}$$

where the positive constant $\chi$ determines the size of the search ellipsoid. Based on the algorithm to determine the size of the search ellipsoid ($\chi$), the LAMBDA method is classified into "search by enumeration" and "search by shrinking" methods [100].

Simply put, LAMBDA optimally finds the nearest integer solution given a float solution but this does not necessarily mean an improvement in precision. Therefore, acceptance testing must be conducted to decide whether to accept or reject the LAMBDA solution.

Currently, there exists acceptance testing based on the concept of Integer Aperture (IA) estimation [101]. An IA estimator makes a decision to accept or to reject based on [101]:

$$\breve{a} \quad = \quad \begin{cases} z, & \text{if } \hat{a} \in \Omega_{\mathbb{Z}} \\ \hat{a}, & \text{if } \hat{a} \notin \Omega \end{cases}, \tag{3.44}$$

where $\Omega$ is the integer acceptance region (fixed solution) and its complement is the integer rejection region (floating solution). However, as can be deduced from (3.44), the IA estimator does not ensure correctness of the integer estimation where the estimated integer ambiguity is the true integer ambiguity [101].

# Chapter 4

# Methodology

This project entails two challenges to meet the aim of the research as described in Section 1.2. The first is the development of an array of time-synchronised sensors to collect IMU measurements and raw GPS observables from each limb segment and the second is the implementation of the state estimation algorithm to reconstruct the motion using the measurements during the measurement update. This chapter provides the outline of the design and implementation process as well as the validation procedures that were taken.

## 4.1 Project Requirements and Specifications

The design process began with the investigation of the relevant literature on MOCAP systems. The literature review was carried out in three phases namely: initial, systemic and empirical literature review, mainly using the database of Google Scholar, Institute of Electrical and Electronics Engineers (IEEE) and National Center for Biotechnology Information (NCBI).

The initial literature review was aimed at obtaining a basic understanding on MOCAP systems to recognise keywords to be used in the systemic literature review. The following keywords were recognised: *MOCAP, method, review, novel, hybrid, fusion, kinematic, kinetic, ground reaction force, torque, Kalman, DGNSS, GNSS, GPS and RTK*. The search was limited to literature in English and some literature was obtained through the citations of the literature found during the initial search.

Based on the systemic review, the project aim, limitations and constraints of the project were realised and design guidelines were established. Thereafter, user requirements and functional requirements of the fusion MOCAP system were identified and the system overview was developed.

The empirical literature review was conducted to evaluate the feasibility of the functional requirements and to discover the learning required to develop and implement the fusion MOCAP system. The empirical literature review also involved a number of meetings with the stakeholders: distributors, manufacturers, project sponsors and supervisor to obtain the unequivocal technical specifications for the array of time-synchronised sensors.

Based on the requirements and specifications, acceptance testing procedures were prepared for the array of time-synchronised sensors and evaluation criteria were prepared to evaluate the performance of the state estimation algorithm. The acceptance testing procedures were prepared in stages from fundamental to advanced features.

## 4.2 Device Development

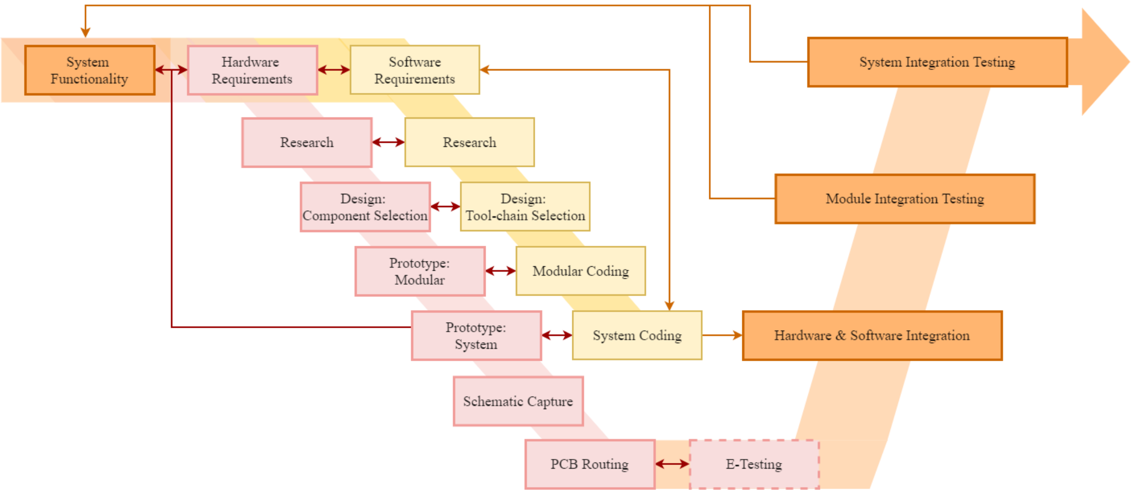

**Figure 4.1:** The co-development process followed during the development of the device which includes a base station and a time-synchronised sensor array. Red represents the hardware development; yellow, the firmware development and orange, the hardware-firmware integrated systems.

The development of an array of time-synchronised sensors involved hardware and firmware development that progressed concurrently as shown in Figure 4.1. The hardware, firmware and hardware-firmware integrated systems are represented by red, yellow and orange shades respectively. This style of co-development eased the verification of the hardware and firmware integration during validation stage, despite them being different in nature and having different requirements and constraints.

The hardware development process was an iterative process involving the realisation of the hardware technical specifications and constraints; research on feasible solutions; component selection; proof-of-concept prototyping; verification of the built prototype; schematic capture; PCB design and integration with software as shown in Figure 4.1.

Similar to the hardware development process, the firmware development process was also an iterative and incremental process involving realisation of firmware specifications and constraints; an empirical literature review on feasible architecture; definition of tasks and task sequence; selection of run-time and middle-ware; coding and implementation on the hardware. A bottom-up style of programming was adapted to ensure the modularity of the design.

As a proof of concept, a working prototype was built by assembling the evaluation and discovery boards of selected components. A prototype that was proven to work was necessary as only one PCB design was fabricated due to the limited budget. One the performance of the prototype was verified, it was used to capture schematics and the PCB was routed using *Altium Designer 18* [102].

*Altium Designer 18* [102] was once again used to output an assembly file and Gerber files including signal, overlay, paste mask and solder mask layers. Gerber files were sent to *Trax Interconnect (PTY) LTD* and *Barracuda Holdings (PTY) LTD* to fabricate the PCB and stencil respectively. Components were placed by *Barracuda Holdings (PTY) LTD* based on the provided assembly file. Then, an electronic test (E-test) was conducted by *Barracuda Holdings (PTY) LTD* to detect any unintended open circuits and shorts that were created during the assembly process.

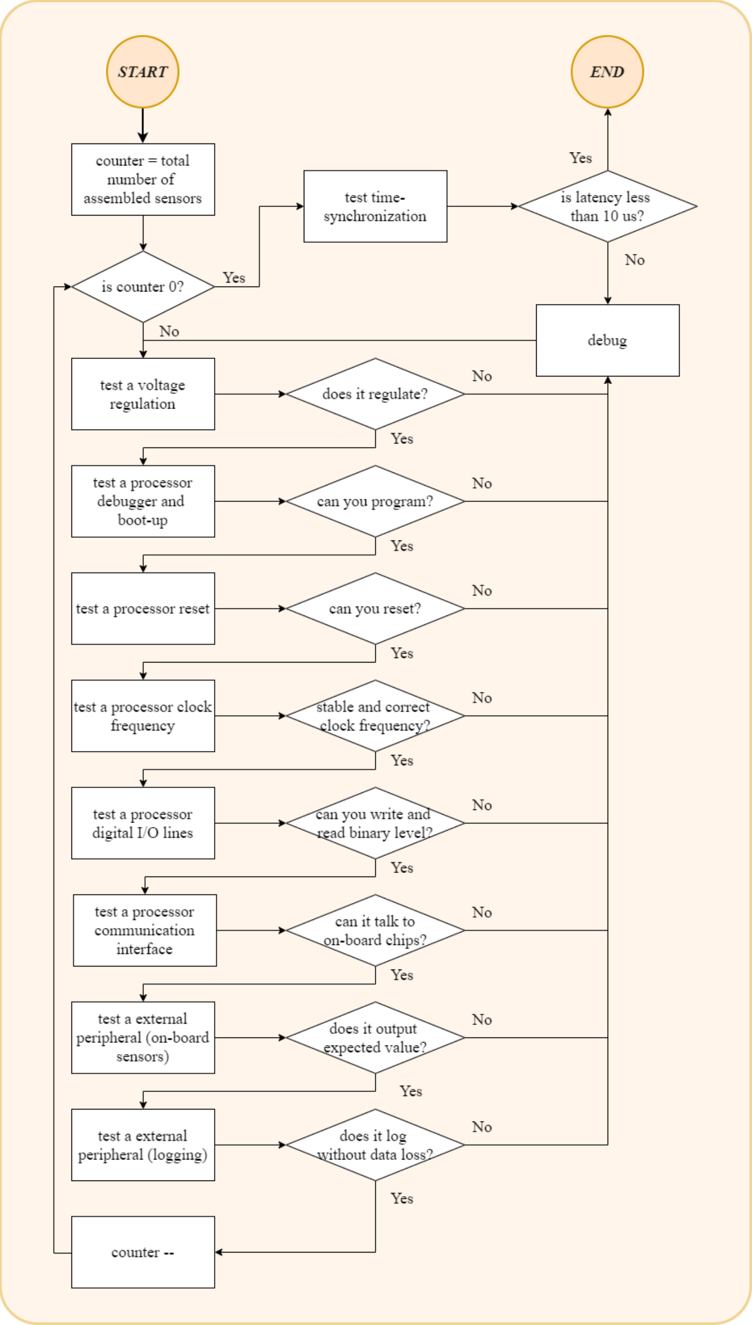

**Figure 4.2:** The testing procedure followed the assessment of the developed device. The procedure progressed from the most fundamental to most advanced feature.

As previously stated, the assessment of the device progressed from the most fundamental feature (voltage regulation) to the most advanced feature (time-synchronisation) as shown in Figure 4.2. The testing procedure with this pyramid structure allowed precise and rapid identification of the source(s) of the bug(s) during the debugging process. Certain hardware and firmware bugs were removed by making modifications to the firmware and hardware respectively, as such solutions were time and cost efficient.

As can be seen from Figure 4.2, the testing of the time-synchronisation only took place when it was confirmed that every sensor unit functioned as per the developed technical specifications. This reduced the number of possible source(s) of the bug(s) if the latency in time-synchronisation was evaluated to be longer than 1% of the lowest sampling period. The complete acceptance testing procedure is documented in Table D.5 Appendix D.

During the testing of the device, the laboratory instruments such as a microscope, soldering iron, power supply, active oscilloscope, multimeter and logic analyser were used during the process. The *ST-Link* debugger and utility were used to communicate with the processor since the chosen processor was of the *STM32* series. The firmware was initially developed in C programming language on *TrueSTUDIO* [103] environment but moved to *STM32 IDE* [104] due to the change in the market trend.

## 4.3 State Estimation Algorithm Development

A top-down approach was adapted to decompose the system into large-scale sub-systems and manageable tasks. This approach provided insights into each task and eased the debugging process by adding modularity into the system. The state estimation algorithm involved three sub-systems, namely: calibration, data fusion and tuning. These sub-systems were developed sequentially.

With a limited project time, it was decided that the development of the geometry-based single-frequency DGPS from the ground up in conjunction with the development of the array of time-synchronised sensors was out of the scope of this project. Consequently, libraries from an open-source software package *goGPS (MATLAB)* [105] were imported and the state estimation algorithm was developed in *MATLAB* [106].

**Figure 4.3:** A photo of the mechanical rig during the data acquisition.

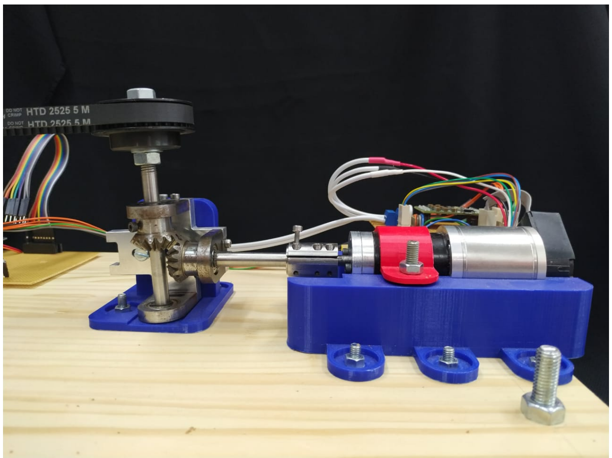

**Figure 4.4:** A photo of the *Maxon* brush-less EC motor driving the bevel gear array to *Contitech* M2 timing belt pulley.

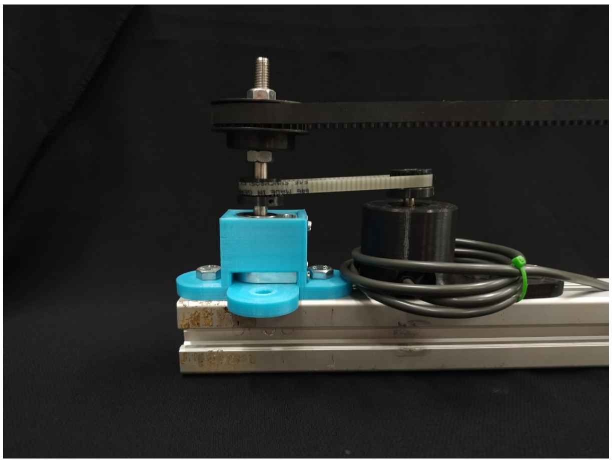

**Figure 4.5:** A photo of the belt driven output shaft and the belt driven encoder with 1:1 ratio.

A commercial outdoor MOCAP system was not available to use as a reference to validate the system, therefore a mechanical rig shown in Figure 4.3 was built for system validation. The mechanical rig was designed to rotate a circular platform mounted on the rig. It was made out of a *Maxon* brush-less EC motor, motor controller, planetary gearbox, bevel gearbox, belt-driven shafts and an encoder as shown in Figure 4.4 and Figure 4.5.

Note that in Figure 4.3, the output shaft was belt-driven approximately 1.2m away from the input-shaft and the system rested on a non-metallic platform to avoid saturation due to the soft and hard iron interference caused by the use of the brush-less EC motor and a near metallic object respectively. The distance between the input-shaft and the output-shaft was determined through trial-and-error process. During the process, the distance was incremented by 0.1m (starting from 0.5m) until the magnetometer measurements from the system were not saturated with the motor running.

The incremental encoder was connected to the output shaft via a belt with 1:1 ratio and measured the relative angle of the output shaft as shown in Figure 4.5. The relative angular position obtained from an encoder[1] with the resolution of $1024 pulse/rev$ was coupled to the base station measurements to synchronise its measurement with the sensor array.

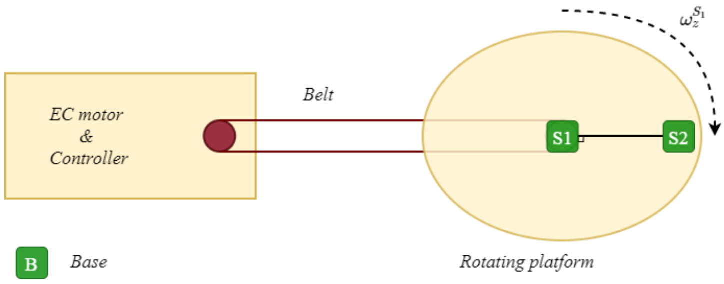

**Figure 4.6:** A diagram depicting the layout of the device during data acquisition.

The developed device was used during the data acquisition to collect the raw GPS observables from the base station (named $B$) as well as the IMU measurements and raw GPS observables from the two time-synchronised sensors (named $S_1$ and $S_2$). $S_1$ and $S_2$ were mounted on the circular platform on the mechanical rig as shown in Figure 4.6. During the testing, $S_1$ remained stationary whilst the $S_2$ rotated around the z-axis of the $S_1$. The motion of $S_2$ relative to $S_1$ was aimed at simulating a motion of a limb segment about its joint with one degree of freedom.

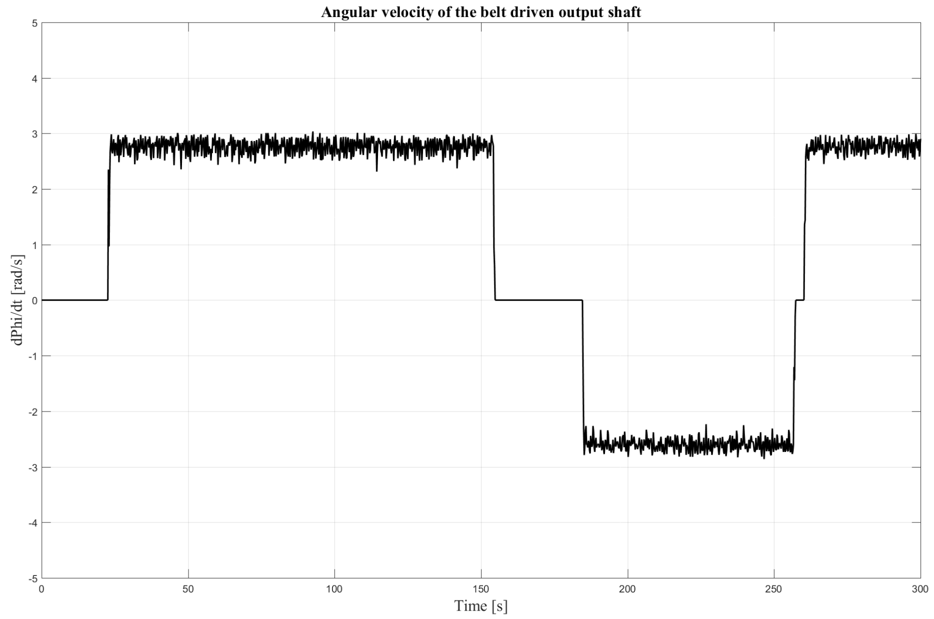

**Figure 4.7:** A plot of the angular velocity of the belt-driven output shaft read by the encoder during data acquisition.

---

[1] *Omron E6B2-CWZ6C*

The research aimed to develop an outdoor MOCAP system that was able to track the steady-state locomotion (a walking) and transient locomotion (a near-instantaneous stop and turn). Therefore, the belt-driven output shaft began or stopped rotation abruptly during the experiment as shown in Figure 4.7.

The peak angular velocity of the belt-driven output shaft ($\approx 3rad/s$) was chosen based on the anatomical study conducted by Hudson et al. [107] and Wilson et al. [44] on the fastest terrestrial *megafauna*, the cheetah (*acinonyx jubatus*). An *acinonyx jubatus* was observed to have a peak angular velocity of $\pm 2rad/s$ and an additional 50% margin was added to this number in order to stress and test the boundary of the developed fusion MOCAP system.

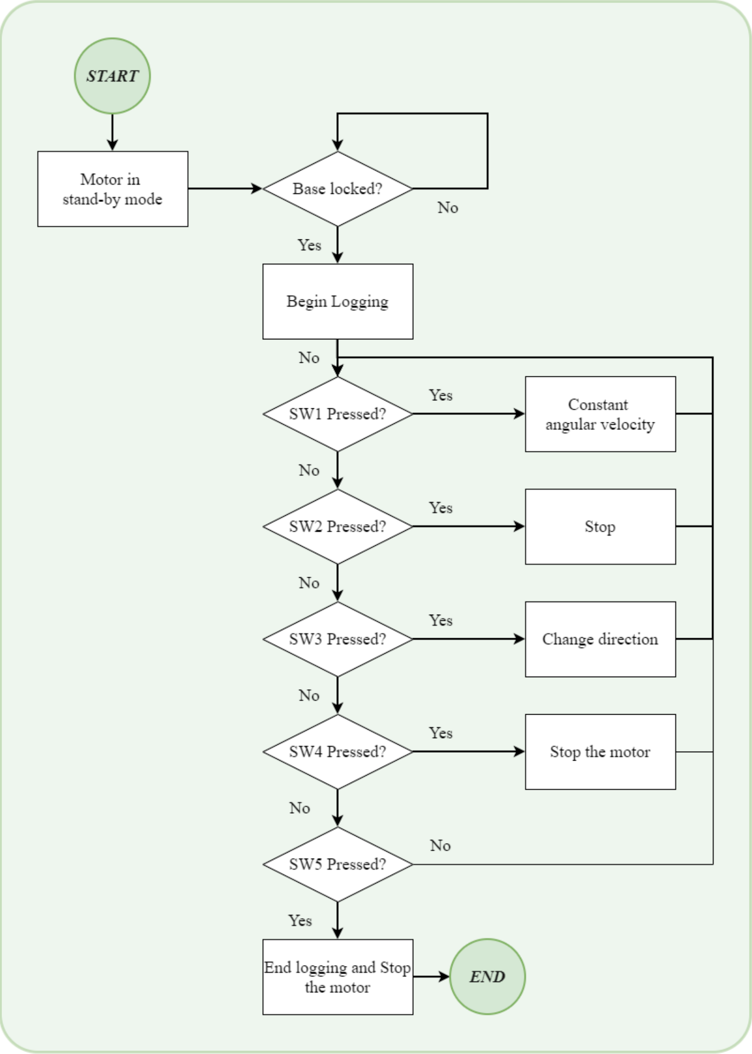

**Figure 4.8:** A flow diagram depicting the operation of the mechanical rig. The motor only accepts the command to initiate the logging once the base station has been successfully locked to a minimum six satellites. The user of the mechanical rig is given four tactile switches to control the rotational motion of the output shaft.

Figure 4.8 depicts the operation of the mechanical rig. The following test procedure was developed and followed during the testing conducted using the mechanical rig:

- Turn on the base station ($B$).
- Begin surveying the ECEF coordinates of the base ($B$).
- Wait until the standard deviation of the surveyed ECEF coordinates of the base ($B$) reach $1m$ as recommended in [108].
- Turn on the mechanical rig.
- Turn on the time-synchronised sensors ($S_1$ and $S_2$).
- Begin data logging on both the mechanical rig and the sensors.
- Perform instantaneous turns and stops.
- Stop data logging on both the mechanical rig and the sensors.
- Shut down all devices.

In order to evaluate the developed fusion MOCAP system and to compare its performance to the existing inertial and fusion MOCAP systems, three state estimation algorithms were developed, namely: *MEMS-IMU*, *DGPS/MEMS-IMU single-receiver* and *DGPS/MEMS-IMU multi-receiver*. These state estimation algorithms are similar in all respects except for their measurement inputs as shown in Figure 4.9.

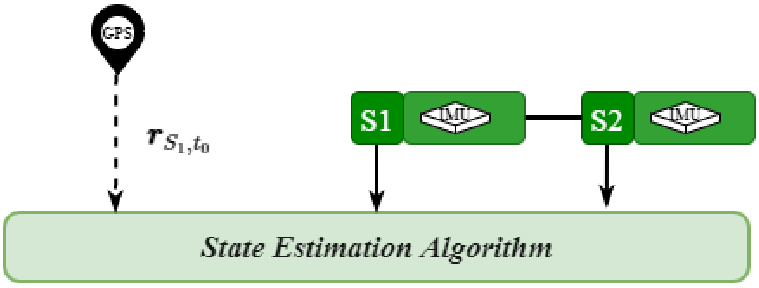

**(a)** A state estimation algorithm which only receives the IMU measurements from both $S_1$ and $S_2$. To enable comparison of this algorithm to the other state estimation algorithms, which received raw GPS observables, the ECEF coordinates of the $S_1$ at $t = 0$ is given to comprehend the estimated Euler angles to global positions.

Figure 4.9a depicts a state estimation algorithm that imitates the existing inertial MOCAP system. Figure 4.9b depicts a state estimation algorithm which imitates the fusion MOCAP system of Supej [47]. Figure 4.9c depicts a state estimation algorithm which was intended for the developed fusion MOCAP system and was influenced by the algorithm in Figure 4.9b. Two of the research questions mentioned in Chapter 1 were answered based on the comparison of these three algorithms. In order to keep the comparison between the above-mentioned three state estimation algorithms, the process and measurement covariances were kept constant throughout the comparison.

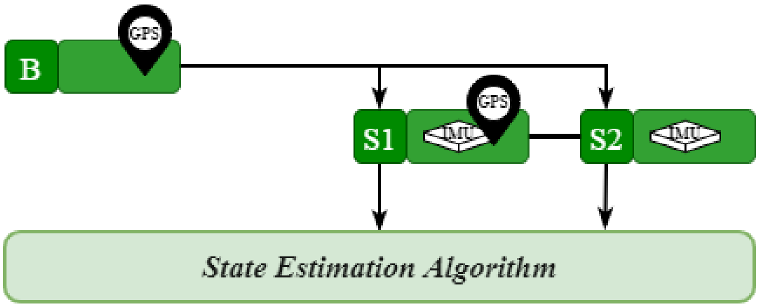

**(b)** A state estimation algorithm which receives the IMU measurements from both $S_1$ and $S_2$ as well as the raw GPS observables from $S_1$.

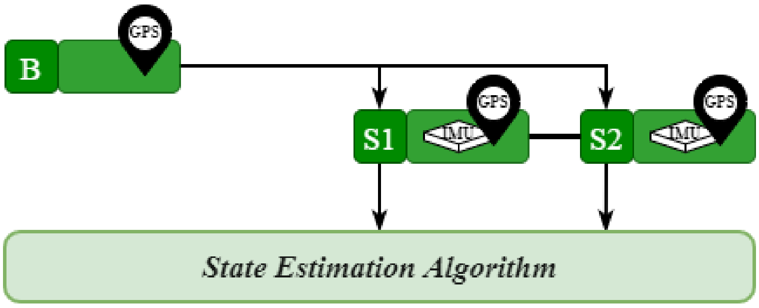

**(c)** A state estimation algorithm for the developed fusion MOCAP system which receives the IMU measurements and the raw GPS observables from both $S_1$ and $S_2$.

**Figure 4.9:** Three state estimation algorithms that are developed in order to evaluate the performance of the developed fusion MOCAP system in comparison to the existing inertial and fusion MOCAP systems.

The research question: ***Does integration of GPS or DGPS improve the applicability and/or performance of the traditional MEMS-IMU MOCAP system?***, was answered by comparing the performance of the *MEMS-IMU* MOCAP system in Figure 4.9a to the performance of the *DGPS/MEMS-IMU single-receiver* MOCAP system in Figure 4.9b.

The research question: ***Is it possible to achieve the positional accuracy of the existing commercial MOCAP systems using a DGPS/MEMS-IMU integrated fusion MOCAP system?***, mentioned in Chapter 1, was answered by comparing the performance of the *DGPS/MEMS-IMU single-receiver* MOCAP system in Figure 4.9b to the performance of the existing commercial MOCAP systems.

The research question: ***Is integration of DGPS on each limb segment beneficial compared to the MEMS-IMU MOCAP system with a single DGPS?***, mentioned in Chapter 1, was answered by comparing the performance of the *DGPS/MEMS-IMU single-receiver* MOCAP system in Figure 4.9b to the performance of the developed fusion MOCAP system (*DGPS/MEMS-IMU multi-receiver*) in Figure 4.9c.

The time-synchronised surveyed position of $S_1$ and encoder measurements were used as the reference to quantify and validate the performance of the state estimation algorithm and hence the fusion MOCAP system. The following cost function was used to compare the developed system against the reference:

$$c = \sqrt[2]{\frac{\sum_{i=1}^{m}(\beta_{filter} - \beta_{encoder})^2}{m}}, \tag{4.1}$$

where $m$ is the number of samples and $\beta$ is the kinematic information of interest along an axis ($i$). The kinematic information of interest can be a linear position ($r_i$), angular position ($\theta_i$), linear velocity ($v_i$) or an angular velocity ($\omega_i$). Therefore, the evaluation of the estimated N-dimensional kinematic information was conducted using the following extended cost function:

$$\vec{c}_{(N\times 1)} = \sqrt[2]{\frac{\sum_{i=1}^{m}(\vec{\beta}_{filter(N\times 1)} - \vec{\beta}_{encoder(N\times 1)})^2}{m}}. \tag{4.2}$$

# Chapter 5

# Fusion MOCAP System

This chapter aims to provide descriptions of the fusion MOCAP system to be developed. A meticulous system overview is a necessity to prepare well-defined technical specifications in order to reduce the number of design iterations. Design iterations are time-consuming and costly by nature and a reduction in the number of iterations was critical for the project as there was limitations on the project budget and time.

Prior to the establishment of the system overview, design guidelines were established to promote consistent design practice and to reduce the number of design iterations. Design guidelines refer to a list of principles and standards that must be applied and considered when making design decisions. Once the design guidelines were established, user requirements and functional requirements were defined. Finally, the system overview was established.

## 5.1 Design Guidelines

Modularisation of the system architecture decreases the complexity of the system and facilitates the ability to respond to future requirement changes with less effort. Furthermore, modularisation of the system into functional groups highlights the flexible platform(s) within the architecture that are likely to change by external factors over time and will require more attention then the others [109].

Error robustness in human-system interaction is critical to provide a comfortable environment for the end-users [110]. It is aimed at permitting errors and providing a platform to undo the erroneous behaviour of the system instead of designing a perfect system with no errors. According to [110] and [111], the following attributes must be attained to develop a modular system architecture with error robustness:

- ***Communality***: re-usability of the functions and modules at a higher hierarchy of the system;
- ***Combinability***: modularisation of the system configuration process for system expansion and change;
- ***Function binding***: one-to-one and many-to-one mapping between functions and modules;
- ***Reversibility***: recovery or return to previous status or operation;
- ***Interface standardisation***: physical standardisation of the system input and output interfaces;
- ***Decoupling***: weaker binding strength between the modules in comparison to the internal binding between the components of a module;
- ***Input limitation***: limited user inputs which reduce possible error cases.

## 5.2 User Requirements

User requirements, listed in Table D.1 in Appendix D, describe the needs of the user and activities that the user performs on and with the system. As previously stated in Section 1.2, the user seeks a system that provides them with the kinematic quantities of the steady-state and transient locomotion of a terrestrial *megafauna* outside a controlled laboratory environment.

As per Section 1.3, the system does not include a strapped-down mechanism while limited to 6 hours of data acquisition time and post-processing. Additionally, *outdoor* is assumed to be in dry conditions at a temperature ranging between $-20\ ^{\circ}C$ and $60\ ^{\circ}C$ and sea-level air pressure ranging between 870 hPa and 1100 hPa which corresponds to the lowest and highest temperature experienced in Africa and sea level air pressure of the world respectively [112].

Consequently, the user needs a portable device that records for at least 6 hours and outputs direct and/or indirect measurements of the motion of a subject in an outdoor environment that is less restrictive than the controlled laboratory condition. The user must be able to interact with the device to begin and stop the data acquisition procedure and must be notified of any erroneous behaviours. Once the measurements are obtained, the user needs a software that post-processes the measurements and outputs the kinematic quantities of the captured motion of a terrestrial *megafauna* based on statistical techniques.

## 5.3 Functional Requirements

Functional requirements, listed in Table D.2 in Appendix D, define the functionalities of a system or its components. To ensure device portability and encourage modularisation of the system as per the design guidelines, the device shall be complete and independent. The minimum and maximum operating temperature of the device shall further be rated at $-20\ ^{\circ}C$ and $60\ ^{\circ}C$ respectively.

The direct and/or indirect measurements of motion were chosen to be IMU measurements and raw GPS observables (see Chapters 2 and 3). Therefore, the device shall read and record these measurements from each limb segment at the rate that ensures no loss of motion information. The data from each limb segments shall be time-synchronised to avoid inaccuracy from latency.

The device shall provide the user with two tactile switches to signal the start and end of the data acquisition process as well as visual feedback on the status of the device. Additionally, to accommodate MOCAP without a pre-defined kinematic chain, the system shall not limit the number of limb segments the user can track. It must also last for a minimum of 6 hours.

The post-processing software shall accept and comprehend the measurements from the device and feed them into the state estimation algorithm. This algorithm requires the kinematic chain and noise covariance matrices. Upon completion of the post-processing, the software shall output a file which contains information for the user to quantitatively analyse the motion as well as the performance of the algorithm.

## 5.4 System Overview

Figure 5.1 depicts the concept of the fusion MOCAP system to be developed, including system architectures, file formats, user inputs and outputs. In Figure 5.1, arrows indicate the flow of information where green is managed by the developer; red by the user and black by third parties such as space and control segments of the GNSS system that are not controlled by the developer or user.

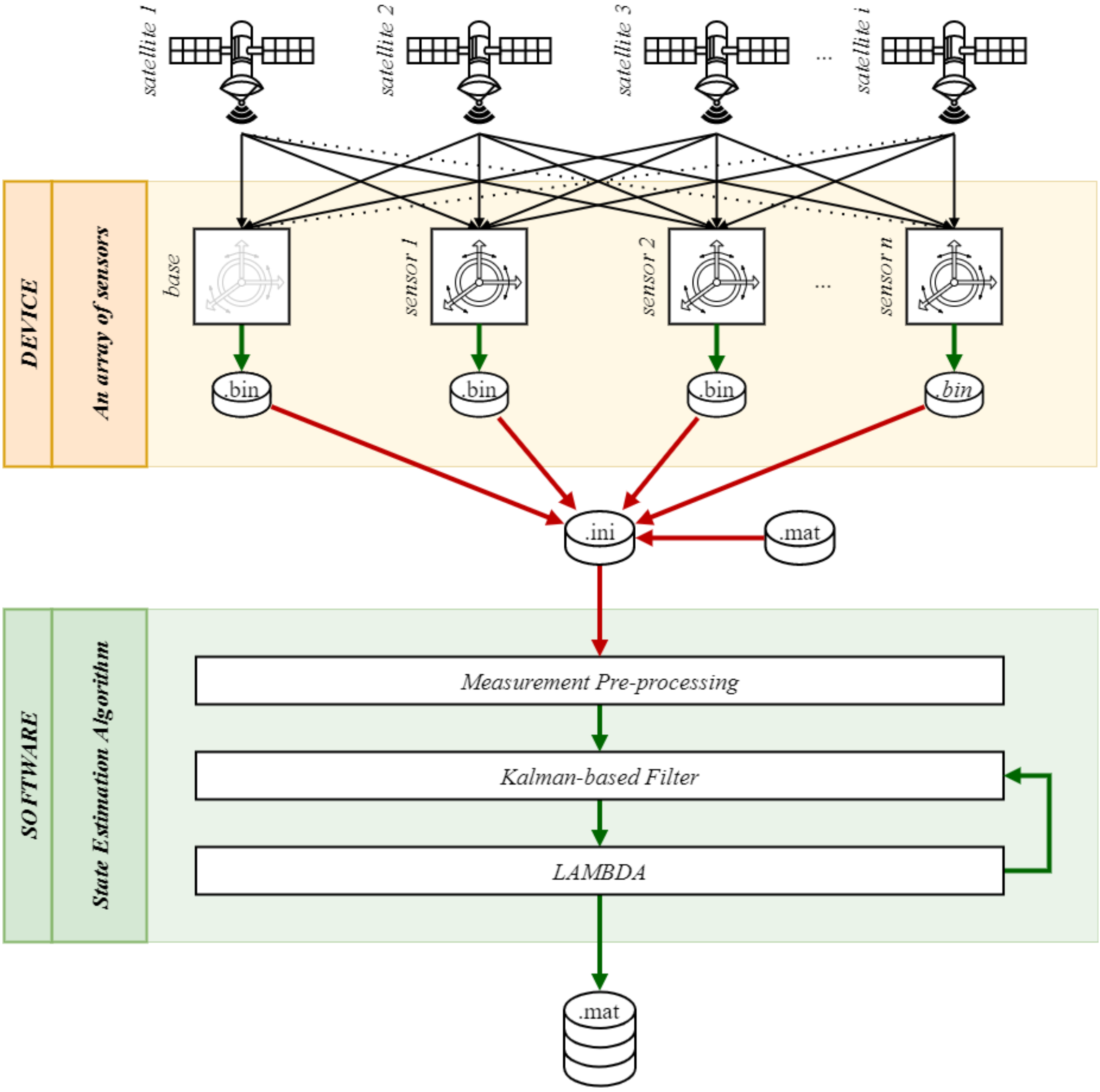

**Figure 5.1:** A diagram depicting the overall system of the proposed fusion MOCAP system. The proposed system consists of the device and the software. The device consists of a base station and a time-synchronised sensor array. The software is responsible for estimation of the kinematic information of the captured motion using the indirect measurements of motion collected by the device.

As can be seen from Figure 5.1, the system consists of two parts, namely the device and the software. The device refers to an array of time-synchronised sensors that are responsible for data acquisition and the software refers to the state estimation algorithm that is responsible for post-processing and reconstruction of 3D motion.

Every individual sensor is capable of outputting a binary file (.bin) containing IMU measurements and raw GPS observables. Each measurement is stamped with the time of acquisition with reference to the standard GPS time for time-synchronisation. By avoiding the use of wireless WPAN, the number of sensors in the array is unlimited.

By disabling the IMU and locating a sensor at a known position as a stationary reference point, a sensor is capable of performing the role of the base station to implement DGPS otherwise it performs the role of the rover. This ensures *communality*, *combinability* and *function binding* within the system.

User inputs are limited to two digital input signals to a sensor: start and end commands for the data acquisition process. The status of a sensor is shown by means of visual feedback. Upon completion of the data acquisition process, the user transfers the binary files to a main processor and provides an initialisation file (`.ini`) to the state estimation algorithm.

An initialisation file lists the path to the binary file(s) (`.bin`) and binary data container format file (`.mat`). The binary file(s) is named according to the kinematic chain of the captured limb segment(s) and contains the indirect measurements of motion collected during the experiment. The binary data container format file contains the process and measurement noise covariance matrices of each sensor. By giving the user write and read access to the initialisation file, the user is allowed to exclude measurements and decouple certain limb segment(s) from the kinematic chain effortlessly.

The state estimation algorithm is designed to pre-process the measurements; initialise the Kalman filter using the kinematic chain and covariance matrices provided by the user; and compute the kinematic quantities of the steady-state and transient locomotion by means of the Kalman filter and LAMBDA. Finally, it outputs a binary data container format file (`.mat`) containing predicted and estimated states; process and measurement noise covariances; priori and posteriori error covariances; residuals; carrier ambiguity floating and fixed solutions for every epoch.

# Chapter 6

# Sensor Development

This chapter aims to justify the decisions made during the development of the device for the fusion MOCAP system described in Chapter 5. Accordingly, it documents the realisation of the technical specifications and constraints; component procurement; prototype assembly; firmware development; schematic capture; PCB routing; testing and results.

## 6.1 Hardware Technical Specifications

In accordance with the system overview in Section 5.4 in Chapter 5, every sensor shall be an independent unit to encourage a lack of hierarchy amongst the array of time-synchronised sensors. The definition of *outdoor* stated in Section 5.2 in Chapter 5 places constraints on the temperature rating of the electronic components during the component procurement process.

Considering the constraints on the operating temperature, the use of FR4 composite material in the PCB was advised. This is because the FR4 composite material is the most common material for multi-layer PCBs with strict requirements for mechanical strength and has an operating temperature ranging from $-50\ ^{\circ}C$ and $+110\ ^{\circ}C$.

The device is responsible for collecting the time-synchronised sets of IMU measurements and raw GPS observables. Considering the broad range of subjects (a family of a terrestrial *megafauna*), the IMU shall have measurement ranges and sampling frequencies to avoid or minimise measurement saturation. Additionally, a loss of GPS signals must be avoided or minimised by careful selection of a GPS receiver and a GPS antenna.

### 6.1.1 IMU

The minimum threshold for the IMU measurement range was based on the anatomical study conducted by Hudson et al. [107] and Wilson et al. [44] on the fastest terrestrial *megafauna*, the cheetah (*acinonyx jubatus*). In [107] and [44], an *acinonyx jubatus* was observed to have a peak lateral acceleration of $\pm 2g$ and femur and tibia angular velocity of $\pm 2rad/s$.

Consequently with an additional 100% design margin, a minimum range of $\pm 4g$ and $\pm 4rad/s$ are required for a 3-axis accelerometer and a 3-axis gyroscope respectively. Although a 3-axis magnetometer is intended to measure the direction of the Earth magnetic field whose magnitude ranges from $25\mu T$ and $65\mu T$ [113], the magnetometer measurement range shall be far greater ($> 1000\mu T$) to account for hard and soft magnets in the vicinity of the 3-axis magnetometer in order to avoid saturation.

Furthermore, no studies have investigated the optimal sampling frequency for a strapped-down inertial MOCAP system. However, it has been shown that a lower sampling frequency results in less accurate reconstruction of the motion [114]. The femur and tibia of the cheetah are modelled as a simple rigid body rotating about a fixed point at $2rad/s$ to find the minimum sampling frequency threshold for a 3-axis gyroscope. The minimum sampling frequency threshold for the 3-axis accelerometer was assumed to be the same as the 3-axis gyroscope.

$$f_{minimum} = round(\frac{2\omega}{\varepsilon}), \tag{6.1}$$

where $\varepsilon$ is the accuracy in degree and a factor of 2 is required to satisfy the Nyquist theorem.

As per (6.1), the minimum sampling frequency of $\sim 600Hz$ is required to achieve the same accuracy as the commercial *Xsens* inertial MOCAP system ($\pm 0.5°$). A 3-axis magnetometer inherently has a low sampling rate typically ranging between $10Hz$ to $20Hz$ [82]. However, this is not a problem as the role of a 3-axis magnetometer measurement is to correct the inherent drift in a 3-axis accelerometer and a 3-axis gyroscope during attitude estimation.

### 6.1.2 GPS Receiver and Antenna

A GPS receiver has two critical requirements. It must output raw GPS observables for civil GPS L1 band (see Table 3.1 in Chapter 3) and have a Pulse per Second (PPS) pin to be used for time-synchronisation. Other than these requirements, there was a preference for a receiver that outputs Signal-to-Noise Ratio (SNR) observable and includes an on-chip Surface Acoustic Wave (SAW) band-pass filter, Low-Noise Amplifier (LNA) and an internal Oven Controlled Crystal Oscillator (OCXO) instead of Temperature Compensated Crystal Oscillator (TCXO) for the following reasons.

As previously mentioned in Chapters 3 and 5, a Kalman filter requires measurement noise covariance. However, the assumption of constant measurement noise covariance is not optimal for the DGPS positioning filter because the quality of the final position depends on both the measurements accuracy and the satellite geometry [96]. Therefore, the availability of raw GPS SNR observable is beneficial to the implementation of a Kalman-based post-processed DGPS because the relationship between the noise covariance and the SNR observables has been observed in [115].

A SAW band-pass filter is necessary to selectively receive the signals within a certain range of frequencies and ignore signals at unwanted frequencies. In conjunction with a LNA, the SNR and sensitivity of the receiver are optimised. By choosing a receiver with the internal SAW and LNA, the schematics and PCB routing can be simplified.

An OCXO is known to have better frequency and temperature stability over a TCXO but it is typically included in high-end receivers that is larger in size, higher in power consumption and more costly [96]. Therefore, this was not a strict requirement as the project was limited by budget to low-cost receivers.

To decide on a type of antenna, one passive patch antenna (*Taoglas FXP.611*) and one active patch antenna (*Titan AA.105.301111*) was connected to each *Ublox NEO-M8T* receiver and positioned stationary, 10*cm* apart. Raw GPS observables were then collected. Since the quality of the DGPS depends on the measurements accuracy and the satellite geometry as stated above and explained in Chapter 3, a number of satellites, raw GPS SNR observables and a DD code and carrier-phase residual from the two different systems (one with the passive patch antenna and the other with the active patch antenna) were compared.

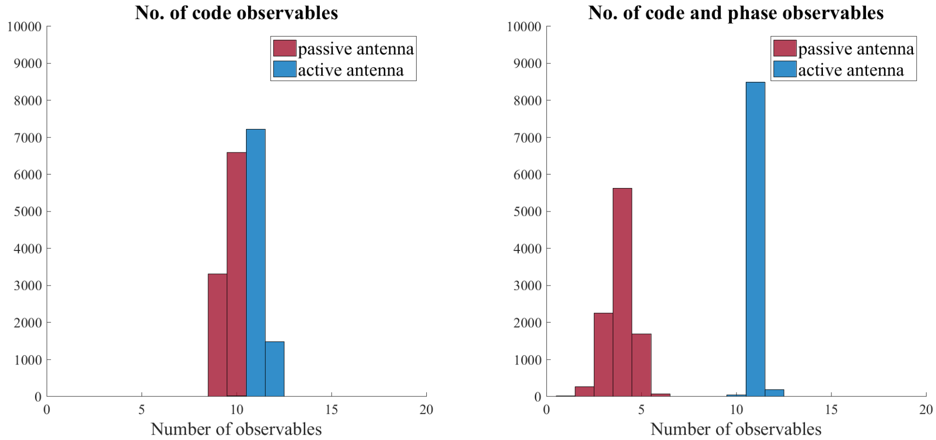

**Figure 6.1:** Two histograms comparing the number of raw GPS observables collected from an active and a passive antenna. On the right is the histogram of the number of raw GPS code observables. On the left is the histogram of the number of raw GPS code observables consisting of both code and carrier-phase observables.

As it can be clearly seen from Figure 6.1, a receiver with an active antenna can see a higher number of satellites throughout the data acquisition. Most importantly, it is clear that a receiver with a passive antenna has less epoch with both code and carrier-phase observables, making it not optimal to implement DGPS.

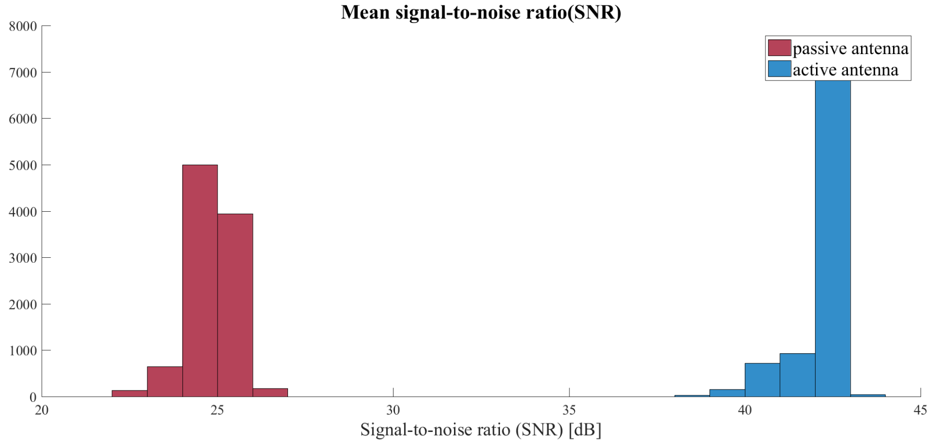

**Figure 6.2:** A histogram comparing the mean GPS SNR observables per epoch seen by an active and a passive antenna.

Figure 6.2 shows the histogram of the mean SNR per epoch seen by the two receivers. A receiver with an active antenna has a far better signal strength through out the data acquisition. The relationship between the noise covariance and SNR observable in [115] infers that an active antenna is less susceptible to noise during data acquisition.

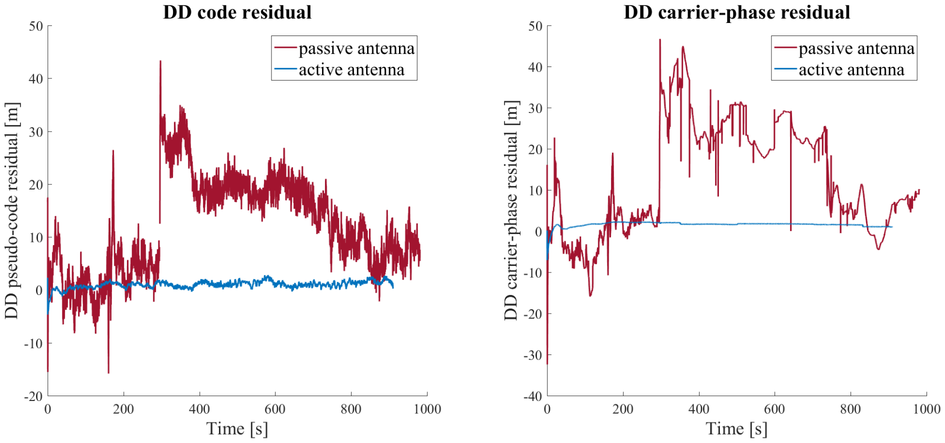

**Figure 6.3:** A plot comparing the DD code (left) carrier-phase (right) residuals from the raw GPS observables collected by an active and a passive antenna.

Finally, in Figure 6.3, the DD code and carrier-phase residuals from two receivers are plotted. A receiver with a passive antenna contains more unstable and greater residuals implying that it is less immune to multipath and unmodelled errors. Therefore, an active antenna was chosen.

In [116], a L1 frequency-band GPS active antenna is recommended to have a low noise figure ($< 1.5dB$), a low level of sensitivity and a high gain ($> 4dBic$) for the optimal performance. However, an active antenna gain is recommended not to exceed $40dB$ but also not lower than $5dB$ since lower overall gain improves the immunity to interference although the higher gain offers better signal strength and sensitivity [117].

### 6.1.3 External Memory

Apart from reading from IMU and GPS, every individual sensors are also responsible for storing the time-synchronised IMU measurements and raw GPS observables onto an external memory for post-processing. Therefore, an individual sensor requires a non-volatile memory that is chosen carefully to avoid data loss.

Table 6.1 summarises the size of a data packet, maximum Output Data Rate (ODR) and corresponding bit rate required to transfer the data acquired at a maximum ODR. According to Table 6.1 and with an additional 50% design margin, a sensor requires a non-volatile memory that has a transfer rate faster than $\sim 67.5kB/s$ and capacity greater than $\sim 1.5GB$ to hold the IMU measurements and raw GPS observables from a 6 hour tracking session.

**Table 6.1:** Summary of the measurement message characteristics of the chosen GPS receiver and MEMS-IMU

| Part number | Message | ODR$_{maximum}$ | Size | Rate |
|---|---|---|---|---|
| NEO-M8T [117] | Observation data | 10 Hz | $\sim 1000B$ | $10.0kB/s$ |
| | Navigation data | 4 Hz | $\sim 1000B$ | $4.0kB/s$ |
| | 1 Hz Time-stamp | 2020 Hz | $32bit$ | $8.08kB/s$ |
| | 10 kHz Time-stamp | 2020 Hz | $32bit$ | $8.08kB/s$ |
| BMX055 [14] | Accelerometer ID | 1000 Hz | $8bit$ | $1.0kB/s$ |
| | Accelerometer x-axis | 1000 Hz | $12bit$ | $1.5kB/s$ |
| | Accelerometer y-axis | 1000 Hz | $12bit$ | $1.5kB/s$ |
| | Accelerometer z-axis | 1000 Hz | $12bit$ | $1.5kB/s$ |
| | Temperature | 1000 Hz | $8bit$ | $1.0kB/s$ |
| | Gyroscope ID | 1000 Hz | $8bit$ | $1.0kB/s$ |
| | Gyroscope x-axis | 1000 Hz | $16bit$ | $2.0kB/s$ |
| | Gyroscope y-axis | 1000 Hz | $16bit$ | $2.0kB/s$ |
| | Gyroscope z-axis | 1000 Hz | $16bit$ | $2.0kB/s$ |
| | Magnetometer ID | 20 Hz | $8bit$ | $1.0kB/s$ |
| | Magnetometer x-axis | 20 Hz | $13bit$ | $32.5B/s$ |
| | Magnetometer y-axis | 20 Hz | $13bit$ | $32.5B/s$ |
| | Magnetometer z-axis | 20 Hz | $15bit$ | $37.5B/s$ |
| | Magnetometer R-hall | 20 Hz | $14bit$ | $35.0B/s$ |
| Total | | | | $\sim 45kB/s$ |

### 6.1.4 Processor

All the components discussed above cannot operate without a processor. A processor is required to supervise and manage the reading of measurements and observables from IMU and GPS respectively and saving them onto a non-volatile memory. Therefore, a processor shall have a clock speed and internal peripherals to communicate with the chosen external peripherals (IMU, GPS receiver and non-volatile memory). Furthermore, it shall contain Read Access Memory (RAM) that is far greater than $135kB$ (see Table 6.1) to enable the sensor to continue to operate even with 3s of backlogged data. $3s$ refers to the time given to the processor to detect the fault and reset the main stream tasks.

### 6.1.5 Power Source

Table 6.2 summarises the electrical ratings of the significant components. For a worst-case scenario where these components are operating at 3.3 V and drawing their maximum current simultaneously, $\sim 1080mW$ is dissipated. Therefore, with an additional $50\%$ design margin and assuming a $85\%$ efficiency and cycle-life factor, a sensor requires a battery with $\sim 2000mAh$ capacity or larger and a discharging rate of $\sim 500mA$ or greater. This will facilitate a minimum operating time of 6 hours.

**Table 6.2:** Summary of the electrical characteristics of the chosen GPS, MEMS-IMU and the processor

| Part number | Parameter | Min | Typ | Max | Unit |
|---|---|---|---|---|---|
| NEO-M8T [117] | Supply voltage | 2.7 | 3.0 | 3.6 | $V$ |
| | Supply voltage (USB) | 3.0 | 3.3 | 3.6 | $V$ |
| | Supply current (GPS only) | - | 25 | 67 | $mA$ |
| | Supply current (multi-constellation) | - | 32 | 67 | $mA$ |
| BMX055 [14] | Supply voltage | 2.4 | 3.0 | 3.6 | $V$ |
| | Supply voltage (I/O) | 1.2 | 2.4 | 3.6 | $V$ |
| | Supply current (accelerometer) | - | - | 130 | $\mu A$ |
| | Supply current (gyroscope) | - | - | 5 | $mA$ |
| | Supply current (magnetometer) | 0.170 | 0.8 | 20 | $mA$ |
| STM32F407 [118] | Supply voltage | 2.4 | - | 3.6 | $V$ |
| | Supply current (source) | - | - | 240 | $mA$ |
| | Supply current (sink) | - | - | 240 | $mA$ |

The characteristics of the four most commonly used rechargeable batteries that meet temperature specifications are outlined in Table 6.3. Based on the comparison, a Li-ion battery was preferred as it does not require regular maintenance; has the highest energy density; the largest number of cycles; low internal resistance and low self-discharge percentage per month. However, the use of lithium batteries places a challenge on the use, storage and handling. This is because lithium-ion batteries are fire-hazards if thermal runaway occurs [20].

**Table 6.3:** Summary of the characteristics of the commonly used rechargeable batteries, namely: NiCd, NiMH, lead acid and Li-ion [20]

| **Description** | **NiCd** | **NiMH** | **lead** | **Li-ion** |
|---|---|---|---|---|
| Energy density ($Wh/kg$) | [45 : 80] | [60 : 120] | [30 : 50] | [110 : 160] |
| Internal resistance ($\Omega$) | [100 : 200] | [200 : 300] | $< 100$ | [150 : 250] |
| Cycle life | 1500 | [300 : 500] | [200 : 300] | [500 : 1000] |
| Overcharge tolerance | moderate | low | high | very low |
| Self-discharge per month | 20% | 30% | 5% | 10% |
| Operating temp. ($^{\circ}C$) | $[-40 : +60]$ | $[-20 : +60]$ | $[-20 : +60]$ | $[-20 : +60]$ |
| Maintenance req. (days) | [30 : 60] | [60 : 90] | [900 : 1800] | not req. |
| Cost per cycle (USD) | 0.04 | 0.12 | 0.10 | 0.14 |

Thermal runaway refers to a rapid self-heating from an internal exothermic chemical reaction caused by internal manufacturing deficiencies, overheating, mechanical abuse (such as puncture) and electrical abuse (such as overcharging and short circuits) [119]. Therefore, an accurate fuel-gauge and shut-down system with low power consumption are necessary to monitor the State-of-Charge (SoC) continuously during operation and shut down the sensor unit if necessary.

Voltage regulation is mandatory in electronics design. The voltage regulator must regulate the input voltage down to 3.3 V and must be capable of sourcing $500mA$ with output noise less than $50mV$ to ensure optimal performance of the *STM32F407* [118]. It shall also have a drop-out voltage less than $0.6V$ at maximum current output to ensure components do not reset due to low power.

Needless to say, the voltage regulator's minimum input voltage must be lower than the battery voltage ($V_{BAT}$) whilst the maximum input voltage shall be greater than the $V_{BAT}$. A voltage regulator with low noise, bias current, voltage variation and quiescent current was preferred. Table D.3 in Appendix D lists the complete hardware specifications for each sensor unit.

## 6.2 Component Procurement

As mentioned previously in Section 1.3, the electronics component distributors were limited to *Digi-key*, *Mouser Electronics*, *RF Design* and *RS Components ZA*. The components must meet the technical specifications (Table D.3 in Appendix D) as well as the following non-functional requirements:

- Status of component;
- Reliable and responsive manufacturer;
- Presence of manufacturer's technical support;
- Presence of developers' community;
- Availability of development or evaluation boards;
- Availability of typical application or reference schematics and layout;
- Availability of tools and accessories required for procurement and usage;
- Availability of required passive components;
- Distributor's minimum order quantity of a unit;
- Tolerable requirement of Custom Clearance Declaration (CCD); and
- Minimal learning required for future developers.

*BMX055* [14], *BMX160* [120], *ICM20948* [9], *LSM9DS1TR* [121] and *MPU9250* [10] are found to satisfy the technical specifications for an IMU as well as the above-mentioned non-functional requirements. Consequently, communication interface, noise spectral density, features and reference schematic were compared (See Table E.2 in Appendix E).

The above-mentioned components provide two types of communication interfaces: Inter Integrated Circuit ($I^2C$) and Serial Peripheral Interface (SPI). $I^2C$ uses a clock frequency ranging between $100kHz$ and $400kHz$ whilst SPI uses a clock frequency ranging between $1MHz$ and $10MHz$. Considering the tasks which a processor must manage (such as reading and storing the IMU measurements acquired at high sampling frequency ($> 600Hz$) and the raw GPS observables of unknown size), the SPI communication interface was preferred over $I^2C$ because of its higher data transfer rate.

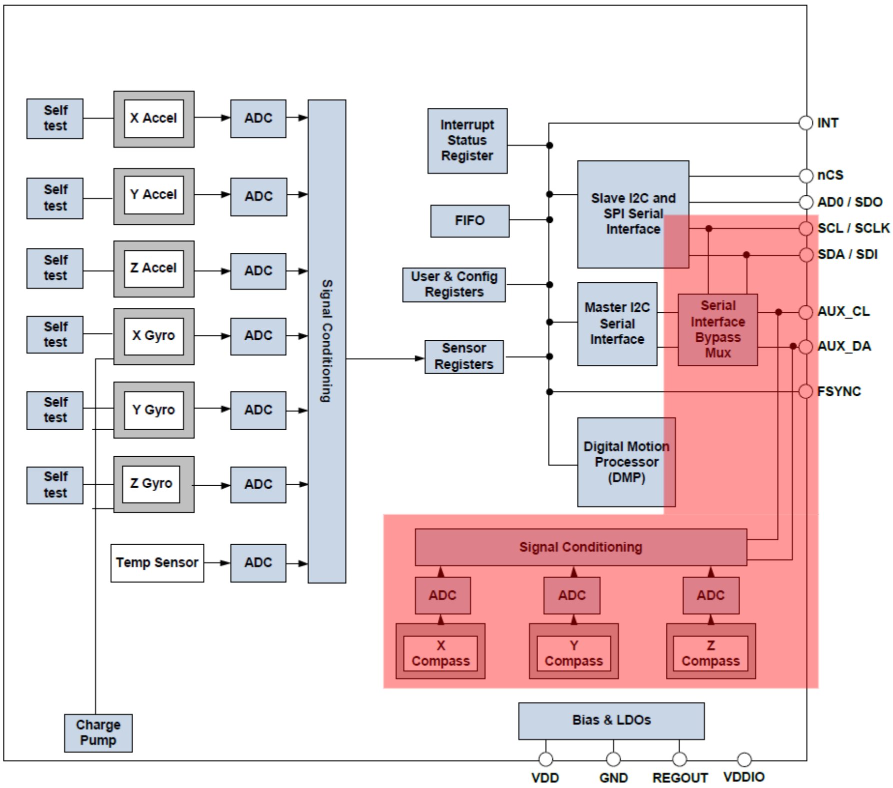

**Figure 6.4:** A block diagram of the internal structure of the ICM20948 [9] and the MPU9250 [10].

Figure 6.4 is the internal block diagram of the *ICM20948* and *MPU9250*. As it is highlighted with red, the magnetometer is designed to communicate on Inter Integrated Circuit ($I^2C$) bus and requires the use of a serial interface bypass multiplexer to communicate via Serial Peripheral Interface (SPI), compromising the advantage of the SPI interface. Consequently, *ICM20948* and *MPU9250* were not selected.

Finally, amongst the *BMX055*, *BMX160* and *LSM9DS1TR*, the *BMX055* was chosen as it is more immune to noise and has external interrupt lines available to indicate the availability of new data, motion detection, low-g, high-g and more. This will provide a platform for future development if motion detection features are to be integrated into the sensor.

Restricted by the *RF Design*[1], the *NEO-M8T* was chosen since it was the only available GPS receiver that met both technical specifications and non-functional requirements at the time of development [117]. In accordance with the antenna technical specifications and recommendations made by *U-blox*, a *Titan AA.105.301111* active antenna was selected [12].

---

[1] RF component distributor

There exists two common types of non-volatile storage for continuous read and write operations at $3.3V$: Electrically Erasable Programmable Read-Only Memory (EEPROM) and flash. EEPROM is intended for storage of less than $4Mb$ that is continuously erased and written. On the other hand, flash is intended for storage up to $256Mb$ and has an inflexible write sequence with a typical minimum sector size of a page ($4096B$). Both EEPROM and flash are not completely feasible owing to their storage size and write sequence respectively.

Consequently, the microSD card was chosen. It is a flash based memory card capable of communicating with a micro-controller via Secure Digital Input Output (SDIO) or SPI and meets security, capacity and performance inherent in audio and video electronic devices. As such, it is a portable non-volatile memory with the capacity varying from $2GB$ up to $128TB$ with a bus speed varying from $2MB/s$ up to $985MB/s$ depending on its type and class with a typical minimum sector size of $512B$.

The *STM32* micro-controller series from *STMicroelectronics* was favoured due to the author's familiarity with the chip. *STMicroelectronics* offers four categories of 32-bit micro-controllers: wireless, ultra-low power, mainstream and high performance. The following micro-controllers are found to meet the technical specifications: *STM32L4*, *STM32F2*, *STM32F4*, *STM32F7* and *STM32H7*.

Table 6.4 compares the processor core type, Central Processing Unit (CPU) clock frequency (FCPU), flash memory and RAM memory size of the *STM32F2*, *STM32F4*, *STM32F7*, *STM32H7* and *STM32L4*. From the comparison, it can be seen that the *STM32F2* series has less than the required $135kB$ RAM whilst the *STM32F4*, *STM32F7*, *STM32H7* and *STM32L4* series have far greater than the required $135kB$ RAM. Therefore, the *STM32F4* series is most optimal in terms of RAM size. Due to the availability of the *STM32F407VGT6* discovery board and vast resources available within the *STMicroelectronics* developers' community, the *STM32F407VGT6* was chosen.

**Table 6.4:** Summary of the high-performance *STM32* series alternatives for a sensor [21]

| **Description** | **STM32F2** | **STM32F4** | **STM32F7** | **STM32H7** | **STM32L4** |
|---|---|---|---|---|---|
| Processor | Cortex-M3 | Cortex-M4 | Cortex-M7 | Cortex-M7 | Cortex-M4 |
| FCPU | $< 120MHz$ | $< 180MHz$ | $< 216MHz$ | $< 480MHz$ | $< 120MHz$ |
| Flash | $< 1Mbyte$ | $< 2Mbyte$ | $< 2Mbyte$ | $< 2Mbyte$ | $< 2Mbyte$ |
| SRAM | $< 128Kbyte$ | $< 384Kbyte$ | $< 512Kbyte$ | $< 1Mbyte$ | $< 640Kbyte$ |

Finally, the 18650 Li-po battery with an external protection circuit attachment was chosen for its availability and advantages whilst preventing over-charge and discharge. The choice of voltage regulator, *TLV2217*, and fuel gauge, *MAX17043* are based on the recommendations given in [122] and [123].

## 6.3 Prototype: Mitigation of Data Loss

A prototype was assembled using the *BMX055* shuttle board [124], *C94-M8P* set [125], *STM32F4* discovery board [126] and microSD card break-out board. The *MAX17043* evaluation board was not included in the prototype because it was unavailable. The purpose of the prototype was to examine the need for modifications to the technical specifications prior to the final schematic capture.

Using the prototype, the *BMX055* new-data interrupt feature was pre-examined. According to [14], an external interrupt line outputs a signal which toggles at a configured sampling frequency when a new-data interrupt is mapped to an external interrupt line. However, this feature was not ideal as shown in Figure 6.5.

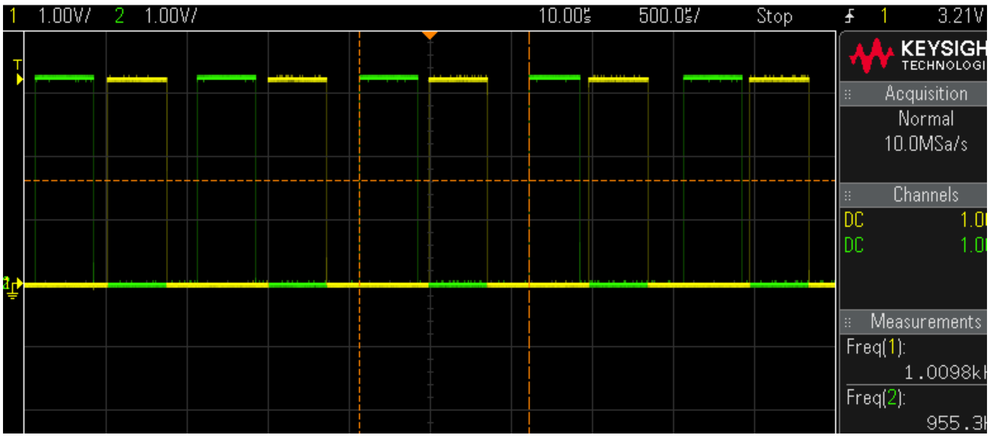

**Figure 6.5:** An oscilloscope screenshot of the new-data interrupt signals from a 3-axis accelerometer (yellow) and 3-axis gyroscope (green) of the *BMX055* while configured to sample at $1kHz$. As it can be seen the frequency of the new-data interrupt signals from a 3-axis accelerometer (yellow) and 3-axis gyroscope (green) of the *BMX055* are not exactly $1kHz$ but instead $1009.8Hz$ and $955.3Hz$ respectively.

In Figure 6.5, channel one (yellow) and two (green) were the new-data interrupt outputs from the accelerometer and gyroscope of the *BMX055* whose sampling frequency was configured to be $1kHz$ respectively. However, the new-data interrupt outputs from both the accelerometer and gyroscope of the *BMX055* did not toggle at $1kHz$ exactly despite the configuration. Instead, the new-data interrupt signals were observed to have $\pm 0.6\%$ tolerance.

The $\pm 0.6\%$ tolerance translates to a total loss of 129600 IMU measurements during 6 hours of motion tracking when the *BMX055* was configured to $1kHz$ sampling frequency. This, in turn, resulted in $129.6s$ of misalignment between IMU measurements and raw GPS observables. This was unacceptable to achieve the accuracy of the commercial MOCAP systems.

Consequently, a timer set to $10kHz$ was used to count the number of clock cycles between each measurement to remove the assumption that the new-data interrupt line toggles exactly at the configured sampling frequency. Furthermore, a High Speed External (HSE) clock with $\pm 0.01\%$ tolerance is used as the processor clock source because the *STM32F407VGT* internal High Speed Internal (HSI) $16MHz$ RC oscillator has $[-8 : 4.5]\%$ tolerance which translates to $\pm[-5 : 2.8]ns$ error per cycle, that is $\pm 28s$ cumulative error every hour.

Data corruption occurred while a buffer with known values was continuously saved onto a microSD card using the SDIO interface. The SDIO lines were probed under both 1-bit and 4-bit mode but no bug was found. Then, several microSD cards with different speed ratings were used in the attempt to rectify the problem, such as the speed class of 2, 4, 6 and 10 as well as the UHS speed class of 1 and 3. However, the data corruption was observed across all. Furthermore, the data corruption only occurred on the SDIO interface but not on the SPI interface. Due to limited time, the microSD card was interfaced with the processor via SPI.

Data loss was observed after data corruption was mitigated. The data loss was found to be caused by an unexpected delay during a write sequence to the microSD card. This delay in turn caused the shortage of the memory buffer that was used to store the acquired measurements temporarily before logging. Due to the shortage of the memory buffer, overflow occurred and new data was written over the old data which was not logged onto the microSD card. To find the appropriate size of the memory buffer, several processing and response times were measured as shown in Table 6.5.

**Table 6.5:** Summary of the processing and response time measured from the built prototype

| Description | Time | Processor | Sample size |
|---|---|---|---|
| **Average time taken to:** | | | |
| read a packet of GPS raw observables | $8.5ms$ | DMA | 30000 |
| initialise and configure *BMX055* | $259.9ms$ | CPU | 15 |
| read a packet of 3-axis accelerometer data | $24.4\mu s$ | CPU | 55534 |
| read a packet of 3-axis gyroscope data | $23.8\mu s$ | CPU | 55039 |
| read a packet of 3-axis magnetometer data | $28.8\mu s$ | CPU | 1110 |
| fill a 512B buffer | $14.3ms$ | CPU | 111683 |
| fill a 1024B buffer | $28.6ms$ | CPU | 111683 |
| fill a 2048B buffer | $57.2ms$ | CPU | 111683 |
| log 512B onto microSD card | $3.7ms$ | DMA | 4863 |
| log 1024B onto microSD card | $4.7ms$ | DMA | 2430 |
| log 2048B onto microSD card | $6.4ms$ | DMA | 1210 |
| **Maximum time taken to:** | | | |
| log 512B onto microSD card | $81.7ms$ | DMA | 4863 |
| log 1024B onto microSD card | $221.6ms$ | DMA | 2430 |
| log 2048B onto microSD card | $322.1ms$ | DMA | 1210 |

As can be observed from the difference in the average and maximum time taken to log 512*B*, 1024*B* and 2048*B* from Table 6.5, a write sequence to the microSD card suffers from an unexpected delay whose duration is proportional to the size of the bytes being logged. This implied that a buffer, capable of holding measurements, read for longer than the observed maximum delay is necessary to avoid data loss.

Based on the observed average time taken to read each measurement and the average time taken for those measurements to fill a buffer of size 512*B*, 1024*B* and 2048*B*, a circular buffer composed of seven 2048*B* sectors was implemented for the IMU measurements. Additionally, a circular buffer composed of three 1024*B* sectors was implemented for the raw GPS observables. Figure 6.6 shows the complete circular buffer scheme that was employed.

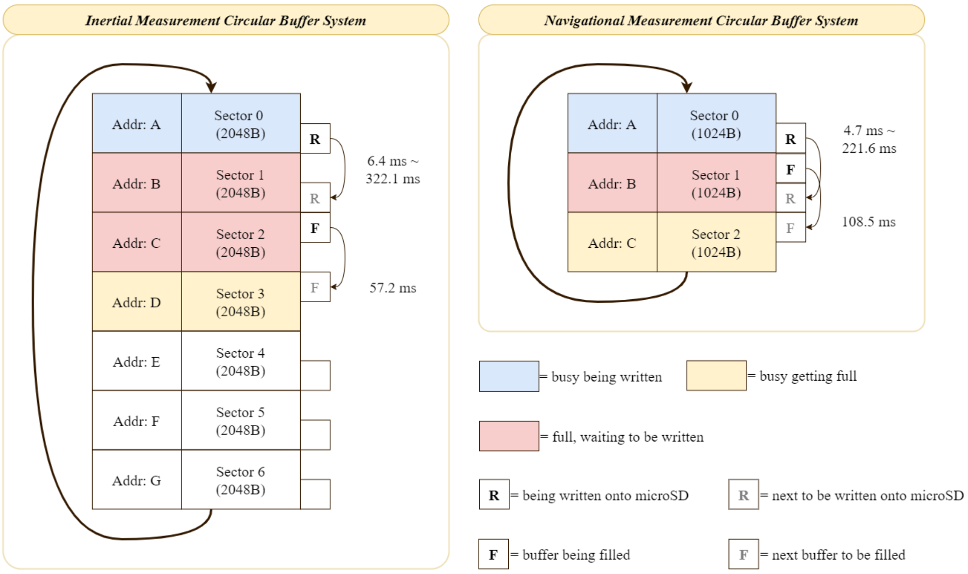

**Figure 6.6:** A diagram depicting the circular buffer scheme to store backlogged MEMS-IMU measurements and raw GPS observables temporarily. Each block represents a sector of a buffer. A sector shaded blue represents a sector being written onto the microSD card; the red represents a backlogged sector that needs to be written onto the microSD card; and yellow represents a sector that is being written with new incoming measurements.

The IMU measurement circular buffer system in Figure 6.6 depicts the situation where sector 0 is being written onto microSD card whilst sector 3 is being filled. This indicates that the delay has occurred while writing sector 0 onto the microSD card since sector 1 and sector 2 are backlogged and waiting to be written onto the microSD card. Since the average time to fill 2048*B* buffer by *BMX055* is 7 times faster than the average time to save 2048*B* buffer onto microSD card (See Table 6.5), a minimum of 7 sectors are required.

The raw GPS observable circular buffer system in Figure 6.6 depicts the situation where sector 0 is being written onto microSD card whilst sector 2 is being filled. This too indicates that the delay has occurred similar to the above IMU measurement scenario depicted in Figure 6.6. Since the average Universal Asynchronous Receiver/Transmitter (UART) active time due to *NEO-M8T* is 2 times faster than the average time to save $1024B$ buffer onto microSD card (See Table 6.5), a minimum of 3 sectors are required.

## 6.4 Firmware Specifications

Firmware is aimed at providing the low-level control for the specific hardware components on a sensor unit. This low-level control involves the following tasks:

- Establishment of communication between the processor and sensing components;
- Configuration of the sensing components to meet the minimum specifications described in Table D.3 in Appendix D;
- Management of the user-system interaction as described in Section 5.4;
- Data transfer from sensing components to processor;
- Storage of inertial and navigational information in a chosen non-volatile memory;
- Realisation of the system attributes.

Summary of the firmware specifications is given in Table D.4 in Appendix D.

## 6.5 Firmware Development

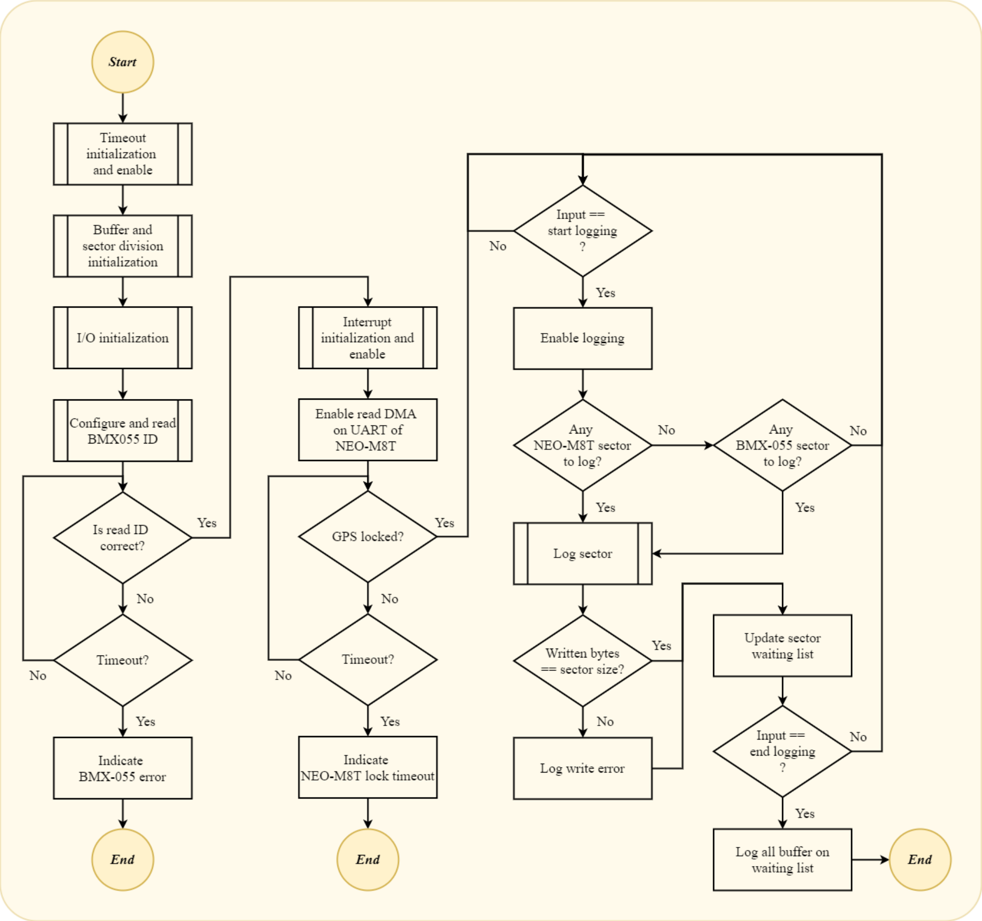

**Figure 6.7:** A flowchart depicting the operation of the *main* thread of the firmware.

Figure 6.7 depicts the flow of the main thread which is the designated entry point of the program. As depicted in Figure 6.7, the main thread is responsible for the initialisation and management of tasks based on the user input and output as well as handling errors.

### 6.5.1 Navigational Information

The challenge in reading the raw GPS observables from the UART-TX line of the *NEO-M8T* exists because the number of bytes to be received is unknown. This is because the message size expands/shortens with an increase/decrease in the number of satellites seen by the GPS receiver. The *STM32* series provides different modes of UART reception, namely: polling, interrupt, Direct Memory Access (DMA) and interrupt with DMA modes [127].

Polling mode is easy to implement but it is not feasible for embedded systems with multiple tasks to handle because the CPU is dedicated for the UART reception task to ensure no data is loss. Polling mode can be improved by employing a Real-Time Operating System (RTOS) but due to the high demand for the buffer, and hence memory resources, it is not suitable for this project.

The interrupt mode allows the CPU to switch between the main stream task(s) and the UART reception task(s) (Interrupt Service Routine (ISR)) based on the status of the UART bus. This mode is not feasible for receiving bursts of data because the ISR is executed for every received byte, stalling the CPU.

The DMA mode transfers data from the UART RX data register to the dedicated memory on the hardware level without CPU interaction. The drawbacks of DMA mode is that the number of bytes to be received must be known in advance. Therefore, the UART reception that receives bursts of data of unknown size requires the integration of the interrupt and DMA mode.

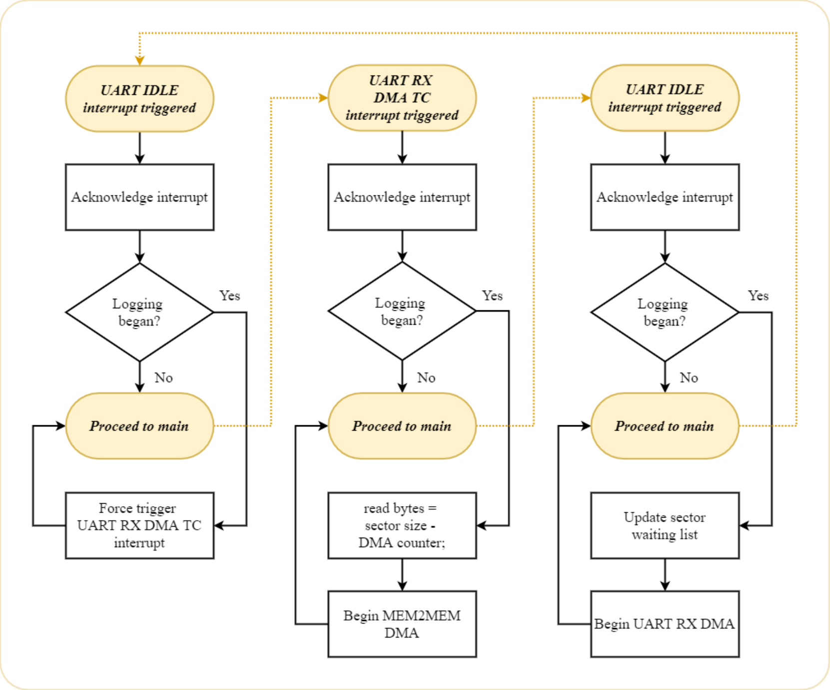

**Figure 6.8:** A flowchart depicting the operation of the ISR threads to implement efficient UART reception. The yellow arrows represent the direction of the consequential ISR triggered due to an acknowledgement of a specific ISR or a clearance of a specific flag.

To implement efficient UART reception of bursts of data of unknown size, the following is required: UART idle interrupt, peripheral-to-memory DMA, memory-to-memory DMA and DMA transfer complete interrupt as shown in Figure 6.8.

The peripheral-to-memory UART-RX DMA is responsible for transmitting data from the UART data register to the dedicated memory space. The UART idle interrupt is triggered when the end of incoming transmission is detected. When the UART idle interrupt is triggered, it forces the completion of the UART-RX DMA by clearing all the status flags. As a result, the DMA transfer complete interrupt is triggered and the memory-to-memory DMA is initiated to back-up and ensure no data loss. Once the back-up is completed, the UART-RX DMA is once again initiated for the next navigational data packet.

### 6.5.2 Inertial Measurements

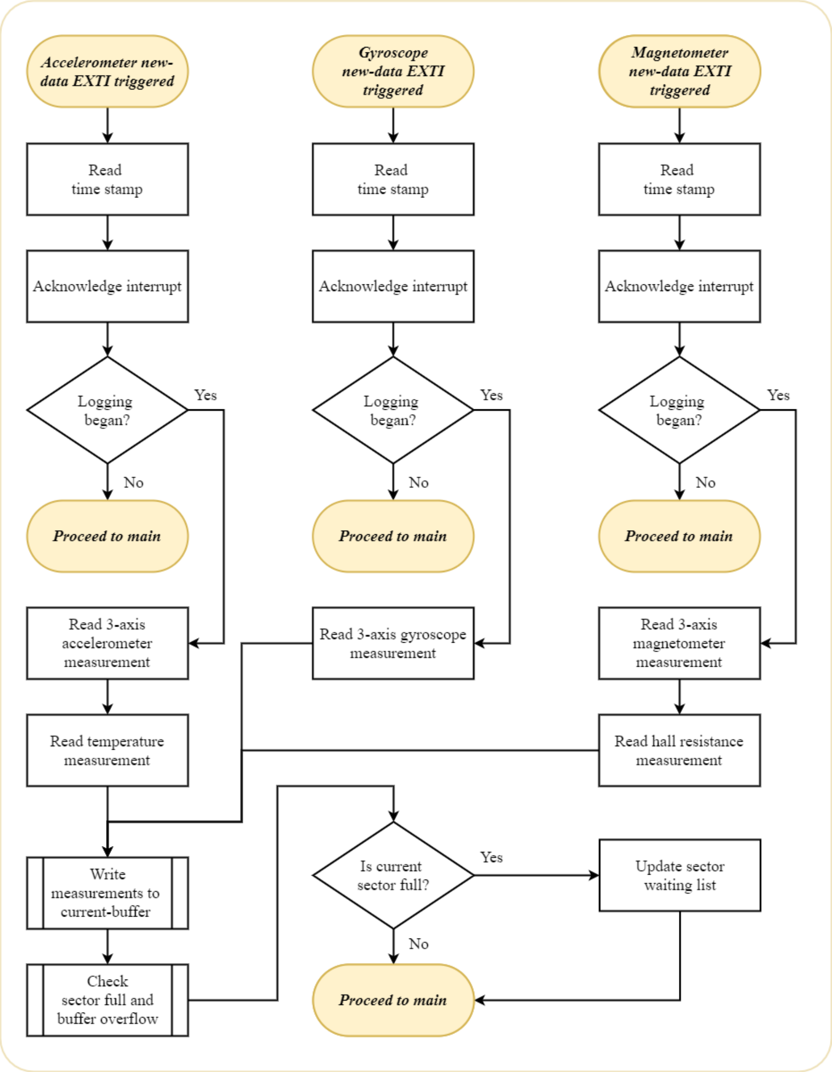

**Figure 6.9:** A flowchart depicting the operation of the ISR triggered by the new-data interrupt signals from the *BMX055*.

As mentioned in Section 6.2 and Section 6.3, the *BMX055* offers external interrupt lines which toggle as a new measurement becomes available for acquisition. The use of new-data interrupt lines on the accelerometer, gyroscope and magnetometer will ensure minimal latency in acquisition time between internal Analogue to Digital Converter (ADC) and data acquisition via SPI. Figure 6.9 is the flowchart of ISR threads implemented for efficient *BMX055* data acquisition.

### 6.5.3 Storage

An open-source generic FAT/exFAT File System (FATFS) middle-ware developed by ChaN [128] is employed. It is designed for small embedded systems and completely separate from the disk I/O layer for compatibility [128]. FATFS is responsible for data management on the storage device such as Multi Media Card (MMC), SD Small Capacity (SDSC) and SD High Capacity (SDHC) as well as maintenance of Basic Input/Output System (BIOS) and Basic Parameter Block (BPB) in the boot sector.

## 6.6 Schematic Capture

Schematics are captured based on the data-sheets ( [117] [14] [118] [129] [12] [130]), hardware integration manuals ( [116] [122]), a software integration manual ( [127]) and evaluation board support-archives ( [125] [131]). Universal Serial Bus (USB) interface is added to configure the *NEO-M8T* using the *U-blox u-center* software package as it was found to be the most convenient method during prototyping.

To aid the debugging and validation process, nodes that are entry points for supply voltage and communication interface lines are designed to be modular using a Surface Mount Device (SMD) jumper and 0Ω resistor. The detailed pin assignments between the micro-controller and external peripherals are listed in Table F.1 in Appendix F. Full schematic is also available in Appendix F.

## 6.7 Printed Circuit Board (PCB) Design

Electronic components are sensitive to Electrostatic Discharge (ESD) and Electromagnetic Interference (EMI). As a result, the random device resets and burn-outs may occur without successfully implementing the protection of the system against ESD and EMI. This is always the case for a PCB with high-frequency and high-speed signal traces and any electronics based on Metal Oxide Semiconductor (MOS) technology.

ESD refers to the momentary and sudden electric current that flows between two objects of different electrical potential due to direct contact or electrostatic field induction. EMI refers to the disturbance caused by the electrostatic coupling or conduction due to the presence of an external source. High frequency refers to a RF signal with a carrier frequency that is higher than 1 MHz. High speed refers to a signal whose path delay is far greater than the signal rise and fall time, where path delay can be evaluated by the signal trace length and its characteristic voltage propagation speed.

The performance of the system protection against an ESD and EMI is influenced by the PCB design, requiring great care during the design process. The following aspects of the PCB design are regarded as significant and are discussed hereafter:

- PCB shape and size
- PCB material and stack
- PCB zoning (floor planning)
- The grounding schemes optimisation
- The style of the corners and vias
- The signal traces
- The design rule

### 6.7.1 PCB Shape and Weight

The weight of the fusion MOCAP system is limited to a maximum of 5% of the body weight of the host in accordance with the weight guideline in [132]. In other words, a sensor unit is designed to weigh less than $100g$ to be able to mount a maximum of 20 sensor units on the lightest *megafauna* animal. Consequently, the PCB board made out of the FR4 substrate is limited to a volume of $\pm 10cm^3$.

The shape of the PCB depends on the maximum weight allowance as well as the circumference of the smallest limb segment of a smallest *megafauna* animal, *genus Pan*. This places very tight shape and size restrictions on the PCB design. Because only one PCB design was allowed to be fabricated and the fusion MOCAP system was intended to be validated on a mechanical rig only, strict restrictions on the shape and weight were reduced. Finally, it was designed to resemble the shape of the *STM32F4* discovery board for familiarity during testing and the debugging process.

### 6.7.2 PCB Material and Stack

As briefly discussed in Section 6.1, the FR4 substrate was chosen. FR4 is more easily available than the other substrate materials because it is commonly used in industrial-quality devices. A ceramic substrate was considered because of its higher thermal conductivity and low frequency loss [133], but was not available at the time of fabrication. As the development and testing were limited to dry-conditions, the moisture absorption of the board material was not considered.

In accordance with the recommendations in [134], a four-layer stack was chosen. Multi-layer boards have several advantages over single- and double-layer boards. It allows better grounding, easy routing and distributed capacitance thus achieving high frequency noise reduction and better EMI rejection.

To maximise the advantages of a multi-layer board, the order of the layers was critical. Shielding on the bottom and top planes is compromised since the signals are exposed [133]. Therefore, a 4-layer board with two external signal layers and two internal power and ground planes was laid out. By placing the ground planes internally, the signal traces can be probed and modified easily during the debugging process.

### 6.7.3 PCB Board Zoning (Floor Planning)

The definition of the location of components based on the component priority and signal property is known as board zoning. To prevent pollution of signal traces from ESD and EMI, high-frequency and high-speed signals were placed in the vicinity of the power management circuitry for shortest current return path and strong grounds [135].

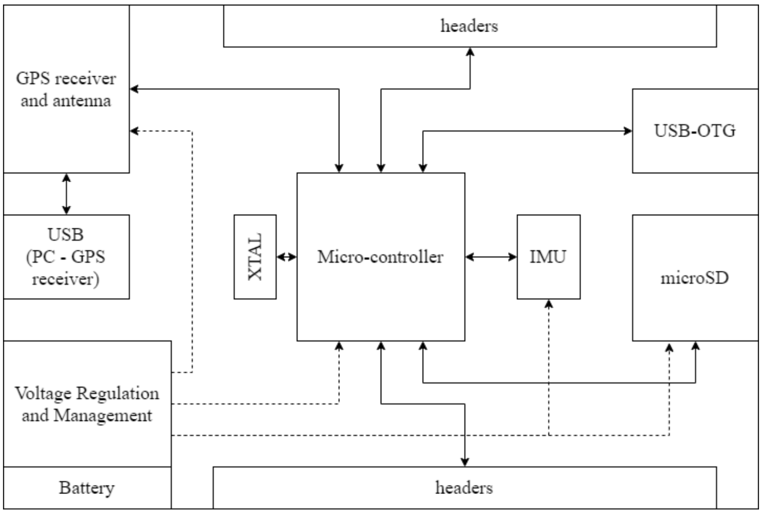

Figure 6.10: A simple diagram depicting the proposed board zoning of a sensor unit.

Consequently, as shown in Figure 6.10, the GPS receiver and the micro-controller were placed in close vicinity to the voltage regulator. The voltage regulator was placed near the entry point of the power source [135]. As advised in [135], an HSE oscillator and an IMU were placed away from the analogue components, low-speed signal sources and connectors. All connectors and external wires were placed on the edge of the PCB as recommended in [134] to keep ESD susceptible circuitry away from them.

### 6.7.4 Grounding Scheme

A ground plane is the return path for the current that flows out from the source to a point, completing a current loop. The density of the return current is the highest directly over or under the signal trace it is sourced from because it has the lowest impedance. If the density of the return current is high near the reference point (the ground), it induces noise that propagates throughout the signal that flows in the circuit with the same reference point [136].

The use of a four-layer board with a stitched ground between the top and bottom planes (as shown inside a blue box in Figure 6.11) allows routing of an optimal ground return path underneath the signal traces [135] and minimises the parasitic inductance as well as the difference in EMI radiation between the signal traces. Therefore, a controlled impedance ground or power trace is not placed to reduce the impedance of the ground plane of the PCB [134].

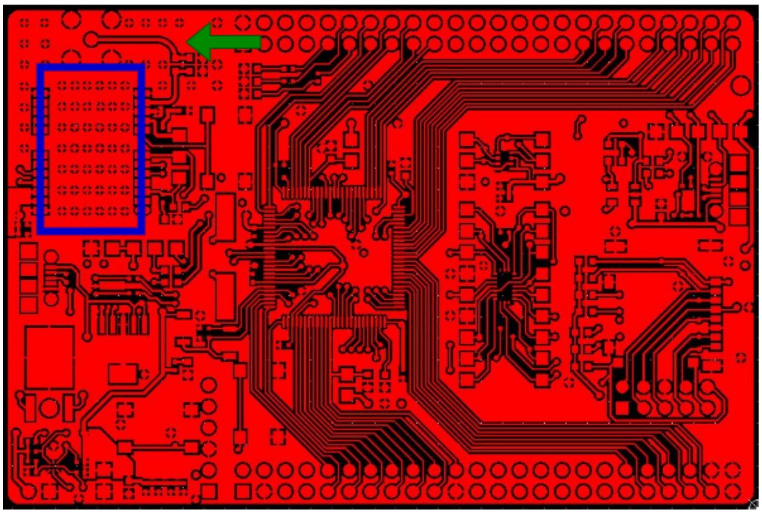

**Figure 6.11:** A picture of a top layer of the PCB. The region outlined by blue line contains a stitched ground and the signal trace pointed by an green arrow has a rounded corner.

Noise is induced when a current spike is generated with a change in the signal state. For this reason, an analogue ground is known to be less noisy than a digital ground because the magnitude of the spike is proportional to the magnitude of the signal change [135]. Consequently, analogue and digital grounds are separated and connected at a single point.

### 6.7.5 Corners and Vias

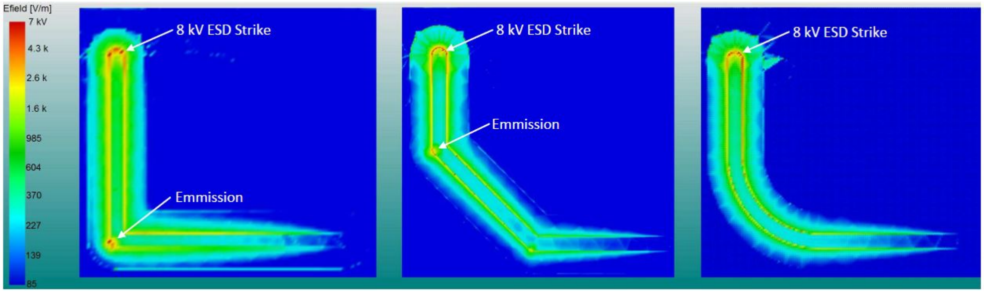

**Figure 6.12:** An image from [11] showing the difference in emission during an 8kV ESD striking event for a 90°, 45° and rounded corner types. The 90° corner has a significant emission in comparison to the rounded corner.

It is best to ahve a straight-line shortest-path traces. If corners are inevitable, 45° corners are acceptable. Rounded corners must be applied when corners are necessary on high-frequency signal traces (as pointed out by a green arrow in Figure 6.11). Right-angled corners must be avoided because the are known to be a strong source of EMI and right-angle routing to component pins are found to cause permanent damage [11] as it can be seen from Figure 6.12.

### 6.7.6 Signal Traces

Noise is induced between parallel traces when capacitive and inductive cross-talk occur [135]. A rising edge on the source causes a rising edge on the casualty in capacitive coupling whereas the change in electrical potential on the source causes an opposite change on the casualty in inductive coupling.

The amount of noise induced on the casualty is proportional to the parallel distance as well as the frequency and amplitude of the electrical potential change on the source, but inversely proportional to the separation distance. Therefore, ground planes are placed underneath the high-frequency and high-speed signal traces. Moreover, any noise-carrying traces are kept away from non-noisy signal traces.

The length of the RF signal traces are recommended to be shorter than $1/10$ of the wavelength of the carrier signal to ensure optimal performance by the *RF Design*. Consequently, the GPS signal trace is kept shorter than $3.81cm$ and its impedance is matched to $50\Omega$.

The length of the signal traces of a communication interface bus was kept approximately constant to each other to ensure the arrival of the signal at the same time. The length was also kept shorter than the distance travelled during one rise/fall time of the clock signal at its characteristic voltage propagation rate to prevent confusion by signal reflection.

### 6.7.7 Design Rule

A design rule in electronics engineering refers to the geometric constraints imposed on electronic components and the PCB. This ensures the design functions reliably and produces an acceptable yield. The design rules with regard to clearance, short-circuit, un-routed net, width, priority, via styles and more were placed due to the nature of a signal through each track, the capabilities of *Trax Interconnect (PTY) LTD* and *Barracuda Holdings (PTY) LTD*. Table 6.6 is the summary of *Trax Interconnect (PTY) LTD* capabilities.

**Table 6.6:** *Trax Interconnect (PTY) LTD* capability summary [22]

| Capabilities | Standard | Experimental |
|---|---|---|
| Maximum number of layers | 16 | 24 |
| Minimum track | 100µm (4mil) | 75µm (3mil) |
| Minimum gap | 100µm (4mil) | 75µm (3mil) |
| Smallest mechanically drilled holes | 250µm (10mil) | 200µm (8mil) |
| Smallest mechanically drilled blind holes | 150µm (6mil) | 150µm (6mil) |
| Smallest buried holes | 250µm (10mil) | 200µm (8mil) |
| Aspect ratio max - through holes | 10:1 | 16:1 |
| Aspect ratio max - blind holes | 0.8:1 | 1:1 |
| Drilled hole edge to copper (M/L rigids) | 250µm (10mil) | 175µm (7mil) |
| Controlled Impedance | +/- 10% | +/- 5% |

## 6.8 Acceptance Testing Procedure and Results

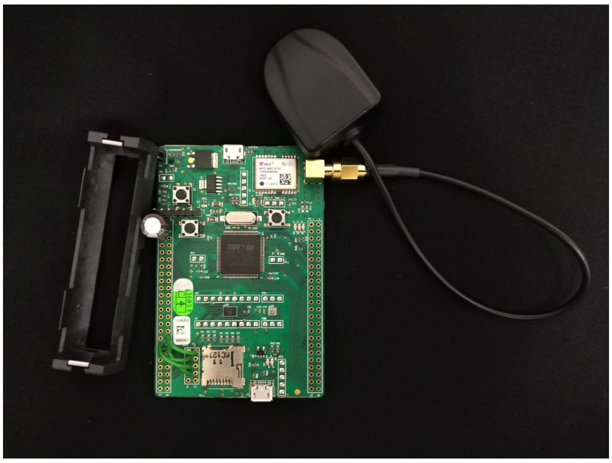

**Figure 6.13:** A photo of the fully assembled sensor unit.

In total eight sensors were assembled as shown in Figure 6.13 and tested progressing from fundamental to advanced features as briefly mentioned in Chapter 4.

### 6.8.1 Voltage Regulation

A stable supply voltage that does not stress above the absolute maximum ratings of the components is essential to avoid permanent damage to the components; ensure good functionality and maintain component reliability. Therefore, the output from the voltage regulator was examined on an oscilloscope with its output voltage disconnected from the rest of the circuits. The following tests were conducted sequentially:

1. Examination of the output voltage with input voltage varying from $3.8V$ to $4.2V$;
2. Examination of the drop-out voltage with a dummy load varying from $50mA$ to $250mA$;
3. Examination of the AC components on the output voltage.

The regulated voltage was measured at $3.27 \pm 0.00645V$ with drop-out voltage of $0.315 \pm 0.00105V$ and agreed with its electrical characteristics as defined in the data-sheet. However, the output noise voltage was measured at $0.120 \pm 0.0408V$ which does not agree with the typical output noise voltage (500 $\mu V$) given in the data-sheet.

The high output noise voltage was understood to be caused by placing the decoupling capacitor on a different layer to the voltage regulator. In other words it was not placed as close as possible to the voltage regulator. Therefore, an additional $100\mu F$ capacitor was soldered directly on the voltage regulator output pin to reduce the noise to $0.040 \pm 0.00408V$ .

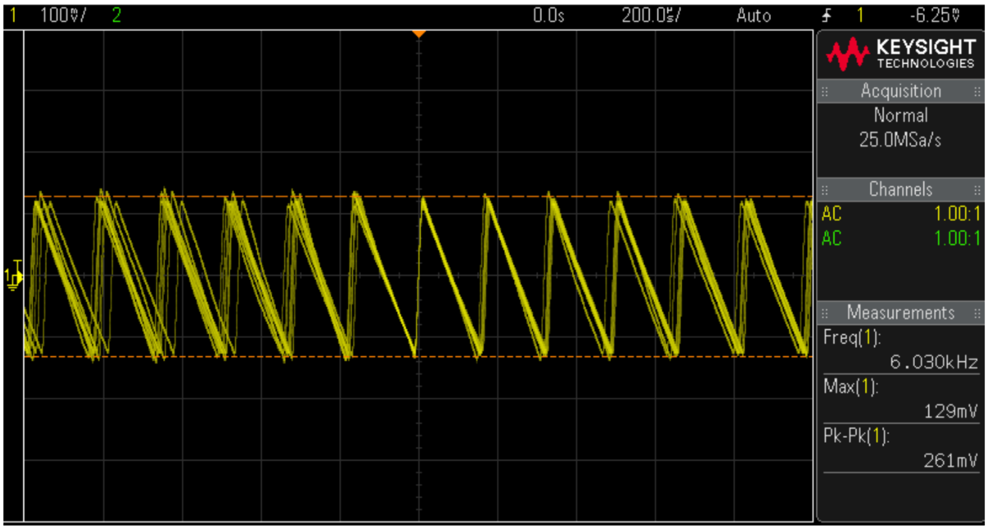

Freq(1): 6.030kHz
Max(1): 129mV
Pk-Pk(1): 261mV

**Figure 6.14:** An oscilloscope screenshot during the observation of the AC component in the regulated output voltage. During the observation, the output pin of the voltage regulator was connected to the rest of the circuit and was sourcing the *STM32F407VGT*, *BMX055*, *NEO-M8T* and microSD card.

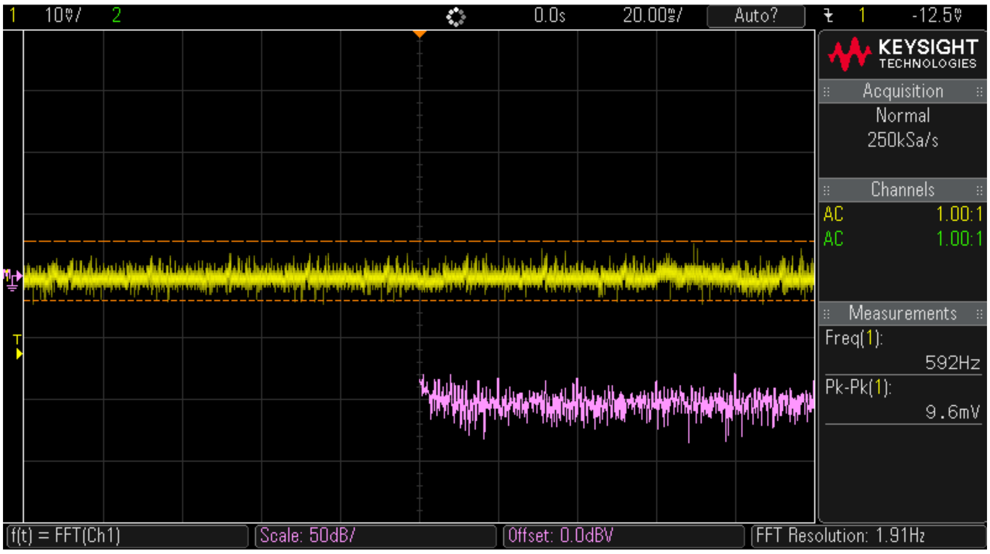

Normal
250kSa/s

AC 1.00:1
AC 1.00:1

Freq(1): 592Hz
Pk-Pk(1): 9.6mV

f(t) = FFT(Ch1)
Scale: 50dB/
Offset: 0.0dBV
FFT Resolution: 1.91Hz

**Figure 6.15:** An oscilloscope screenshot during the observation of the AC component in the regulated output voltage with an additional $220\mu F$ connected to the output pin of the voltage regulator. The yellow signal is the regulated output voltage signal and the pink signal is the fast Fourier transformation of the yellow signal. During the observation, the output pin of the voltage regulator was connected to the rest of the circuit and was sourcing the *STM32F407VGT*, *BMX055*, *NEO-M8T* and microSD card.

Unfortunately, with the rest of the circuits connected and supplied with the regulated output voltage from the voltage regulator, the output noise resembled a saw-tooth waveform with increased peak-to-peak AC voltage of $0.261 \pm 0.00410V$ as shown in Figure 6.14. Consequently, the value of the additional decoupling capacitor was increased to $220\mu F$ to reduce the noise to $0.0096 \pm 0.00041V$ with white noise characteristics as shown in Figure 6.15.

### 6.8.2 Processor Debugger, Boot, Reset and Clock Frequency

The sensor cannot function without a programmable micro-controller. It was confirmed that the presence of the micro-controller is recognised by the *ST-Link* debugger and utility. It was then confirmed that the main flash memory was selected as the boot space and the micro-controller resets under manual reset. The stability of the micro-controller clock frequency and the communication with the external peripherals such as the *BMX055*, *NEO-M8T* and microSD card were examined.

The stability of the clock frequency is critical to predict the behaviour of the micro-controller and to ensure reliable and robust communication between the micro-controller (the *STM32F407VGT*) and the other components (the *BMX055*, *NEO-M8T* and microSD card). Most importantly, without a stable clock, the quality of time and data synchronisation cannot be guaranteed. Therefore, using a Micro-controller Clock Output (MCO) pin, HSI, HSE, Phase Locked Loop (PLL) and timer clocks were examined.

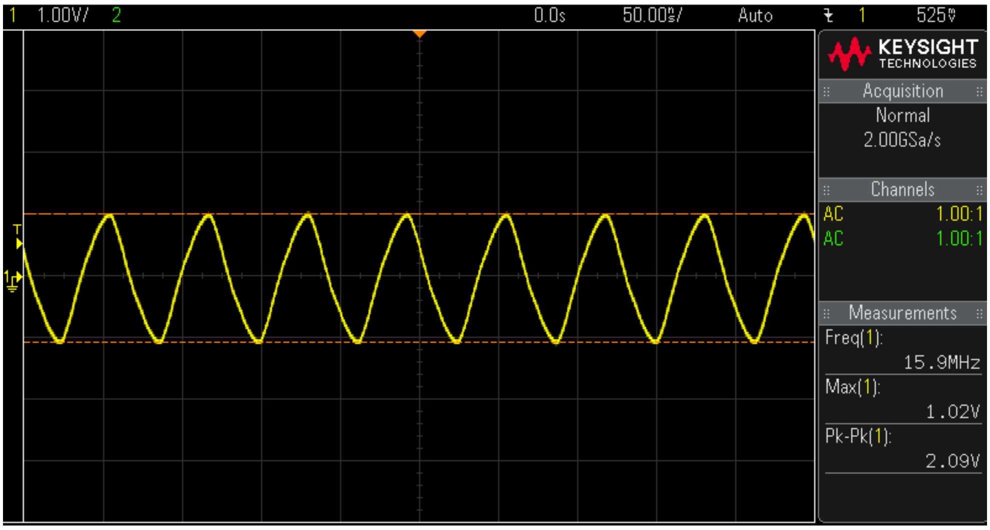

**Figure 6.16:** An oscilloscope screenshot during the observation of the AC component in HSI signal from the Micro-controller Clock Output (MCO) pin of the *STM32F407VGT*.

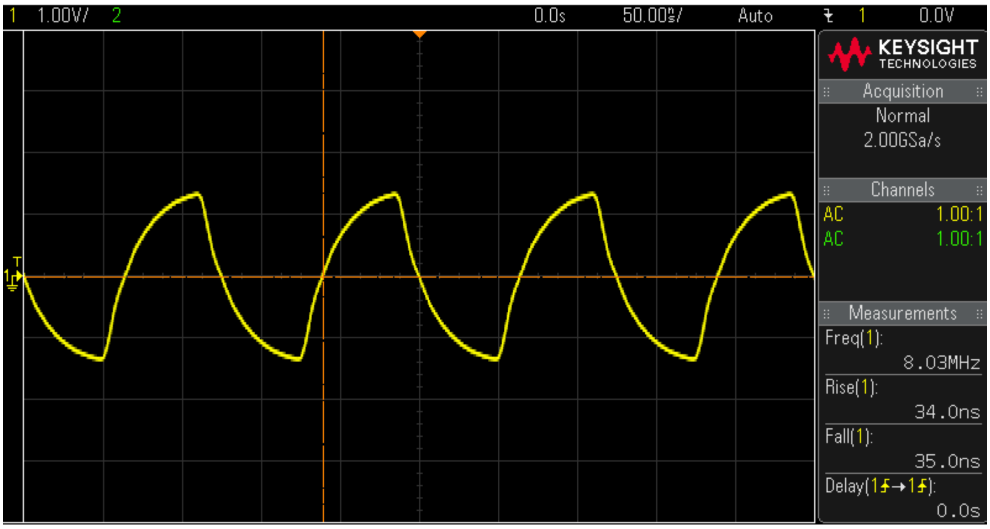

**Figure 6.17:** An oscilloscope screenshot during the observation of the AC component in HSE signal from the Micro-controller Clock Output (MCO) pin of the *STM32F407VGT*.

The frequency of the HSI clock was measured at $15.9 \pm 0.516 MHz$ whilst the frequency of the HSE clock was measured at $8.03 \pm 0.131 MHz$ as shown in Figures 6.16 and 6.17 respectively. The frequency of the PLL clock with HSE clock source for the *STM32F407VGT* is defined by (6.2) and was configured to be $84 MHz$ by setting the $M$, $N$ and $P$ factors to 4, 84 and 2 respectively.

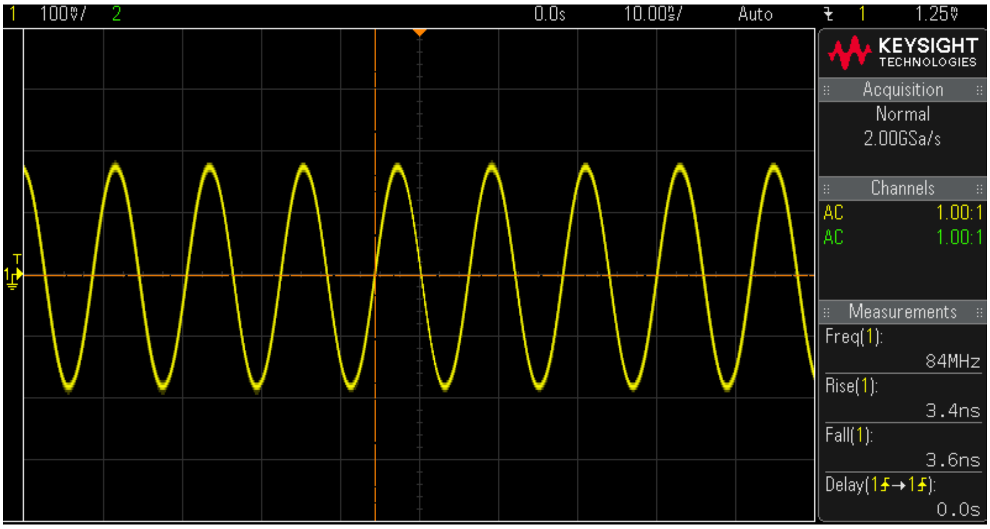

Normal
2.00GSa/s

AC 1.00:1
AC 1.00:1

Freq(1): 84MHz
Rise(1): 3.4ns
Fall(1): 3.6ns
Delay(1→1): 0.0s

**Figure 6.18:** An oscilloscope screenshot during the observation of the AC component in PLL signal from the Micro-controller Clock Output (MCO) pin of the *STM32F407VGT*.

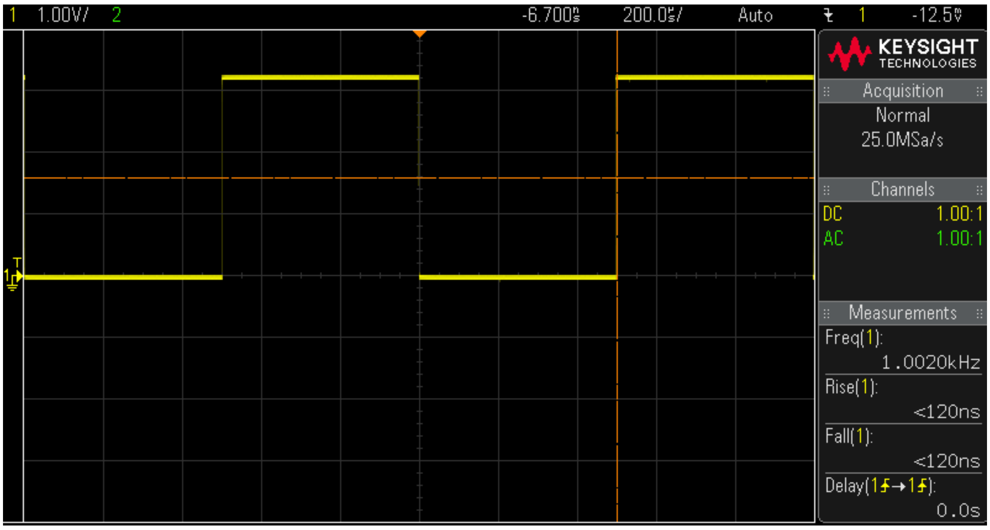

Normal
25.0MSa/s

DC 1.00:1
AC 1.00:1

Freq(1): 1.0020kHz
Rise(1): <120ns
Fall(1): <120ns
Delay(1→1): 0.0s

**Figure 6.19:** An oscilloscope screenshot during the observation of the digital I/O pin of the *STM32F407VGT* that was programmed to toggle at $10kHz$ using the internal generic timer peripheral of the *STM32F407VGT*.

The frequency of the PLL clock was measured at $84.0 \pm 2.88MHz$ as shown in Figure 6.18. Finally, the timer configured to overflow at $10kHz$ was measured at a frequency of $1002.0 \pm 8.198Hz$ as shown in Figure 6.19.

$$f_{PLL} = \frac{f_{SOURCE} \cdot N}{M \cdot P}. \tag{6.2}$$

### 6.8.3 Digital I/O Lines and the Communication Interface

The micro-controller digital I/O pins were initialised to binary input, binary output and then analogue input modes to conduct a binary test (pass or fail). A binary test was then conducted on the USB interface to confirm reliable communication between the *NEO-M8T* and *U-blox u-center* software. Each *NEO-M8T* receiver was configured to output raw GPS observables on the UART port at $115200 bits/s$ with a sampling frequency of $10Hz$. Finally, the communication interfaces were initialized and the reliability of the communication between the micro-controller and the external peripherals were tested by:

- Reading the *WHO AM I* register of the IMU (that contains the pre-defined constant value given in the data-sheet) 100 times consecutively without a single failure;
- Saving memory buffers of size $1024B$ and $2048B$ (that contain pre-defined characters) onto the microSD card 100 times consecutively without data loss or data corruption; and
- Reading raw GPS observables from the GPS receiver for an hour with less than $5\%$ conversion error to *RINEX* format.

Every digital I/O pin was successfully initialised and functioned under binary input, binary output and analogue input modes. All *NEO-M8T* receivers were able to be configured using *u-center* software. Every sensor was observed to have reliable communication between the micro-controller and the external peripherals.

Finally, the IMU measurements and raw GPS observables were acquired and recorded for $600 \pm 48s$ and its output binary file size was examined. According to Table 6.1, approximately $45kB$ of data was logged every second. The size of the binary file that falls within $27.0 \pm 4.32MB$ was deemed not to have a data loss problem. No sensor with a data loss problem was found.

### 6.8.4 External Peripheral

**Inertial sensor: *BMX055***

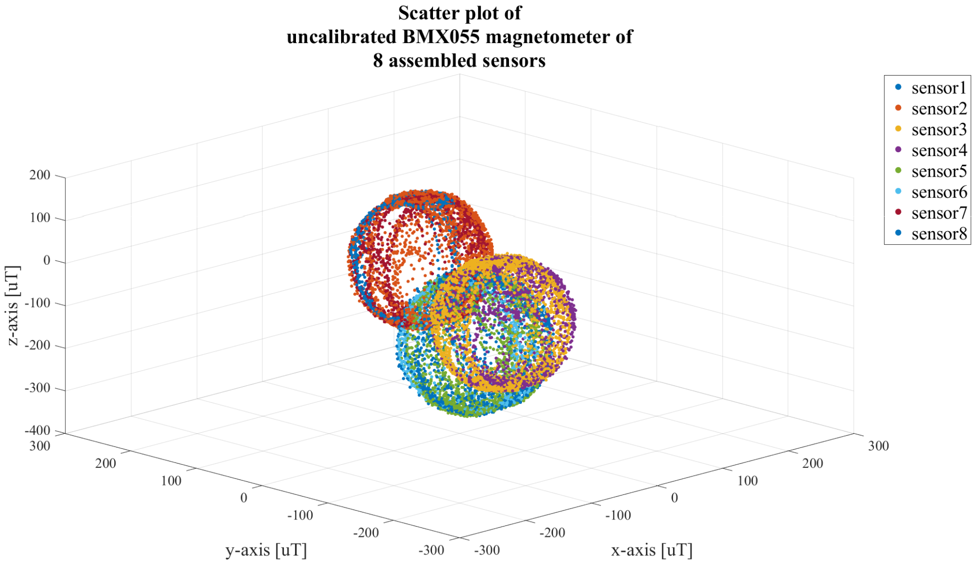

**Figure 6.20:** A scatter plot of the uncalibrated magnetometer measurements from eight fully assembled sensor units with antenna magnets removed.

To validate the performance of the *BMX055*, external restriction calibration was conducted as follows:

- Accelerometer readings were taken while the *BMX055* was positioned such that the two axes experience zero-g while the other experiences 1-g. This was repeated so that each axis experienced the gravitational acceleration;
- Gyroscope readings were taken while the *BMX055* was positioned on a mechanical rig so that only one of the three axes experienced known angular velocity at a time. This was repeated so that each axis experienced the known angular velocity.
- Magnetometer readings were taken while it was rotated through all the angles to plot a sphere centred at the origin. (Practically, due to the hard and soft iron interference, cross-axis interference and sensor non-orthogonality, an ellipsoid centred off the origin was produced. Therefore, an ellipsoid in the vicinity of the origin was deemed acceptable as shown in Figure 6.20.)

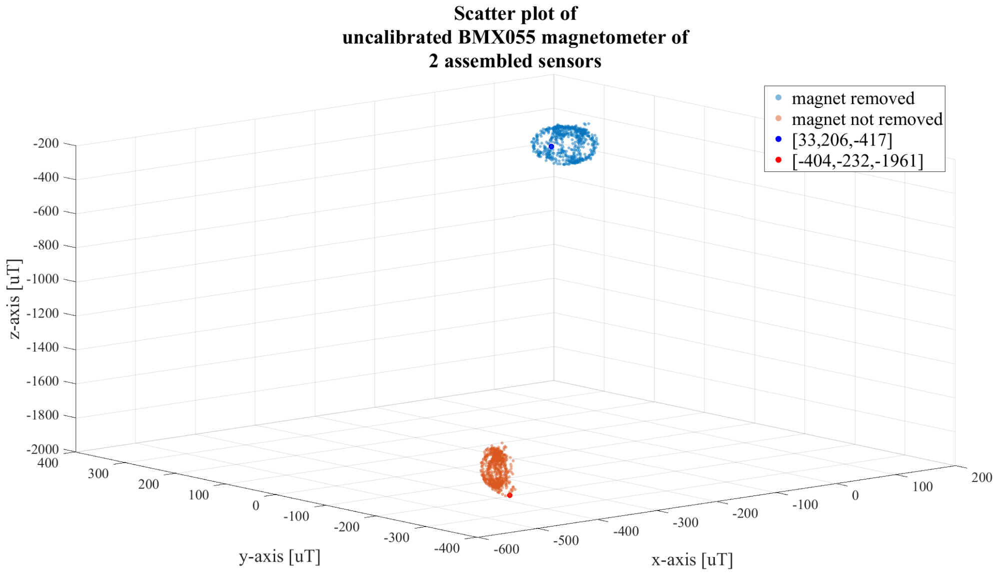

**Figure 6.21:** A scatter plot of the uncalibrated magnetometer measurements from two sensor units; one with antenna magnet removed and the other without antenna magnet removed to observe the effect of the magnet on the magnetometer measurements.

*BMX055* magnetometer has a typical measurement range of $\pm 1300\mu T$ for x- and y-axis and $\pm 2500\mu T$ for z-axis. During the examination of the magnetometer, it was found that the magnets inside the GPS antenna puts stress on the measurement range and increases the possibility of data saturation as shown in Figure 6.21. Therefore the GPS antenna magnets were removed.

### Navigational sensor: *NEO-M8T*

As stated before, the quality of the DGPS depends on the satellite geometry as well as the measurement quality and the noise covariance of the measurement has been witnessed to be related to the raw GPS SNR observable in [115].

Thus, the sensors and the *NEO-M8P* evaluation board (*C94-M8P*) were placed as close as possible and the raw GPS observables were read simultaneously. Then, SNR observable values from the sensors were compared to that of the *C94-M8P* (under the assumption that the *C94-M8P* guarantees good data quality) to examine the quality of the data from the *NEO-M8T*. The raw GPS SNR observables from the sensors agreed within $\pm 4dB$ with the raw GPS SNR observable from the *C94-M8P*, requiring no debugging process.

### 6.8.5 Sensor Array Time Synchronisation

Finally and most importantly, the mean delay between PPS signals from the sensors was measured at $145.000 \pm 17.0100 ns$ as shown in Figure 6.22. This was acceptable as it met the specification.

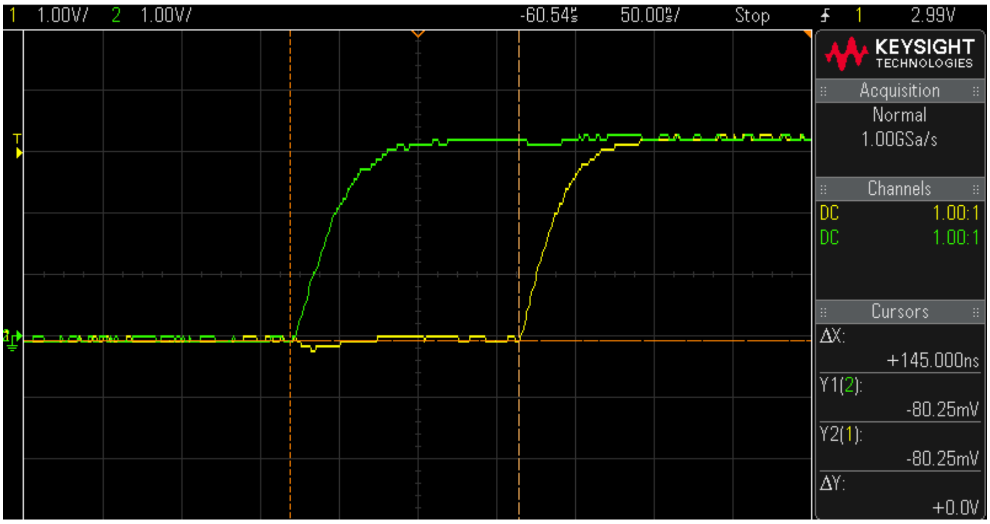

**Figure 6.22:** An oscilloscope screenshot during the simultaneous observation of the $1Hz$ PPS signals from the two sensor units. The latency between the two signals was calculated by the oscillator to be $145.000ns$.

# Chapter 7

# State Estimation Algorithm Development

The fusion MOCAP system was hypothesised to achieve commercial-level accuracy in tracking the global trajectories of the limb segments of interest while inheriting the advantages of the traditional inertial MOCAP system. By integrating raw GPS observables from each limb segment of interest to the traditional inertial MOCAP system, the fusion MOCAP system aims to provide future students, researchers and engineers with a method to track the steady-state and transient locomotion of an animal in an outdoor environment that is less restrictive than the controlled laboratory condition for gait analysis.

In Chapter 6, the device was developed to obtain the IMU measurements and raw GPS observables from each limb segment of interest. However, these measurements are indirect measurements of motion and they must be fed into the state estimation algorithm, along with the information on the kinematic chain of the captured limb segment(s) as well as the process and measurement noise covariance matrices of each sensor, to reconstruct the motion of the subject.

This chapter aims to justify the decisions made during the development of the state estimation algorithm. Accordingly, it begins by describing the kinematic chain of the sensor layout that was set up on the mechanical rig during the evaluation process. It explains the architecture of the state estimation algorithm followed by the Kalman filter design as well as the process and measurement noise covariance analysis. Finally, the Kalman filter testing results are provided.

## 7.1 Sensor Layout on the Mechanical Rig

The device, consisting of a base station and an array of time-synchronised sensors (see Chapter 6), was used to collect the raw GPS observables from the base station (named $B$) and the IMU measurements and raw GPS observables from two time-synchronised sensors (named $S_1$ and $S_2$). $S_1$ was placed on the center and $S_2$ was placed on the edge of the circular platform of the mechanical rig. This layout was aimed at simulating the motion of a limb segment about its joint with one degree of freedom, as previously stated (see Chapter 4).

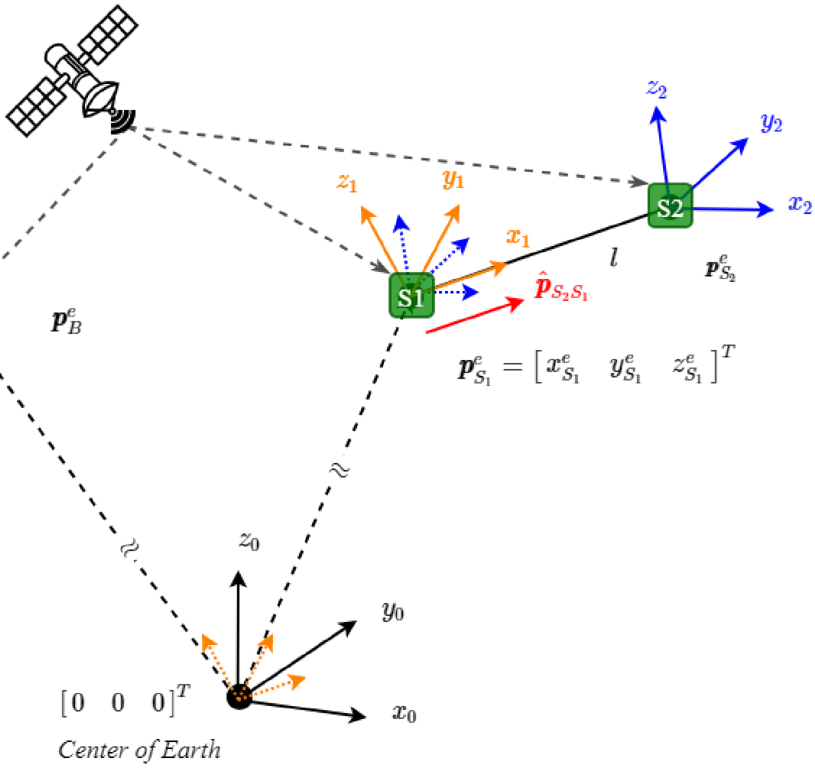

**Figure 7.1:** A diagram depicting the kinematic relationship between the base ($B$) and two sensor units ($S_1$ and $S_2$) during data acquisition.

$S_1$ and $S_2$ were modelled as two point masses constrained by a rigid beam of length $l$ as shown in Figure 7.1. As previously described (see Chapter 4), $S_1$ was positioned such that its x-axis was aligned with the unit vector, $\boldsymbol{p}_{S_2S_1}$, that is a vector of length 1 with the same direction as the $\boldsymbol{p}_{S_2} - \boldsymbol{p}_{S_1}$. Consequently, the position of the $S_2$ in $S_1$'s frame can be expressed as:

$$\boldsymbol{p}^{S_1}_{S_2} = \begin{bmatrix} l \\ 0 \\ 0 \end{bmatrix}^{S_1} . \tag{7.1}$$

## 7.2 State Estimation Algorithm Architecture

As previously mentioned (see Chapter 3), Kalman filters are one of the common prediction and estimation algorithms used in the development of the inertial MOCAP systems. It is regarded as the optimal estimator for the LQG problem which involves the estimation of the instantaneous state of a linear dynamic system perturbed by Gaussian white noise. Consequently, EKF was chosen which is the non-linear version of the Kalman filter.

The EKF architecture can be classified into a loosely-coupled and a tightly-coupled architecture. In the case of GPS/MEMS-IMU integration using a Kalman filter, a loosely-coupled architecture uses the position obtained from the GPS and the orientation obtained from the IMU measurements whereas a tightly-coupled architecture estimates the position and orientation by using the IMU measurements and GPS raw observables during the measurement update.

In the literature, the benefits of a tightly-coupled architecture are highlighted and its accuracy is found to be better than a loosely-coupled architecture. This is expected as a loosely-coupled architecture does not make use of the detailed error models of the GPS and MEMS-IMU (see Chapter 3).

In [137], Falco et al. developed and compared a tightly-coupled architecture and a loosely-coupled architecture for GNSS/Inertial Navigation System (INS) application. The tightly-coupled architecture was found to outperform in urban areas that are known to have a higher risk of multipath errors. It limited the positional error in the case of GNSS receiver outage.

Nonetheless, a loosely-coupled architecture has advantages in the development process as it provides modularity and scalability to the system, isolating the bugs to either front-end or back-end. In [138], Zihajehzadeh et al. integrated GPS and MEMS-IMU using a loosely-coupled Kalman filter for trajectory determination. It was found that the loosely-coupled architecture improves computational efficiency.

The computational efficiency of a loosely-coupled architecture is expected to be more evident with an increase in the size of the time-synchronised sensor array. Consequently, a hybrid of a tightly-coupled and a loosely-coupled architecture is proposed for the fusion MOCAP system.

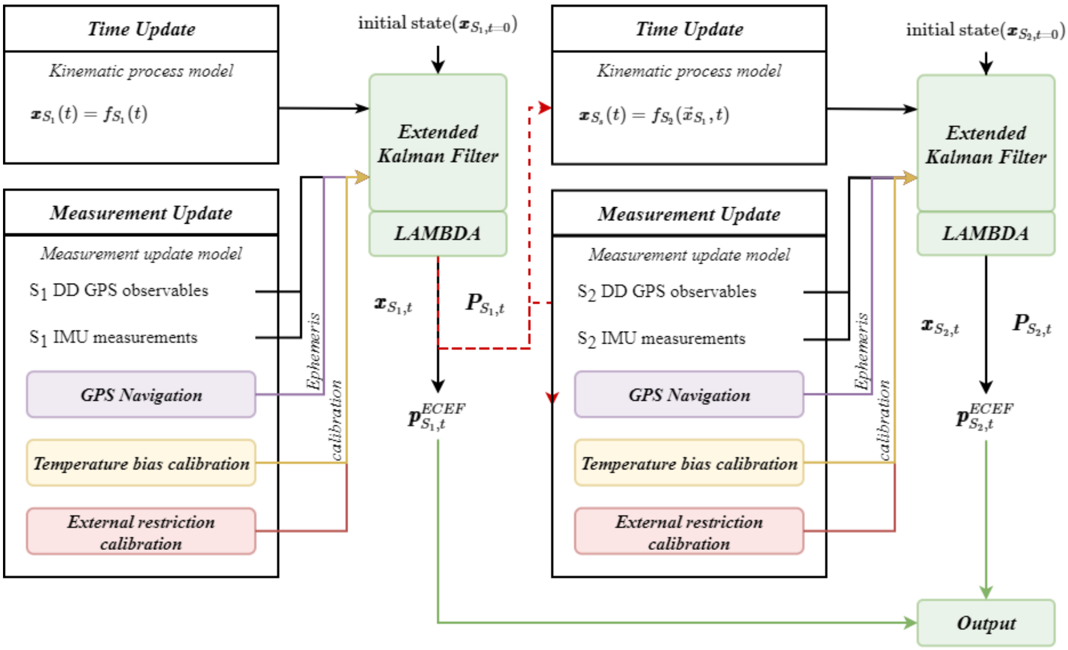

**Figure 7.2:** A block diagram of the proposed state estimation algorithm architecture.

Figure 7.2 shows a block diagram of the proposed hybrid architecture for the state estimation algorithm that estimates the global positions of $S_1$ ($\boldsymbol{r}_{S_1}(t)$) and $S_2$ ($\boldsymbol{r}_{S_2}(t)$). As it can be seen from Figure 7.2, the estimation of $\boldsymbol{r}_{S_1}(t)$ and $\boldsymbol{r}_{S_2}(t)$ are designed to be carried out sequentially. Such cascaded EKF scheme made the state estimation algorithm modular and scalable.

Additionally, it can be seen that the state variables and the state estimation error covariances from the $S_1$ positioning filter are used during the time update and the measurement update of the $S_2$ positioning filter. Consequently, the kinematic relationship between $S_1$ and $S_2$ are loosely-coupled whilst the IMU measurements and raw GPS observables are used during the measurement update, resembling the conventional tight-coupled GPS/MEMS-IMU Kalman filter.

In essence, the proposed hybrid architecture for the fusion MOCAP system creates a parent ($S_1$) and a child ($S_2$) relationship due to loosely-coupled kinematic chain information. A parent refers to the unconstrained point mass or a center of mass of the rigid beam whereas a child refers to the point mass or a center of mass of the rigid beam whose motion is constrained.

## 7.3 Extended Kalman filter (EKF) Design

The discrete EKF is a non-linear version of the discrete Kalman filter and considers a discrete-time controlled process. The discrete-time controlled process is governed by a non-linear stochastic difference equation and involves a process that is non-linear and/or a observed measurement that is non-linearly related to the states.

As the discrete Kalman filter considers a discrete LQG problem, the derivation of the discrete EKF relies on the assumption that the non-linear dynamics can be represented by the linearised dynamics. The linearisation involves assessment of the stability of an equilibrium point of a non-linear system and is carried out via Taylor series expansion as follows:

$$\begin{aligned} f(x) &= f(\bar{x}) + \frac{df}{dx}\bigg|_{x=\bar{x}}(x-\bar{x}) + \frac{1}{2}\frac{df^2}{dx^2}\bigg|_{x=\bar{x}}(x-\bar{x})^2 + \frac{1}{6}\frac{df^3}{dx^3}\bigg|_{x=\bar{x}}(x-\bar{x})^3 + \dots \\ &\approx \lim_{\bar{x}\to x}\left(f(\bar{x}) + \frac{df}{dx}\bigg|_{x=\bar{x}}(x-\bar{x})\right). \end{aligned} \tag{7.2}$$

As can be seen from (7.2), the approximation is more accurate with the inclusion of higher order terms. In [114], Lee et al. investigated the effect of the integration order and sampling rate on the estimation accuracy. Their experimental results showed that the effect of the integration order was small when the sampling frequency was high. However, with a decrease in the sampling rate, the effect of the integration order was observed to increase.

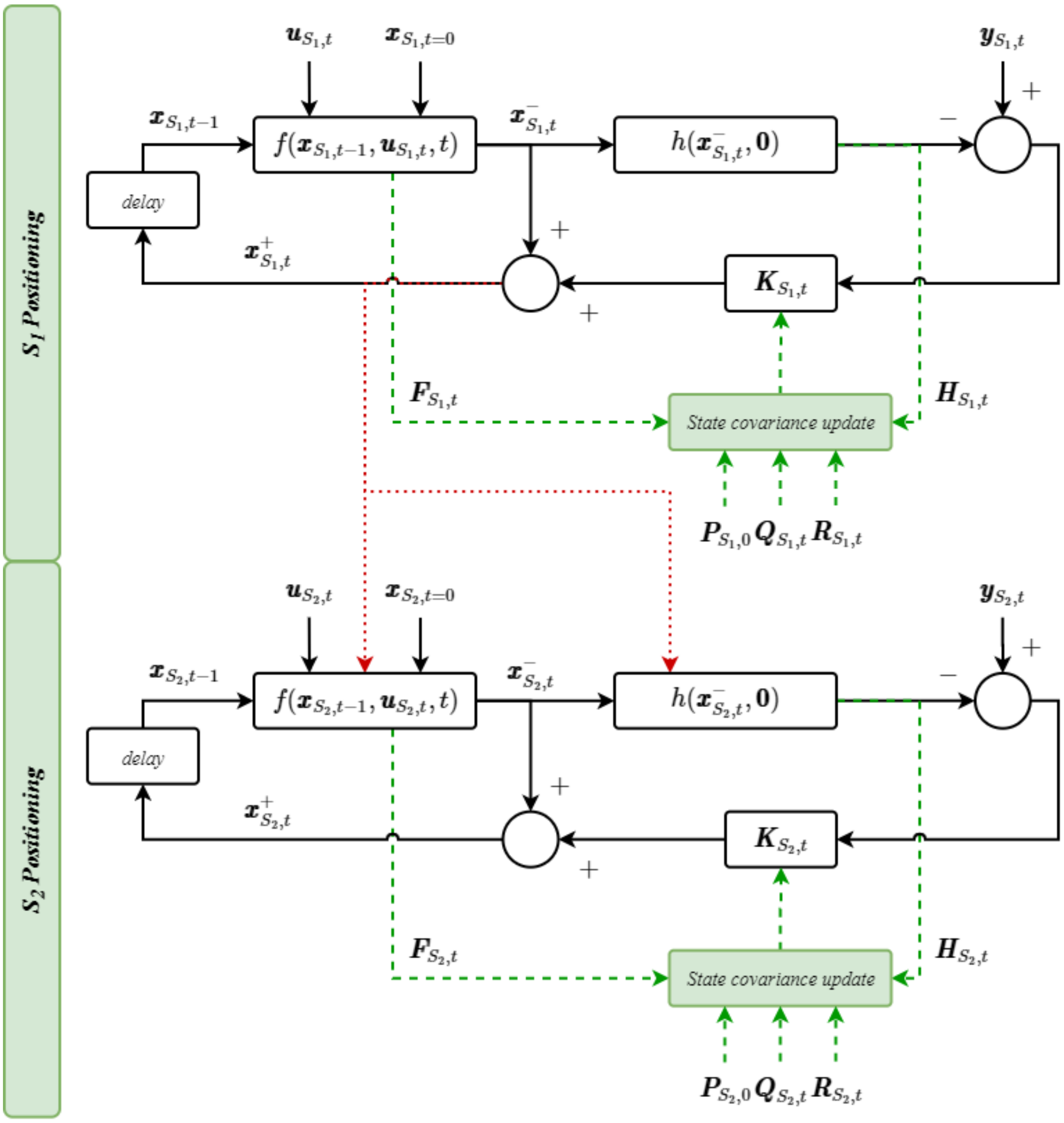

**Figure 7.3:** A block diagram of the operation of the EKF.

Based on [114], a higher order EKF was not investigated because the device developed in Chapter 6 is capable of sampling inertial measurements at a frequency as high as $2kHz$. Figure 7.3 shows a diagram of the EKF. It follows the hybrid architecture proposed in Figure 7.2 and shows the clear division between the positioning of $S_1$ (the parent) and $S_2$ (the child).

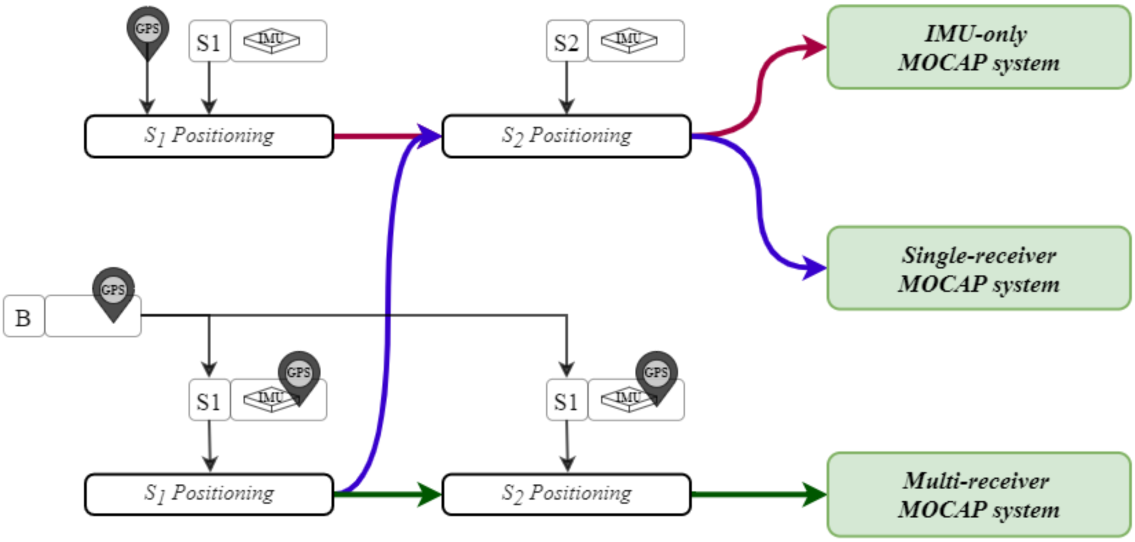

**Figure 7.4:** A block diagram of the implementation of the *MEMS-IMU*, *DGPSMEMS-IMU single-receiver* and *DGPSMEMS-IMU multi-receiver* MOCAP system. Red, blue and green lines represent the direction of the flow of information for the *MEMS-IMU*, *DGPSMEMS-IMU single-receiver* and *DGPSMEMS-IMU multi-receiver* MOCAP system respectively.

The scalability of the proposed architecture and hence the clear division between the positioning of $S_1$ and $S_2$ eased the implementations of the *MEMS-IMU*, *DGPSMEMS-IMU single-receiver* and *DGPSMEMS-IMU multi-receiver* MOCAP system. As previously mentioned in Chapter 4, these implementations were intended to compare the performance of the proposed fusion MOCAP system[1] to that of inertial MOCAP system[2] and the fusion MOCAP system in [47][3]. It was also previously informed in Chapter 4 that these three state estimation algorithms are only differ in their measurement inputs as depicted in Figure 7.4.

---

[1] *DGPSMEMS-IMU multi-receiver*

[2] *MEMS-IMU*

[3] *DGPSMEMS-IMU single-receiver*

### 7.3.1 $S_1$ (the Parent) Process and Measurement Models

**Process Model**

The $S_1$ positioning filter was aimed at estimating the ECEF coordinates of $S_1$ and its orientation with respect to the ECEF frame. Consequently, the state variables included the ECEF coordinates of $S_1$ ($\boldsymbol{p}^e_{S_1} = \begin{bmatrix} x^e_{S_1} & y^e_{S_1} & z^e_{S_1} \end{bmatrix}^T$); the Euler angles describing the rotation from the body frame of $S_1$ to ENU (navigational) frame ($\boldsymbol{r}_{nS_1} = \begin{bmatrix} \phi_{nS_1} & \theta_{nS_1} & \psi_{nS_1} \end{bmatrix}^T$); the rate of change of the Euler angles ($\dot{\boldsymbol{r}}_{nS_1}$); and the DD integer phase ambiguities ($\nabla\Delta\boldsymbol{N}^{i,k}_{S_1,B}$) of the DD carrier-phase observables collected by $S_1$ such that:

$$\begin{aligned}
\text{static: } \boldsymbol{x}_{S_1} &= \begin{bmatrix} \boldsymbol{p}^e_{S_1} & \boldsymbol{r}_{nS_1} & \dot{\boldsymbol{r}}_{nS_1} & \nabla\Delta\boldsymbol{N}^{i,k}_{S_1,B} \end{bmatrix}^T && (7.3)\\
\text{const. velocity: } \boldsymbol{x}_{S_1} &= \begin{bmatrix} \boldsymbol{p}^e_{S_1} & \dot{\boldsymbol{p}}^e_{S_1} & \boldsymbol{r}_{nS_1} & \dot{\boldsymbol{r}}_{nS_1} & \nabla\Delta\boldsymbol{N}^{i,k}_{S_1,B} \end{bmatrix}^T && (7.4)\\
\text{const. acceleration: } \boldsymbol{x}_{S_1} &= \begin{bmatrix} \boldsymbol{p}^e_{S_1} & \dot{\boldsymbol{p}}^e_{S_1} & \ddot{\boldsymbol{p}}^e_{S_1} & \boldsymbol{r}_{nS_1} & \dot{\boldsymbol{r}}_{nS_1} & \nabla\Delta\boldsymbol{N}^{i,k}_{S_1,B} \end{bmatrix}^T. && (7.5)
\end{aligned}$$

Knowing that the ECEF coordinates of $S_1$ remained unchanged throughout the testing procedure, the static process model ($f$), expressed by (7.6), was chosen to predict $\boldsymbol{p}_{t+1}$ during the time update. Nonetheless, the constant velocity model (7.7) as well as the constant acceleration model (7.8) were also implemented for comparison.

$$\begin{aligned}
\text{static: } \boldsymbol{p}_{t+1} &= \boldsymbol{p}_t && (7.6)\\
\text{const. velocity: } \boldsymbol{p}_{t+1} &= \boldsymbol{p}_t + \dot{\boldsymbol{p}}_{t+1} \cdot \Delta t &&\\
\dot{\boldsymbol{p}}_{t+1} &= \dot{\boldsymbol{p}}_t && (7.7)\\
\text{const. acceleration: } \boldsymbol{p}_{t+1} &= \boldsymbol{p}_t + \dot{\boldsymbol{p}}_{t+1} \cdot \Delta t &&\\
\dot{\boldsymbol{p}}_{t+1} &= \dot{\boldsymbol{p}}_t + \ddot{\boldsymbol{p}}_{t+1} \cdot \Delta t &&\\
\ddot{\boldsymbol{p}}_{t+1} &= \ddot{\boldsymbol{p}}_t. && (7.8)
\end{aligned}$$

Because a 3-axis gyroscope measurement was used during the measurement update to correct the transition in the estimated orientation of $S_1$ with respect to the ECEF frame, the constant angular velocity model was implemented as follows:

$$\begin{aligned}
\boldsymbol{r}_{t+1} &= \boldsymbol{r}_t + \dot{\boldsymbol{r}}_{t+1} \cdot \Delta t &&\\
\dot{\boldsymbol{r}}_{t+1} &= \dot{\boldsymbol{r}}_t. && (7.9)
\end{aligned}$$

The integer phase ambiguity ($N_u^i$) of the carrier-phase observable represents the carrier-phase cycle between the satellite on frequency $i$ and the receiver $u$ at the start of tracking (see Chapter 3). This means that the integer phase ambiguity value remains unchanged from the start of tracking until the occurrence of the cycle slip or the termination of the tracking session.

A cycle slip refers to the continuous phase lock and is caused by many factors such as atmospheric interference; low SNR; signal obstruction; power loss and more [6]. A cycle slip is known to influence the accuracy of the carrier-phase positioning as the integer ambiguity becomes an unknown on the occurrence of the cycle slip, requiring zeroing of the estimated integer ambiguity for re-establishment [139]. This means that the process model for the DD integer phase ambiguities remains the same throughout the estimation process regardless of a cycle clip as follows so that:

$$\nabla\Delta \boldsymbol{N}^{i,k}_{(S_1,B),t+1} = \nabla\Delta \boldsymbol{N}^{i,k}_{(S_1,B),t}. \tag{7.10}$$

As can be seen from (7.6), (7.7), (7.8) and (7.10), the governing process model for $S_1$ positioning was linear with zero optimal control input ($\boldsymbol{u}_t$). Therefore, the process state transition matrix ($\boldsymbol{F}$) for $\boldsymbol{x}$ (7.3) with $n$ number of locked satellites was:

$$\text{static: } \boldsymbol{F} = \begin{bmatrix} \boldsymbol{I}_{(3\times3)} & \mathbf{0}_{(3\times6)} & \mathbf{0}_{(3\times n)} \\ \mathbf{0}_{(6\times3)} & \boldsymbol{T} & \mathbf{0}_{(6\times n)} \\ \boldsymbol{I}_{(n\times3)} & \mathbf{0}_{(n\times6)} & \boldsymbol{I}_{(n\times n)} \end{bmatrix} \tag{7.11}$$

$$\text{const. velocity: } \boldsymbol{F} = \begin{bmatrix} \boldsymbol{I}_{(3\times3)} & \Delta t\cdot\boldsymbol{I}_{(3\times3)} & \mathbf{0}_{(3\times6)} & \mathbf{0}_{(3\times n)} \\ \mathbf{0}_{(3\times3)} & \boldsymbol{I}_{(3\times3)} & \mathbf{0}_{(3\times6)} & \mathbf{0}_{(3\times n)} \\ \mathbf{0}_{(6\times3)} & \mathbf{0}_{(6\times3)} & \boldsymbol{T} & \mathbf{0}_{(6\times n)} \\ \mathbf{0}_{(n\times3)} & \mathbf{0}_{(n\times3)} & \mathbf{0}_{(n\times6)} & \boldsymbol{I}_{(n\times n)} \end{bmatrix} \tag{7.12}$$

$$\text{const. acceleration: } \boldsymbol{F} = \begin{bmatrix} \boldsymbol{I}_{(3\times3)} & \Delta t\cdot\boldsymbol{I}_{(3\times3)} & \mathbf{0}_{(3\times3)} & \mathbf{0}_{(3\times6)} & \mathbf{0}_{(3\times n)} \\ \mathbf{0}_{(3\times3)} & \boldsymbol{I}_{(3\times3)} & \Delta t\cdot\boldsymbol{I}_{(3\times3)} & \mathbf{0}_{(3\times6)} & \mathbf{0}_{(3\times n)} \\ \mathbf{0}_{(3\times3)} & \mathbf{0}_{(3\times3)} & \boldsymbol{I}_{(3\times3)} & \mathbf{0}_{(3\times6)} & \mathbf{0}_{(3\times n)} \\ \mathbf{0}_{(6\times3)} & \mathbf{0}_{(6\times3)} & \mathbf{0}_{(6\times3)} & \boldsymbol{T} & \mathbf{0}_{(6\times n)} \\ \mathbf{0}_{(n\times3)} & \mathbf{0}_{(n\times3)} & \mathbf{0}_{(n\times3)} & \mathbf{0}_{(n\times6)} & \boldsymbol{I}_{(n\times n)} \end{bmatrix} \tag{7.13}$$

$$\text{where: } \boldsymbol{T} = \begin{bmatrix} \boldsymbol{I}_{(3\times3)} & \Delta t\cdot\boldsymbol{I}_{(3\times3)} \\ \mathbf{0}_{(3\times3)} & \boldsymbol{I}_{(3\times3)} \end{bmatrix}.$$

Because the base station ($B$) was positioned in the vicinity of the testing area (within $10m$ in radius) and there is no direct or indirect information to approximate the initial value of $\nabla\Delta \boldsymbol{N}^{i,k}_{S_1,B}$, the following initial states were given:

$$\boldsymbol{x}_{S_1,0} = \begin{bmatrix} \boldsymbol{p}^e_B & \mathbf{0}_{(1\times3)} & \mathbf{0}_{(1\times n)} \end{bmatrix}^T. \tag{7.14}$$

### Measurement Model

$S_1$ collected DD code observables ($\nabla\Delta\boldsymbol{P}_{S_1,B}^{i,pivot}$), DD carrier-phase observables ($\nabla\Delta\boldsymbol{\Phi}_{S_1,B}^{i,pivot}$), 3-axis accelerometer ($\boldsymbol{f}^{S_1}$), 3-axis gyroscope ($\boldsymbol{\omega}_{iS_1}^{S_1}$) and 3-axis magnetometer ($\boldsymbol{m}^{S_1}$). Therefore, the measurements in (7.15) were available for the use during measurement update. The measurements in (7.15) were rarely used collectively during the measurement update but they were updated on the availability of a measurement because of their different measurement incoming frequencies.

$$z_{S_1} = \begin{bmatrix} \nabla\Delta\boldsymbol{P}_{S_1,B}^{i,pivot} & \nabla\Delta\boldsymbol{\Phi}_{S_1,B}^{i,pivot} & \boldsymbol{f}^{S_1} & \boldsymbol{\omega}_{iS_1}^{S_1} & \boldsymbol{m}^{S_1} \end{bmatrix}^T . \tag{7.15}$$

The error-less relationship between the state variables and the GPS DD code and carrier-phase observations from $S_1$ (expressed by (7.16) and (7.17)) were previously found based on the geometry (see Chapter 3):

$$\begin{bmatrix} \nabla\Delta P_{S_1,B}^{1,pivot} \\ \nabla\Delta P_{S_1,B}^{2,pivot} \\ \vdots \\ \nabla\Delta P_{S_1,B}^{i,pivot} \end{bmatrix} = \begin{bmatrix} -(\mathbf{1}_B^1 - \mathbf{1}_B^{pivot}) \\ -(\mathbf{1}_B^2 - \mathbf{1}_B^{pivot}) \\ \vdots \\ -(\mathbf{1}_B^i - \mathbf{1}_B^{pivot}) \end{bmatrix} \cdot (\boldsymbol{p}_{S_1}^e - \boldsymbol{p}_B^e) \tag{7.16}$$

$$\begin{bmatrix} \nabla\Delta \Phi_{S_1,B}^{1,pivot} \\ \nabla\Delta \Phi_{S_1,B}^{2,pivot} \\ \vdots \\ \nabla\Delta \Phi_{S_1,B}^{i,pivot} \end{bmatrix} = \begin{bmatrix} -(\mathbf{1}_B^1 - \mathbf{1}_B^{pivot}) \\ -(\mathbf{1}_B^2 - \mathbf{1}_B^{pivot}) \\ \vdots \\ -(\mathbf{1}_B^i - \mathbf{1}_B^{pivot}) \end{bmatrix} \cdot (\boldsymbol{p}_{S_1}^e - \boldsymbol{p}_B^e) - \lambda \begin{bmatrix} \nabla\Delta N_{S_1,B}^{1,pivot} \\ \nabla\Delta N_{S_1,B}^{2,pivot} \\ \vdots \\ \nabla\Delta N_{S_1,B}^{i,pivot} \end{bmatrix} . \tag{7.17}$$

The error-less relationship between the state variables of the $S_1$ positioning filter and the IMU measurements from $S_1$ expressed by (7.18), (7.19) and (7.20) was found based on the previously described IMU measurement models (see Chapter 3). Attitude representation using an orthonormal rotation matrix, coordinate system and transformation are explained in Appendix A and Appendix B.

$$
\begin{aligned}
\boldsymbol{f}^{S_1} &= \boldsymbol{R}_n^{S_1}\boldsymbol{R}_e^n\left(\ddot{\boldsymbol{p}}_{S_1}^e - \boldsymbol{g}\right) && (7.18)\\
\text{where: } \ddot{\boldsymbol{p}}_{S_1}^e &= \begin{cases} \boldsymbol{0}, & \text{if static or const.velocity} \\ \ddot{\boldsymbol{p}}_{S_1}^e, & \text{if const. acceleration} \end{cases} \\
\text{(Euler 123): } \boldsymbol{\omega}_{iS_1}^{S_1} &= \boldsymbol{R}(\phi_{nS_1})\boldsymbol{R}(\theta_{nS_1}) \begin{bmatrix} 0 \\ 0 \\ \dot{\psi}_{nS_1} \end{bmatrix} + \boldsymbol{R}(\phi_{nS_1}) \begin{bmatrix} 0 \\ \dot{\theta}_{nS_1} \\ 0 \end{bmatrix} + \begin{bmatrix} \dot{\phi}_{nS_1} \\ 0 \\ 0 \end{bmatrix} && (7.19)\\
\boldsymbol{m}^{S_1} &= \boldsymbol{R}_n^{S_1} \begin{bmatrix} m_x^n \\ m_y^n \\ m_z^n \end{bmatrix} && (7.20)
\end{aligned}
$$

As can be seen from (7.16), (7.17), (7.18), (7.19) and (7.20), the measurements were non-linearly related to the state variables ($\boldsymbol{x}_{S_1}$). Therefore, the noiseless measurement update matrix ($\boldsymbol{H}$) was obtained by evaluating the Jacobian matrix ($J$) of the error-less relationship between the state variables of EKF and the measurements.

### 7.3.2 $S_2$ (the Child) Process and Measurement Models for EKF

#### Process Model

The $S_2$ positioning filter was also aimed at estimating the ECEF coordinates of $S_2$ and its orientation with respect to the ECEF frame. Therefore, similar to the $S_1$ positioning filter, the state vector included ECEF coordinates of $S_2$ ($\boldsymbol{p}_{S_1}^e$) as well as the DD integer phase ambiguities ($\nabla\Delta\boldsymbol{N}_{S_2,B}^{i,pivot}$) of the DD carrier-phase observables collected by $S_2$.

However, unlike the $S_1$ positioning filter, the state vector of the $S_2$ positioning did not include the Euler angles describing the rotation from the body frame of $S_2$ to the ECEF frame ($\boldsymbol{r}_{iS_2}$). Given that $\boldsymbol{r}_{iS_2}$ can be expressed in terms of $\boldsymbol{r}_{iS_1}$ and $\boldsymbol{r}_{S_1S_2}$, the Euler angles describing the rotation from the body frame of $S_2$ to the body frame of $S_1$ ($\boldsymbol{r}_{S_1S_2}$) were included instead as shown in (7.21) and (7.22):

$$
\begin{aligned}
\text{const. velocity: } \boldsymbol{x}_{S_2} &= \begin{bmatrix} \boldsymbol{p}_{S_2}^e & \boldsymbol{r}_{S_1S_2} & \dot{\boldsymbol{r}}_{S_1S_2} & \nabla\Delta\boldsymbol{N}_{S_2,B}^{i,pivot} \end{bmatrix}^T && (7.21)\\
\text{const. acceleration: } \boldsymbol{x}_{S_2} &= \begin{bmatrix} \boldsymbol{p}_{S_2}^e & \boldsymbol{r}_{S_1S_2} & \dot{\boldsymbol{r}}_{S_1S_2} & \ddot{\boldsymbol{r}}_{S_1S_2} & \nabla\Delta\boldsymbol{N}_{S_2,B}^{i,pivot} \end{bmatrix}^T. && (7.22)
\end{aligned}
$$

Additionally, $S_2$ was not stationary throughout the testing procedure but instead it was rotating about the z-axis of $S_1$. Therefore, the static process model was not implemented but the constant velocity model (7.23) and the constant acceleration model (7.24) were implemented and compared. The implemented process transition functions are expressed by (7.23) and (7.24) respectively:

$$\begin{aligned}
\text{const. velocity: } \boldsymbol{p}^e_{S_2} &= T_{\boldsymbol{p}^e_n}\boldsymbol{R}^n_{S_1}\boldsymbol{p}^{S_1}_{S_2} \\
\boldsymbol{r}_{S_1S_2,t+1} &= \boldsymbol{r}_{S_1S_2,t} + \dot{\boldsymbol{r}}_{S_1S_2,t+1} \cdot \Delta t \\
\dot{\boldsymbol{r}}_{S_1S_2,t+1} &= \dot{\boldsymbol{r}}_{S_1S_2,t} \qquad (7.23) \\
\text{const. acceleration: } \boldsymbol{p}^e_{S_2} &= T^e_n R^n_{S_1}\boldsymbol{p}^{S_1}_{S_2} \\
\boldsymbol{r}_{S_1S_2,t+1} &= \boldsymbol{r}_{S_1S_2,t} + \dot{\boldsymbol{r}}_{S_1S_2,t+1} \cdot \Delta t \\
\dot{\boldsymbol{r}}_{S_1S_2,t+1} &= \dot{\boldsymbol{r}}_{S_1S_2,t} + \ddot{\boldsymbol{r}}_{S_1S_2,t+1} \cdot \Delta t \\
\ddot{\boldsymbol{r}}_{S_1S_2,t+1} &= \ddot{\boldsymbol{r}}_{S_1S_2,t}. \qquad (7.24)
\end{aligned}$$

Because DD integer phase ambiguities ($\nabla\Delta\boldsymbol{N}^{i,pivot}_{S_2,B}$) remain unchanged from the start of tracking until the cycle slip has occurred or the tracking session is terminated, the process transition function for $\nabla\Delta\boldsymbol{N}^{i,pivot}_{S_2,B}$ is the same as the $\nabla\Delta\boldsymbol{N}^{\boldsymbol{i,k}}_{\boldsymbol{S_1,B}}$ such that:

$$\nabla\Delta\boldsymbol{N}^{i,pivot}_{(S_2,B),t+1} = \nabla\Delta\boldsymbol{N}^{i,pivot}_{(S_2,B),t}. \qquad (7.25)$$

As can be seen from (7.23), (7.24) and (7.25), the governing process model for $S_2$ positioning included non-linearity. Therefore, the Jacobian matrix ($J$)of the process model with respect to the state variables was evaluated to obtain the time update matrix ($\boldsymbol{F}$).

The following initial states were given:

$$\text{const. velocity: } \boldsymbol{x}_{S_2,0} = \left[T_{\boldsymbol{p}^e_n}\boldsymbol{R}^n_{S_1}\boldsymbol{p}^{S_1}_{S_2} \quad \boldsymbol{0}_{(1\times3)} \quad \boldsymbol{0}_{(1\times3)} \quad \boldsymbol{0}_{(1\times n)}\right]^T \qquad (7.26)$$

$$\text{const. acceleration: } \boldsymbol{x}_{S_2,0} = \left[T_{\boldsymbol{p}^e_n}\boldsymbol{R}^n_{S_1}\boldsymbol{p}^{S_1}_{S_2} \quad \boldsymbol{0}_{(1\times3)} \quad \boldsymbol{0}_{(1\times3)} \quad \boldsymbol{0}_{(1\times3)} \quad \boldsymbol{0}_{(1\times n)}\right]^T \qquad (7.27)$$

### Measurement Model

Similar to $S_1$, $S_2$ collected the following measurements: DD code observables ($\nabla\Delta \boldsymbol{P}^{i,pivot}_{S_2,B}$), DD carrier-phase observables ($\nabla\Delta \boldsymbol{\Phi}^{i,pivot}_{S_2,B}$), 3-axis accelerometer ($\boldsymbol{f}^{S_2}$), 3-axis gyroscope ($\boldsymbol{\omega}^{S_2}_{iS_2}$) and 3-axis magnetometer ($\boldsymbol{m}^{S_2}$). Therefore, the measurement vector of the $S_2$ positioning filter included:

$$\boldsymbol{z} \;=\; \begin{bmatrix} \nabla\Delta \boldsymbol{P}^{i,pivot}_{S_2,B} & \nabla\Delta \boldsymbol{\Phi}^{i,pivot}_{S_2,B} & \boldsymbol{f}_{S_2} & \boldsymbol{\omega}^{ii}_{S_2} & \boldsymbol{m}_{S_2} \end{bmatrix}^T . \tag{7.28}$$

The error-less relationship between the state variables of $S_2$ and its GPS DD observables (see (7.30) and (7.31)) and IMU measurements (see (7.32),(7.33) and (7.34)) were similar to that of $S_1$. However, the term $\ddot{\boldsymbol{p}}^e_{S_2}$ was evaluated as follows:

$$\begin{aligned} \boldsymbol{p}^e_{S_2} &= T_{\boldsymbol{p}^e_n} \boldsymbol{R}^n_{S_1} \boldsymbol{p}^{S_1}_{S_2} \\ \dot{\boldsymbol{p}}^e_{S_2} &= Jacobian(\boldsymbol{p}^e_{S_2}, \boldsymbol{r}_{S_2}) \dot{\boldsymbol{r}}_{S_2} \\ \ddot{\boldsymbol{p}}^e_{S_2} &= Jacobian(\dot{\boldsymbol{p}}^e_{S_2}, \dot{\boldsymbol{r}}_{S_2}) \ddot{\boldsymbol{r}}_{S_2}. \end{aligned} \tag{7.29}$$

$$\begin{bmatrix} \nabla\Delta P^{1,pivot}_{S_2,B} \\ \nabla\Delta P^{2,pivot}_{S_2,B} \\ \vdots \\ \nabla\Delta P^{i,pivot}_{S_2,B} \end{bmatrix} = \begin{bmatrix} -(\mathbf{1}^1_B - \mathbf{1}^{pivot}_B) \\ -(\mathbf{1}^2_B - \mathbf{1}^{pivot}_B) \\ \vdots \\ -(\mathbf{1}^i_B - \mathbf{1}^{pivot}_B) \end{bmatrix} (\boldsymbol{p}^e_{S_2} - \boldsymbol{p}^e_{Base}) \tag{7.30}$$

$$\begin{bmatrix} \nabla\Delta \Phi^{1,pivot}_{S_2,B} \\ \nabla\Delta \Phi^{2,pivot}_{S_2,B} \\ \vdots \\ \nabla\Delta \Phi^{i,pivot}_{S_2,B} \end{bmatrix} = \begin{bmatrix} -(\mathbf{1}^1_B - \mathbf{1}^{pivot}_B) \\ -(\mathbf{1}^2_B - \mathbf{1}^{pivot}_B) \\ \vdots \\ -(\mathbf{1}^i_B - \mathbf{1}^{pivot}_B) \end{bmatrix} (\boldsymbol{p}^e_{S_2} - \boldsymbol{p}^e_{Base}) - \lambda \begin{bmatrix} \nabla\Delta N^{1,pivot}_{S_2,B} \\ \nabla\Delta N^{2,pivot}_{S_2,B} \\ \vdots \\ \nabla\Delta N^{i,pivot}_{S_2,B} \end{bmatrix} \tag{7.31}$$

$$\boldsymbol{f}^{S_2} = R^{S_2}_n R^n_e (\ddot{\boldsymbol{p}}^e_{S_2} - g) \tag{7.32}$$

$$\text{(Euler 123): } \boldsymbol{\omega}^{S_2}_{iS_2} = \boldsymbol{R}(\phi_{nS_2}) \boldsymbol{R}(\theta_{nS_2}) \begin{bmatrix} 0 \\ 0 \\ \dot{\psi}_{nS_2} \end{bmatrix} + \boldsymbol{R}(\phi_{nS_2}) \begin{bmatrix} 0 \\ \dot{\theta}_{nS_2} \\ 0 \end{bmatrix} + \begin{bmatrix} \dot{\phi}_{nS_2} \\ 0 \\ 0 \end{bmatrix} \tag{7.33}$$

$$\boldsymbol{m}^{S_2} = \boldsymbol{R}^{S_2}_n \begin{bmatrix} m^n_x \\ m^n_y \\ m^n_z \end{bmatrix} \tag{7.34}$$

The measurements of $S_2$ were also non-linearly related to the state variables ($\boldsymbol{x}_{S_1}$). Therefore, Jacobian matrix ($J$)of the error-less relationship between the state variables and the measurements of $S_2$ was evaluated to obtain the noiseless measurement update matrix ($\boldsymbol{H}$).

## 7.4 Covariance Tuning

In an EKF, the optimal gain ($\boldsymbol{K}$) is evaluated using (7.35). As can be deduced from (7.35), the accuracy of the estimated state using EKF depends not only on the accuracy of the process and measurement models but also on the accuracy of the process ($\boldsymbol{Q}_t$) and the measurement noise covariances ($\boldsymbol{R}_t$). Therefore, the analysis of the process and measurement noise covariances are critical in achieving the aim of the research.

$$\begin{aligned} \boldsymbol{K}_t &= \boldsymbol{P}_t^- \boldsymbol{H}_t^T (\boldsymbol{H}_t \boldsymbol{P}_t^- \boldsymbol{H}_t^T + \boldsymbol{V}_t \boldsymbol{R}_t \boldsymbol{V}_t^T)^{-1} \\ \text{where: } \boldsymbol{P}_t^- &= \boldsymbol{F}_t \boldsymbol{P}_{t-1} \boldsymbol{F}_t^T + \boldsymbol{W}_t \boldsymbol{Q}_{t-1} \boldsymbol{W}_t^T \end{aligned} \tag{7.35}$$

### 7.4.1 Process Noise Covariance

The process noise represents the statistical noise within the prediction model. It is assumed to have the Gaussian distribution model with zero cross-correlation. As can be seen from (7.6), (7.7), (7.8), (7.23) and (7.24), the implemented process models involve either unity relationship or a simple integral of the form:

$$\boldsymbol{y}(t) = \sum_{n=1}^{t} \boldsymbol{x}(t). \tag{7.36}$$

Using the law of propagation of uncertainty, the covariance propagation model for a simple integral expressed by (7.36) can be driven as a function of the uncertainty matrix of the variable $x$ ($U_x$) and a column vector of sensitivity coefficients ($F$) [140]:

$$\begin{aligned} U_{\boldsymbol{y}} &= F_{\boldsymbol{y}} U_{\boldsymbol{x}} F_{\boldsymbol{y}}^T \\ &= J(\boldsymbol{y},\boldsymbol{x}) U_{\boldsymbol{x}} J(\boldsymbol{y},\boldsymbol{x})^T \\ &= J\Big(\sum_{n=1}^{t} \boldsymbol{x}(t), \boldsymbol{x}(t)\Big) U_{\boldsymbol{x}} J\Big(\sum_{n=1}^{t} \boldsymbol{x}(t), \boldsymbol{x}(t)\Big)^T \\ &= \boldsymbol{I}^T (\boldsymbol{I} U_{\boldsymbol{x}} \boldsymbol{I}^T) \boldsymbol{I} \\ &= U_{\boldsymbol{x}}. \end{aligned} \tag{7.37}$$

Consequently, the process noise covariance matrices for static, constant velocity and constant acceleration models are expressed by (7.38), (7.39) and (7.40) respectively. It is to be noted that these process noise covariance matrices are not valid if the integral at time $t$ is evaluated using the integrand at time $t$, unlike the process model expressed by (7.6), (7.7), (7.8), (7.23) and (7.24):

$$\text{static: } \boldsymbol{Q}_t = \begin{bmatrix} \boldsymbol{\sigma}^2_{\boldsymbol{x},t} \end{bmatrix} \tag{7.38}$$

$$\text{const. velocity: } \boldsymbol{Q}_t = \begin{bmatrix} \Delta t \boldsymbol{\sigma}^2_{\dot{\boldsymbol{x}},t} & \boldsymbol{0} \\ \boldsymbol{0} & \boldsymbol{\sigma}^2_{\dot{\boldsymbol{x}},t} \end{bmatrix} \tag{7.39}$$

$$\text{const. acceleration: } \boldsymbol{Q}_t = \begin{bmatrix} \Delta t^2 \boldsymbol{\sigma}^2_{\ddot{\boldsymbol{x}},t} & \boldsymbol{0} & \boldsymbol{0} \\ \boldsymbol{0} & \Delta t \boldsymbol{\sigma}^2_{\ddot{\boldsymbol{x}},t} & \boldsymbol{0} \\ \boldsymbol{0} & \boldsymbol{0} & \boldsymbol{\sigma}^2_{\ddot{\boldsymbol{x}},t} \end{bmatrix}. \tag{7.40}$$

The $\boldsymbol{\sigma}^2_{\boldsymbol{r}}$, $\boldsymbol{\sigma}^2_{\dot{\boldsymbol{r}}}$ and $\boldsymbol{\sigma}^2_{\ddot{\boldsymbol{r}}}$ were decided based on the subjective observation of the system. For instance, given $S_2$ is visually observed to make a turn around the z-axis of the body frame of $S_1$ every 2 seconds, the expected angular velocity along the z-axis of $S_2$ is $\approx 3 rad/s$. The expected angular velocity ($E[\omega_z]$) is discretised and therefore the noise covariance ($\sigma^2_{\dot{\boldsymbol{\omega}}_z}$) of the angular velocity along the z-axis of $S_2$ is $E[\omega_z]^2(\Delta t)^2$. Unfortunately, the process covariance matrices required post-tuning because they were based on the subjective analysis of the system.

### 7.4.2 Measurement Model and Noise Covariance

The measurement noise represents the statistical noise inherent to the measurements and it is also assumed to have the Gaussian distribution model with zero cross-correlation. Being inherent to the developed device which includes MEMS-IMU and GPS, analysis of IMU measurements and raw GPS observables are inevitable in order to evaluate the measurement noise covariance ($R$) for the EKF.

#### MEMS-IMU measurement

The form of the measurement noise covariance matrices with zero cross-correlation for a 3-axis accelerometer, 3-axis gyroscope and 3-axis magnetometer is given by (7.41), (7.42) and (7.43) respectively:

$$\text{accelerometer: } \boldsymbol{R}_t = \begin{bmatrix} \sigma^2_{a_{xx},t} & 0 & 0 \\ 0 & \sigma^2_{a_{yy},t} & 0 \\ 0 & 0 & \sigma^2_{a_{zz},t} \end{bmatrix} \tag{7.41}$$

$$\text{gyroscope: } \boldsymbol{R}_t = \begin{bmatrix} \sigma^2_{\omega_{xx},t} & 0 & 0 \\ 0 & \sigma^2_{\omega_{yy},t} & 0 \\ 0 & 0 & \sigma^2_{\omega_{zz},t} \end{bmatrix} \tag{7.42}$$

$$\text{magnetometer: } \boldsymbol{R}_t = \begin{bmatrix} \sigma^2_{m_{xx},t} & 0 & 0 \\ 0 & \sigma^2_{m_{yy},t} & 0 \\ 0 & 0 & \sigma^2_{m_{zz},t} \end{bmatrix}. \tag{7.43}$$

$\sigma^2_{a_{xx}}$, $\sigma^2_{a_{yy}}$m $\sigma^2_{a_{zz}}$, $\sigma^2_{\omega_{xx}}$, $\sigma^2_{\omega_{yy}}$, $\sigma^2_{\omega_{zz}}$, $\sigma^2_{m_{xx}}$, $\sigma^2_{m_{yy}}$ and $\sigma^2_{m_{zz}}$ were computed by evaluating the variance ($\sigma^2$) of the noise and model uncertainties along nine sensitive axes of the 9-axis MEMS-IMUs. The noise and model uncertainties of the MEMS-IMU was isolated by conducting temperature-biased calibration and external restriction calibration.

#### GPS raw observables

As previously mentioned, the quality of the DGPS depends on the satellite geometry and the measurement quality. Unfortunately, the relationship between the satellite elevation, raw GPS SNR observable and residual covariance are not well defined for both DD code and DD carrier-phase observables.

It must be further noted that the GPS antenna is designed for use in a Line-of-Sight (LOS) condition. However, the attachment of the GPS antenna on a terrestrial *megafauna* places a challenge to this and may result in a Non-Line-of-Sight (NLOS) condition. Therefore, the analysis and modelling of the relationship between the satellite elevation, raw GPS SNR observable and residual covariance for both DD code and DD carrier-phase observables in LOS and NLOS conditions were carried out.

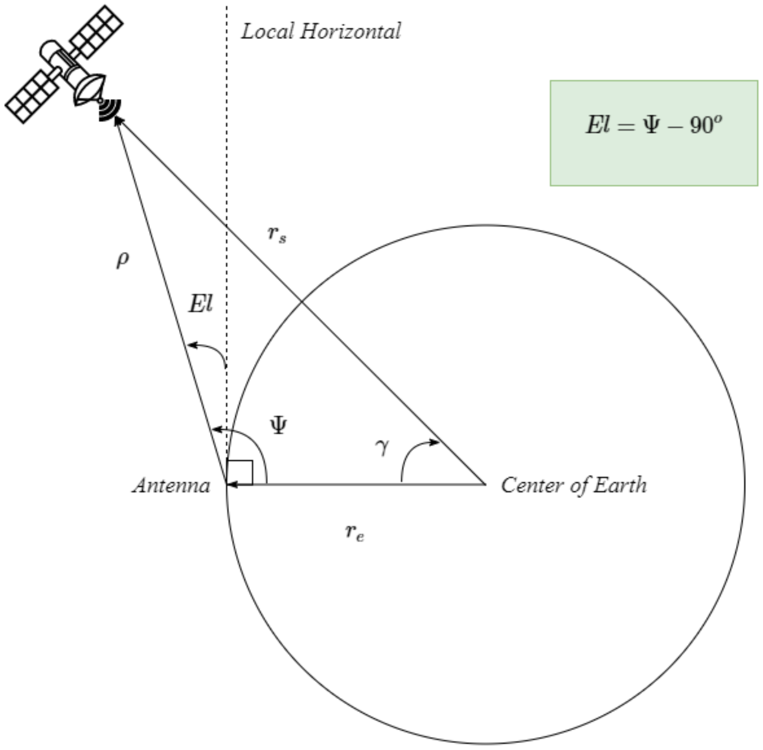

**Figure 7.5:** A simple diagram explaining the satellite elevation using geometry.

Satellite elevation refers to the angle between the LOS line between an antenna and a satellite and the local horizontal plane of an antenna as shown in Figure 7.5. It is a well-known practice to remove the measurements from the satellites with low elevation angle as the influence of the atmospheric errors and signal multipath are greatest on the horizon [96].

To obtain DD code and DD carrier-phase residuals and corresponding elevation and SNR, two time-synchronised sensors were placed as close as possible to the *NEO-M8P* evaluation board (base station) and raw GPS observables were collected for both the two sensors and the reference station. Two sensors were places as follows:

1. The z-axis of one sensor's antenna was positioned parallel to that of the reference station's antenna's z-axis;
2. The other sensor's antenna was positioned perpendicular to that of the reference station's antenna's z-axis.

Using the known coordinates of the reference station, DD range and DD integer ambiguity were computed. These were then subtracted from the DD code and DD carrier-phase observables collected from the experiment to compute DD code and DD carrier-phase residuals. Therefore, DD code and DD carrier-phase residuals are essentially a sum of the DD multipath ($\nabla\Delta m_{u,r}^{i,k}$) and DD unmodelled error ($\nabla\Delta\varepsilon_{u,r}^{i,k}$).

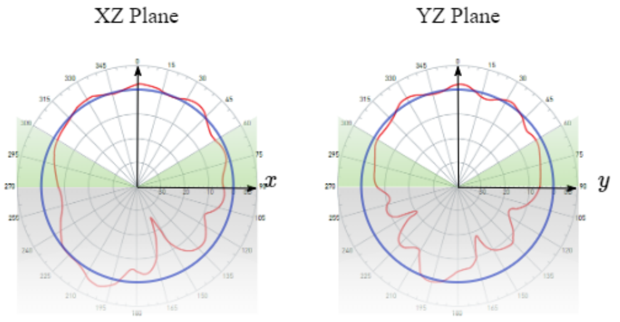

**(a)** A diagram depicting the signal entry point under the LOS condition where the antenna is attached parallel to the local horizontal line.

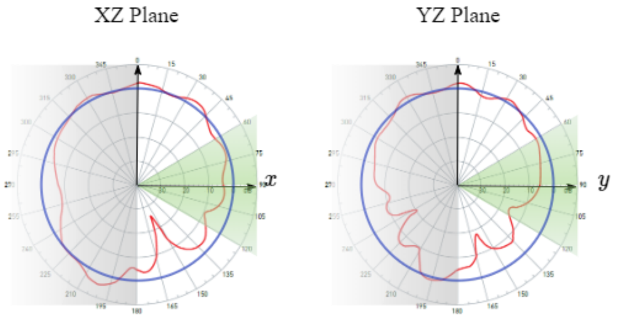

**(b)** A diagram depicting the signal entry point under the NLOS condition where the antenna is attached perpendicular to the local horizontal line.

**Figure 7.6:** A diagram comparing the signal entry point of the LOS and the NLOS conditions for the *Titan AA.105.301111* active antenna. The red line represents the radiation pattern of the *Titan AA.105.301111* active antenna during far-field testing [12]; the blue line represents the $0dB$ line; the grey shaded region represents the blocked area due to the antenna attachment; the green shaded region represents low elevation and the non-shaded area represents the most probable region at which the signals would enter.

Prior to the experiment, two hypotheses were made. Firstly, it was hypothesised that the residuals from a LOS condition would be smaller and more stable than that from a NLOS condition. This hypothesis was based on the comparison of the exposed radiation patterns between LOS and NLOS conditions as shown in Figure 7.6.

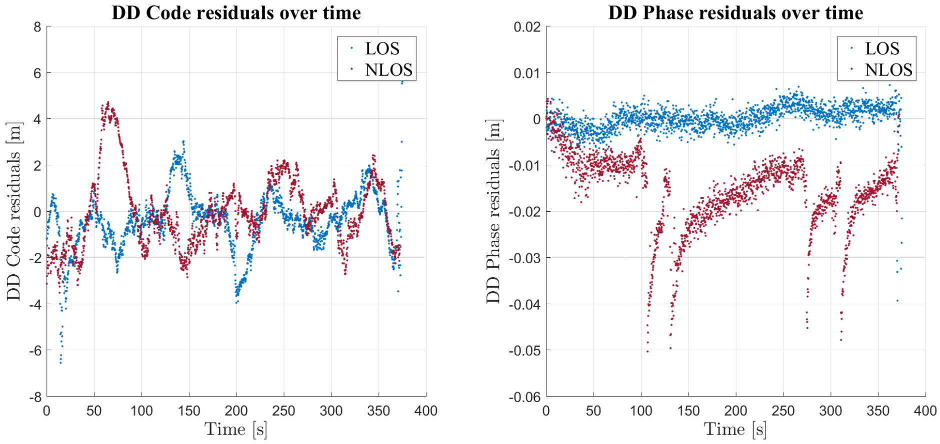

**Figure 7.7:** A plot comparing the DD residuals from the LOS and NLOS condition. On the left is the code residual and on the right is the carrier-phase residual.

By comparing Figure 7.6a and Figure 7.6b, it can be deduced that there is a greater loss in signal strength in the low elevation region and the NLOS condition results in a greater loss in signal strength than the LOS condition. As hypothesised, the residuals from the NLOS condition were observed to be higher and more unstable that the LOS condition as shown in Figure 7.7.

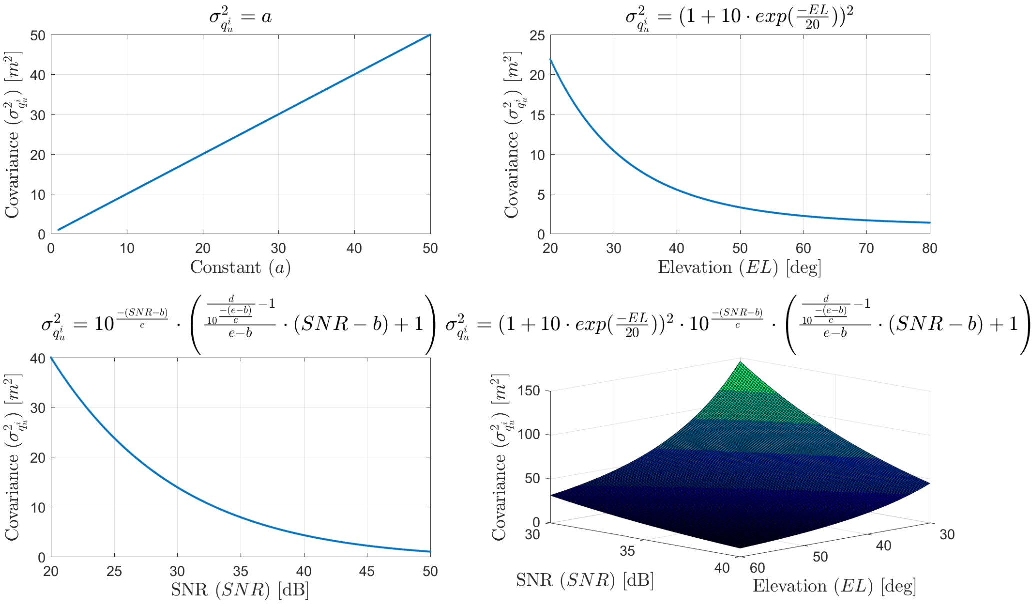

**Figure 7.8:** Plots of four types of covariance model for the raw GPS code and carrier-phase observables implemented in *goGPS*. Constants $b$, $c$, $d$, $e$ and $f$ are set to 20, 50, 30, 40 and 20 respectively.

Secondly, it was hypothesised that the DD code and DD carrier-phase residual covariances would increase with a decrease in elevation and SNR. This was based on the covariance model implemented in *goGPS*. *goGPS* provides four types of covariance models for the GPS code and carrier-phase observables which are based on a given constant, satellite elevation, SNR or both as shown in Figure 7.8. Using this, the covariance models for the DD code and DD carrier-phase observables were computed using (7.44).

$$\sigma^2_{q^{i,k}_{u,r}} = (\sigma^2_{q^k_u} + \sigma^2_{q^k_r}) + (\sigma^2_{q^i_u} + \sigma^2_{q^i_r}) \tag{7.44}$$

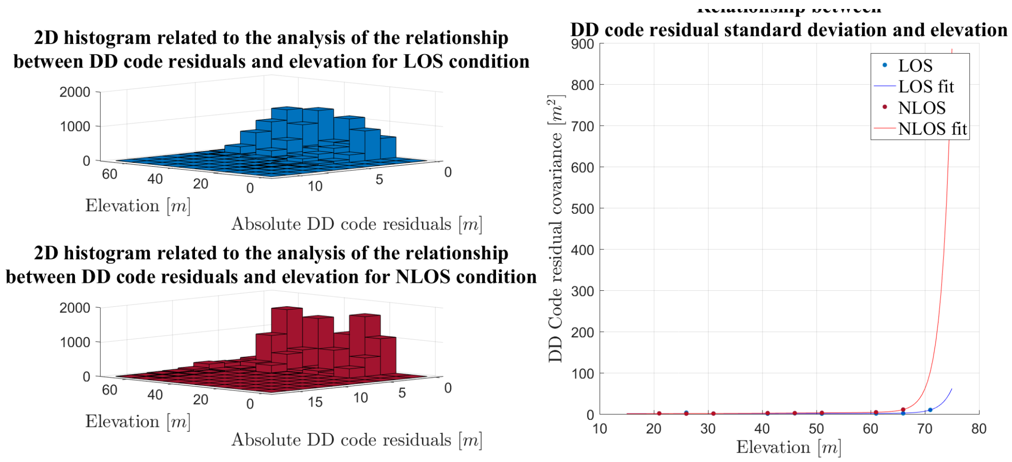

**Figure 7.9:** An analysis of the relationship between the DD code residual and elevation for LOS and NLOS condition.

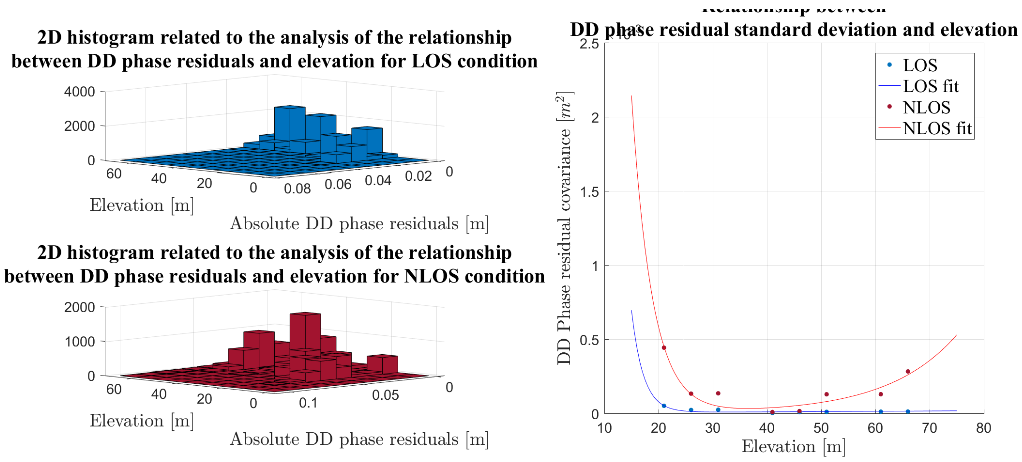

**Figure 7.10:** An analysis of the relationship between the DD phase residual and elevation for LOS and NLOS condition.

The second hypothesis was not met completely. As can be observed from Figures 7.9 and 7.10, the DD code covariance increased with an increase in elevation whereas a parabolic relationship was observed between the DD carrier-phase covariance and elevation. Nonetheless, the first expectation was still met as the DD code and DD carrier-phase covariances from the NLOS condition can be observed to be greater than that of the LOS condition.

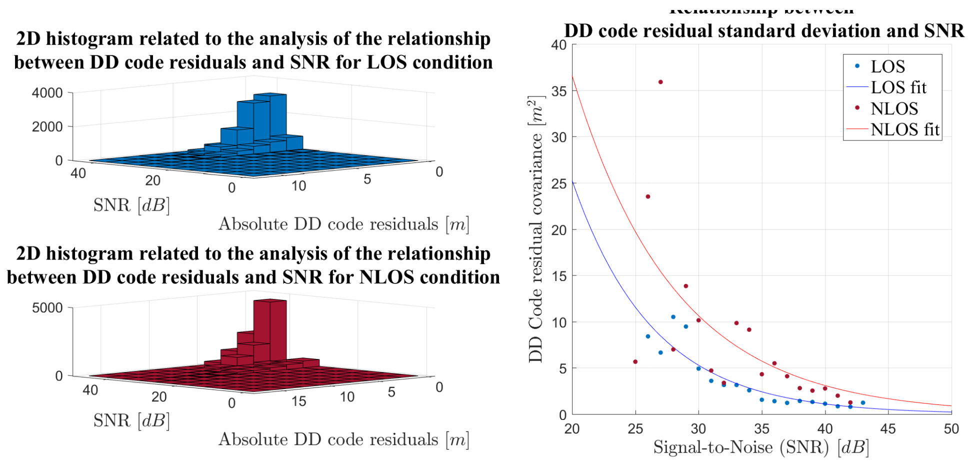

**Figure 7.11:** An analysis of the relationship between the DD code residual and SNR for LOS and NLOS condition.

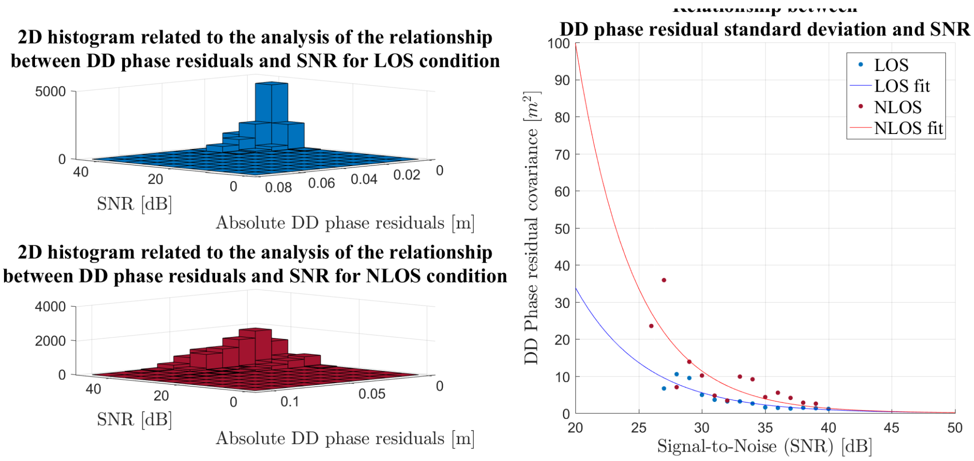

**Figure 7.12:** An analysis of the relationship between the DD phase residual and SNR for LOS and NLOS condition.

Unlike the observed relationship between the elevation and DD code and DD carrier-phase covariances, the observed relationship between the SNR and DD code and DD carrier-phase covariances have shown a similar trend to that of *goGPS*'s SNR based covariance model. This can be seen from Figures 7.11 and 7.12. The DD code and DD carrier-phase covariances from the NLOS condition was again observed to be greater than that of the LOS condition.

In summary, the relationship between the elevation and DD code covariance was observed to be different to the relationship between the elevation and DD carrier-phase covariance. Furthermore, both relationships disagreed with the covariance model implemented in *goGPS*. Nonetheless, the relationships between the SNR and both the DD code and carrier-phase observables were observed to be exponential and found to have a similar trend to the covariance models implemented in *goGPS*.

Consequently, it was decided to model the DD code and DD carrier-phase covariances based on the corresponding SNR and an angle of attachment as expressed in (7.45) and (7.46) respectively:

$$\sigma^2_{P^{i,k}_{u,r}}(SNR) = a|1+0.5sin(\theta)| \cdot e^{b|1+0.3sin(\theta)| \cdot SNR} \tag{7.45}$$

$$\sigma^2_{\Psi^{i,k}_{u,r}}(SNR) = a|1+5cos(\theta)| \cdot e^{b|1+0.3cos(\theta)| \cdot SNR}, \tag{7.46}$$

where an angle of attachment ($\theta$) refers to an angle between local vertical plane and antenna z-axis.

## 7.5 $S_1$ Positioning Results

### 7.5.1 Filter direction

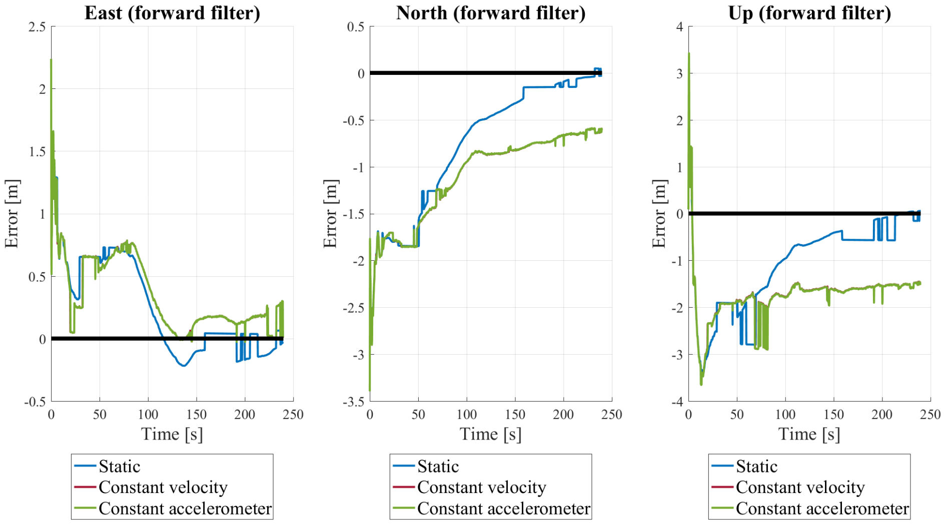

**Figure 7.13:** Plots of error in the estimated the ECEF coordinates of $S_1$ using the forward EKF represented in the ENU coordinate system.

Figure 7.13 is a plot of the error in the estimated ECEF coordinates of $S_1$, represented in the ENU coordinate system. The true data was obtained through a survey process where the ECEF coordinates of $S1_1$ was collected over two hours using the *U-blox u-center* software. According to the *U-blox u-center* software, the surveyed position was evaluated to have a positional standard deviation of $0.699m$ at the end of the survey. As it can be seen from Figure 7.13, the filter has an unsatisfactory convergence rate. This was understood to be caused by the estimation of the DD integer ambiguity ($\nabla\Delta\Phi_{S_1,r}^{i,k}$).

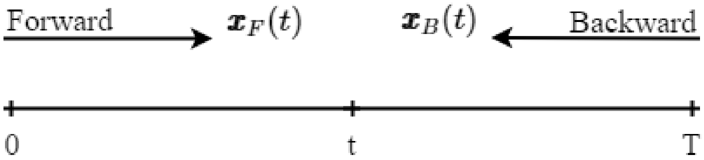

**Figure 7.14:** A simple diagram depicting the relationship between the forward and backward filters. [13]

Consequently, the forward filter, backward filter and optimal smoother were investigated and implemented with the aim to improve the convergence rate of the filter output. A forward filter utilises all data prior to time $t$ and estimates $\boldsymbol{x_F}(t)$ whereas a backward filter utilises all the data after time $t$ and estimates $\boldsymbol{x_B}(t)$ [13]. The relationship between a forward and backward filter is depicted in Figure 7.14. Finally, the smoother utilises the forward and backward estimate error covariances and solutions to minimise the trace of its estimate error covariance [13].

There are three types of optimal smoothing filters, namely: fixed-interval, fixed-point and fixed-lag smoothing [13]. Fixed-interval smoother estimates $\boldsymbol{x}(t|T)$ as $t$ varies from 0 to $T$; fixed-point smoother estimates $\boldsymbol{x}(t|T)$ as $T$ varies from 0 to $T$ whereas fixed-lag smoother estimates $\boldsymbol{x}(T-\Delta|T)$ as $T$ varies from 0 to $T$ with constant $\Delta$. Because the fusion MOCAP system aims to estimate the ECEF coordinates of the limb segments of interest that progress with time using the measurements obtained over a fixed interval, fixed-interval smoothing was implemented.

Implemented fixed-interval smoother utilised the forward and backward estimate error covariances ($P_F(t)$ and $P_B(t)$) and their solutions ($\boldsymbol{x_F}(t)$ and $\boldsymbol{x_B}(t)$). The most compact expressions for optimal smoother estimate error covariance ($P(t|T)$) and solution ($\boldsymbol{x}(t|T)$) are given by (7.47) and (7.48) [13]:

$$\begin{aligned} P(t|T) &= (P_F(t)+P_B(t))^{-1} && (7.47)\\ \boldsymbol{x}(t|T) &= P(t|T)[P_F^{-1}(t)\boldsymbol{x_F}(t)+P_B^{-1}(t)\boldsymbol{x_B}(t)]. && (7.48) \end{aligned}$$

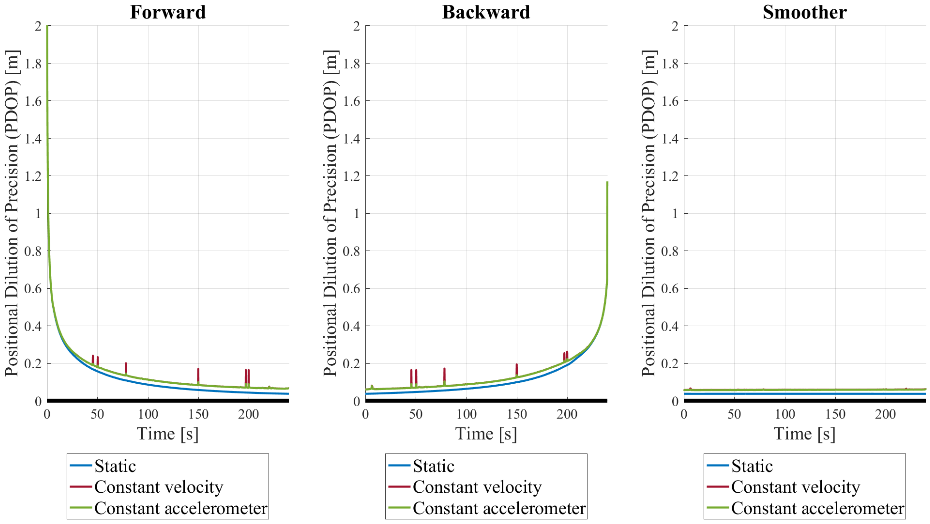

**Figure 7.15:** A comparison of the PDOP between the forward filter, backward filter and the optimal smoother.

Figure 7.15 compares the Positional Dilution of Precision (PDOP) (expressed by (7.49)) obtained from the forward, backward and optimal smoothing filter. As can be seen from Figure 7.15, a significant reduction in the trace of the estimated error covariance was observed in the smoother in comparison to the forward and backward filters.

$$PDOP = \sqrt{\sigma_{xx}^2 + \sigma_{yy}^2 + \sigma_{zz}^2} \tag{7.49}$$

Three different process models: the static, constant velocity and constant acceleration models were implemented and their results were plotted and compared in Figure 7.15. It can be seen that the previously mentioned hypothesis was correct and the $S_1$ positioning filter with the static process model was observed across all three filters (the forward, backward and optimal smoother) to perform better than the filters with the constant velocity and constant acceleration process model.

Table 7.1 summarises the performance of the forward, backward and smoothing filters for static, constant velocity and constant acceleration process models. The RMS errors in Table 7.1 represent the difference between the estimated position of $S_1$ and the observed position of $S_1$. The RMS errors were calculated based on the error in the estimation of $S_1$ during five experiments. Each experiment lasted approximately 4 minutes which is equivalent to the acquisition of approximately 1200 raw GPS observables and 60000 MEMS-IMU measurements.

**Table 7.1:** A summary of the RMS error evaluated to assess the performance of the state estimation algorithm of the $S_1$ positioning filter

| **Algorithm direction** | **Process model** | **RMS error [m]**<br>**East** | <br>**North** | <br>**Up** | <br>**Overall** |
|---|---|---|---|---|---|
| Forward | static | 0.1218 | 0.3049 | 0.5130 | 0.3516 |
| Forward | const. velocity | 0.1676 | 0.7618 | 1.5915 | 1.0233 |
| Forward | const. acceleration | 0.1671 | 0.7610 | 1.5958 | 1.0253 |
| Backward | static | 0.2239 | 0.1210 | 0.4234 | 0.1923 |
| Backward | const. velocity | 0.4233 | 0.5538 | 0.9118 | 0.6627 |
| Backward | const. acceleration | 0.4234 | 0.5542 | 0.9144 | 0.6640 |
| Smoother | static | 0.0298 | 0.0321 | 0.0523 | **0.0394** |
| Smoother | const. velocity | 0.3052 | 0.7021 | 1.4242 | 0.9335 |
| Smoother | const. acceleration | 0.3050 | 0.7022 | 1.4274 | 0.9351 |

As highlighted in Table 7.1, the optimal smoother with a static process model had the highest accuracy with the RMS positioning error of $\pm 0.2690m$.[4] This was anticipated because the optimal smoother is known to minimise the convergence rate of the filter and $S_1$ remained stationary throughout five experiments (see Chapter 4).

As previously mentioned, the surveyed true data was informed by *Ublox uCenter*, to have a standard deviation of $0.699m$ that is a variance of $0.489m$. Consequently, the estimated ECEF coordinates of $S_1$ from the smoothing filter with the static process model agrees with the true data.

### 7.5.2 MEMS-IMU and DGPS/MEMS-IMU filters

In Chapter 2, it was found that an inertial MOCAP system suffers from inherent noisy sensor measurements that compound over time. Based on the work of Brodie et al. [46], Supej [47] and Gilgien et al. [48], the proposed fusion MOCAP system was hypothesised to diminish the inaccuracy due to the bias, scale factor and sensor noise of a MEMS-IMU.

It was mentioned in Chapter 4 that a MEMS-IMU MOCAP system would be implemented to validate the above-mentioned hypothesis. This implementation was to answer the research question: ***Does integration of Global Positioning Systems (GPS) or Differential Global Positioning Systems (DGPS) improve the applicability and/or performance of the traditional Micro Electro Mechanical Systems (MEMS)-Inertial Measurement Units (IMU) MOCAP system?***.[5]

---

[4] From this point forward, a filter refers to a smoothing filter.

[5] See Chapter 1.

As a result of the proposed hybrid architecture (Figure 7.2), the $S_1$ positioning filter was easily modified to use IMU measurements only by excluding the measurements and measurement models related to raw GPS observables. However, the position of $S_1$ at $t = 0$ was fed to enable comparison of the $S_1$ positioning with only IMU measurements to that with the IMU measurements as well as the raw GPS observables.

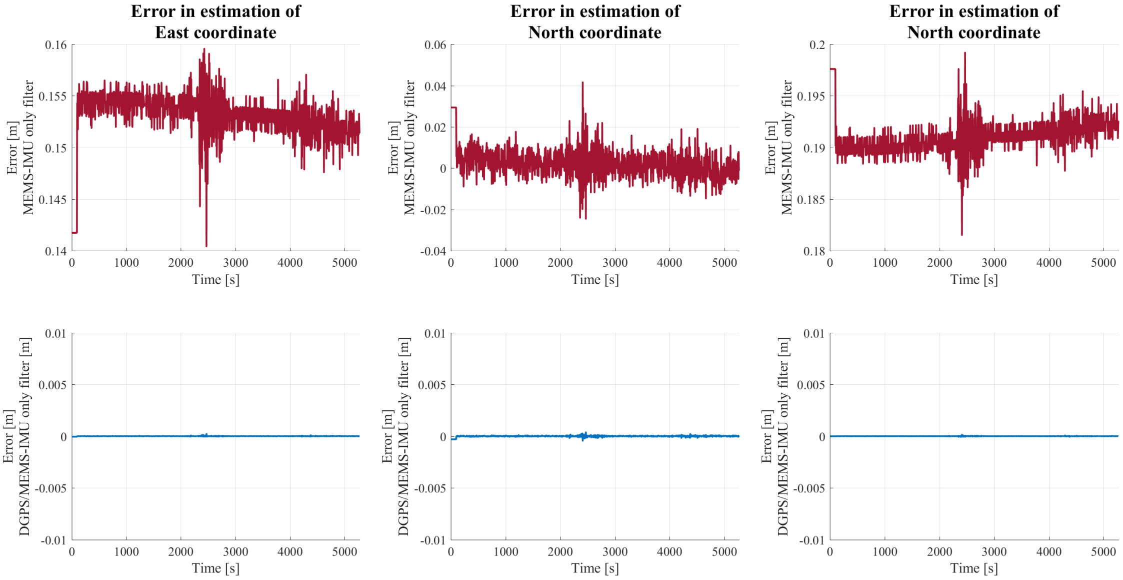

**Figure 7.16:** A comparison of the errors in estimated position between the MEMS-IMU only filter (red) and the DGPS/MEMS-IMU filter (blue) represented in ENU coordinate system.

Figure 7.16 is the comparison of the errors in the estimated position of $S_1$ from the MEMS-IMU only filter and the DGPS/MEMS-IMU filter. Only one experiment was conducted for 5271.2 seconds (1.46 hours). This experiment took longer so that the influence of the non-repetitive and unstable errors inherent to the MEMS-IMU could be observed.[6] During this experiment, 26378 raw GPS observables and 13231856 IMU measurements were collected.

As can be seen from Figure 7.16, the MEMS-IMU only filter suffers from noise and drift more than the DGPS/MEMS-IMU filter by two orders of magnitude. Using the linear polynomial model[7], the offset and the gradient of the errors in the estimated East, North and Up coordinates of $S_1$ were evaluated for both the MEMS-IMU filter and the DGPS/MEMS-IMU filter. They are listed in Table 7.2.

---

[6] The repetitive and stable errors were removed during the calibration process. See Chapter 3.

[7] $y(t) = mx(t) + c$

**Table 7.2:** The offset and the gradient of the errors in the estimated ENU coordinates of $S_1$

| Filter | Coordinate | Gradient ($m$) [m] | Offset ($c$) [m] |
|---|---|---|---|
| MEMS-IMU only | East | $-0.3042 \times 10^{-6}$ | 0.1539 |
| | North | $-1.697 \times 10^{-6}$ | 0.006827 |
| | Up | $-0.3078 \times 10^{-6}$ | 0.1902 |
| DGPS/MEMS-IMU | East | $1.807 \times 10^{-9}$ | $-3.097 \times 10^{-6}$ |
| | North | $8.512 \times 10^{-9}$ | $-24.63 \times 10^{-6}$ |
| | Up | $0.4118 \times 10^{-9}$ | $-1.458 \times 10^{-6}$ |

## 7.6 $S_2$ Positioning Results

The novelty of the fusion MOCAP system lies in the integration of the raw GPS observables from each limb segment of interest. However, the novelty is unnecessary if such integration does not improve the existing fusion MOCAP system which fuses the navigational information of the subject into the traditional inertial MOCAP system. Therefore, it was crucial to answer the question: ***Is the integration of DGPS on each limb segments beneficial in comparison to the Micro Electro Mechanical Systems (MEMS)-Inertial Measurement Units (IMU) MOCAP system with a single DGPS?***.

In Chapter 4, it was mentioned that a *DGPS/MEMS-IMU single-receiver* fusion MOCAP system and a *DGPS/MEMS-IMU multi-receiver* fusion MOCAP system were implemented for comparison. Similar to the implementation of the MEMS-IMU only filter using the $S_1$ positioning filter, the $S_2$ positioning filter was easily modified to use IMU measurements only. This was done by excluding the GPS raw measurements during the measurement update of the $S_2$ positioning.

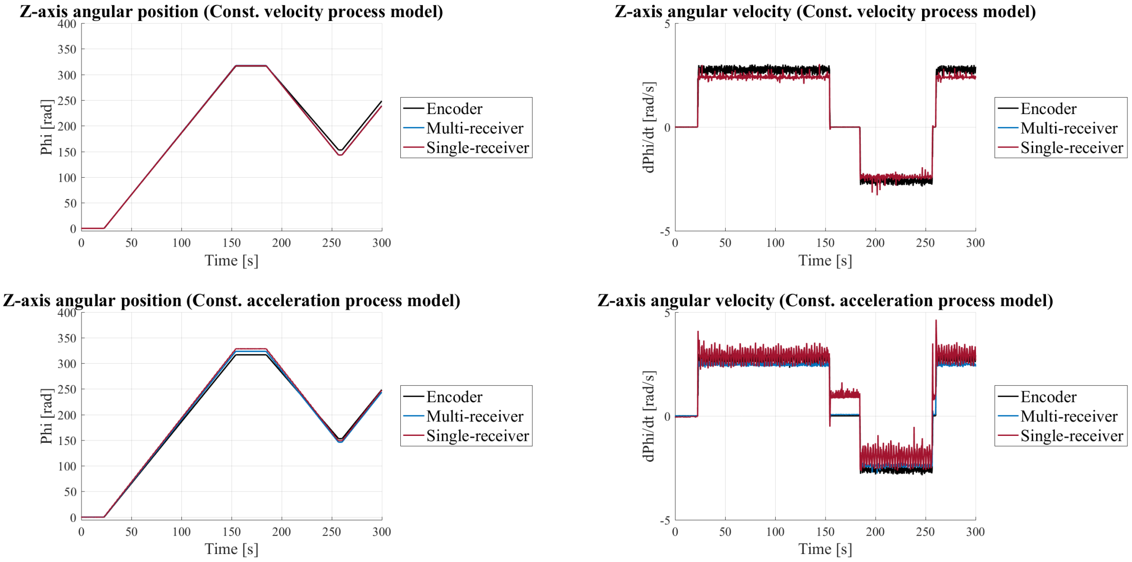

**Figure 7.17:** Plots of the estimated angular position (left) and angular velocity (right) of $S_2$ about z-axis of $S_1$. Data points of the first and second row of plots are obtained from the $S_2$ positioning filter using the constant velocity and constant acceleration process model respectively. Each plot provides the comparison between the *single-receiver* and the *multi-receiver* filter performances.

In Figure 7.17, the estimated angular positions and velocities of $S_2$ along the z-axis of $S_1$ (that is the axis of the output shaft) from both the *DGPS/MEMS-IMU single-receiver* and the *DGPS/MEMS-IMU multi-receiver* fusion MOCAP system are plotted against the true data obtained from the encoder. This compares the *DGPS/MEMS-IMU single-receiver* and the *DGPS/MEMS-IMU multi-receiver* MOCAP system and the fairness of the comparison was ensured by feeding the same process and measurement noise covariances to both filters.

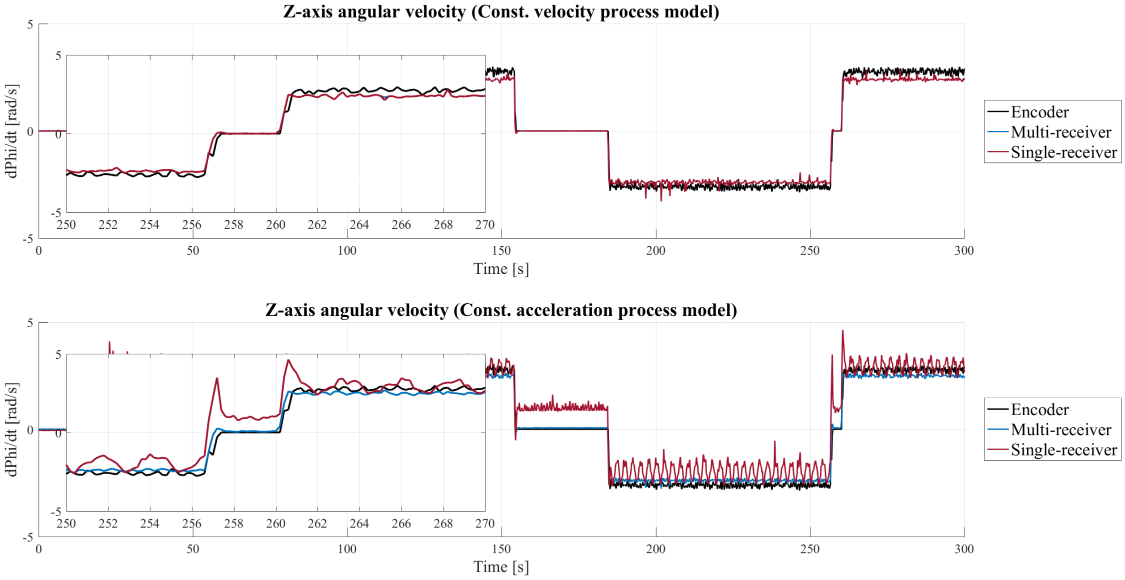

**Figure 7.18:** Plots of the estimated angular velocity of $S_2$ about z-axis of $S_1$ between 250$s$ and 270 when the instantaneous stop and turns occurred. Data points of the first and second row of plots are obtained from the $S_2$ positioning filter using the constant velocity and constant acceleration process model respectively.

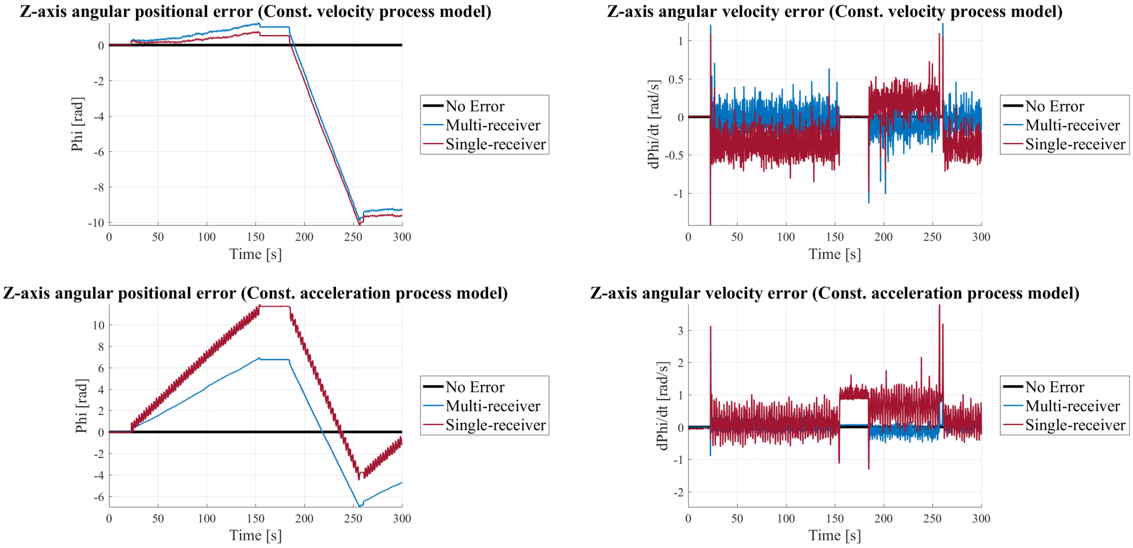

**Figure 7.19:** Plots of the error in the estimated angular position (left) and angular velocity (right) of $S_2$ about z-axis of $S_1$. Data points of the first and second row of plots are obtained from the $S_2$ positioning filter using the constant velocity and constant acceleration process model respectively. Each plot provides the comparison between the single-receiver and the multi-receiver filter performances.

In Figure 7.17, it was observed that the single-receiver system suffers from noise with higher magnitude and experiences greater overshoots during instantaneous stops and turns. This observation is more evident in Figures 7.18 and 7.19. Figure 7.18 gives different perspective of Figure 7.17 and shows the response of the filter when instantaneous stops and turns occur. Figure 7.19 is a plot of the error in the estimated angular positions and velocities of $S_2$ along the z-axis of $S_1$.

The performance of the $S_2$ was quantitatively evaluated by calculating the RMS error in the estimation. Table 7.3 provides a clear comparison of the RMS error between the *DGPS/MEMS-IMU single-receiver* and *DGPS/MEMS-IMU multi-receiver* MOCAP system and between the two process models: the constant velocity and constant acceleration. The RMS errors were calculated based on the error in the estimation of the $S_2$ position during five experiments. Each experiment lasted approximately 4 minutes which is equivalent to the acquisition of approximately 1200 raw GPS observables and 60000 MEMS-IMU measurements.

**Table 7.3:** A summary of the RMS error evaluated to assess the performance of the state estimation algorithm of the $S_2$ positioning filter

| **Measurement** | **Process model** | **RMS error** | | | |
|---|---|---|---|---|---|
| **Angular position [rad]** | | $\phi$ | $\theta$ | $\psi$ | **overall** |
| multi-receiver | const. velocity | 0.0002 | 0.0230 | 5.6003 | 3.2334 |
| single-receiver | const. velocity | 3.5153 | 0.0223 | 5.7310 | 3.8817 |
| multi-receiver | const. acceleration | 0.0000 | 0.0000 | 4.0836 | 2.3576 |
| single-receiver | const. acceleration | 0.0000 | 0.0000 | 5.0161 | 2.8961 |
| **Angular velocity [rad/s]** | | $d\phi/dt$ | $d\theta/dt$ | $d\psi/dt$ | **overall** |
| multi-receiver | const. velocity | 0.1282 | 0.0000 | 0.1455 | 0.2473 |
| single-receiver | const. velocity | 1.3900 | 0.0000 | 0.2704 | 0.8176 |
| multi-receiver | const. acceleration | 0.0000 | 0.0000 | 0.1502 | 0.1393 |
| single-receiver | const. acceleration | 0.0000 | 0.0000 | 0.5092 | 0.2940 |
| **ENU [m]** | | **overall** | | | |
| multi-receiver | const. velocity | 0.0007390 | | | |
| single-receiver | const. velocity | 0.0007477 | | | |
| multi-receiver | const. acceleration | 0.0006497 | | | |
| single-receiver | const. acceleration | 0.0006918 | | | |

# Chapter 8

# Discussion

A MOCAP system is a tool that allows the researchers to analyse the gait of an animal quantitatively and it is used extensively in the field of medicine, sport science, bio-mimicry and robotics as well as animation. To date, there exists no MOCAP system that allows accurate tracking of the absolute positions of the limb segments of an animal during its encounter with other animals in an outdoor environment.

The outdoor environment refers to an environment that is less restrictive than an indoor laboratory environment with undefined capture volume and uncontrolled environmental condition. Moreover, literature suggest that the accuracy of existing MOCAP systems decreases during the reconstruction of highly dynamic transient locomotion, limiting studies to analysis of steady-state locomotion.

As a result, this research aimed to develop a MOCAP system that can track the steady-state and transient locomotion of an animal in the outdoor environment. This allows the researchers to conduct kinematic and kinetic analysis of an animal gait. Based on the literature review, it was hypothesised that a DGPS/MEMS-IMU fusion MOCAP system has potential to meet the aim of the research.

A DGPS/MEMS-IMU fusion MOCAP system was previously implemented by Brodie et al. [46], Supej [47] and Gilgien et al. [48]. Supej [47] fused a Real Time Kinematic (RTK) to an inertial MOCAP system to obtain a global horizontal and vertical trajectory accuracy of $10 \pm 0.5mm$ and $20 \pm 0.5mm$ respectively. Unfortunately, the absolute positional accuracy of each limb segment was not quantitatively validated.

This research aimed to study the benefit of integrating an inertial MOCAP system and DGPS on each limb segment of interest. No literature has yet covered this. Development of the proposed the *DGPS/MEMS-IMU multi-receiver* fusion MOCAP system occurred in two stages, namely the development of the device and then the development of the state estimation algorithm as explained in Chapter 5.

## 8.1 Sensor Development

The device which includes a base station and an array of time-synchronized sensors was developed in Chapter 6. The device collected an unsaturated and uncorrupted indirect motion measurements such as the MEMS-IMU measurements and raw GPS observables. These measurements were then used in the state estimation algorithm to estimate the kinematic quantities of the limb segments of interest.

Extensive hardware and firmware technical specifications were developed in Chapter 6 to reduce the number of design iterations. This was because of the limited time and budget restrictions. The technical specifications included but were not limited to the measurement range, sampling frequency and non-volatile memory capacity. Based on the technical specifications, the acceptance testing procedure was developed which was followed during the testing of the assembled device.

An acceptance testing procedure was conducted as demonstrated in Chapter 6. The eight fully assembled sensors saved the IMU measurements and raw GPS observables onto their microSD cards successfully without the problem of data corruption, loss and measurement saturation. The array of sensors were synchronized with mean latency of $145.0 \pm 17.01 ns$ which translates to a loss of $3.132 \pm 0.3672 s$ over 6 hours of MOCAP. This transfers to a maximum loss of 0.017% of tracking time.

The developed device satisfied the user, functional and technical specifications as well as the established sensor attributes. Moreover, it was deemed more accessible to individuals and small organizations in terms of cost than the commercial inertial MOCAP products. For instance, it was found in Chapter 2 that the *Xsens Technologies* inertial MOCAP kit for full-body tracking costs EUR 52,140.00 (R 837,745.77 at EUR 1.00 to R 16.07 currency rate) whilst it costs R 22122.83 to fabricate and assemble a device consisting of 12 time-synchronized sensors for full body tracking.[1]

## 8.2 State Estimation Algorithm Development

The Kalman-based state estimation algorithm was developed with the hybrid coupling architecture. A mechanical rig was built and used to assess and validate the developed system because a gold-standard commercial optical MOCAP system such as the *PhaseSpace* and *Vicon* optical MOCAP systems was not available. The mechanical rig was limited to a simulation of the motion of a single limb segment about its joint with one degree of freedom. Using the developed fusion MOCAP system, the following research questions were answered:

---

[1] See Appendix G for pricing.

1. Does integration of Global Positioning Systems (GPS) or Differential Global Positioning Systems (DGPS) improve the applicability and/or performance of the traditional Micro Electro Mechanical Systems (MEMS)-Inertial Measurement Units (IMU) MOCAP system?
2. Is it possible to achieve the positional accuracy of the existing commercial MOCAP systems using a DGPS/MEMS-IMU integrated fusion MOCAP system?
3. Is integration of DGPS on each limb segment beneficial compared to the MEMS-IMU MOCAP system with a single DGPS?

The $S_1$ positioning filter was used to compare the accuracy in the estimation of the position of a point mass of the MEMS-IMU and the DGPS/MEMS-IMU MOCAP system. Using the measurements collected from the 5271.2 seconds long experiment, the motion tracking with the MEMS-IMU measurements only was more influenced by the non-repetitive and unstable errors such as drift and an offset error than the motion tracking with the DGPS/MEMS-IMU measurements. This is evident in Figure 8.1 where the significance of the drift in the estimated trajectory output of $S_1$ from the *MEMS-IMU* MOCAP system can be observed.

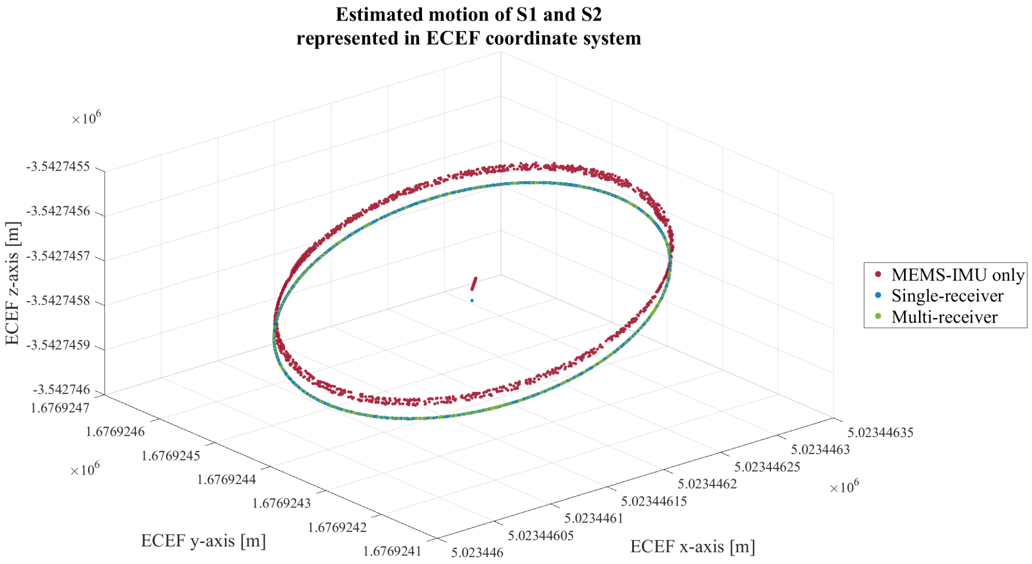

**Figure 8.1:** A plot of the estimated trajectory of $S_1$ and $S_2$ represented in the ECEF coordinate system from the *MEMS-IMU*, *DGPS/MEMS-IMU single-receiver* and the *DGPS/MEMS-IMU multi-receiver* MOCAP system.

The developed *DGPS/MEMS-IMU multi-receiver* fusion MOCAP system was capable of providing global trajectory information ($S_1$ positioning filter) whereas the *MEMS-IMU* MOCAP system could not. The accuracy of the global trajectory information was influenced by the correctness in the process model. The final tuned smoothing filter with a constant acceleration model provided a global trajectory RMS error of $\pm 39.4mm$ with the horizontal RMS error of $\pm 3.10mm$ and vertical RMS error of $\pm 52.3mm$.

The accuracy of the global trajectory information obtained from the developed *DGPS/MEMS-IMU multi-receiver* fusion MOCAP system is worse than the dual-frequency multi-constellation RTK implemented by Supej in [47]. This result was anticipated because the developed *DGPS/MEMS-IMU multi-receiver* fusion MOCAP system was limited to a single-frequency DGPS.

In [48], Gilgien et al. compared different GNSS methods on positioning accuracy for global trajectory determination application. They observed that at an elevation angle of $30^\circ$, single-frequency DGPS had a standard deviation of $1.37m$ whilst dual-frequency multi-constellation had a standard deviation of $0.01m$. Moreover, at an elevation angle of $30^\circ$, single-frequency DGPS took $51.54 \pm 46.54s$ to fix whilst dual-frequency multi-constellation took $0.06 \pm 0.06s$.

The performance of the two fusion MOCAP systems, namely the *DGPS/MEMS-IMU single-receiver* and the *DGPS/MEMS-IMU multi-receiver* fusion MOCAP system, were evaluated to analyse the benefit in attaching a GPS receiver on every limb segment. The *single-receiver* system fused single set of raw GPS observables from an array of $N$ sensors and the *multi-receiver* system fused all $N$ sets of raw GPS observables.

Similar to the accuracy of the estimated global trajectory, the accuracy in tracking of the limb segments was influenced by the correctness of the implemented process model. The analytical cost function for the estimated ENU coordinates, angular position and angular velocity of $S_2$ relative to the $S_1$'s body frame of the *DGPS/MEMS-IMU multi-receiver* fusion MOCAP system were better than the *single-receiver* system, regardless of the implemented process model.

The estimated angular position and angular velocity of $S_2$ relative to the $S_1$'s body frame as well as the overall ENU coordinates were evaluated to have a RMS error of $2.3576^\circ$, $0.1393^\circ/s$ and $0.6497mm$ respectively. The *DGPS/MEMS-IMU single-receiver* MOCAP system was assessed to have the higher RMS error of $2.8961^\circ$, $0.2940^\circ/s$ and $0.6918mm$ in the estimated angular position, angular velocity and the overall ENU coordinates respectively. The *DGPS/MEMS-IMU single-receiver* MOCAP system responded instantaneous change in motion with higher overshoots than the *DGPS/MEMS-IMU multi-receiver* MOCAP system. *DGPS/MEMS-IMU multi-receiver* MOCAP system can track transient locomotion better than the *DGPS/MEMS-IMU single-receiver* MOCAP system.

Despite the achievement of the sub-millimetre accuracy (of a gold-standard optical MOCAP system), the developed *DGPS/MEMS-IMU multi-receiver* MOCAP system was not comparable to the commercial inertial MOCAP system from *Xsens Technologies*. The *Xsens Technologies* inertial MOCAP system has the roll/pitch and heading angular positional RMS error of $0.75^\circ$ and $1.5^\circ$ respectively.

The unavailability of the commercial gold-standard optical MOCAP system; the restricted project time and limited budget forced the use of the mechanical rig which has limited motion. Considering that the surveyed true data had a standard deviation of $0.699m$ and the encoder data had a resolution of $0.72^\circ/pulse$, the evaluation and validation processes were further restricted by the use of true data obtained from a surveying process and an encoder.

Additionally, the developed state estimation algorithm had the following prerequisites for implementation:

1. Understanding of the system;
2. Analysis of the process and measurement noise covariance;
3. Availability of the unsaturated and uncorrupted measurements.

On top of above-mentioned prerequisites, the developed state estimation algorithm required post-tuning to improve the absolute position tracking accuracy. It was strictly limited to post-processing due to the implementation of the optimal smoother.

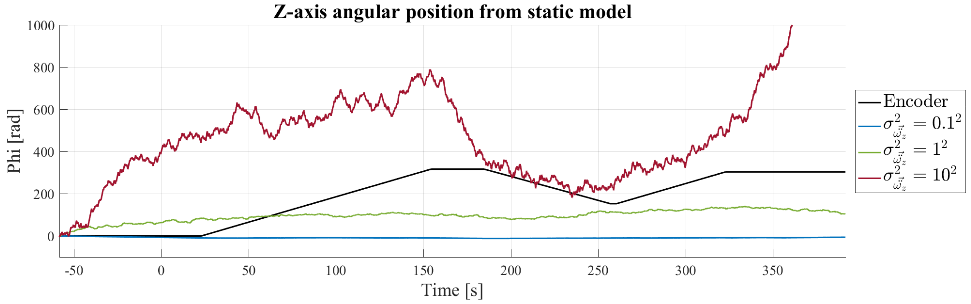

**(a)** Plots of the estimated angular position of $S_2$ about the z-axis of $S_1$. Data points were obtained from the $S_2$ positioning filter using the static process model with process model covariance varying from $0.1^2 rad^s/s^s$ to $10^2 rad^s/s^s$

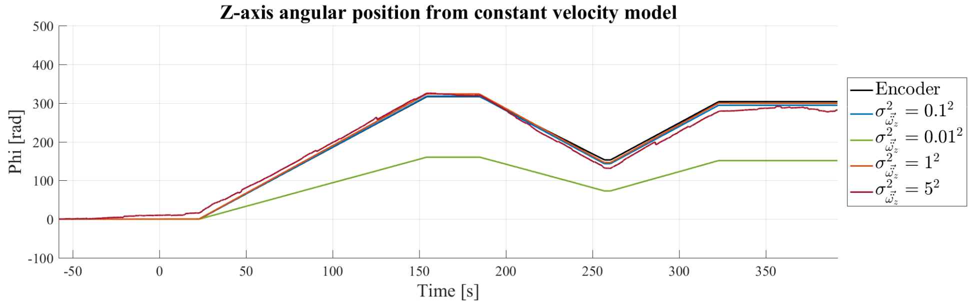

**(b)** Plots of the estimated angular position of $S_2$ about the z-axis of $S_1$. Data points were obtained from the $S_2$ positioning filter using the constant velocity process model with process model covariance varying from $0.01^2 rad^s/s^s$ to $5^2 rad^s/s^s$

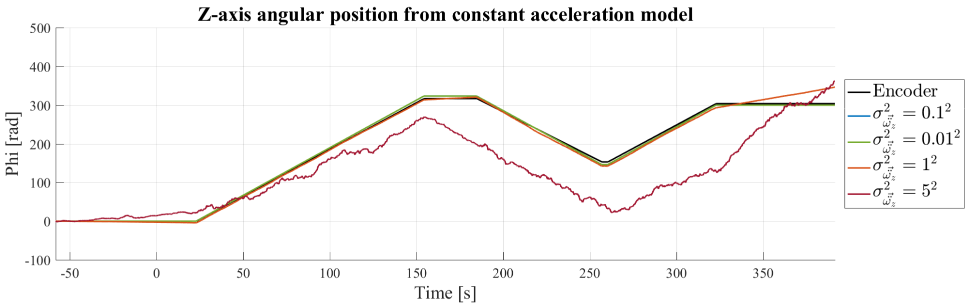

**(c)** Plots of the estimated angular position of $S_2$ about the z-axis of $S_1$. Data points were obtained from the $S_2$ positioning filter using the constant acceleration process model with process model covariance varying from $0.01^2 rad^s/s^s$ to $5^2 rad^s/s^s$

**Figure 8.2:** Plots of the estimated angular position of $S_2$ about z-axis of $S_1$ for different process models with varying process model covariance.

The significance of the post-tuning process, depicted in Figure 8.2, shows that the accuracy of the state estimation algorithm depends on both the employed process model and its covariance. The static, constant velocity and constant acceleration process models with varying process covariance were employed during the estimation of the angular position of $S_2$ about the z-axis of $S_1$. It was plotted in Figure 8.2a, Figure 8.2b and Figure 8.2c respectively.

In Figure 8.2a, the static process model was employed to estimate angular position of $S_2$ about z-axis of $S_1$. The output did not resemble the true data even with a increase in the process model covariance. Worse, with increase in the process model covariance (that means a higher confidence level in the precision of the measurements than the process transition function), the estimated output inherited more noise from the MEMS-IMU measurements.

In Figure 8.2b and 8.2c, the constant velocity and a constant acceleration process model were employed respectively. The accuracy in the estimated angular position of $S_2$ about the z-axis of $S_1$ decreased as the process covariance deviated from $0.1^2 rad^s/s^s$. This highlights the necessity of post-tuning.

Unlike the case in Figure 8.2a and Figure 8.2c, the estimated angular positions of $S_2$ about z-axis of $S_1$ in Figure 8.2b closely resembled the shape of the true data despite the variation in the process model covariance from $0.01^2 rad^s/s^s$ to $5^2 rad^s/s^s$. Knowing that $S_2$ rotated about z-axis of $S_1$ at constant angular velocity except during the abrupt stops and turns, this highlights that the accuracy of the state estimation algorithm improves as the employed process model resembles the true system.

# Chapter 9

# Conclusions and Recommendations

The *DGPS/MEMS-IMU multi-receiver* fusion MOCAP system was developed to provide future researchers with a method to capture the motion of a terrestrial *megafauna* accurately in an outdoor environment. The outdoor environment is less-restrictive than the laboratory environment with undefined capture volume and uncontrolled environmental conditions. In the course of the development, the research questions stated in Chapter 1 were answered as follows:

1. The non-optical inertial MOCAP system has advantage over other traditional MOCAP systems in capturing the motion of a subject in an outdoor environment. However, the inertial system cannot provide global trajectory of the subject for kinetic analysis and its accuracy decreases during tracking of the transient locomotion.
2. A fusion MOCAP system which integrates the navigational information of a subject to the traditional inertial MOCAP system is capable of estimating the global trajectory of the subject. Hence it has better applicability than the non-optical inertial MOCAP system.
3. It is possible to achieve the positional accuracy of a gold-standard commercial MOCAP system using a DGPS/MEMS-IMU fusion MOCAP system.
4. It is beneficial to integrate raw GPS observables from each limb segment. It is observed that the *DGPS/MEMS-IMU multi-receiver* MOCAP system responds better to instantaneous change in motion and can estimate transient locomotion better than the *DGPS/MEMS-IMU single-receiver* MOCAP system.

The results in Chapters 6 and 7, discussed in Chapter 8, show that the *DGPS/MEMS-IMU multi-receiver* fusion MOCAP system achieved comparable sub-millimetre accuracy as the commercial optical MOCAP system. The accuracy was evaluated using true data obtained from a surveying process and an encoder.

To date, no researchers have quantitatively analysed the steady-state and transient locomotion of a terrestrial *megafauna* in an outdoor environment. Consequently, the motion of a terrestrial *megafauna* during its encounter with other animals or in its natural habitat has not been quantitatively analysed. This research has developed a first version of the *DGPS/MEMS-IMU multi-receiver* fusion MOCAP system that is more accessible than the existing commercial MOCAP systems and reduces the existing limitations and constraints in the kinematic and kinetic analysis of the animal gait.

The research did not include the development of the sensor strapped-down system. Strict sensor size and weight specifications were removed during the development process because the need for an operational prototype was a higher priority considering the limitations and constraints mentioned in Chapter 1. Therefore, with the vision to use the developed fusion MOCAP system to track the motion of a wild terrestrial *megafauna* in its natural habitat, following recommendations are made:

## 9.1 Re-design of the Device

The device in its current state (version 1) is physically too large and rigid for its intended purpose on a wild terrestrial *megafauna*. Therefore, it is recommended to reconsider the sensor size and weight requirements in the next iteration of the design. Furthermore, investigation into a sensor strapped down system is recommended to minimize the sensor rotation about its own axis during the MOCAP.

A replacement of the single-frequency DGPS with the multi-frequency DGNSS is also recommended in th enext iteration of the design. This is because the accuracy and convergence rate of the global trajectory estimation using a multi-frequency DGNSS is better than a single-frequency DGPS [48].

## 9.2 Investigation Into Optimal LAMBDA Method

The LAMBDA method, developed in [101], was cascaded with the EKFs, as it can be seen from Figure 7.2 in Chapter 7. The decision to include the LAMBDA method was based on the literature review and its usage in the *RTKLIB* [139] and the *goGPS* [105].

However, no research was conducted to analyse the benefit of including the LAMBDA method in the developed fusion MOCAP system during as this was outside the scope of this project. Therefore, it is recommended to conduct the research to:

1. Determine the correctness of the LAMBDA method;
2. Understand the advantages and disadvantages of different types of LAMBDA methods;
3. Analyse the benefit of including the LAMBDA method in the developed fusion MOCAP system.

## 9.3 Investigation Into Precise Observation Models

The GPS SD and DD observation models were derived based on the following assumptions:

- The same signal propagation error is assumed for all receivers positioned in a spatially closed system;
- The same receiver clock error and the hardware delay error are assumed for all receivers manufactured by the same manufacturers.

It was found in Chapter 3 that the UERE of the ionospheric delays, tropospheric delays and the receiver error are $\pm 5m$, $\pm 0.5m$ and $\pm 0.3m$ respectively, with the standard deviation of the UERE for civilian (coarse/acquisition) code observables ($3\sigma_R C/A$) being $\pm 6.7m$. From these figures, it is inferred that the minor errors in the GPS DD observation models compound the errors in the estimated global trajectory of the subject. Therefore, it is recommended to characterise the signal propagation error and the receiver error to obtain more precise DD observation models.

# Bibliography

[1] A. Sant'Anna, "A symbolic approach to human motion analysis using inertial sensors: Framework and gait analysis study," Ph.D. dissertation, Högskolan i Halmstad, Sweden, 2012. [Online]. Available: http://hh.diva-portal.org/smash/get/diva2:516246/FULLTEXT02.pdf

[2] T. Nath, A. Mathis, A. Chen, A. Patel, M. Bethge, and M. Mathis, "Using deeplabcut for 3d markerless pose estimation across species and behaviors," *Nature Protocols*, vol. 14, no. 7, pp. 2152–2176, Jun. 2019.

[3] (2019) Bosch mems sensors. [Online]. Available: https://www.mordorintelligence.com/industry-reports/3d-motion-capture-market.

[4] "(an4399) high-precision calibration of a three-axis accelerometer," Freescale Semiconductor, Austin, Texas, United States.

[5] G. Welch and G. Bishop, "An introduction to the kalman filter," unpublished.

[6] N. Inc., *An Introduction to GNSS*. Calgary, AB., Canada: NovAtel Inc., 2010.

[7] G. Blewitt, *Basics of the GPS Technique: Observation Equations*. In Geodetic Applications of GPS, 1997.

[8] M. Vitus, "Carrier phase techniques," 2005.

[9] "(ds-000189) icm-20948: Small, world's lowest power 9-axis mems motiontracking device," InvenSense, California, United States.

[10] "(ps-mpu-9250a-01) mpu-9250: Product specification," InvenSense, California, United States.

[11] "(slva680) esd protection layout guide," Texas Instruments, Dallas, Texas.

[12] "(spe-12-8-024) aa.105.301111: Titan gps antenna aa.105," Taoglas Ltd., Wexford, Ireland.

[13] Analytic Sciences Corporation. Technical Staff, Analytic Sciences Corporation, *Applied Optimal Estimation*. Cambridge, Massachusetts, United States: MIT Press, 1974.

[14] "(bst-bmx055-ds000-01) bmx055: Small, versatile 9-axis sensor module," Bosch Sensortec, Reutlingen, Germany.

[15] A. Al-Fuqaha, “Wireless personal area networks (wpans),” unpublished.

[16] A. Kornhauser, “Global navigation satellite system (gnss),” unpublished.

[17] GALILEO, “Mission high level definition (hld),” European Commission and European Space Agency (Intergovernmental), Paris, France, Tech. Rep., Apr. 2001.

[18] S. Radicella, B. Nava, and P. Coïsson, “Ionospheric models for gnss single frequency range delay corrections,” *Fisica de la Tierra*, vol. 20, pp. 27–39, Jun. 2008.

[19] P. Teunissen, P. Joosten, and C. Tiberius, “A comparison of tcar, cir and lambda gnss ambiguity resolution,” in *15th International Technical Meeting of the Satellite Division of the Institute of Navigation*, Portland, Oregon, Sep. 2002.

[20] (2017) Battery university - what’s the best battery? [Online]. Available: https://batteryuniversity.com/learn/archive/whats_the_best_battery.

[21] “(brstm320218) stm32 32-bit mcu family - leading supplier of arm cortex-m microcontrollers,” STMicroelectronics, Geneva, Switzerland.

[22] (2019) Trax - capabilities. [Online]. Available: https://www.trax.co.za/capabilities

[23] A. M. de-la Herran, B. Garcia-Zapirain, and A. Mendez-Zorrilla, “Gait analysis methods: An overview of wearable and non-wearable systems, highlighting clinical applications,” *Sports Technology*, vol. 14, no. 2, pp. 3362–3394, Feb. 2014.

[24] W. Taylor, M. Heller, G. Bergmann, and G. Duda, “Tibio-femoral loading during human gait and stair climbing,” *Journal of Orthopaedic Research*, vol. 22, no. 3, pp. 625–632, May 2004.

[25] S. Savic, G. Devedzic, B.Ristic, A. Matic, N. Prodanovic, and R. Stojanovic, “Clinical application of a portable motion capture system: A methodology,” in *2018 7th Mediterranean Conference on Embedded Computing (MECO)*, Budva, Montenegro, Jun. 2018.

[26] Dharmayanti, M. Iqbal, A. Suhendra, and A. Mutiara, “Velocity and acceleration analysis from kinematics linear punch using optical motion capture,” in *2017 Second International Conference on Informatics and Computing (ICIC)*, Jayapura, Indonesia, Feb. 2018.

[27] B. Pueo and J. Jimenez-Olmedo, “Application of motion capture technology for sport performance analysis,” *Retos: nuevas tendencias en educación física, deporte y recreación*, vol. 32, pp. 241–247, Jul. 2017.

[28] Y. Adesida, E. Papi, and A. McGregor, “Exploring the role of wearable technology in sport kinematics and kinetics: A systematic review,” *Sensors (Basel)*, vol. 19, no. 7, Apr. 2019.

[29] M. Supej and H. Holmberg, “Recent kinematic and kinetic advances in olympic alpine skiing: Pyeongchang and beyond,” *frontiers in Physiology*, vol. 10, p. 111, Feb. 2019.

[30] A. Patel and M. Braae, "Rapid turning at high-speed: Inspirations from the cheetah's tail," in *2013 IEEE/RSJ International Conference on Intelligent Robots and Systems*, Tokyo, Japan, Nov. 2013, pp. 5506–5511.

[31] C. Fisher and A. Patel, "Preparation of papers for ifac conferences & symposia: Flipbot: A lizard inspired stunt robot," *IFAC Proceedings Volumes*, vol. 47, no. 3, pp. 4837–4842, 2014.

[32] D. Gong, L. Fu, G. Zuo, and Y. Du, "Motion capture data reveal the important role of waist flexibility in human gait," in *2015 IEEE International Conference on Cyber Technology in Automation, Control, and Intelligent Systems (CYBER)*, Shenyang, China, Jun. 2015, pp. 1864–1868.

[33] R. Yunardi and Winarno, "Marker-based motion capture for measuring joint kinematics in leg swing simulator," in *2017 5th International Conference on Instrumentation, Control, and Automation (ICA)*, Yogyakarta, Indonesia, Aug. 2017.

[34] R. Yunardi, A. Firdaus, E. Agustin, and Pujiyanto, "Implementation of motion capture system for trajectory planning of leg swing simulator," in *2017 International Seminar on Sensors, Instrumentation, Measurement and Metrology (ISSIMM)*, Surabaya, Indonesia, Dec. 2017.

[35] R. Arai and K. Murakami, "Hierarchical human motion recognition by using motion capture system," in *2018 International Workshop on Advanced Image Technology (IWAIT)*, Chiang Mai, Thailand, Jan. 2018.

[36] F. Attal, S. Mohammed, M. Dedabrishvili, F. Chamroukhi, L. Oukhellou, and Y. Amirat1, "Physical human activity recognition using wearable sensors," *Sensors (Basel)*, vol. 15, no. 12, p. 31314–31338, Dec. 2015.

[37] H. Rahmani and A. Mian, "3d action recognition from novel viewpoints," in *2016 IEEE Conference on Computer Vision and Pattern Recognition (CVPR)*, Las Vegas, NV, USA, Jun. 2016.

[38] Muhtadin, S. Sumpeno, and A. Dyaksa, "Affective human pose classification from optical motion capture," in *2017 International Seminar on Intelligent Technology and Its Applications (ISITIA)*, Surabaya, Indonesia, Aug. 2017.

[39] X. Meng, J. Pan, and H. Qin, "Motion capture and retargeting of fish by monocular camera," in *2017 International Conference on Cyberworlds (CW)*, Chester, UK, Sep. 2017.

[40] M. Chuang, J. Hwang, K. Williams, and R. Towler, "Tracking live fish from low-contrast and low-frame-rate stereo videos," *IEEE Transactions on Circuits and Systems for Video Technology*, vol. 25, pp. 167–179, Jan. 2014.

[41] L. Egorova and A. Lavrov, "Determination of workspace for motion capture using kinect," Riga, Latvia, Dec. 2015.

[42] M. Kagaya, S. Tanaka, H. Matsui, and T. Moriya, “Visualization technique of maintenance work with a motion capture sensor,” in *2016 International Symposium on Semiconductor Manufacturing (ISSM)*, Tokyo, Japan, Dec. 2016.

[43] E. van der Kruk and M. Reijne, “Accuracy of human motion capture systems for sport applications; state-of-the-art review,” *Retos: nuevas tendencias en educación física, deporte y recreación*, vol. 18, no. 6, pp. 806–819, May 2018.

[44] J. Wilson, M. Mills, R. Wilson, G. P. M. Mills, J. Speakman, S. Durant, N. Bennett, N. Marks, and M. Scantlebury, “Cheetahs, acinonyx jubatus, balance turn capacity with pace when chasing prey,” *Biology Letters*, vol. 9, no. 5, Jun. 2013.

[45] J. Wilson, L. Lowe, K. Rowskilly, P. Hudson, K. Golabek, and J. McNutt, “Locomotion dynamics of hunting in wild cheetahs,” *Nature*, vol. 498, pp. 185–189, 2013.

[46] M. Brodie, A. Walmsley1, and W. Page, “Fusion motion capture: A prototype system using inertial measurement units and gps for the biomechanical analysis of ski racing,” *Sports Technology*, vol. 1, pp. 17–28, Jan. 2008.

[47] M. Supej, “3d measurements of alpine skiing with an inertial sensor motion capture suit and gnss rtk system,” *Journal of Sports Science*, vol. 28, no. 7, pp. 759–769, May 2010.

[48] M. Gilgien, J. S. rri, J. Chardonnens, J. Kröll, and E. Müller, “Determination of external forces in alpine skiing using a differential global navigation satellite system,” *Sensors (Basel)*, vol. 13, no. 8, pp. 9821–9835, Aug. 2013.

[49] T. Seel, J. Raisch, and T. Schauer, “Imu-based joint angle measurement for gait analysis,” *Sensors (Basel)*, vol. 14, no. 4, pp. 6891–6909, Apr. 2014.

[50] G. Logar and M. Munih, “Estimation of joint forces and moments for the in-run and take-off in ski jumping based on measurements with wearable inertial sensors,” *Sensors (Basel)*, vol. 15, no. 5, pp. 11 258–11 276, May 2015.

[51] A. Karatsidis, G. Bellusci, M. Schepers, M. de Zee, M. Andersen, and P. Veltink, “Estimation of ground reaction forces and moments during gait using only inertial motion capture,” *Sensors (Basel)*, vol. 17, no. 1, Jan. 2017.

[52] N. Mostashiri, J. Dhupia, A. Verl, and W. Xu, “A novel spatial mandibular motion-capture system based on planar fiducial markers,” *IEEE Sensors Journal*, vol. 18, pp. 10 096–10 104, Dec. 2018.

[53] D. Vlasic, R. Adelsberger, G. Vannucci, J. Barnwell, M. H. Gross, W. Matusik, and J. Popovic, “Practical motion capture in everyday surroundings,” *ACM Trans. Graph.*, vol. 26, no. 3, p. 35, Jul. 2007.

[54] L. Xu, Y. Liu, W. Cheng, K. Guo, G. Zhou, Q. Dai, and L. Fang, “Flycap: Markerless motion capture using multiple autonomous flying cameras,” *IEEE Transaction on Visualization and Computer Graphics*, vol. 24, no. 8, pp. 2284–2297, Aug. 2018.

[55] G. B. Guerra-filho, “Optical motion capture: Theory and implementation,” *Journal of Theoretical and Applied Informatics (RITA)*, vol. 12, pp. 61–89, Jan. 2005.

[56] (2018) 3d motion capture market - growth, trends, and forecast (2019–2024). [Online]. Available: https://www.mordorintelligence.com/industry-reports/3d-motion-capture-market.

[57] (2019) Phasespace - 3d character creation. [Online]. Available: http://phasespace.com/applications/3dcharactercreation.

[58] (2019) Vicon - biomechanics and sport. [Online]. Available: https://www.vicon.com/motion-capture/biomechanics-and-sport.

[59] L. Mündermann, S. Corazza, and T. Andriacchi, “The evolution of methods for the capture of human movement leading to markerless motion capture for biomechanical applications,” *Journal of NeuroEngineering and Rehabilitation*, pp. 3–6, Mar. 2006.

[60] A. Cappozzo, F. Catani, A. Leardini, M. Benedetti, and U. D. Croce, “Position and orientation in space of bones during movement: experimental artefacts,” *Clinical Biomechanics*, vol. 11, no. 2, pp. 90–100, Mar. 1996.

[61] A. Aurand, J. Dufour, and W. Marras, “Accuracy map of an optical motion capture system with 42 or 21 cameras in a large measurement volume,” *Journal of Biomechanics*, vol. 58, pp. 237–240, Jun. 2017.

[62] R. Tsai, “A versatile camera calibration technique for high-accuracy 3d machine vision metrology using off-the-shelf tv cameras and lenses,” *Computer Vision and Pattern Recognition (CVPR)*, vol. 3, no. 4, pp. 364–374, Jan. 1986.

[63] ——, “An efficient and accurate camera calibration technique for 3d machine vision,” *IEEE Journal on Robotics and Automation*, pp. 323–344, Aug. 1987.

[64] “(biwi-tr-263) quick guide to multi-camera self-calibration,” Computer Vision Lab, Swiss Federal Institute of Technology, Zürich, Switzerland.

[65] K. D. Ulhaas, “Robust optical user motion tracking using a kalman filter,” vol. 2, Jan. 2003.

[66] Q. Wu and P. Boulanger, “Real-time estimation of missing markers for reconstruction of human motion,” in *2011 XIII Symposium on Virtual Reality*, Uberlandia, Brazil, May 2011, pp. 161–168.

[67] A. Aristidou, J. Cameron, and J. Lasenby, “Real-time estimation of missing markers in human motion capture,” in *2008 2nd International Conference on Bioinformatics and Biomedical Engineering*, Shanghai, China, May 2008, pp. 1343–1346.

[68] U. Lugŕis, R. Vilela, E. Sanjurjo, F. Mouzo, and F. Michaud, “Implementation of an extended kalman filter for optical motion capture with real–time 3d visualization,” in *The 5th Joint International Conference on Multibody System Dynamics*, Lisboa, Portugal, Jun. 2018.

[69] B. Rosenhahn, C. Schmaltz, T. Brox, J. Weickert, D. Cremers, and H. Seidel, "Markerless motion capture of man-machine interaction," in *2008 IEEE Conference on Computer Vision and Pattern Recognition*, Anchorage, AK, USA, Jun. 2008, pp. 1063–6919.

[70] M. Perrott, T. Pizzari, J. Cook, and J. McClelland, "Comparison of lower limb and trunk kinematics between markerless and marker-based motion capture systems," *Gait & Posture*, vol. 52, pp. 57–61, Feb. 2017.

[71] E. Ceseracciu, Z. Sawacha, and C. Cobelli, "Comparison of markerless and marker-based motion capture technologies through simultaneous data collection during gait: Proof of concept," *PLOS one*, vol. 9, no. 3, p. e87640, Mar. 2014.

[72] D. Takahashi. (2011) Organic motion launches new platform to capture motion. Internet article. [Online]. Available: https://venturebeat.com/2011/08/09/organic-motion-launches-new-platform-to-capture-motion.

[73] E. Volná, M. Kotyrba, and R. Jarusek, "Acoustic signal processing via neural network towards motion capture systems," 2013.

[74] P. Nogueira, "Motion capture fundamentals a critical and comparative analysis on real-world applications," 2012.

[75] (2019) Metamotion gypsy technology. [Online]. Available: https://metamotion.com/gypsy/gypsy-motion-capture-system-mocap.htm.

[76] (2019) Xsens - customer cases. [Online]. Available: https://www.xsens.com/customer-cases.

[77] (2019) Notch. [Online]. Available: https://wearnotch.com.

[78] M. Lapinski, E. Berkson, T. Gill, and M. R. J. Paradiso, "A distributed wearable, wireless sensor system for evaluating professional baseball pitchers and batters," in *2009 International Symposium on Wearable Computers*, Linz, Austria, Sep. 2009.

[79] K. Cahill-Rowley and J. Rose, "Temporal–spatial reach parameters derived from inertial sensors: Comparison to 3d marker-based motion capture," *Journal of Biomechanics*, vol. 52, pp. 11–16, Feb. 2017.

[80] J. Lin, R. Zhang, J. Chen, L. Zeng, L. Jiang, S. McGrath, and J. Yang, "Using hybrid sensoring method for motion capture in volleyball techniques training," in *2018 Twelfth International Conference on Sensing Technology (ICST)*, Limerick, Ireland, Dec. 2018, pp. 217–222.

[81] H. Jung, M. Kim, and J. Lyou, "Realization of a hybrid human motion capture system," in *2017 17th International Conference on Control, Automation and Systems (ICCAS)*, Jeju, South Korea, Oct. 2017.

[82] A. Filippeschi, N. Schmitz, M. Miezal, G. Bleser, E. Ruffaldi, and D. Stricker, "Survey of motion tracking methods based on inertial sensors: A focus on upper limb human motion," *Sensors (Basel)*, vol. 17, no. 6, p. 1257, Jun. 2017.

[83] A. Piltan, M. Piltan, and R. Ghodsi, “Mems technology in automotive industry: Trends and applications,” in *1st International and 5th Conference for the Iranian Association of Management of Technology (IRAMOT)*, Tehran, Iran, Nov. 2011.

[84] M. Kok, J. Hol, and T. Schön, *Using Inertial Sensors for Postition and Orientation Estimation*. Foundations and Trends in Signal Processing, 2017, vol. 11, no. 1-2.

[85] T. Haslwanter, *3D Kinematics*. Cham, Switzerland: Springer International Publishing, 2018.

[86] N. Inc., *IMU Errors and Their Effects*. Calgary, AB., Canada: NovAtel Inc., 2014.

[87] M. Grewal and A. Andrews, *Kalman filtering: theory and practice using MATLAB*. New Jersey, United States: Wiley, 2001.

[88] H. Unbehauen, *Control Systems, Robotics and Automation – Volume VIII: Advanced Control Systems-II*. Paris, France.: EOLSS Publications, 2009.

[89] T. Lacey, “Tutorial: The kalman filter,” unpublished.

[90] J. Rodríguez, “On generalized signal waveforms for satellite navigation,” Ph.D. dissertation, Universität der Bundeswehr München, Germany, Jun. 2008. [Online]. Available: http://137.193.200.7:8081/doc/86167/86167.pdf

[91] N. Khojasteh, M. Jamshidi, E. Vahedi, and S. Telikani, “Introduction to global navigation satellite systems and its errors,” *International Academic Institute for Science and Technology*, vol. 3, no. 3, pp. 53–61, Mar. 2016.

[92] T. Schüler, “On ground-based gps tropospheric delay estimation,” Ph.D. dissertation, Universität der Bundeswehr München, Germany, Feb. 2001. [Online]. Available: https://athene-forschung.unibw.de/85231?sortfield0=year&sortfield1=&show_id=85240

[93] Y. Yao, Z. Sun, and C. Xu, “Establishment and evaluation of a new meteorological observation-based grid model for estimating zenith wet delay in ground-based global navigation satellite system (gnss),” *Remote Sens*, vol. 10, no. 11, p. 1718, Oct. 2018.

[94] (2019) European global navigation satellite systems agency (gsa) - what is sbas? [Online]. Available: https://www.gsa.europa.eu/european-gnss/what-gnss/what-sbas

[95] W. Gurtner and L. Estey, “Rinex the receiver independent exchange format version 3.01,” unpublished.

[96] S. Carcanague, “Low-cost gps/glonass precise positioning algorithm in constrained environment,” Ph.D. dissertation, Institut National Polytechnique de Toulouse, France, Mar. 2013. [Online]. Available: http://oatao.univ-toulouse.fr/9119/

[97] S. Zhao, X. Cui, F. Guan, and M. Lu, “A kalman filter-based short baseline rtk algorithm for single-frequency combination of gps and bds,” *Sensors (Basel)*, vol. 14, no. 8, pp. 15 415–15 433, Aug. 2014.

[98] K. O'Keefe, M. Petovello, W. Cao, G. Lachapelle, and E. Guyader, "Comparing multicarrier ambiguity resolution methods for geometry-based gps and galileo relative positioning and their application to low earth orbiting satellite attitude determination," *International Journal of Navigation and Observation*, p. 592073, 2009.

[99] P. Teunissen, "Least-squares estimation of the integer gps ambiguities," in *Invited lecture, section IV theory and methodology, IAG general meeting*, Beijing, China, Aug. 1993.

[100] S. Verhagen and B. Li, "Lambda software package: Matlab implementation, version 3.0," unpublished.

[101] P. Teunissen and S. Verhagen, "Integer aperture estimation - a framework for gnss ambiguity acceptance testing," *InsideGNSS*, vol. 9, pp. 66–73, Mar. 2011.

[102] *Altium Designer*, Altium Limited, San Diego, California, United States, 2001, version 18.

[103] *TrueSTUDIO for STM32*, Atollic, Jönköping, Sweden, 2018, version 9.0.0.

[104] *STM32IDE*, STMicroelectronics, Geneva, Switzerland, 2019.

[105] *goGPS*, goGPS Project, Politecnico di Milano, Como Campus, 2015, release v0.4.3.

[106] *MATLAB*, MathWorks, Natick, Massachusetts, United States, 1984, version 2016a.

[107] P. Hudson, S. Corr, R. Payne-Davis, S. Clancy, E. Lane, and A. Wilson, "Functional anatomy of the cheetah (acinonyx jubatus)hindlimb," *Journal of Anatomy*, vol. 218, no. 4, pp. 363–374, Apr. 2011.

[108] "(ubx-15031066) c94-m8p: u-blox rtk application board package," U-blox, Thalwil, Switzerland.

[109] E. Greve and D. Krause, "An assessment of methods to support the design of future robust modular product architectures," in *2018 15th International Design Conference (DESIGN)*, Cavtat, Dubrovnik, Croatia, May 2018, pp. 335–346.

[110] I.-T. .-S. 4, "Ergonomics of human-system interaction — part 210: Human-centred design for interactive systems," International Organization for Standardization, Standard 2, Jul. 2019.

[111] F. Salvador, "Toward a product system modularity construct: Literature review and reconceptualization," *IEEE Transactions on Engineering Management*, vol. 54, no. 2, pp. 219–240, May 2007.

[112] (2019) World meteorological organization global weather & climate extremes archive. [Online]. Available: https://wmo.asu.edu/content/world-meteorological-organization-global-weather-climate-extremes-archive

[113] C. C. Finlay and e. a. S. Maus, “International geomagnetic reference field: the eleventh generation,” *Geophysical Journal International*, vol. 183, no. 3, pp. 1216–1230, Dec. 2010.

[114] J. Lee and M. Choi, “Effect of strapdown integration order and sampling rate on imu-based attitude estimation accuracy,” *Sensors (Basel)*, vol. 18, no. 9, p. 2775, Aug. 2018.

[115] R. Langley, “Gps receiver system noise,” *GPS World*, vol. Innovation, Jun. 1997.

[116] “(gps-x-08014-a1) gps antennas: Rf design considerations for u-blox gps receivers,” U-blox, Thalwil, Switzerland.

[117] “(ubx-15025193) neo/lea-m8t: u-blox m8 concurrent gnss timing modules,” U-blox, Thalwil, Switzerland.

[118] “(docid022152) stm32f405xx stm32f407xx: Arm cortex-m4 32b mcu+fpu, 210dmips, up to 1mb flash/192+4kb ram, usb otg hs/fs, ethernet, 17 tims, 3 adcs, 15 comm. interfaces & camera,” STMicroelectronics, Geneva, Switzerland.

[119] C. Mikolajczak, M. Kahn, K. White, and R. Long, “Lithium-ion batteries hazard and use assessment,” Fire Protection Research Foundation, Standard, Jul. 2011.

[120] “(bst-bmx160-ds000-11) bmx160: Small, low power 9-axis sensor module,” Bosch Sensortec, Reutlingen, Germany.

[121] “(docid025715) lsm9ds1: inemo inertial module: 3d accelerometer, 3d gyroscope, 3d magnetometer,” STMicroelectronics, Geneva, Switzerland.

[122] “(ubx-15029985) neo-8q/neo-m8: u-blox 8/m8 gnss modules hardware integration manual,” U-blox, Thalwil, Switzerland.

[123] (2019) Particle - datasheets. [Online]. Available: https://docs.particle.io/datasheets/wi-fi/photon-datasheet.

[124] “(bst-dhw-fl021-00) bmx055 shuttle board,” Bosch Sensortec, Reutlingen, Germany.

[125] “(ubx-15024894) c94-m8p: u-blox rtk application board package,” U-blox, Thalwil, Switzerland.

[126] “(docid022204) stm32f4discovery: Discovery kit with stm32f407vg mcu,” STMicroelectronics, Geneva, Switzerland.

[127] “(rm0090) reference manual - stm32f405/415, stm32f407/417, stm32f427/437 and stm32f429/439 advanced arm based 32-bit mcus,” STMicroelectronics, Geneva, Switzerland.

[128] (2019) Fatfs - generic fat filesystem module. [Online]. Available: http://elm-chan.org/fsw/ff/00index_e.html.

[129] "Max17043/max17044: 1-cell/2-cell fuel gauge with modelgauge and low-battery alert," Maxim Integrated Products, Inc., California, United States.

[130] "(slvs067m) tlv2217: Low-dropout fixed-voltage regulators," Texas Instruments, Dallas, Texas.

[131] "(mb997) schematics - stm32f4discovery," STMicroelectronics, Geneva, Switzerland.

[132] W. Cochran, "Wildlife telemetry," in *Wildlife management techniques manual*, S. Schemnitz, Ed. Michigan, US: Wildlife Society, 1980.

[133] B. Carter, *Op Amps for Everyone*. Dallas, Texas: Texas Instruments., 2008.

[134] "(snla302) tlv2217: High-speed layout guidelines for reducing emi for lvds serdes designs," Texas Instruments, Dallas, Texas.

[135] "(szza009) pcb design guidelines for reduced emi," Texas Instruments, Dallas, Texas.

[136] "(slyp173) high speed pcb layout techniques," Texas Instruments, Dallas, Texas.

[137] G. Falco, M. Pini, and G. Marucco, "Loose and tight gnss/ins integrations: Comparison of performance assessed in real urban scenarios," *Sensors (Basel)*, vol. 17, no. 2, p. 255, Jan. 2017.

[138] S. Zihajehzadeh, D. Loh, M. Lee, R. Hoskinson, and E. Park, "A cascaded kalman filter-based gps/mems-imu integration for sports applications," *Measurement*, vol. 73, pp. 200–210, May 2015.

[139] T. Takasu and A. Yasuda, "Development of the low-cost rtk-gps receiver with an open source program package rtklib," *International Symposium on GPS/GNSS*, Jan. 2009.

[140] E. Woolliams, "Determining the uncertainty associated with integrals of spectral quantities," European Association of National Metrology Institutes: Metrology for Solid State Lighting, Tech. Rep., Apr. 2013.

[141] F. Hover and H. Chin, "Design of electromechanical robotic systems," unpublished.

[142] M. Güder, "Ch robotics an-1005 unerstandig euler angles," unpublished.

[143] K. Großekatthöfer and Z. Yoon, "Introduction into quaternions for spacecraft attitude representation," unpublished.

[144] A. Noureldin, T. Karamat, and J. Georgy, *Fundamentals of Inertial Navigation, Satellite-based Positioning and their Integration*. Berlin, Heidelberg: Springer Science & Business Media, 2013.

[145] G. Cai, B. Chen, and T. Lee, *Unmanned Rotorcraft Systems*. London, United Kingdom: Springer Science & Business Media, 2011.

[146] R. Langley, “Dilution of precision,” *GPS World*, vol. Innovation, May 1999.

[147] “Sd input/output (sdio) card specification,” SD Association, California, United States.

[148] M. Young and A. Crumer, *Encyclopedia of Animal Cognition and Behavior: Reaction Time*. Basel, Switzerland: Springer, 2018.

# Appendix A

# Attitude Representation

To define the attitude of a rigid body in a three-dimensional Euclidean space, three parameters are required. There are various parametrisation methods to represent the attitude of a rigid body using rotation matrices, namely: Euler angles, direction cosine matrices and quaternions. Each method has its own strengths and drawbacks.

Rotation involves an orthonormal rotation matrix which is denoted by $R_b^a$ where $a$ is the target frame and $b$ is the initial frame. As the rotation is orthonormal the following holds:

$$(\boldsymbol{R}_b^a)^{-1} = (\boldsymbol{R}_b^a)^T \tag{A.1}$$

## A.1 Euler angles

Euler's rotation theorem states that the displacement of a rigid body with a fixed point is equivalent to a single rotation about an axis through its fixed point [141]. This statement can be extended to state that a single rotation in $\Re^3$is formed by a sequence of three Euler angles namely: roll ($\phi$), pitch ($\theta$) and yaw ($\psi$) corresponding to rotation about the x ($\boldsymbol{R}_x(\phi)$), y ($\boldsymbol{R}_y(\theta)$) and z-axis ($\boldsymbol{R}_z(\psi)$) respectively [142]. Therefore, given the following:

$$\boldsymbol{R}_x(\phi) = \begin{bmatrix} 1 & 0 & 0 \\ 0 & cos\phi & -sin\phi \\ 0 & sin\phi & cos\phi \end{bmatrix} \tag{A.2}$$

$$\boldsymbol{R}_y(\theta) = \begin{bmatrix} cos\theta & 0 & sin\theta \\ 0 & 1 & 0 \\ -sin\theta & 0 & cos\theta \end{bmatrix} \tag{A.3}$$

$$\boldsymbol{R}_z(\psi) = \begin{bmatrix} cos\psi & -sin\psi & 0 \\ sin\psi & cos\psi & 0 \\ 0 & 0 & 1 \end{bmatrix} \tag{A.4}$$

There are twelve possible rotation sequences to represent a single rotation of a rigid body with a fixed point as shown in Table A.1.

**Table A.1:** Twelve possible Euler sequences

| Order of rotation | Rotation matrix | Order of rotation | Rotation matrix |
|---|---|---|---|
| roll-pitch-yaw | $\boldsymbol{R}_x(\phi)\boldsymbol{R}_y(\theta)\boldsymbol{R}_z(\psi)$ | pitch-roll-yaw | $\boldsymbol{R}_y(\theta)\boldsymbol{R}_x(\phi)\boldsymbol{R}_z(\psi)$ |
| roll-pitch-roll | $\boldsymbol{R}_x(\phi)\boldsymbol{R}_y(\theta)\boldsymbol{R}_x(\phi)$ | pitch-roll-pitch | $\boldsymbol{R}_y(\theta)\boldsymbol{R}_x(\phi)\boldsymbol{R}_y(\theta)$ |
| roll-yaw-pitch | $\boldsymbol{R}_x(\phi)\boldsymbol{R}_z(\psi)\boldsymbol{R}_y(\theta)$ | yaw-roll-pitch | $\boldsymbol{R}_z(\psi)\boldsymbol{R}_x(\phi)\boldsymbol{R}_y(\theta)$ |
| roll-yaw-roll | $\boldsymbol{R}_x(\phi)\boldsymbol{R}_z(\psi)\boldsymbol{R}_x(\phi)$ | yaw-roll-yaw | $\boldsymbol{R}_z(\psi)\boldsymbol{R}_x(\phi)\boldsymbol{R}_z(\psi)$ |
| pitch-yaw-roll | $\boldsymbol{R}_y(\theta)\boldsymbol{R}_z(\psi)\boldsymbol{R}_x(\phi)$ | yaw-pitch-roll | $\boldsymbol{R}_z(\psi)\boldsymbol{R}_y(\theta)\boldsymbol{R}_x(\phi)$ |
| pitch-yaw-pitch | $\boldsymbol{R}_y(\theta)\boldsymbol{R}_z(\psi)\boldsymbol{R}_y(\theta)$ | yaw-pitch-yaw | $\boldsymbol{R}_z(\psi)\boldsymbol{R}_y(\theta)\boldsymbol{R}_z(\psi)$ |

Parametrisation using Euler angles is intuitive and easy but it can suffer from a singularity known as a Gimbal lock from loss of one degree of freedom [141].

## A.2 Direction Cosine Matrix (DCM)

A DCM is a rotation matrix that is composed of three direction cosine values between the initial frame and the target frame. Therefore, parametrisation by a DCM involves 9 parameters as shown in (A.5) and is computationally intense to define the attitude of a rigid body in a three-dimensional Euclidean space [141].

The DCM matrix formed by roll-pitch-yaw Euler sequence is:

$$\boldsymbol{R} = \begin{bmatrix} cos\theta cos\psi & sin\phi sin\theta cos\psi - cos\phi sin\psi & cos\phi sin\theta cos\psi + sin\phi sin\psi \\ cos\theta sin\psi & sin\phi sin\theta sin\psi + cos\phi cos\psi & cos\phi sin\theta sin\psi - sin\phi sin\psi \\ -sin\theta & sin\phi cos\theta & cos\phi cos\theta \end{bmatrix} \tag{A.5}$$

## A.3 Quaternions

Quaternion representation is based on the Euler rotation theorem and parametrise a single rotation using four elements as (A.6) [143]. Parametrisation using quaternion representation does not suffer from a singularity and it is computationally efficient but not intuitive [141].

$$\boldsymbol{q} = \begin{bmatrix} s \\ \boldsymbol{v} \end{bmatrix} = \begin{bmatrix} s \\ v_x \\ v_y \\ v_z \end{bmatrix} = \begin{bmatrix} q_s \\ q_x \\ q_y \\ q_z \end{bmatrix} = \begin{bmatrix} cos\frac{\theta}{2} \\ \|\boldsymbol{e}\| sin\frac{\theta}{2} \end{bmatrix} \tag{A.6}$$

where $\boldsymbol{e}$ is the normalized rotational axis and $\theta$ is the transformation angle.

# Appendix B

# Coordinate Systems and Transformations

Fusion of different measurements and analysis of kinematic quantities are only meaningful if their coordinate system and frame are known. Coordinate system refers to a mechanism to locate points within a frame. A frame refers to three mutually orthogonal unit-length direction vectors with an associated origin (possibly time dependent) that uniquely locates and orientates the coordinate system to which measurements and assessment of motion can be made.

This chapter describes a number of coordinate systems and their frames that are necessary to understand when integrating inertial and navigational information, namely: Earth-Centered Inertial (ECI), Earth-Centered Earth-Fixed (ECEF), geodetic, local ENU and body co-ordinate systems as shown in Figure B.1 and B.2.

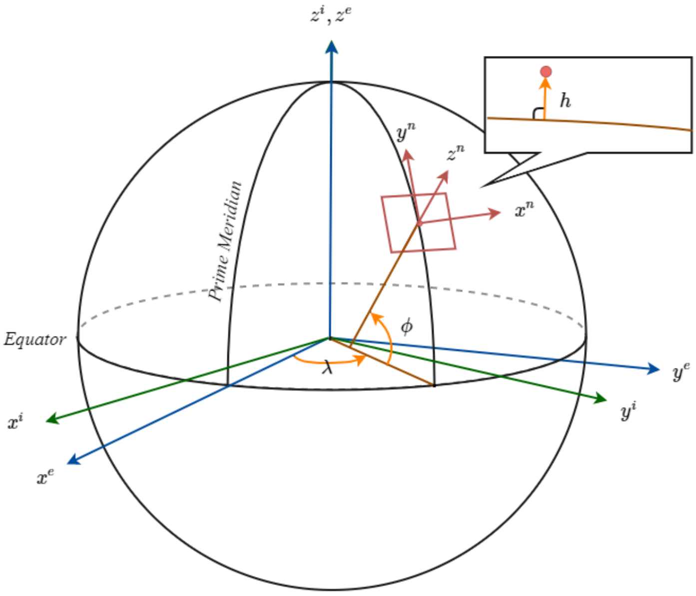

**Figure B.1:** A diagram showing Earth-Centered Inertial (ECI), Earth-Centered Earth-Fixed (ECEF), geodetic, ENU coordinate frames.

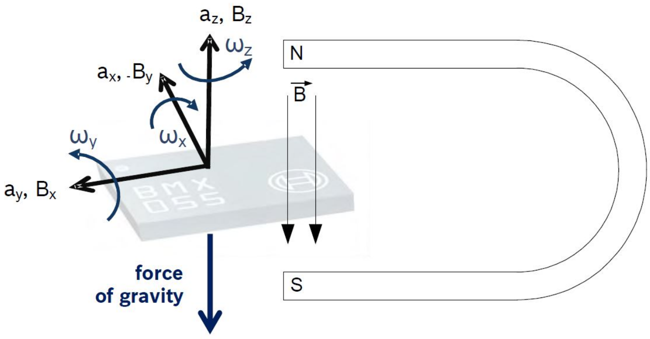

**Figure B.2:** The sensitive axes of the BMX055 forming its body coordinate frame. Image from [14].

## B.1 Coordinate Systems

### B.1.1 Earth-Centered Inertial (ECI) Coordinate System

The ECI coordinate frame is a stationary frame with its origin at the center of the Earth's mass [144]. Its z-axis is through the conventional terrestrial pole (CTP) along the axis of the Earth's rotation. The x-axis is in the equatorial plane pointing to the vernal equinox with y-axis completing a right-handed coordinate system.

### B.1.2 Earth-Centered Earth-Fixed (ECEF) Coordinate System

The ECEF coordinate frame is similar to the ECI coordinate frame, having the same origin and coinciding z-axes. However, the ECEF coordinate frame rotates with the Earth because it has axes that are fixed with respect to the Earth [144]. Its x-axis is along the intersection of the equatorial plane and the Greenwich meridian with y-axis completing a right-handed coordinate system.

### B.1.3 Geodetic Coordinate System

The geodetic coordinate system is not a Cartesian coordinate system but is used to coordinate a position on the surface of the Earth in terms of longitude, latitude and altitude denoted by $\lambda$, $\varphi$ and $h$ respectively [144]. The longitude is the rotational angle between the Prime Meridian and the position on the Earth's surface. The latitude is the angle between the equatorial plane and the normal of the reference ellipsoid that passes through the measured point. The altitude is the local vertical distance between the measured point and the reference ellipsoid.

### B.1.4 East-North-Up (ENU) Coordinate System

The ENU coordinate frame is a local geographic frame and known as the navigation coordinate system [144]. Its frame is fixed to the surface of the Earth and its origin is an arbitrary point on the Earth's surface with x-axis pointing towards the geodetic east; y-axis pointing towards the geodetic north and z-axis pointing upwards along the ellipsoid normal.

### B.1.5 Body Coordinate Frame

The body coordinate frame refers to the coordinate system described by the sensitive axes of the inertial sensor or a moving platform [145]. The origin typically coincide with the center of gravity of the body with x-axis pointing towards the transverse direction (pitch axis); y-axis pointing towards the forward direction (roll axis) and z-axis pointing towards the vertical axis (yaw axis), completing a right-handed coordinate system.

## B.2 Coordinate Transformation

Großekatthöfer and Yoon [143] define transformation as an operation which describes a vector $\boldsymbol{v}$ of a coordinate system $A$ in a coordinate system $B$. By its definition, coordinate transformation is not equivalent to vector rotation. Rotation is defined as an operation where a vector $\boldsymbol{v}$ in a coordinate system $A$ is represented differently in the coordinate system $A$ [143]. Therefore, rotation of $\boldsymbol{v}$ changes the orientation of $\boldsymbol{v}$ in both coordinate system $A$ and $B$.

### B.2.1 Transformation Between ECI and ECEF

Unlike the ECI coordinate frame, the ECEF coordinate frame rotates with the Earth at Earth rate. The angular velocity vector of the ECEF coordinate frame with respect to the ECI coordinate frame expressed in the ECEF coordinate frame is [145]:

$$\boldsymbol{\omega}_{ie}^{e} = \begin{pmatrix} 0 & 0 & \omega_{ie} \end{pmatrix}^{T} \tag{B.1}$$

where $\omega_{ie}$ is approximately $7.29 \times 10^{-5} rad/s$ [84].

Transformation from the ECI coordinate frame to the ECEF coordinate frame is expressed as [144]:

$$\boldsymbol{R}_{i}^{e} = \begin{bmatrix} cos\omega_{ie}t & sin\omega_{ie}t & 0 \\ -sin\omega_{ie}t & cos\omega_{ie}t & 0 \\ 0 & 0 & 1 \end{bmatrix} \tag{B.2}$$

where $\boldsymbol{R}_{e}^{i} = \boldsymbol{R}_{i}^{e-1}$.

### B.2.2 Transformation Between Geodetic and ECEF

Given a point in the geodetic coordinate frame, as for an example:

$$\boldsymbol{r}^{g} = \begin{pmatrix} \lambda & \varphi & h \end{pmatrix}^{T} \tag{B.3}$$

its coordinate in the ECEF coordinate frame is defined as [144]:

$$\boldsymbol{r}^{e} = \begin{bmatrix} x_e \\ y_e \\ z_e \end{bmatrix} = \begin{bmatrix} (N_E + h)cos\varphi cos\lambda \\ (N_E + h)cos\varphi sin\lambda \\ [N(1-e^2)+h]sin\varphi \end{bmatrix} \tag{B.4}$$

where $e$ is the first eccentricity and $N_E$ is the prime vertical radius of curvature.

### B.2.3 Transformation Between ECEF and ENU

Given a point in the ECEF coordinate frame and the position of the origin of the ENU coordinate frame, its coordinate in the ENU coordinate frame is given by [144]:

$$\boldsymbol{r}^n = \boldsymbol{R}_e^n(\boldsymbol{r}^e - \boldsymbol{r}_{n,ref}^e) \tag{B.5}$$

where $\boldsymbol{r}_{n,ref}^e$ is the the ECEF coordinates of the origin of the ENU coordinate frame, and $\boldsymbol{R}_e^n$ is given by [144]:

$$\boldsymbol{R}_e^n = \begin{bmatrix} -sin\varphi_{n,ref} & cos\varphi_{n,ref} & 0 \\ -sin\varphi_{n,ref}cos\lambda_{n,ref} & -sin\varphi_{n,ref}sin\lambda_{n,ref} & cos\varphi_{n,ref} \\ cos\varphi_{n,ref}cos\lambda_{n,ref} & cos\varphi_{n,ref}sin\lambda_{n,ref} & sin\varphi_{n,ref} \end{bmatrix} \tag{B.6}$$

As demonstrated in (B.5) and (B.6), transformation from the ECEF coordinate frame to the ENU coordinate frame involves translation from the ECEF coordinate frame's origin to the ENU coordinate frame's origin and requires geodetic coordinate of the chosen local ENU coordinates frame's origin.

# Appendix C

# Dilution of Precision (DOP)

DOP is the metric used to quantify the the effect of satellite geometry on a receiver position error [6]. The concept of DOP can be understood from Figure C.1. Figure C.1 depicts a scenario in which a receiver measures its range to two transmitters in order to determine its horizontal coordinate based on the horizontal coordinate of two transmitters and the time of flight information with uncertainty. Due to the uncertainties, the exact horizontal coordinate of the receiver cannot be determined instead a region in which the receiver may lie can be determined.

In Figure C.1a, the transmitters are located far apart from each other, resulting in a relatively small region in which the receiver may lie whereas in Figure C.1b, the transmitters are located close to each other, resulting in a relatively large region in which the receiver may lie. Therefore, the precision in Figure C.1b scenario is diluted in comparison to the precision in Figure C.1a scenario. Consequently, one has higher confidence level in the precision with the lower DOP value [146].

Given the variances of the east ($E$), north ($N$) and up ($U$) components of the estimated receiver position as well as the variance of the estimated receiver clock offset ($t$), following DOP can be determined [146]:

$$\begin{aligned}
\text{horizontal DOP: } HDOP &= \sqrt{\sigma_{EE}^2 + \sigma_{NN}^2} && \text{(C.1)} \\
\text{vertical DOP: } VDOP &= \sqrt{\sigma_{UU}^2} && \text{(C.2)} \\
\text{positional DOP: } PDOP &= \sqrt{\sigma_{EE}^2 + \sigma_{NN}^2 + \sigma_{UU}^2} && \text{(C.3)} \\
\text{time DOP: } TDOP &= \sqrt{\sigma_{tt}^2} && \text{(C.4)} \\
\text{geodetic DOP: } GDOP &= \sqrt{\sigma_{EE}^2 + \sigma_{NN}^2 + \sigma_{UU}^2 + \sigma_{tt}^2} && \text{(C.5)}
\end{aligned}$$

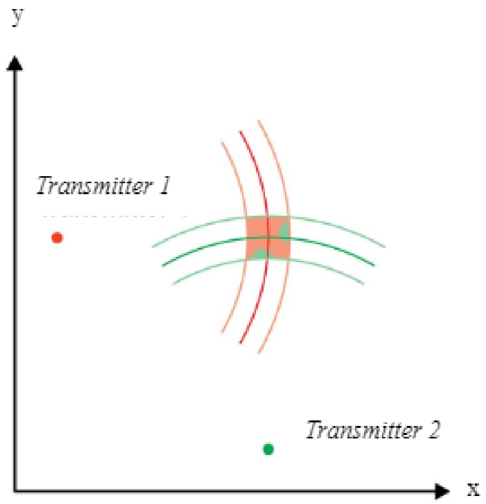

**(a)** A diagram of a relatively small region of uncertainty in the receiver's position. Image from [146]

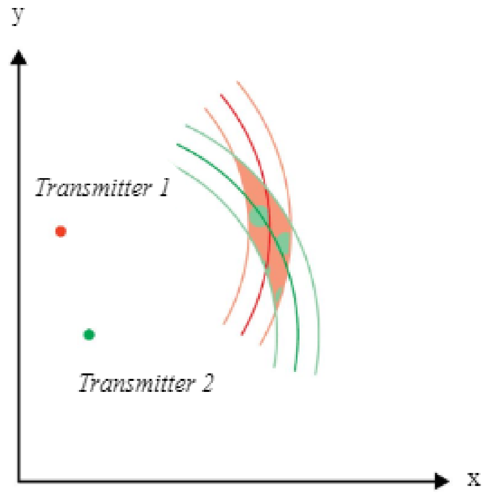

**(b)** A diagram of a relatively large region of uncertainty in the receiver's position. Due to the closely allocated transmitters, the precision in the estimation of the receiver's position is diluted. Image from [146]

**Figure C.1:** A diagram depicting the effect of transmitter geometry on the level of confidence in the precision. The patterned region indicates the uncertainty in the receiver's position.

# Appendix D

# Requirements, Specifications and Testing Procedures

## D.1 User Requirements

**Table D.1:** The fusion MOCAP system user requirements

| Req. I.D. | User requirement descriptions |
|---|---|
| U.R. 1 | The user needs a portable and outdoor array of sensors to measure IMU measurements and raw GPS observables of each limb segment of a terrestrial *megafauna* of interest during its steady-state and transient motion. |
| U.R. 2 | The user needs to interact with the sensor(s) to begin and stop the procedure and to acknowledge errors. |
| U.R. 3 | The user needs access to the recordings of sensor measurements. |
| U.R. 4 | The user needs to power the sensor(s) outdoor during capturing process for maximum duration of 6 hours. |
| U.R. 5 | The user needs mechanism to mount the sensor(s) on a terrestrial *megafauna* of interest ethically, safely and without impeding the motion. |
| U.R. 6 | The user needs software that manages the sensor measurements. |
| U.R. 7 | The user needs software that pre-processes the sensor measurements. |
| U.R. 8 | The user needs access to the pre-processed sensor measurements. |
| U.R. 9 | The user needs software that estimates the kinematic quantities of a terrestrial *megafauna* of interest using the sensor measurements. |
| U.R. 10 | The user needs access to the kinematic quantities of the tracked motion. |

## D.2 Functional Requirements

**Table D.2:** The fusion MOCAP system functional requirements

| Req. I.D. | Functional requirement descriptions |
|---|---|
| F.R. 1.1 | The sensor(s) shall be a self-contained unit(s). |
| F.R. 1.2 | The sensor(s) shall operate in dry environment at temperature ranging between $-20\ ^{\circ}C$ and $60\ ^{\circ}C$ with air pressure ranging between 870 hPa and 1100 hPa. |
| F.R. 1.3 | The sensor(s) shall have an IMU on board. |
| F.R. 1.4 | The sensor(s) shall have a GPS receiver on board. |
| F.R. 1.5 | The sensor unit shall include a GPS antenna. |
| F.R. 1.6 | The sensor(s) shall contain sensor components that will not saturate to avoid loss of motion information. |
| F.R. 1.7 | The sensor(s) shall sample measurements at a frequency that avoids loss of motion information. |
| F.R. 1.8 | The sensor measurements of every unit shall be time-synchronized to avoid loss of motion information and inaccuracy due to latency. |
| F.R. 2.1 | The sensor(s) shall provide a tactile switch to begin and end the motion capture procedure. |
| F.R. 2.2 | The sensor(s) shall provide visual feedback on the status of the battery, sampling of measurements and external flash memory. |
| F.R. 3.1 | The sensor(s) shall have external non-volatile memory on board to store inertial and navigational information. |
| F.R. 4.1 | The sensor(s) shall be powered from a battery during the capturing process. |
| F.R. 5.1 | The sensor(s) shall be strapped down on a motion capture subject non-invasively. |
| F.R. 5.2 | The sensor(s) will not impede the motion of a motion capture subject. |
| F.R. 5.3 | The sensor mounting mechanism shall account for different limb segment radii. |
| F.R. 5.4 | The sensor mounting mechanism shall prevent sensors from deviating from initial mounted position. |
| F.R. 6.1 | The data management software shall name the measurements accordingly. |
| F.R. 6.2 | The data management software shall output an initialization file per motion capture session which contains the directory of all sensor measurements associated with the session. |
| F.R. 6.3 | The data management software shall record the changes to a file. |
| F.R. 7.1 | The measurement pre-processing software shall convert sensor measurements into a format that is comprehensible. |
| F.R. 7.2 | The measurement pre-processing software shall synchronize all the measurements from a motion capture session with reference to the GPS standard time. |

Continued on next page

**Table D.2 – continued from previous page**

| Req. I.D. | Functional requirement descriptions |
|---|---|
| F.R. 7.3 | The measurement pre-processing software shall remove unwanted frequency components of inertial measurements. |
| F.R. 7.4 | The measurement pre-processing software shall estimate and correct the GPS receiver errors within navigational information. |
| F.R. 7.5 | The measurement pre-processing software shall remove any invalid measurements. |
| F.R. 7.6 | The measurement pre-processing software shall evaluate measurement covariance. |
| F.R. 8.1 | The measurement pre-processing software shall output and save a binary data container format file containing time-synchronised and limb-segment identified measurements from a session in chronological order. |
| F.R. 9.1 | The state estimation algorithm software shall use pre-processed inertial and navigational information as well as a kinematic model of the subject to estimate position, velocity and acceleration of the limb segment(s) of interest. |
| F.R. 10.1 | The state estimation algorithm software shall output and save a binary data container format file containing time-synchronised and limb-segment identified estimated position, velocity and acceleration in chronological order. |

## D.3 Technical Specifications

**Table D.3:** A sensor unit hardware technical specifications for the fusion MOCAP system

| Req. I.D. | Hardware specification descriptions | | Der. from |
|---|---|---|---|
| H.S. 1 | **Accelerometer**: | | |
| | measurement range: | $> \pm 4g$ | F.R. 1.2 |
| | output data rate: | $> 230Hz$ | F.R. 1.3 |
| | operating temp.: | $[-20\,°C : +60\,°C]$ | F.R. 1.6 |
| | storage temp.: | $[-20\,°C : +60\,°C]$ | F.R. 1.7 |
| H.S. 2 | **Gyroscope**: | | |
| | measurement range: | $> \pm 230°/s$ | F.R. 1.2 |
| | output data rate: | $> 230Hz$ | F.R. 1.3 |
| | operating temp.: | $[-20\,°C : +60\,°C]$ | F.R. 1.6 |
| | storage temp.: | $[-20\,°C : +60\,°C]$ | F.R. 1.7 |
| H.S. 3 | **Magnetometer**: | | |

Continued on next page

**Table D.3 – continued from previous page**

| Req. I.D. | Hardware specification descriptions | | Der. from |
|---|---|---|---|
| | measurement range: | $\gg 65\mu T$ | F.R. 1.2 |
| | output data rate: | $\geq 10Hz$ | F.R. 1.3 |
| | operating temp.: | $[-20\ ^{\circ}C : +60\ ^{\circ}C]$ | F.R. 1.6 |
| | storage temp.: | $[-20\ ^{\circ}C : +60\ ^{\circ}C]$ | F.R. 1.7 |
| H.S. 4 | **GPS (GNSS) receiver**: | | |
| | type: | GPS L1 C/A | F.R. 1.2 |
| | message: | raw data | F.R. 1.4 |
| | oscillator: | OCXO (optional) | F.R. 1.5 |
| | noise figure: | on-chip LNA (optional) | F.R. 1.8 |
| | anti jamming: | on-chip SAW (optional) | |
| | output data rate: | $\geq 1Hz$ | |
| | operating temp.: | $[-20\ ^{\circ}C : +60\ ^{\circ}C]$ | |
| | storage temp.: | $[-20\ ^{\circ}C : +60\ ^{\circ}C]$ | |
| H.S. 5 | **GPS (GNSS) antenna**: | | |
| | center frequency: | $1575.42 \pm 3MHz$ | F.R. 1.2 |
| | impedance: | $50\Omega$ | F.R. 1.4 |
| | gain: | $> 4dBic$ | F.R. 1.5 |
| | noise: | $< 2dB$ | F.R. 1.8 |
| | operating temp.: | $[-20\ ^{\circ}C : +60\ ^{\circ}C]$ | |
| | storage temp.: | $[-20\ ^{\circ}C : +60\ ^{\circ}C]$ | |
| H.S. 6 | **Tactile switch**: | | |
| | circuit: | SPST | F.R. 2.1 |
| | switch function: | normally open (NO) | |
| | contact rating: | $< 0.01A@50VDC$ | |
| | operating temp.: | $[-20\ ^{\circ}C : +60\ ^{\circ}C]$ | |
| | storage temp.: | $[-20\ ^{\circ}C : +60\ ^{\circ}C]$ | |
| H.S. 7 | **Light emitting diode (LED)**: | | |
| | forward voltage: | $< 2V$ | F.R. 2.2 |
| | forward current: | $< 5mA$ | |
| | operating temp.: | $[-20\ ^{\circ}C : +60\ ^{\circ}C]$ | |
| | storage temp.: | $[-20\ ^{\circ}C : +60\ ^{\circ}C]$ | |
| H.S. 8 | **Non-volatile memory**: | | |
| | operating voltage: | $\pm 3.3V$ | F.R. 3.1 |
| | capacity: | $> 2GB$ | |
| | throughput: | $> 100kB/s$ | |
| | operating temp.: | $[-20\ ^{\circ}C : +60\ ^{\circ}C]$ | |
| | storage temp.: | $[-20\ ^{\circ}C : +60\ ^{\circ}C]$ | |
| H.S. 9 | **Battery**: | | |

Continued on next page

**Table D.3 – continued from previous page**

| Req. I.D. | Hardware specification descriptions | | Der. from |
|---|---|---|---|
| | operating voltage: | $> 3.3V$ | F.R. 3.1 |
| | capacity: | $> 2000mAh$ | |
| | discharge rate: | $> 500mA$ | |
| | operating temp.: | $[-20\ °C : +60\ °C]$ | |
| | storage temp.: | $[-20\ °C : +60\ °C]$ | |
| H.S. 10 | **Voltage regulator**: | | |
| | input voltage: | $> 3.7V$ | F.R. 4.1 |
| | output voltage: | $3.3V$ | |
| | output current: | $> 500mA$ | |
| | drop-out voltage: | $< 0.6V @ 500mA$ | |
| | output noise: | $< 0.060V @ 500mA$ | |
| | operating temp.: | $[-20\ °C : +60\ °C]$ | |
| | storage temp.: | $[-20\ °C : +60\ °C]$ | |
| H.S. 11 | **Fuel gauge**: | | |
| | input voltage: | $> 3.7V$ | F.R. 4.1 |
| | precision: | $< \pm 50mV$ | |
| | active current: | $< \pm 100\mu AmA$ | |
| | operating temp.: | $[-20\ °C : +60\ °C]$ | |
| | storage temp.: | $[-20\ °C : +60\ °C]$ | |
| H.S. 12 | **Processor**: | | |
| | operating voltage: | $3.3V$ | F.R. 1.1 to F.R. 4.1 |
| | system clock: | $\gg 20MHz$ | |
| | memory (RAM): | $\gg 90kB$ | |
| | comm. interface: | UART, I$^2$C, SPI and SDIO | |
| | operating temp.: | $[-20\ °C : +60\ °C]$ | |
| | storage temp.: | $[-20\ °C : +60\ °C]$ | |

**Table D.4:** A sensor unit firmware technical specifications for the fusion MOCAP system

| Req. I.D. | Firmware specification descriptions | | Der. from |
|---|---|---|---|
| F.S. 1 | **Communication interface - UART**: | | |
| | mode: | full-duplex | H.S. 4 |
| | word length: | 8 bit | [117] |
| | stop bits: | 1 bit | |
| | baud rate: | [9.6 kHz : 115.200 kHz] | |
| F.S. 2 | **Communication interface - I$^2$C**: | | |

Continued on next page

**Table D.4 – continued from previous page**

| **Req. I.D.** | **Firmware specification descriptions** | | **Der. from** |
|---|---|---|---|
| | mode: | master (*STM32F407*) | H.S. 10 |
| | address: | slave (0b0110110) | [129] |
| | stop generation: | 1 stop generation | |
| | start generation: | repeated start generation | |
| | acknowledge (ack): | acknowledge enabled | |
| | clock speed: | [50 kHz : 400 kHz] | |
| F.S. 3 | **Communication interface - SPI**: | | |
| | mode: | master (*STM32F407*) | H.S. 1 |
| | direction: | full-duplex | H.S. 2 |
| | data size: | 8 bit | H.S. 3 |
| | clock polarity: | high | [14] |
| | clock phase: | second clock transition | |
| | baud rate: | [1 MHz : 10 MHz] | |
| F.S. 4 | **Communication interface - SDIO**: | | |
| | middle-ware: | FatFs | H.S. 8 |
| | mode: | 4-bit wide bus | [147] |
| | maximum sector size: | 4096B | |
| | minimum sector size: | 512B | |

## D.4 System Attributes

**Table D.5:** A sensor unit system attribute specifications for the fusion MOCAP system

| **Req. I.D.** | **System attribute descriptions** | **Der. from** |
|---|---|---|
| A.1 | **System attribute - response time**: | |
| | Upon indication of measurement availability from sensing components, the processor shall dedicate stream to read the data within 5% of the communication clock period. | F.R. 1.7<br>Table 6.1 |
| A.2 | **System attribute - response time**: | |
| | Upon user input, status change or detection of an error, the status of a sensor unit shall be indicated within 0.25 seconds which corresponds to the shortest human reaction time as observed in [148]. | F.R. 2.1<br>F.R. 2.2 |
| A.3 | **System attribute - dependability**: | |
| | The raw inertial and navigational information output from a capturing session shall be $> 95\%$ of the estimated output file size. | F.R. 3.1<br>Table 6.1 |

Continued on next page

**Table D.5 – continued from previous page**

| Req. I.D. | System attribute descriptions | Der. from |
|---|---|---|
| A.4 | **System attribute - maintainability**:<br>The firmware shall be easy to expand and allow easy implementation of new tasks. | Section 5.1 |
| A.5 | **System attribute - portability**:<br>The firmware development environment shall be portable between different operating systems: Windows, Linux and Mac. | Section 5.1 |
| A.6 | **System attribute - safety**:<br>Upon estimation and detection of rapid discharging, overheating and under-voltage, the processor shall initiate a sensor shut-down process immediately. | F.R. 4.1 |

# D.5 Acceptance Testing Procedure

**Table D.6:** A sensor unit acceptance testing procedure for the fusion MOCAP system

| Req. I.D. | Acceptance testing procedure descriptions | Der. from |
|---|---|---|
| A.T.P. 1.1 | The $V_{IN}$ pin of the chosen voltage regulator shall be measured with its $V_{BAT}$ pin connected to a source ranging from $3.8V$ to $4.2V$ and its $V_{OUT}$ pin disconnected from the rest of the circuit to observe the loss in voltage due to wire. The result shall be accepted if the measured loss is less than $0.1V$. | H.S. 10 |
| A.T.P. 1.2 | The $V_{OUT}$ pin of the chosen voltage regulator shall be measured with its $V_{BAT}$ pin connected to a source ranging between from $3.8V$ to $4.2V$ and its $V_{OUT}$ pin disconnected from the rest of the circuit. The result shall be accepted if the measured regulated voltage is $3.3 \pm 0.1V$ with output noise less than $0.05V$. | H.S. 10 |
| A.T.P. 1.3 | The $V_{OUT}$ pin of the chosen voltage regulator shall be measured with its $V_{BAT}$ pin connected to a source ranging between from $3.8V$ to $4.2V$ and its $V_{OUT}$ pin disconnected from the rest of the circuit but with a dummy load of $500mA$ connected. The result shall be accepted if the measured drop-out voltage is less than $0.6V$ with output noise less than $0.05V$. | H.S. 10 |

Continued on next page

**Table D.6 – continued from previous page**

| Req. I.D. | Acceptance testing procedure descriptions | Der. from |
|---|---|---|
| A.T.P. 1.3 | The bias current of the chosen voltage regulator shall be measured with its $V_{BAT}$ pin connected to a source ranging between from $3.8V$ to $4.2V$ and its $V_{OUT}$ pin disconnected from the rest of the circuit but with a dummy load of $500mA$ connected. The result shall be accepted if the measured bias current agrees with the data-sheet of the chosen voltage regulator. | H.S. 10 |
| A.T.P. 2.1 | The continuity test shall be conducted on every switch to ensure it is normally open. | H.S. 6 |
| A.T.P. 2.2 | The diode polarity test shall be conducted on every light emitting diodes. | H.S. 7 |
| A.T.P. 3.1 | The connection between the chosen processor and the chosen programming and debugging interface shall be observed. The result shall be accepted if the chosen processor is connected to the chosen programming and debugging interface and every address is accessible and erasable via utility. | H.S. 12 |
| A.T.P. 3.2 | A simple incremental counter shall be programmed and written on the processor and its boot memory shall be assessed. The result shall be accepted if the processor boots from the chosen boot memory. | H.S. 12 |
| A.T.P. 3.3 | A line of code pointed by the program counter shall be observed when the NRST pin of the processor is toggled to force reset. The result shall be accepted if the pointer points back to the first line of code on reset. | H.S. 12 |
| A.T.P. 3.4 | The clock frequency of the high-frequency internal clock of the processor shall be measured. The result shall be accepted if the measured clock frequency agrees with the book-value of the chosen processor. | H.S. 12 |
| A.T.P. 3.5 | The clock frequency of the high-frequency external clock of the processor shall be measured. The result shall be accepted if the measured clock frequency agrees with the frequency of the chosen external oscillator. | H.S. 12 |
| A.T.P. 4.1 | Every digital I/O pin of the processor shall be programmed in output mode to output high level voltage and the voltage at a programmed digital I/O pin shall be measured. The result shall be accepted if the measured output voltage on a programmed digital I/O pin agrees with book-value of the chosen processor. | H.S. 12 |

Continued on next page

**Table D.6 – continued from previous page**

| Req. I.D. | Acceptance testing procedure descriptions | Der. from |
|---|---|---|
| A.T.P. 4.2 | Every digital I/O pin of the processor shall be programmed in input mode to read high level voltage. The result shall be accepted if every programmed digital I/O pin reads logic 1. | H.S. 12 |
| A.T.P. 4.3 | Every digital I/O pin of the processor shall be programmed in analogue mode to read $0.5V_{AVDD}$. The result shall be accepted if every programmed digital I/O pin reads $\approx 0.5(2^n - 1)$ where $n$ is the resolution. | H.S. 12 |
| A.T.P. 4.4 | The communication interface to the chosen external peripherals shall be programmed according to Table F.1. The communication interface shall be deemed to perform correctly if:<br>• the clock frequency of the clock line of a synchronous communication interface agrees with the program.<br>• the communication interface lines are observed to be free from eyeing-phenomena.<br>• the processor is capable of sending 0*xAA* value across a communication interface. | F.S. 1 - F.S. 4 |
| A.T.P. 4.5 | The chosen processor shall read/receive message from the chosen external peripherals via chosen communication interface. The result shall be accepted if:<br>• the *WHO AM I* register from the chosen MEMS-IMU is read correctly.<br>• the raw GPS observables are received.<br>• a buffer of size 1024*B* and 2048*B* with pre-defined characters are correctly saved onto the chosen microSD card. | F.S. 1 - F.S. 4 |

Continued on next page

**Table D.6 – continued from previous page**

| Req. I.D. | Acceptance testing procedure descriptions | Der. from |
|---|---|---|
| A.T.P. 5.1 | The processor shall read measurements from the chosen MEMS-IMU. The result shall be accepted if:<br>• the magnitude of the 3-axis accelerometer measurement vector is approximately $1g$ during steady-state locomotion.<br>• the 3-axis gyroscope measurement agrees to the pre-defined angular velocity under external restriction calibration.<br>• the 3-axis magnetometer measurement draws an ellipsoid as it is rotated through all the angles. | H.S. 1 - H.S. 3<br>F.S. 3 |
| A.T.P. 5.2 | The incoming GPS SNR observables shall be compared with that of *C94-M8P* simultaneously. The result shall be agreed if two sets of GPS SNR observables agree within $5dB$. | H.S. 4 - H.S. 5<br>F.S. 1 |
| A.T.P. 6.1 | The incoming *PPS* from sensors shall be observed and the latency between signals shall be evaluated simultaneously. The result shall be agreed if the latency is less than the $1\%$ of the lowest sampling period. | F.R. 1.8 |

# Appendix E

# Component Alternatives

**Table E.1:** A list of component alternatives considered during the component procurement process

| **Req. I.D.** | **Part number** | **Req. I.D.** | **Part number** |
|---|---|---|---|
| H.S. 1 - H.S.3 | • BMX055<br>• BMX160<br>• ICM20948<br>• LSM9DS1TR<br>• MPU9250 | H.S. 12 | • STM32F2xx<br>• STM32F4xx<br>• STM32F7xx<br>• STM32H7xx<br>• STM32L4xx |
| H.S. 4 | • NEO-M8x<br>• ZOE-M8x<br>• UBX-M9140/UBX-G8020-KT<br>• SAM-M8x<br>• EVA-M8x | H.S. 5 | • GLONASS 9 M<br>• AA.160.301111<br>• AA.161.301111<br>• B3G02G-S3-01-A<br>• Amotech AGA363913-S0-A1 |

**Table E.2:** A detailed comparison of MEMS-IMU alternatives considered during the component procurement process

| **Description** | **BMX055** [14] | **BMX160** [120] | **ICM20948** [9] | **LSM9DS1TR** [121] | **MPU9250** [10] |
|---|---|---|---|---|---|
| **Manufacturer** | | | | | |
| ODR/refresh rate | *Bosch Sensortec* | *Bosch Sensortec* | *InvenSense* | *STMicroelectronics* | *InvenSense* |
| **Accelerometer** | | | | | |
| range | $\pm2/\pm4/\pm8/\pm16g$ | $\pm2/\pm4/\pm8/\pm16g$ | $\pm2/\pm4/\pm8/\pm16g$ | $\pm2/\pm4/\pm8/\pm16g$ | $\pm2/\pm4/\pm8/\pm16g$ |
| max. ODR (with filter) | $1000Hz$ | $1600Hz$ | $1125Hz$ | $952Hz$ | $4000Hz$ |
| sensitivity @ max. range | $125LSB/g$ | $2130LSB/g$ | $2050LSB/g$ | $1333LSB/g$ | $2048LSB/g$ |
| noise density @ normal mode | $150\mu g/\sqrt{Hz}$ | $180\mu g/\sqrt{Hz}$ | $230\mu g/\sqrt{Hz}$ | - | $300\mu g/\sqrt{Hz}$ |
| **Gyroscope** | | | | | |
| range | $\pm125/\pm250/\pm500/$ $\pm1000/\pm2000dps$ | $\pm125/\pm250/\pm500/$ $\pm1000/\pm2000dps$ | $\pm245/\pm500/\pm1000/$ $\pm2000dps$ | $\pm245/\pm500/$ $\pm2000dps$ | $\pm125/\pm250/\pm500/$ $\pm1000/\pm2000dps$ |
| max. ODR (with filter) | $2000Hz$ | $3200Hz$ | $1125Hz$ | $952Hz$ | $1000Hz$ |
| sensitivity @ max. range | $262.4LSB/dps$ | $17.1LSB/dps$ | $16.4LSB/dps$ | $14.3LSB/dps$ | $16.4LSB/dps$ |
| noise density | $0.014dps/\sqrt{Hz}$ | $0.07dps/\sqrt{Hz}$ | $0.015dps/\sqrt{Hz}$ | - | $0.01dps/\sqrt{Hz}$ |

Continued on next page

**Table E.2 – continued from previous page**

| **Description** | **BMX055** [14] | **BMX160** [120] | **ICM20948** [9] | **LSM9DS1TR** [121] | **MPU9250** [10] |
|---|---|---|---|---|---|
| **Magnetometer** | | | | | |
| range | $\pm 1300\mu T$ (x,y)<br>$\pm 2500\mu T$ (z) | $\pm 1300\mu T$ (x,y)<br>$\pm 2500\mu T$ (z) | $\pm 4900\mu T$ | $\pm$400/$\pm$800/<br>$\pm$1200/$\pm$1600$\mu T$ | $\pm 4900\mu T$ |
| max. ODR (with filter) | $300Hz$ | $800Hz$ | $100Hz$ | $80Hz$ | $8Hz$ |
| sensitivity @ max. range | $0.3\mu T/LSB$ | $0.3\mu T/LSB$ | $0.15\mu T/LSB$ | $0.058\mu T/LSB$ | $0.6\mu T/LSB$ |
| noise | $< 1.4\mu T$ | $< 1.4\mu T$ | - | - | - |
| **Temperature Sensor** | | | | | |
| ODR/refresh rate | $1000Hz$ | $100Hz$ | $1125Hz$ | $50Hz$ | ADC |
| **Electrical Characteristics** | | | | | |
| Supply voltage (VDD) | $[2.4 : 3.6]V$ | $[1.71 : 3.6]V$ | $[1.71 : 3.6]V$ | $[1.9 : 3.6]V$ | $[2.4 : 3.6]V$ |
| I.O supply voltage | $[1.2 : 3.6]V$ | $[1.2 : 3.6]V$ | $[1.71 : 1.95]V$ | $[1.71 : VDD + 0.1]V$ | $[1.71 : VDD]V$ |
| supply current @ normal mode | $< 5mA$ | $< 2mA$ | $< 4mA$ | $< 5mA$ | $< 4mA$ |
| Operating temperature | $[-40\,^{\circ}C : +85\,^{\circ}C]$ | $[-40\,^{\circ}C : +105\,^{\circ}C]$ | $[-40\,^{\circ}C : +85\,^{\circ}C]$ | $[-40\,^{\circ}C : +85\,^{\circ}C]$ | $[-40\,^{\circ}C : +85\,^{\circ}C]$ |
| Storage temperature | $[-50\,^{\circ}C : +150\,^{\circ}C]$ | $[-50\,^{\circ}C : +150\,^{\circ}C]$ | $[-40\,^{\circ}C : +125\,^{\circ}C]$ | $[-40\,^{\circ}C : +125\,^{\circ}C]$ | $[-40\,^{\circ}C : +125\,^{\circ}C]$ |

# Appendix F

# Schematics

**Table F.1:** A pin assignment between the *STM32F407VGT* and the chosen external peripherals

| ***STM32F407VGT*** | **(LQFP100)** | **Ext. Peripheral** | |
|---|---|---|---|
| **pin no.** | **pin name** | **pin no.** | **pin name** |
| **Initial & Final *NEO-M8T* (UART)** | | | |
| 92 (PB6) | USART1-TX | 21 | RXD |
| 93 (PB7) | USART1-RX | 20 | TXD |
| 29 (PA4) | GPIO-EXTI4 | 3 | TIMEPULSE |
| **Initial & Untested *MAX17043* (I$^2$C)** | | | |
| 47 (PB10) | I$^2$C-SCL | A2 | SCL |
| 48 (PB11) | I$^2$C-SDA | A3 | SDA |
| 46 (PE15) | GPIO-EXTI15 | C1 | ALEART |
| **Initial & Final *BMX055* (SPI)** | | | |
| 23 (PA0) | GPIO-EXTI0 | 19 | INT1A |
| 24 (PA1) | GPIO-EXTI1 | 14 | INT1G |
| 25 (PA2) | GPIO-EXTI2 | 2 | DRDYM |
| 30 (PA5) | SPI1-SCK | 8 | SCK |
| 31 (PA6) | SPI1-MISO | 12 & 17 | SDO |
| 32 (PA7) | SPI1-MOSI | 11 | SDI |
| 38 (PE7) | GPIO-OUT | 16 | CSBA |
| 39 (PE8) | GPIO-OUT | 5 | CSBG |
| 40 (PE9) | GPIO-OUT | 20 | CSBM |
| **Initial *microSDHC* (SDIO)** | | | |
| 65 (PC8) | SDIO-D0 | 7 | DAT0 |
| 66 (PC9) | SDIO-D1 | 8 | DAT1 |
| 78 (PC10) | SDIO-D2 | 1 | DAT2 |
| 79 (PC11) | SDIO-D3 | 2 | DAT3 |
| 80 (PC12) | SDIO-CK | 5 | CLK |
| 83 (PD2) | SDIO-CMD | 3 | CMD |
| 84 (PD3) | GPIO-IN | SW | DETECT |

Continued on next page

**Table F.1 – continued from previous page**

| *STM32F407VGT* pin no. | (LQFP100) pin name | Ext. Peripheral pin no. | pin name |
|---|---|---|---|
| 85 (PD4) | GPIO-IN | DT | SWITCH |
| **Modified final *microSDHC* (SPI)** | | | |
| 51 (PB12) | SPI2-CS | 2 | DAT3 |
| 52 (PB13) | SPI2-SCK | 5 | CLK |
| 53 (PB14) | SPI2-MISO | 7 | DAT0 |
| 54 (PB15) | SPI2-MOSI | 3 | CMD |
| 84 (PD3) | GPIO-IN | SW | DETECT |
| 85 (PD4) | GPIO-IN | DT | SWITCH |
| **Initial & Final Light Emitting Diode (LED)** | | | |
| 3 (PE4) | GPIO-OUT | - | - |
| 4 (PE5) | GPIO-OUT | - | - |
| 5 (PE6) | GPIO-OUT | - | - |
| **Initial & Final Switch** | | | |
| 16 (PC1) | GPIO-IN | - | - |

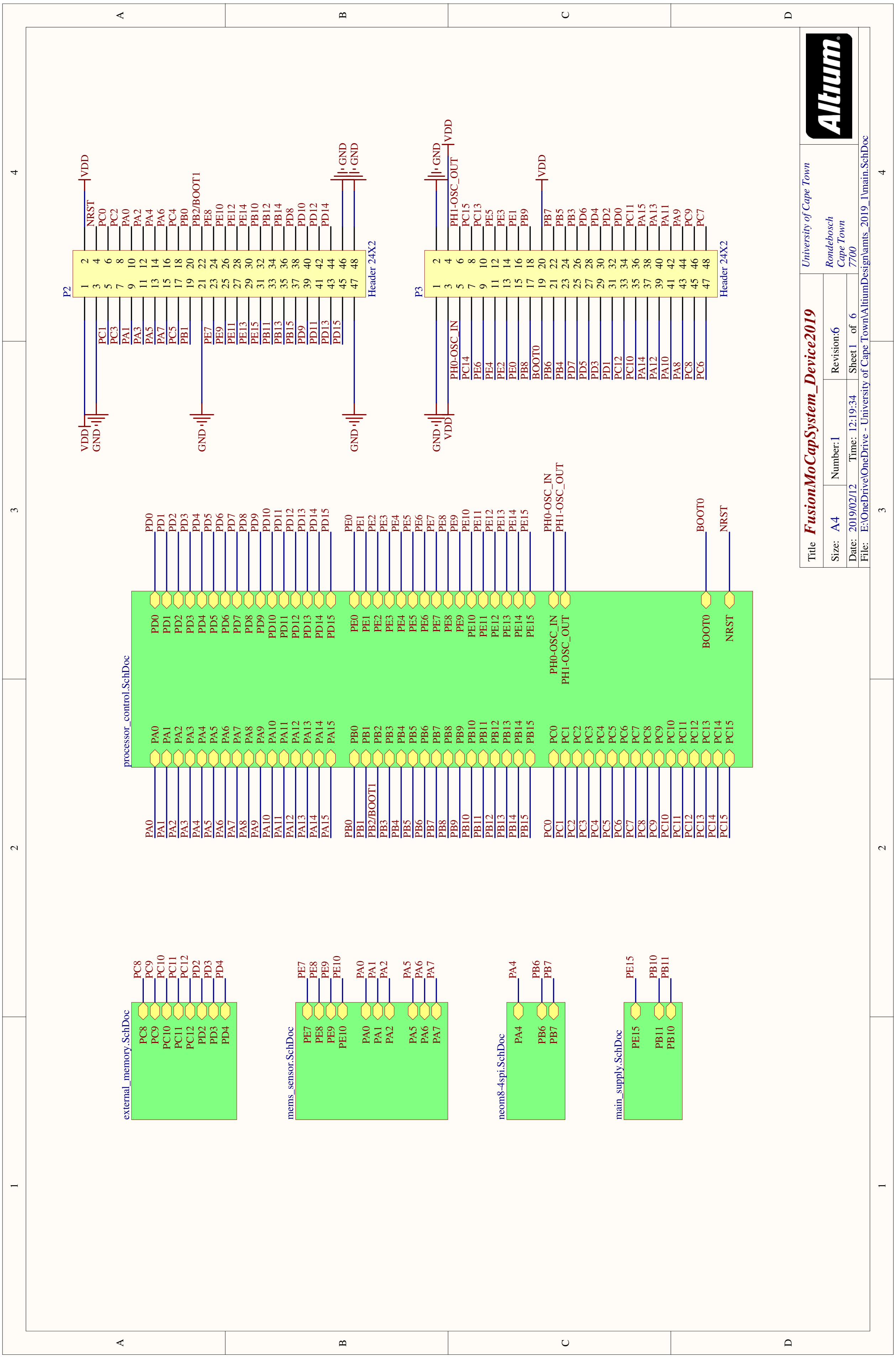

**Figure F.1:** Sheet 1 of 6 of the captured schematic of a sensor unit, capturing the processor pin assignment layout.

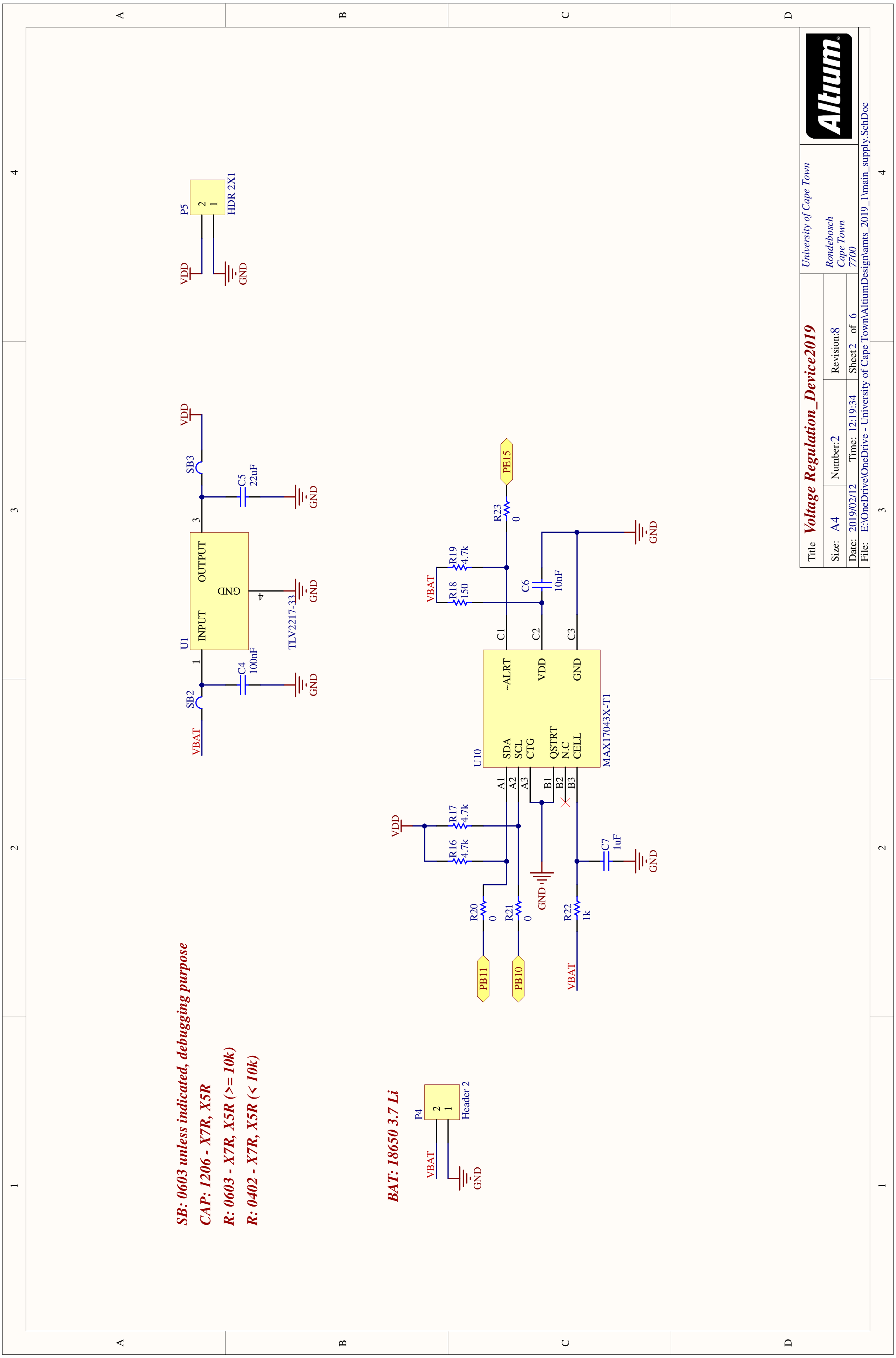

**Figure F.2:** Sheet 2 of 6 of the captured schematic of a sensor unit, capturing the voltage regulator.

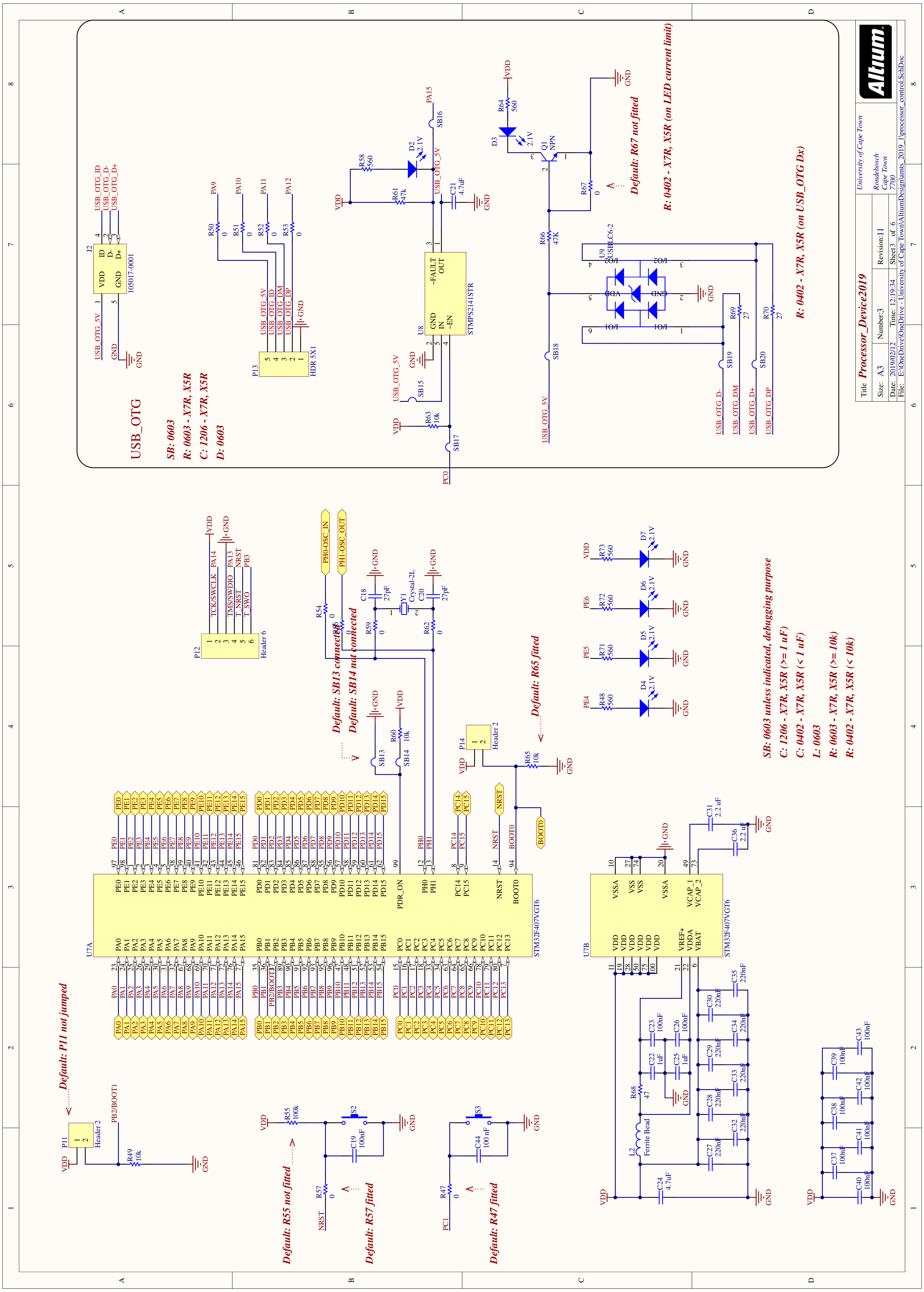

**Figure F.3:** Sheet 3 of 6 of the captured schematic of a sensor unit, capturing the processor.

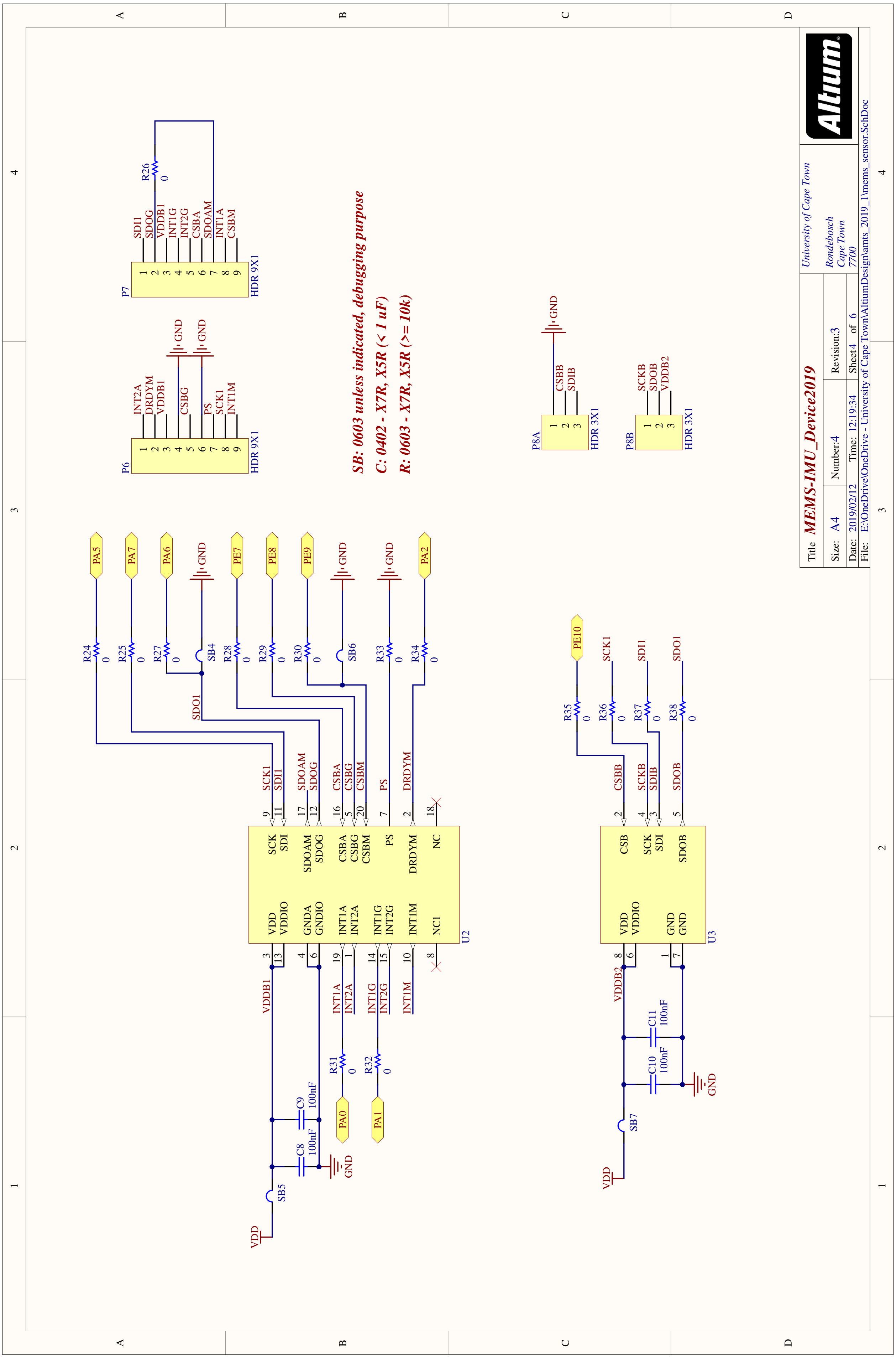

**Figure F.4:** Sheet 4 of 6 of the captured schematic of a sensor unit, capturing the MEMS-IMU.

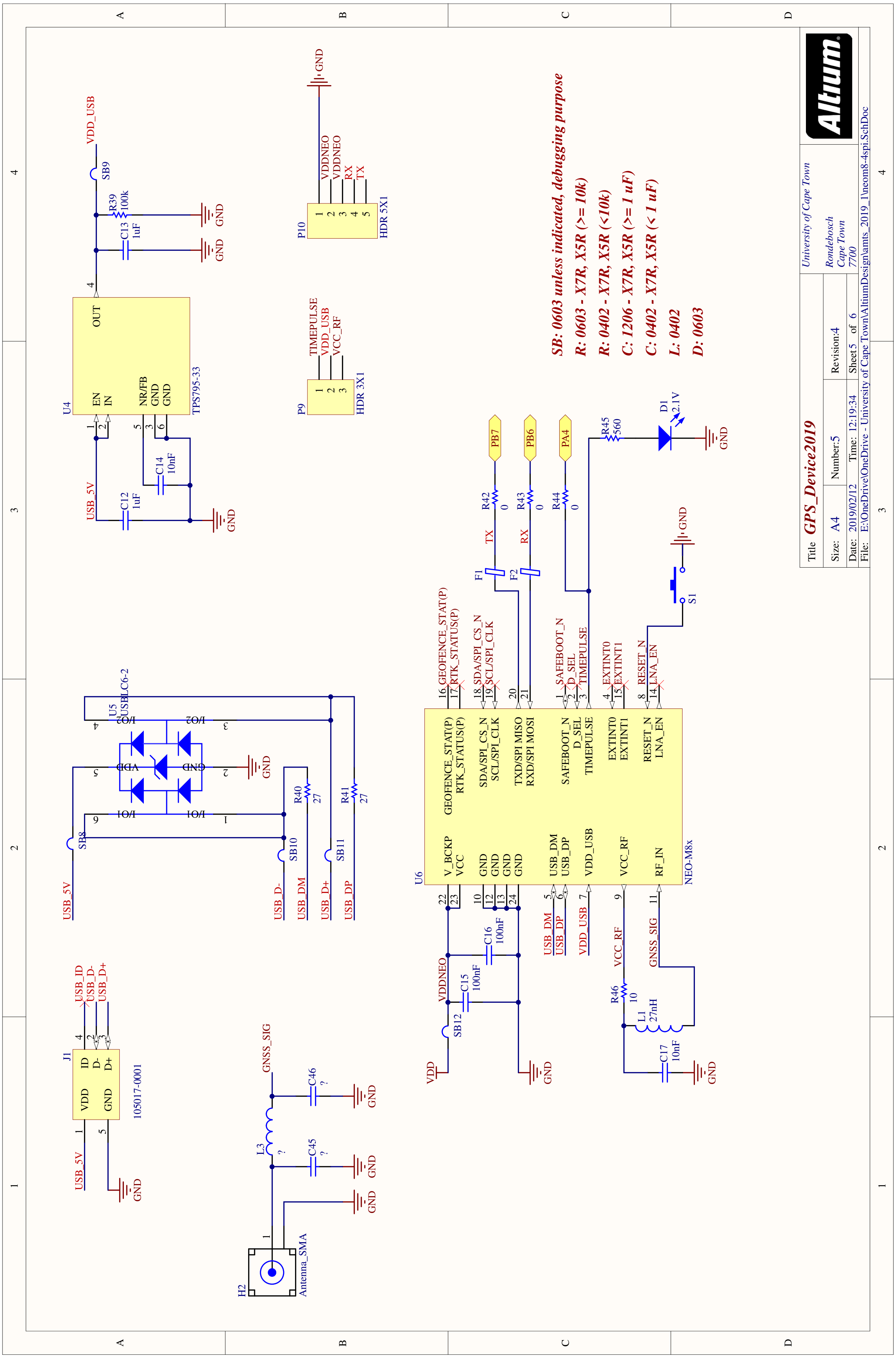

**Figure F.5:** Sheet 5 of 6 of the captured schematic of a sensor unit, capturing the GPS receiver and the GPS antenna.

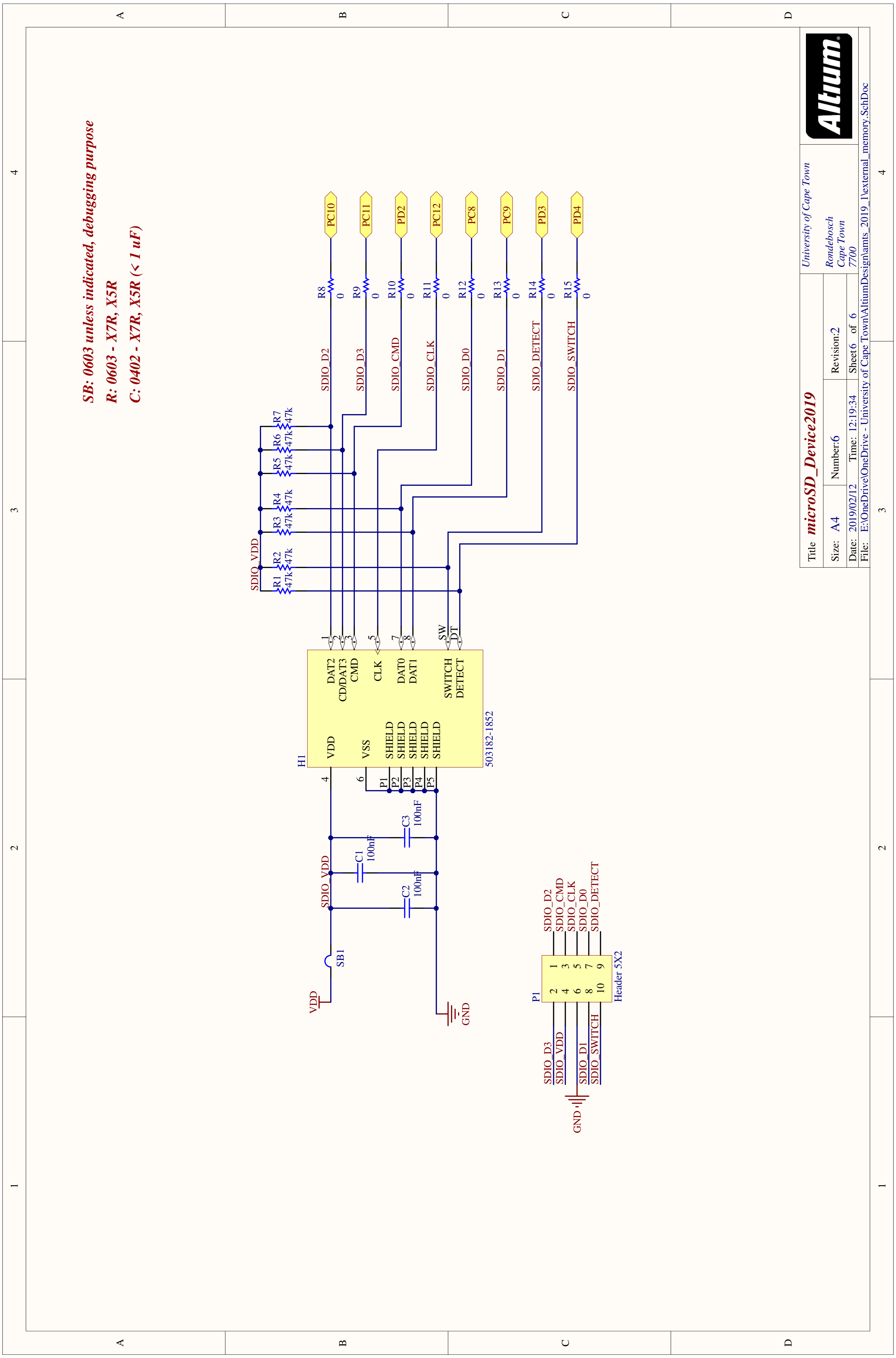

**Figure F.6:** Sheet 6 of 6 of the captured schematic of a sensor unit, capturing the non-volatile memory (microSD card).

# Appendix G

# Cost and Pricing

## G.1 Cost of Developed Sensor

**Table G.1:** The cost to assemble 12 sensors for the multi-receiver DGPS/MEMS-IMU fusion MOCAP system

| Comment | Total Qty | Total Cost [R] |
|---|---|---|
| Capacitor (SMT 0402) | 348 | 45.36 |
| Capacitor(SMT 0603) | 120 | 587.52 |
| Capacitor(SMT 1206) | 24 | 9.5 |
| BLM15HD102SN1 | 24 | 65.52 |
| Antenna (SMA) | 12 | 563.7 |
| 105017-0001 | 24 | 271.58 |
| Inductor(SMT 0805) | 12 | 41.76 |
| Resistor(SMT 0603) | 168 | 122.02 |
| Resistor(SMT 0402) | 228 | 183.03 |
| TLV2217-33 | 12 | 220.53 |
| BMX055 | 12 | 0 (sample) |
| BMP280 | 12 | 390.38 |
| TPS795-33 | 12 | 388.37 |
| USBLC6-2 | 24 | 181.02 |
| NEO-M8x | 12 | 6000 |
| STM32F407VGT6 | 12 | 2237.52 |
| STMPS2141STR | 12 | 75.02 |
| AA.105.301111 | 12 | 3440 |
| PCB fabrication | | 1500 |
| Stencil | | 1000 |
| PCB assembly | | 4800 |
| **Total cost for 12 sensors** | | 22122.83 |

## G.2 Pricing of Commercial MOCAP System

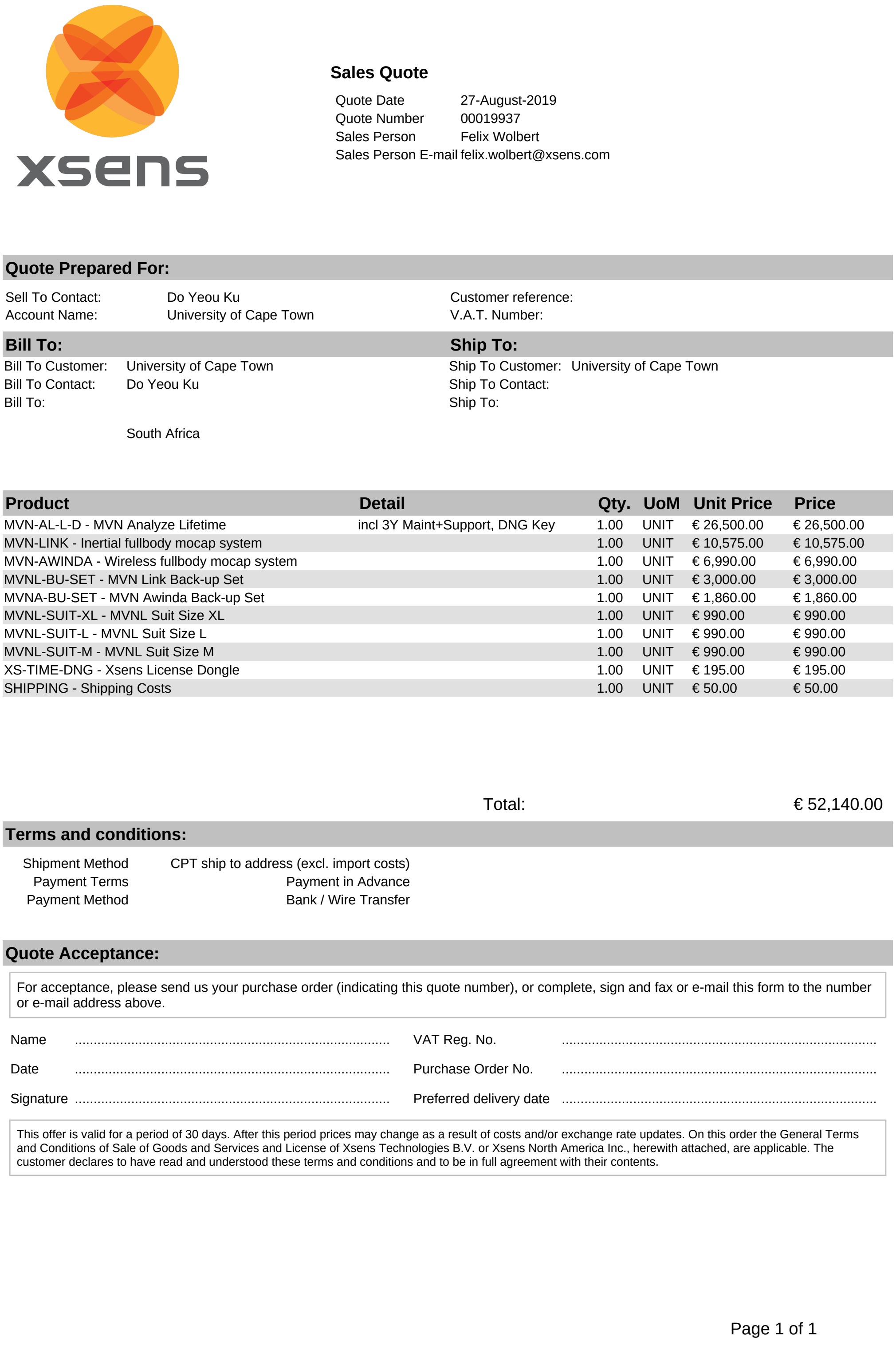

**Sales Quote**

| | |
|---|---|
| Quote Date | 27-August-2019 |
| Quote Number | 00019937 |
| Sales Person | Felix Wolbert |
| Sales Person E-mail | felix.wolbert@xsens.com |

**Quote Prepared For:**

| | | | |
|---|---|---|---|
| Sell To Contact: | Do Yeou Ku | Customer reference: | |
| Account Name: | University of Cape Town | V.A.T. Number: | |

**Bill To:**

Bill To Customer: University of Cape Town
Bill To Contact: Do Yeou Ku
Bill To:

South Africa

**Ship To:**

Ship To Customer: University of Cape Town
Ship To Contact:
Ship To:

| Product | Detail | Qty. | UoM | Unit Price | Price |
|---|---|---|---|---|---|
| MVN-AL-L-D - MVN Analyze Lifetime | incl 3Y Maint+Support, DNG Key | 1.00 | UNIT | € 26,500.00 | € 26,500.00 |
| MVN-LINK - Inertial fullbody mocap system | | 1.00 | UNIT | € 10,575.00 | € 10,575.00 |
| MVN-AWINDA - Wireless fullbody mocap system | | 1.00 | UNIT | € 6,990.00 | € 6,990.00 |
| MVNL-BU-SET - MVN Link Back-up Set | | 1.00 | UNIT | € 3,000.00 | € 3,000.00 |
| MVNA-BU-SET - MVN Awinda Back-up Set | | 1.00 | UNIT | € 1,860.00 | € 1,860.00 |
| MVNL-SUIT-XL - MVNL Suit Size XL | | 1.00 | UNIT | € 990.00 | € 990.00 |
| MVNL-SUIT-L - MVNL Suit Size L | | 1.00 | UNIT | € 990.00 | € 990.00 |
| MVNL-SUIT-M - MVNL Suit Size M | | 1.00 | UNIT | € 990.00 | € 990.00 |
| XS-TIME-DNG - Xsens License Dongle | | 1.00 | UNIT | € 195.00 | € 195.00 |
| SHIPPING - Shipping Costs | | 1.00 | UNIT | € 50.00 | € 50.00 |

Total: € 52,140.00

**Terms and conditions:**

| | |
|---|---|
| Shipment Method | CPT ship to address (excl. import costs) |
| Payment Terms | Payment in Advance |
| Payment Method | Bank / Wire Transfer |

**Quote Acceptance:**

For acceptance, please send us your purchase order (indicating this quote number), or complete, sign and fax or e-mail this form to the number or e-mail address above.

| | | | |
|---|---|---|---|
| Name | ................................................................................... | VAT Reg. No. | ................................................................................... |
| Date | ................................................................................... | Purchase Order No. | ................................................................................... |
| Signature | ................................................................................... | Preferred delivery date | ................................................................................... |

This offer is valid for a period of 30 days. After this period prices may change as a result of costs and/or exchange rate updates. On this order the General Terms and Conditions of Sale of Goods and Services and License of Xsens Technologies B.V. or Xsens North America Inc., herewith attached, are applicable. The customer declares to have read and understood these terms and conditions and to be in full agreement with their contents.

Page 1 of 1

**Figure G.1:** Sales quote for suit-inertial MOCAP system from *Xsens Technologies*.

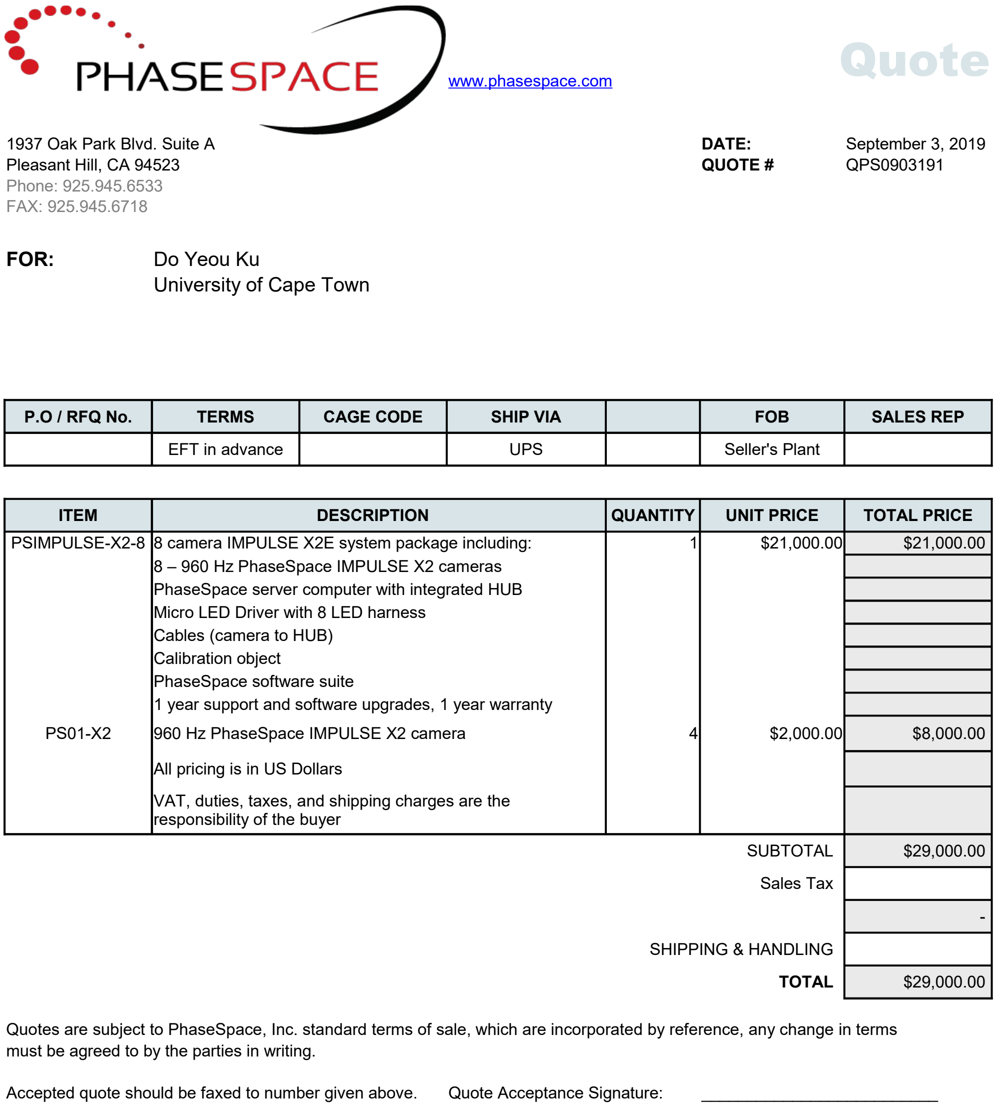

PHASESPACE www.phasespace.com

**Quote**

1937 Oak Park Blvd. Suite A
Pleasant Hill, CA 94523
Phone: 925.945.6533
FAX: 925.945.6718

**DATE:** September 3, 2019
**QUOTE #** QPS0903191

**FOR:** Do Yeou Ku
University of Cape Town

| P.O / RFQ No. | TERMS | CAGE CODE | SHIP VIA | | FOB | SALES REP |
|---|---|---|---|---|---|---|
| | EFT in advance | | UPS | | Seller's Plant | |

| ITEM | DESCRIPTION | QUANTITY | UNIT PRICE | TOTAL PRICE |
|---|---|---|---|---|
| PSIMPULSE-X2-8 | 8 camera IMPULSE X2E system package including:<br>8 – 960 Hz PhaseSpace IMPULSE X2 cameras<br>PhaseSpace server computer with integrated HUB<br>Micro LED Driver with 8 LED harness<br>Cables (camera to HUB)<br>Calibration object<br>PhaseSpace software suite<br>1 year support and software upgrades, 1 year warranty | 1 | $21,000.00 | $21,000.00 |
| PS01-X2 | 960 Hz PhaseSpace IMPULSE X2 camera | 4 | $2,000.00 | $8,000.00 |
| | All pricing is in US Dollars | | | |
| | VAT, duties, taxes, and shipping charges are the responsibility of the buyer | | | |

| | |
|---|---|
| SUBTOTAL | $29,000.00 |
| Sales Tax | |
| | - |
| SHIPPING & HANDLING | |
| **TOTAL** | $29,000.00 |

Quotes are subject to PhaseSpace, Inc. standard terms of sale, which are incorporated by reference, any change in terms must be agreed to by the parties in writing.

Accepted quote should be faxed to number given above. Quote Acceptance Signature: ____________________________

**Figure G.2:** Sales quote for 12-camera indoor optical MOCAP system from *PhaseSpace*.

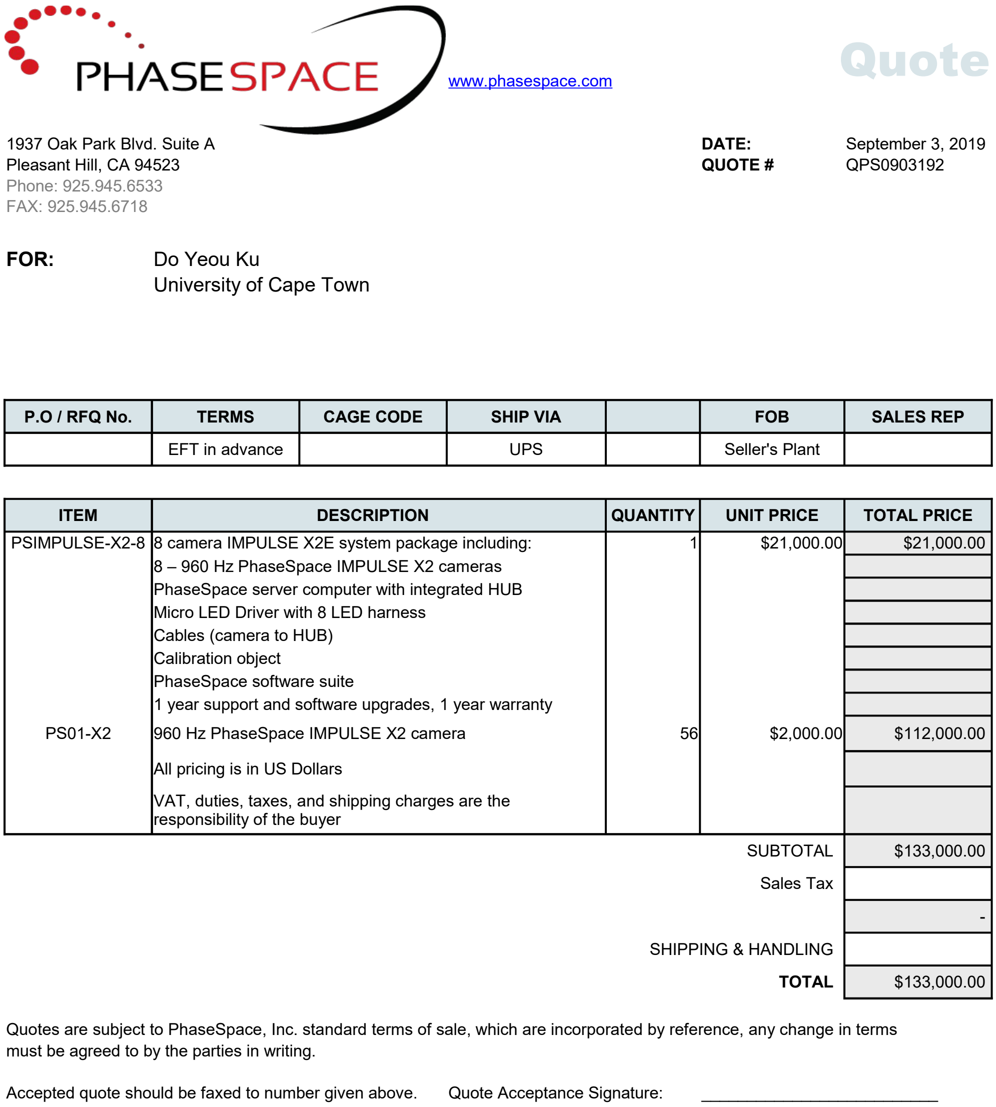

PHASESPACE www.phasespace.com

**Quote**

1937 Oak Park Blvd. Suite A
Pleasant Hill, CA 94523
Phone: 925.945.6533
FAX: 925.945.6718

**DATE:** September 3, 2019
**QUOTE #** QPS0903192

**FOR:** Do Yeou Ku
University of Cape Town

| P.O / RFQ No. | TERMS | CAGE CODE | SHIP VIA | | FOB | SALES REP |
|---|---|---|---|---|---|---|
| | EFT in advance | | UPS | | Seller's Plant | |

| ITEM | DESCRIPTION | QUANTITY | UNIT PRICE | TOTAL PRICE |
|---|---|---|---|---|
| PSIMPULSE-X2-8 | 8 camera IMPULSE X2E system package including: | 1 | $21,000.00 | $21,000.00 |
| | 8 – 960 Hz PhaseSpace IMPULSE X2 cameras | | | |
| | PhaseSpace server computer with integrated HUB | | | |
| | Micro LED Driver with 8 LED harness | | | |
| | Cables (camera to HUB) | | | |
| | Calibration object | | | |
| | PhaseSpace software suite | | | |
| | 1 year support and software upgrades, 1 year warranty | | | |
| PS01-X2 | 960 Hz PhaseSpace IMPULSE X2 camera | 56 | $2,000.00 | $112,000.00 |
| | All pricing is in US Dollars | | | |
| | VAT, duties, taxes, and shipping charges are the responsibility of the buyer | | | |

| | |
|---|---|
| SUBTOTAL | $133,000.00 |
| Sales Tax | |
| | - |
| SHIPPING & HANDLING | |
| **TOTAL** | $133,000.00 |

Quotes are subject to PhaseSpace, Inc. standard terms of sale, which are incorporated by reference, any change in terms must be agreed to by the parties in writing.

Accepted quote should be faxed to number given above. Quote Acceptance Signature: ____________________________

**Figure G.3:** Sales quote for 64-camera indoor optical MOCAP system from *PhaseSpace*.

# APPLICATION FORM

**Please Note:**
Any person planning to undertake research in the Faculty of Engineering and the Built Environment (EBE) at the University of Cape Town is required to complete this form **before** collecting or analysing data. The objective of submitting this application *prior* to embarking on research is to ensure that the highest ethical standards in research, conducted under the auspices of the EBE Faculty, are met. Please ensure that you have read, and understood the **EBE Ethics in Research Handbook** (available from the UCT EBE, Research Ethics website) prior to completing this application form: http://www.ebe.uct.ac.za/ebe/research/ethics1

| **APPLICANT'S DETAILS** | | |
|---|---|---|
| Name of principal researcher, student or external applicant | | Do Yeou Ku |
| Department | | Electrical Engineering Department |
| Preferred email address of applicant | | Kxxdoy001@myuct.ac.za |
| If Student | Your Degree: e.g., MSc, PhD, etc | MSc |
| | Credit Value of Research: e.g., 60/120/180/360 etc | 180 |
| | Name of Supervisor (if supervised): | Dr Amir Patel |
| If this is a research contract, indicate the source of funding/sponsorship | | RC&I Explorer and RC&I Concept fund |
| Project Title | | MEMS-IMU and GPS/RTK integration for motion capture system |

**I hereby undertake to carry out my research in such a way that:**

- there is no apparent legal objection to the nature or the method of research; and
- the research will not compromise staff or students or the other responsibilities of the University;
- the stated objective will be achieved, and the findings will have a high degree of validity;
- limitations and alternative interpretations will be considered;
- the findings could be subject to peer review and publicly available; and
- I will comply with the conventions of copyright and avoid any practice that would constitute plagiarism.

| **SIGNED BY** | Full name | Signature | Date |
|---|---|---|---|
| **Principal Researcher/ Student/External applicant** | Do Yeou Ku | | 24 Oct 2018 |

| **APPLICATION APPROVED BY** | Full name | Signature | Date |
|---|---|---|---|
| **Supervisor** (where applicable) | Dr Amir Patel | | 24 Oct 2018 |
| **HOD (or delegated nominee)** Final authority for all applicants who have answered NO to all questions in Section1; and for all Undergraduateresearch (Including Honours) | A/Prof Olabisi Falowo<br>~~Prof Edward Boje~~ | | 30/10/18<br>~~24 Oct 2018~~ |
| **Chair : Faculty EIR Committee** For applicants other than undergraduate students who have answered YES to any of the above questions. | | | |